Defects have a strong influence on phase transitions, especially in systems with lower dimensionality. In quasi-1D or 2D systems that exhibit a Charge Density Wave (CDW) transition, due the collective nature of the phenomena, a small proportion of microscopic disorder can control the global properties. Defects would produce pre-transitional effects, affecting CDW. On the other hand, the interaction of mobile defects with CDW would lead to alignment of defects, or Defect Density Waves (DDW). In this dynamic model the distribution of defects would no longer be either random or static. Instead defects would align their positions to optimize the energy of the pinned CDW.

A new view of the phase transitions occurring in quasi-2D systems: α-phase of Sn/Ge(111) and α-phase of Sn/Si(111) is presented. While previous studies were devoted to the elucidating the nature of the room temperature (RT) and low temperature (LT) phases, my Variable Temperature STM observations showed how these phases evolve. It has become clear that point defects – substitutional atoms and vacancies – play a crucial role. A response of the system to a defect in its vicinity has a form of density waves with the symmetry of LT phase. These waves have a short range at RT and decay exponentially with the distance from defects. When temperature is lowered the range of these waves grows. As characteristic decay length of the perturbation reaches the average distance between defects, the defect-defect interaction becomes strong enough to make defects exchange their positions with their nearest neighbors. This motion brings waves originated on different defects into coherence and to the disorder-order phase transition in defect distribution. Defects smear out the critical temperature and change the properties of the phase transition. My STM observations and modeling imply that the transition temperature of the pure system is the temperature at which the decay length of defect-induced waves becomes infinite. For Sn/Ge(111) this temperature is ~ 70 K. This is 140 K lower than the temperature measured by electron diffraction with 3% density of defects. A new model is presented that predicts the configuration of domain walls at LT.

ROLE OF DEFECTS IN TWO-DIMENSIONAL PHASE TRANSITIONS

A Dissertation

Presented for the

Doctor of Philososphy

Degree

The University of Tennessee, Knoxville

ANATOLI V. MELECHKO

May 2001

DEDICATION

To my parents

Nina and Vasili Meleshko,

and to my brothers Nikolai and Sergei,

who made me who I am

ACKNOWLEDGMENTS

My graduate career was a piece of sheer luck. Deep in Siberia I was approached by Alexander Karpushin (who was contacted by his friend Evgenii Chulkov) who told me that “some American professor was looking for an ‘aspirant’ (Russian term for a graduate student). I immediately said yes. All that mattered then was that I could do physics again! No more selling tires!

Now after 4.5 years, I really appreciate how lucky I was that this “some American professor” happened to be Ward Plummer. I am very grateful to Ward for giving me an opportunity to work on the leading edge of physics and most importantly for teaching me how to be on that leading edge.

One of the big advantages of working with Ward was that he attracted a lot of excellent physicists. I would like to thank a lot of people without whom this thesis would never happen. I would like to thank Hanno Weitering who has taught me a lot in many fields, whether it is science or the art of cleaning chamber from contamination with ‘laughing gas’. It so happened that I missed our STM guru, Joe Carpinelli, just by about a month, and Hanno was the one who carried over to me the art of JEOL STMing.

I would like to thank Jens Braun who taught me how to work. I am still striving to reach the level of efficiency he set up. The day he arrived Ward told us that I had to be chained to him. For a year an invisible chain was connecting us in the best collaboration of my life. I would call work with him a definition of partnership (no chance to goof off). The results presented in the Part 4 are the product of this collaboration. Part 6 is the result of work with another great experimentalist attracted by Ward, Luca Ottaviano. What is

the most important that the work and ‘life’ (as in ‘get a life’) with these two people acquired me two of my best friends.

I want to thank Aubrey Hanbicki for teaching me America, Nikki Page for helping me to survive in America, Girish Gvalani for making my ‘cultural shock’ in the new environment (ORNL) smoothed out and for his friendship. I thank David Zehner for his gentle hospitality in his kingdom. My special thanks go to Joe Carpinelli. This thesis is build upon the heritage he left for me. I am grateful to Larry Pai with whom we learned the art of putting together a new laboratory, to John Wendelken who let us use his designs, equipment, and his wisdom, Rene Matzdorf, for sharing his knowledge of experimentalist and attempts to bring any order to the STM lab, Myung Noh (aka “Dr. No”), Karsten Pohl, Jiandi Zhang, Kathy Lin and Ismail for giving me their insights in experimental physics. I would like thank Alexander Chernyshev for sharing his encyclopedic knowledge of physics and his friendship we carry on from college years across the countries and continents. I am grateful to many people for fixing things (Jim Hendrix), cutting wafers (Pam Flemming), machining parts (Jodie Millward, Randy McMillan, Alvin Peak, and Frank Spencer), and letting me ‘borrow’ stuff (Gary Ownby). Thanks to Mary Jo Fox for taking care of me in the last part of this adventure. I had great time with Ismail, JP (John Pierce), Dane Gillespie, Alex Thesen and He Jian learning, working, having fun and just sharing the fate of being Ward’s students.

I would like to thank Marianne Breinig for training me to overcome the dreaded Prelims, and who is the only hope for many students on this path (her handwritten notes are passed from generation to generation), John Quinn for teaching me solid state physics and how it was being made (he was the first American I could actually understand in my

first month in US), and Geoff Canright for his gentle and challenging way of teaching Classical Mechanics.

My deepest thanks and appreciation goes to Nagiza for her friendship and support, and for keeping me sane these years and to our great little helper Katya for adding fun to the process.

I would also like to extend my thanks the thesis committee members (Profs. David Mandrus, David Joy, John Quinn) for their time and just for agreeing to review the following 300 pages.

ABSTRACT

Imperfections and defects have a strong influence on phase transitions, especially in systems with lower dimensionality, where fluctuations can be strong enough to prevent long-range order. In quasi-1D or 2D systems that exhibit a Charge Density Wave transition defects play a very special role. There, due the collective nature of the phenomena, a small proportion of microscopic disorder can control the global properties. Defects would produce pre-transitional effects such as charge oscillations in their vicinity, affecting CDW. On the other hand, the interaction of mobile defects with CDW would lead to alignment of defects, or Defect Density Waves (DDW). In this dynamic model the distribution of defects would no longer be either random or static. Instead defects would align their positions to optimize the energy of the pinned CDW.

In this thesis I present a new view of the phase transitions occurring in quasi-2D systems of ultra-thin films of a metal deposited on a semiconductor surface: α-phase of Sn/Ge(111) and α-phase of Sn/Si(111). While most of the previous studies were devoted to the elucidating the nature of the room temperature (RT) and low temperature (LT) phase, that is, electronic and lattice structure at two temperatures, above and below the transition temperature, my Variable Temperature STM observations showed how these phases evolve into each other. From these observations it has become clear that point defects – substitutional atoms and vacancies – play a crucial role. The perturbation of the lattice and electronic structure induced as a response of the system to a defect in its vicinity has a form of density waves with the symmetry of LT phase. These waves have a

short range at RT and decay exponentially with the distance from defects. When the temperature is lowered the range of these waves grows. As characteristic decay length of the perturbation reaches the average distance between defects, the density wave mediated defect-defect interaction becomes strong enough to make defects exchange their positions with their nearest neighbors. This motion brings waves originated on different defects into coherence and defects into partial ordering leading to the disorder-order phase transition in defect distribution. Defects dictate the structure of phases both above and below critical temperature. Moreover their presence smears out the critical temperature and changes the properties of the phase transition. My STM observations and modeling imply that the transition temperature of the pure system without defects should be the temperature at which the decay length of defect-induced waves becomes infinite. For Sn/Ge(111) this temperature is ~ 70 K. This is about **140** K (!!!) lower than the temperature measured by electron diffraction and still widely cited in literature. The sharp domain walls are the features that distinguish the low temperature phase. A new model is presented that allows to predict the configuration of domain walls for a given defect distribution.

TABLE OF CONTENTS

LIST OF TABLES

LIST OF FIGURES

Part 1

Physics in Two Dimensions

1.1. Introduction

Condensed Matter Physics provides a framework for describing the behavior of very large groups of interacting particles (of order $10^{23\text{-}27}$). We cannot possibly predict the motion of each particle in such a big system. We can however predict some macroscopic properties. First of all, this requires knowledge of interactions between particles on microscopic level. Probably the most important concept that lies in the basis of Condensed Matter Physics is that macroscopic properties are governed by conservation laws and broken symmetries.

Phase transitions are the phenomena associated with the processes of breaking symmetry. At high temperatures, all systems are disordered, uncorrelated, uniform and isotropic. This high temperature state has the full rotational and translational symmetry of free space. As temperature is lowered, new thermodynamically stable states condense. These states have progressively lower symmetry as temperature is lowered. For example, a periodic crystal is invariant with respect to only a discrete set of translations rather than to the continuum of translations that leave the high-temperature state unchanged.

The behavior of the system is strongly affected by its dimensionality. There are many materials and systems that behave as though they were either one- or two-dimensional rather than three-dimensional. A large variety of new phenomena emerge when the dimensionality is reduced to two (2D), one (1D) or zero (0D) dimensions due to change in interactions. Phase transitions also strongly depend on dimensionality. As dimension is reduced, fluctuations become increasingly important. Below certain critical dimension, fluctuations become so large that they can destroy the

ordered state and finite-temperature phase transition. For instance a theorem had been proven that long-range order cannot occur in a one-dimensional system whose elements interact through finite-range forces (Landau 1970).

Associated with each broken-symmetry phase are distortions, defects, and dynamical modes that provide paths to restore the symmetry of the original high-temperature state. The properties of each broken-symmetry phase are largely controlled by these distortions, defects, and modes. It is generally believed, that defects play a larger role in phase transitions in low-dimensional systems (Nelson 1983), though microscopic evidence has been limited. The invention of Scanning Tunneling Microscope opened the opportunity to gain this knowledge.

Surfaces of solids are an ideal playground to study physics in reduced dimensionality, since surface phenomena are naturally bound to 2D. Undoubtedly, our abilities were recently greatly enhanced by the invention of Scanning Tunneling Microscope (STM) by Binning and Rorer in 1981 (Binning 1982). This instrument allows us to "see" on the atomic scale. We don't have to derive (or usually guess) the behavior of atoms from indirect transport or k-space measurements. The "atomic vision" provided by STM promises a new level of understanding of the processes occurring in real space with atomic resolution. This ability is extremely important in understanding effects that involve microscopic spatial inhomogeneities in the system. One such area where the STM could be instrumental is the study of the influence of defects and impurities on electronic properties and structure of surfaces and phase transitions.

In this thesis I present a new view of the phase transitions occurring in quasi-2D systems of ultra-thin films of a metal deposited on a semiconductor surface. The system

studied was α-phase of Sn/Ge(111) and α-phase of Sn/Si(111). While most of the previous studies were devoted to the elucidating the nature of the room temperature (RT) and low temperature (LT) phase, that is, electronic and lattice structure at temperatures above and below the transition temperature, my variable temperature STM observations showed the evolution of these phases with temperature. From these observations it has become clear that point defects – substitutional atoms and vacancies – play a crucial role. The perturbation of the lattice and electronic structure induced as a response of the system to a defect in its vicinity has the form of density waves with the symmetry of LT phase. These waves have a short range at RT and decay exponentially with the distance from defects. When the temperature is lowered the range of these waves grows. Figure 1.1 displays a calculated image of the pattern that is seen in the STM image induced by a defect, with balls representing atoms and their brightness representing relative charge density (See Part 4 for details.). As characteristic decay length of the perturbation reaches the average distance between defects, the density-wave-mediated defect-defect interaction becomes strong enough to force defects exchange their positions with their nearest neighbors. This motion brings the waves originated on different defects into coherence and defects into partial ordering leading to the disorder-order phase transition in defect distribution. Defects dictate the structure of phases both above and below the critical temperature. Moreover their presence can lead to a change of the critical temperature. My STM observations and modeling imply that the transition temperature of the pure system without defects should be the temperature at which the decay length of defect-induced waves becomes infinite. For Sn/Ge(111) this temperature is ~ 70 K. This

a)

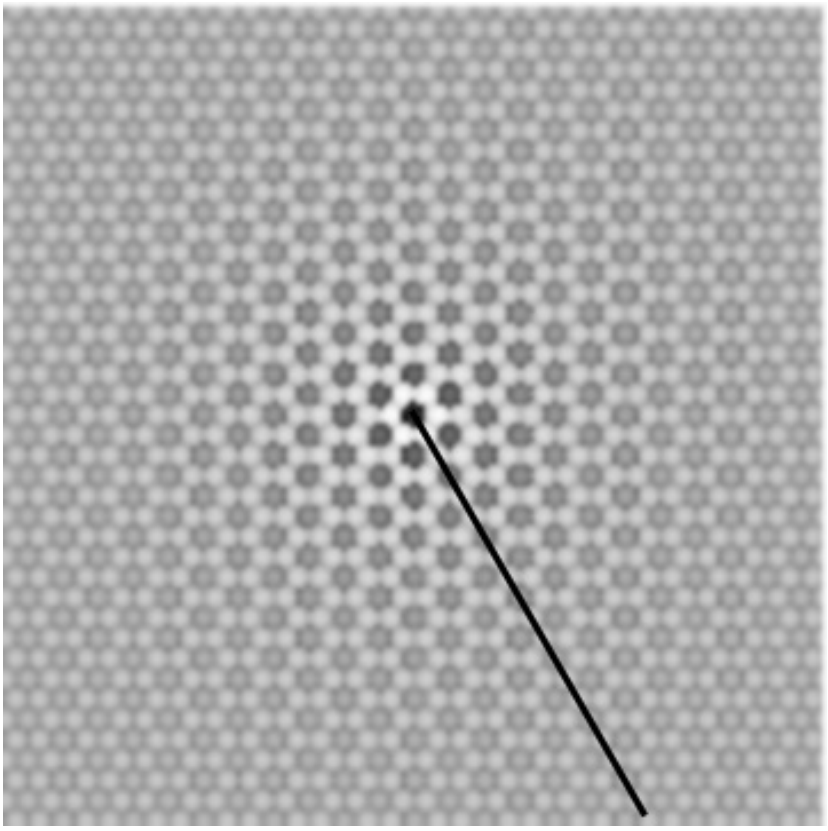

b)

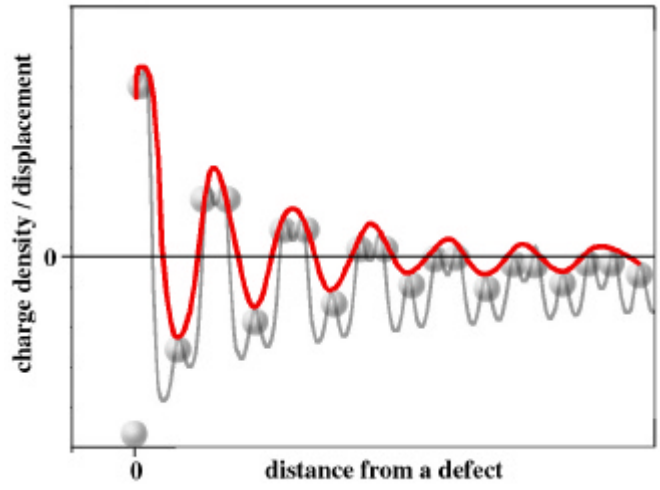

Figure 1.1 Defect-induced waves

a) Pattern induced by a defect. Gray balls represent atoms. The brightness corresponds to charge density and/or displacement out off plane.

The light gray curve is a line profile along the black line in a). A solid (red) curve is the exponentially decaying cosine envelope function. (atomic displacement is not in scale)

is about **140** K (!!!) lower than the temperature measured by electron diffraction for surfaces with 2-4 % of defects. The sharp domain walls are the features that distinguish the low temperature phase. I introduced a new model that allows one to predict the configuration of domain walls for a given defect distribution. The results presented in this thesis elucidate the role of defects in 2D phase transitions.

1.2. Phase Transitions: Basic Concepts

Let me first introduce the interrelated concepts associated with the physics of phase transitions such as broken symmetry, order parameter, long-range order, critical exponents, correlation functions, etc.

Phase transition (PT) ***is*** *called a transition between two equilibrium phases of matter whose signature is a singularity or discontinuity in the derivatives of a thermodynamic potential.* (Chaikin 1995)

Although this could be a working definition of a phase transition, the issue of defining a phase transition in the "real" world is not that trivial (White 1979). The definition given above holds for many very different phase transitions. The thermodynamic potential could be a function of some parameter, such as pressure p, concentration of doping x, and so on. In the rest of the dissertation though a more narrow definition will be used, where such a thermodynamic potential is Free depending on temperature,

$$F = U - TS \,. \qquad (1.1).$$

Phase transitions occur because all systems in thermodynamic equilibrium seek to minimize their free energy. One phase will change to another at a given temperature because different phases partition their free energy between the internal energy U(T) and the entropy S(T) in different ways. This implies that a PT can happen only in systems of interacting particles (White 1979). In the absence of interaction there will be no discontinuity in the free energy function or any of its temperature derivatives as the system is cooled from its high-temperature state to its low-temperature state of zero entropy.

One of the most frequently used examples is the ferromagnetic-paramagnetic transition. Ferromagnetism is very complex phenomenon and I am going to use only a sketchy description. Certain materials (iron, nickel, cobalt, etc.) can be magnetized at room temperature. Microscopically speaking this means that electrons in an incomplete inner shell have their spins aligned in one and the same direction (Fig. 1.2a). Since there is a magnetic moment associated with every spin, such alignment implies that all these magnetic moments add, thus producing a macroscopic magnet. When a ferromagnet is heated above a certain temperature T_c called a Curie temperature, its magnetization disappears, and the material becomes paramagnetic. The tendency of the spins to align is due to an interaction between them that favors such a configuration. At high temperatures thermal agitation tends to destroy this configuration (Fig. 1.2b), thus causing the magnetization to vanish. In this case the heat capacity at constant pressure C_p, which is proportional to the second derivative of free energy has a singularity at $T=T_c$ (Fig. 1.3a).

One of the starting points to gain the understanding of phase transitions is based on symmetry and in particular the related concept of long-range order (LRO).

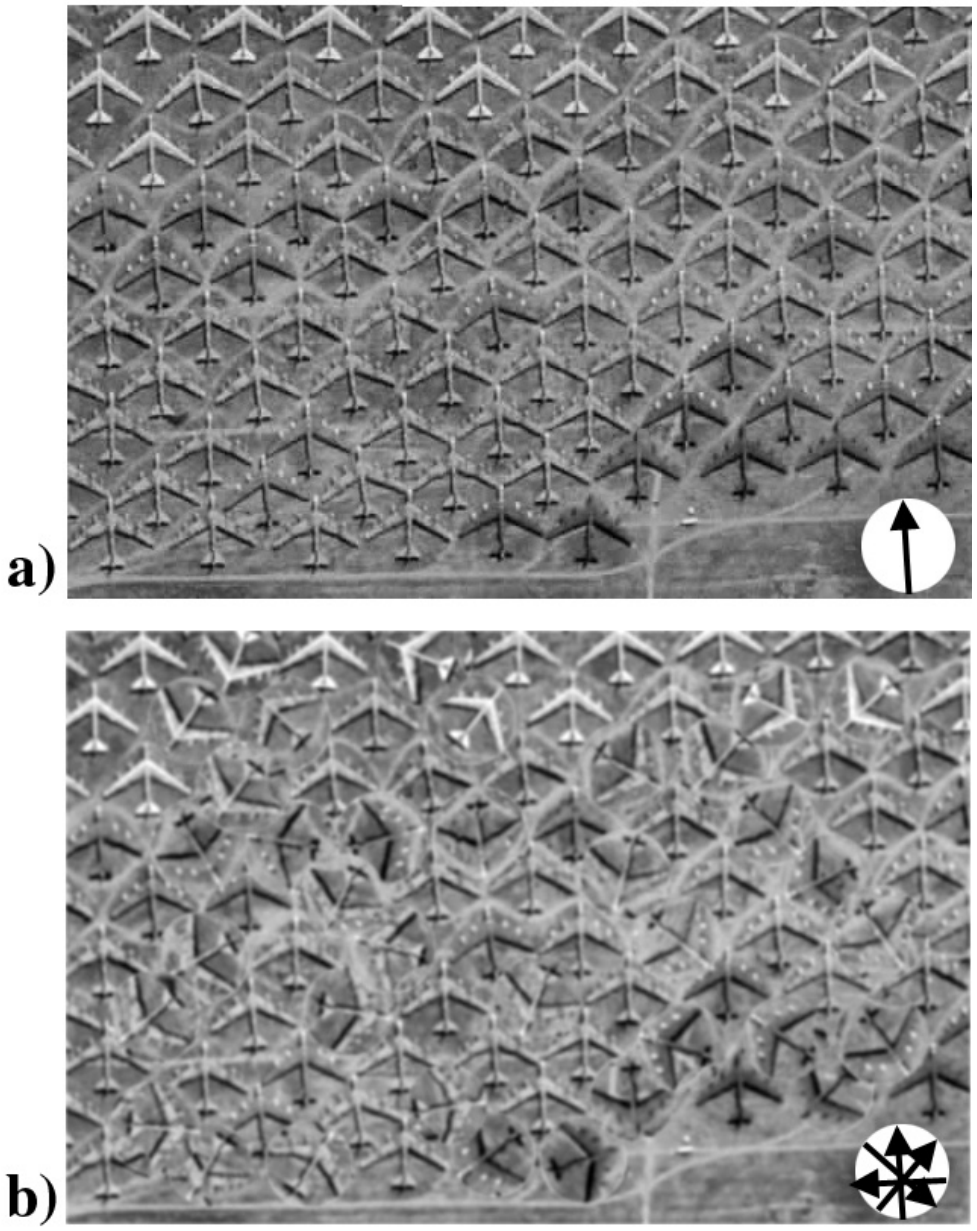

Figure 1.2 Ferromagnetic-Paramagnetic phase transition demonstrated by U.S. Air Force (Tuscon, Arizona).

a) T<Tc (T~0K) (military ordered state)
b) T>Tc

(from http://www.terraserver.microsoft.com)

Long-range order (LRO) *refers to the situation in which the value of some property at a given point in a system is correlated with its value at a point infinitely far away.*

The most general description of PT is based on the fact that most of the PTs are characterized by appearance of some nonzero quantity in the ordered state. Such quantity is called the order parameter.

Order parameter (OP) *is a parameter distinguishing an ordered from a disordered phase.*

More generally, the order parameter is the average $<f>$ of an operator, f, which is a function of the dynamical variables in the system Hamiltonian H. $<f>$ is zero in the disordered (high-temperature, entropy-dominated equilibrium) phase and nonzero in the ordered (broken symmetry) phase. It is chosen to have values in different equivalent ordered phases reflecting the symmetry of the Hamiltonian H (i.e. transform under an irreducible representation of the symmetry group of H.) (Chaikin 1995)

This concept is very convenient but finding the appropriate OP is not always easy. And usually its determination is equivalent to understanding the phase transition. In case of ferromagnet, the magnetization M, zero in the high-temperature phase and non-zero in the low-temperature phase, is such an order parameter (Fig. 1.3b).It grows when the temperature falls, and has a maximum at T=0. All spins are aligned in the same direction. For $0<T<Tc$ the spins still have a tendency to align in the same direction, but thermal agitation allows only a partial alignment.

Other examples of OPs found in nature are: density difference between liquid and vapor, the value of the Fourier components (crystallization), energy gap (superconductivity), and amplitude of a specific phonon mode (structural phase

a)

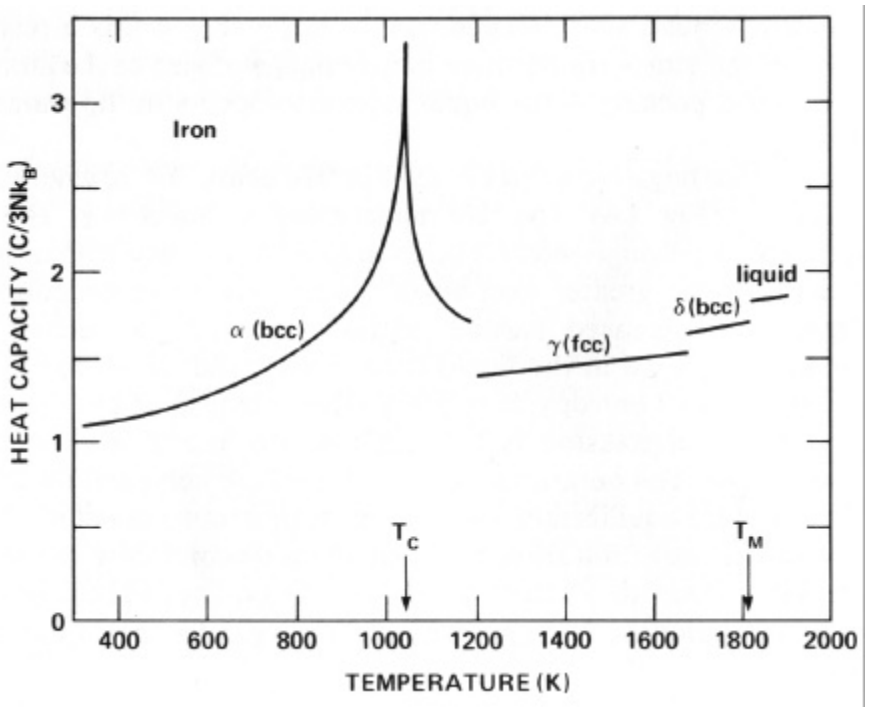

b)

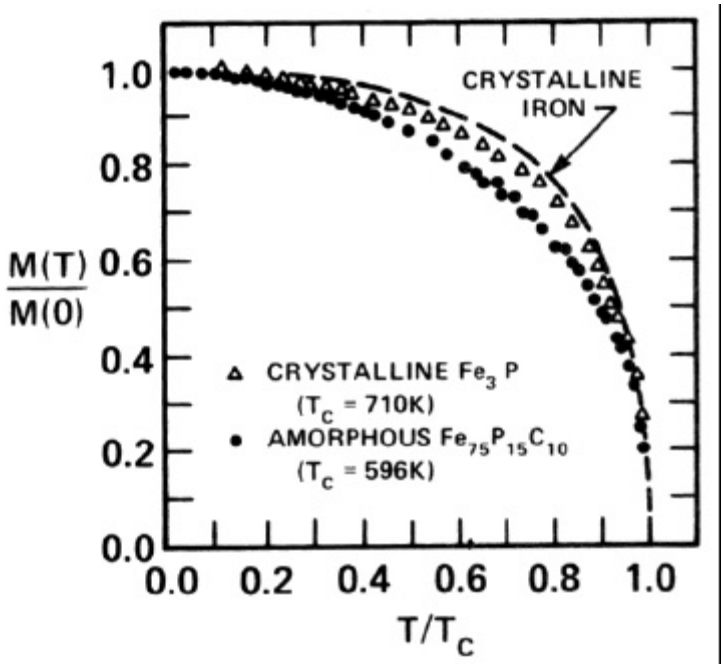

Figure 1.3 Heat capacity and magnetization of Fe

a) Heat capacity of iron as a function of temperature. T_c is the Curie point. (Adopted from (Orr 1967))

b) Temperature dependence of the magnetization in Fe (Adopted from (Tsuei 1976))

transitions). In Part5 I will define two OPs for two interlocked symmetry lowering PTs in Sn/Ge(111): root mean square of charge on an atom for CDW transition and correlation probability of the defect distribution in defect ordering transition.

Broken symmetry is *the term applied to the situation in which the ground state of a system does not have the full symmetry possessed by the Hamiltonian H used to describe the system.*

This notion is very easy to illustrate on a mechanical example. Let's consider a vertical cylindrical rod subject to a vertical compressive force **F** along its axis (Fig. 1.4). Under large-enough force **F** the rod eventually buckles, even though the situation is, *a priori*, perfectly invariant under rotations around the axis. This is the case of *broken symmetry*.

Spontaneous magnetization of a ferromagnet is a nice example of broken symmetry. The spin Hamiltonian is rotation-invariant, and there are no preferred directions in space. For T>Tc one can identify no preferred direction in ferromagnetic sample either. By contrast, for T<Tc there is a preferred direction, that of the magnetization. The state of the sample is no longer invariant under all rotations, but only under rotations around axes parallel to the magnetization direction.

Order of a phase transition is defined by the way in which the symmetry is broken. Most of them fall into one of the two categories (Landau 1970; White 1979):

1) **first-order** if the order parameter is discontinuous across the transition
2) **continuous (second-order)** if the order parameter is continuous

Even though this classification covers most of the transitions, there are others that cannot be classified this way (e.g. Kosterlitz-Thoughless type transitions (Kosterlitz 1973)). In a

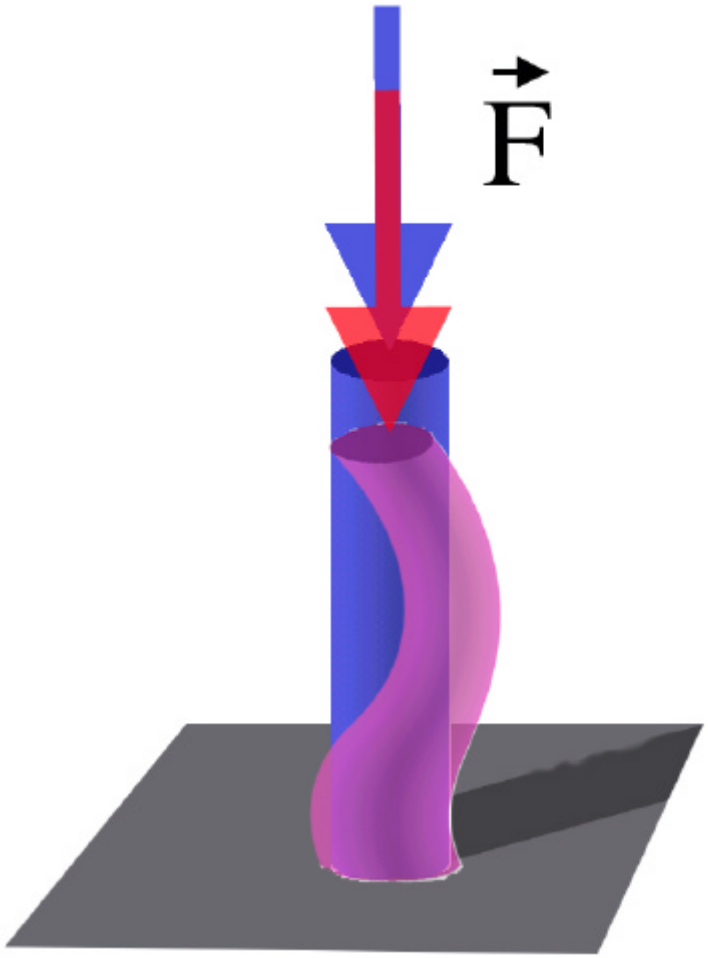

Figure 1.4 Broken symmetry

If a force applied in a vertical direction to a vertically standing rod it will eventually bend. Even though the Hamiltonian of such a system is invariant under rotations around vertical axes, its solution is not.

first-order phase transition, a discontinuous change in the particle configuration occurs at the transition temperature Tc. This implies that quantities such as internal energy U or the entropy S change discontinuously (but the free energy F=U-TS is continuous), and the latent heat is involved in the transition (e.g. melting ice). In a second-order phase transition, the particle configuration changes continuously at T_c but the symmetry of the system changes discontinuously.

An earlier classification, suggested by Ehrenfest in 1933, was that phase transitions could be characterized by discontinuities in the derivatives of the Gibbs free energy. Thus a first-order transition would be one in which a first derivative of the Gibbs free energy is discontinuous, while a second-order transition would be characterized by a discontinuity in its second derivative (see Fig. 1.5). However, not all transitions satisfy the Ehrenfest criteria. More general definition given above has to be used to avoid problem with divergent derivatives.

Parameters called **critical exponents** characterize the divergences in second-order phase transitions**.** In that case we expect the physical properties of the system to behave in a smooth fashion. We therefore assume that near T_c the temperature dependence of these physical properties may be described by a power series expansion in the parameter $\varepsilon \equiv (T-Tc)/Tc$. As we get closer to the transition temperature the behavior of the physical properties are dominated by the leading term in this expansion. Thus the exponent of ε for this leading term acquires a particular significance and is referred to as the **critical exponent.** For example, in case of a magnetic system magnetization M (order parameter) is proportional to $M \propto (-e)^b$ when $T \rightarrow T_c^-$, where β is corresponding critical exponent.

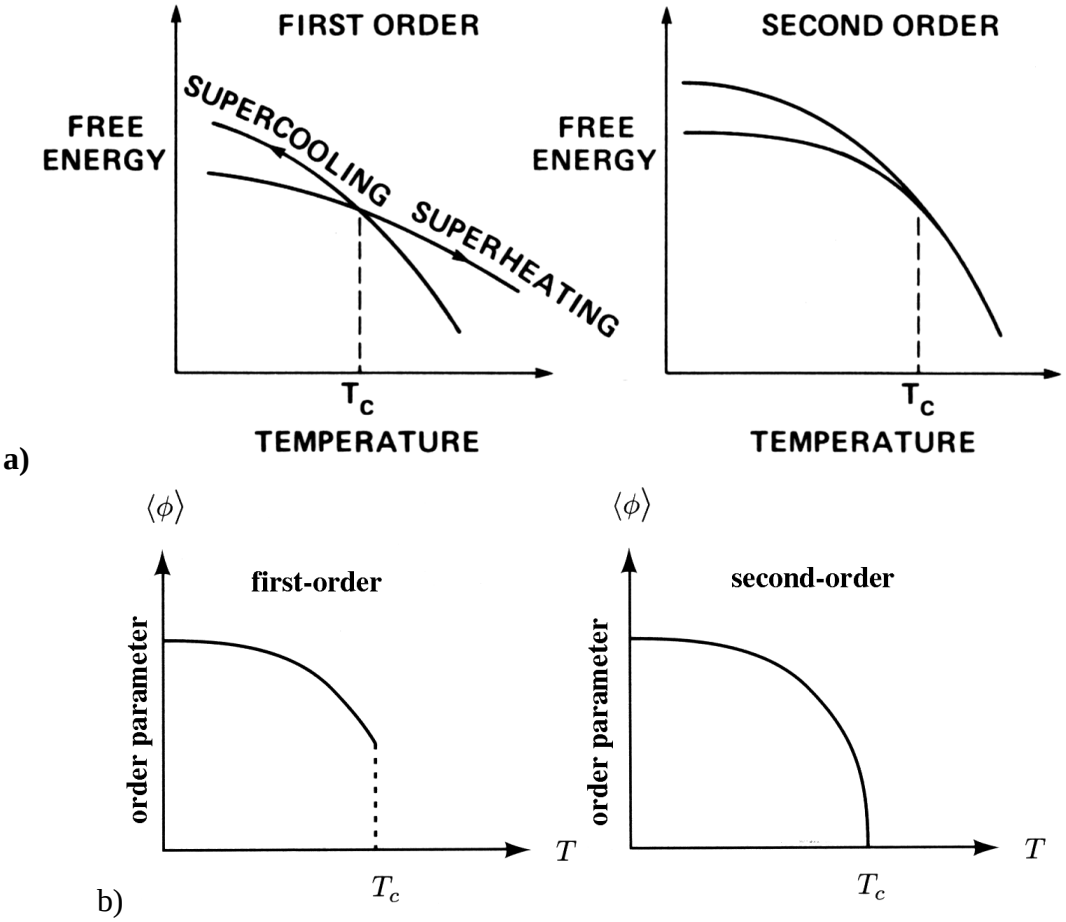

Figure 1.5 Free energy and order parameter in first and second order phase transitions

a) General behaviors of the free energies as functions of temperature for first- and second-order transitions (adopted from (White 1979)).
b) Behaviors of the order parameters as functions of temperature for first- and second-order transitions.

Landau and Lifshitz have given a necessary condition for a phase transition to be of second order (Landau 1970): Let $\rho(x)$ denote some property of the system directly affected by the phase change, (e.g. the surface atom density (time averaged) of the crystal, or spin density etc.) in the high-temperature phase. This function is invariant under the symmetry operations of the corresponding surface space group, G_0. For $T<T_c$, the surface is described by a new density function $\rho'(x)= \rho(x)+\delta\rho(x)$ which is invariant under the symmetry operations of a new space group G. The Landau-Lifshitz rule states that the transition can be continuous only if G is a subgroup of G_0 and the function $\delta\rho(x)$ transforms according to a single irreducible representation of G_0. The transition will be of first order if this condition is not met.

The reduction of a system's energy through loss of symmetry underlies the mechanism for the variety of phenomena (Tosatti 1995): Peierls distortions, Jahn-Teller effect, Spin Density Waves, Charge Density Waves and so on. Since they involve the transitions between different crystallographic states, these phase transitions are called **structural transitions** (White 1979)(p.27). The basic degrees of freedom in a solid are electronic and vibrational. The structural phase transitions can be classified by whether they are driven primarily by electronic and vibrational instabilities (Tosatti 1974). These degrees of freedom are, of course, strongly coupled. In fact, this is the reason that an electronic instability manifests itself in a structural change in the first place. The underlying principles are equivalent for metals and for insulators. In an insulator composed of ions with orbitally degenerate ground states it is possible to lower the electronic energy by splitting these degenerate levels apart by means of a lower symmetry distortion. Such transitions are referred to as cooperative Jahn-Teller

transitions (Gehring 1975). Even though the system can be characterized by the appearance of a spontaneous electric quadrupole moment, the order parameter is usually taken to be the splitting of the electronic states. The amplitude of the distortion corresponds to the phonon mode. When phonons themselves are responsible for a structural transition it may result in a displacive transition. In such cases the amplitude of the distortion acts as the order parameter. And another type, order-disorder transitions, is not accompanied by "soft phonon modes".

In case of metals the electronic degrees of freedom are characterized by a Fermi surface. If additional periodicities are introduced into such a system by virtue of a lattice distortion or by waves in the electron system then the Fermi surface and the electronic energy will be modified. In one dimension a conducting chain is unstable with respect to a periodic lattice distortion with a wavelength $\lambda=\pi/k_F$ and undergoes a so-called Peierls transition. It defers from Jahn-Teller distortion primarily in the nature of the symmetry that is broken. In the Jahn-Teller case this is a point symmetry whereas in the Peierls case it is a transitional symmetry. Instabilities similar to Peierls are possible in two-dimensional metals. In such materials a periodic lattice distortion is coupled to the periodic modulation of charge. This is called Charge Density Wave (CDW) and will be discussed in the next section.

1.3. Charge Density Waves in low-dimensional metals

Charge Density Wave usually is defined *as a periodic symmetry-lowering redistribution of charge within a material, accompanied by a rearrangement of electronic bands (such*

that the total electronic energy is decreased) and usually a small periodic lattice distortion.

Although first predicted by Peierls (Peierls 1955) several decades earlier, it was not until in the 1970's that quasi-one- and quasi-two-dimensional metals were first synthesized and CDW-related phenomena observed (see Bennet 1999 for references). In the late 60's Overhauser proposed that electron-electron interactions create "exchange instabilities" that should lead to CDWs in simple metals (like potassium) (Overhauser 1968). Since that time, CDW have been identified in an extremely diverse collection of materials including organic charge transfer salts such as TTF-TCNQ (Comes 1975), numerous oxides such as the blue bronzes $K_{0.3}MoO_3$ and $Rb_{0.3}MoO_3$ and the Magneli phase η-Mo_4O_{11} (Schlenker 1989), metallic elements like α-U (Axe 1994) and Cr (Dubiel 1995), and martensitic precursor phases occurring in certain intermetallic alloys (Hwang 1983a; Hwang 1983b) . A lot of research focused on CDWs in transition metal chalcogenides (Boswell 1999) MX_2, MX_3, MX_4, (here M refers to the transition metal elements V, Ti, Zr, Nb, Ta, or Hf while X refers to the chalcogenides S, Se and Te). CDWs observed at surfaces of Pb/Ge(111) and Sn/Ge(111), that will be discussed in this Dissertation, were reported to 2D CDWs that are completely localized in the surface layer (Carpinelli 1996; Carpinelli 1997).

Most of the essential aspects of the theory can be illustrated using a simple model and physical arguments. In a metal, the electron states are described by Bloch waves whose energies E_k near bottom of the energy bands varies according to a dispersion relation

$$E_k = \frac{\hbar^2 k^2}{2m^*} \qquad (1.2).$$

For an ideal one-dimensional chain of metal atoms, the Fermi surface consists of parallel planes at $\pm k_F$. A structural modulation with wavevector $q=2k_F$ will couple electron states lying on the two planes of the Fermi surface, creating a gap 2Δ in the energy spectrum at E_F. A reduction in the electronic energy results from a lowering of the occupied band states energies below the new energy gap while the states that are correspondingly raised in energy remain unoccupied (Figure 1.6). For a one-dimensional metal, the reduction in electronic energy will always exceed the elastic energy cost of the lattice modulation, stabilizing the CDW (Bennet 1999). For temperatures above 0K, thermal excitations of electrons lead to an eventual closing of the CDW energy gap at a transition temperature T_c. The energy gap and the transition temperature have a BCS-like (as in superconductor) (Bardeen 1957) relation

$$\Delta = 2H \exp\left(-\frac{A}{N}\right) = 1.76 k_B T_c \qquad (1.3)$$

where N is the density of states, A is the electron-lattice coupling constant and H is a electronic parameter on the order of E_F (Gruner 1994).

The CDW ground state develops in low-dimensional metals as a consequence of electron-phonon interactions. A phonon with momentum $2k_F$ within the 1D crystal will be efficiently screened and its frequency will be reduced. Such a behavior is called a Kohn anomaly (Kohn 1959) or “softening” of a phonon (Fig.1.7a). This change in phonon spectrum is strongly temperature-dependent due to temperature dependence of the electronic response, with phonon frequency going to zero at $q=2k_F$ at finite

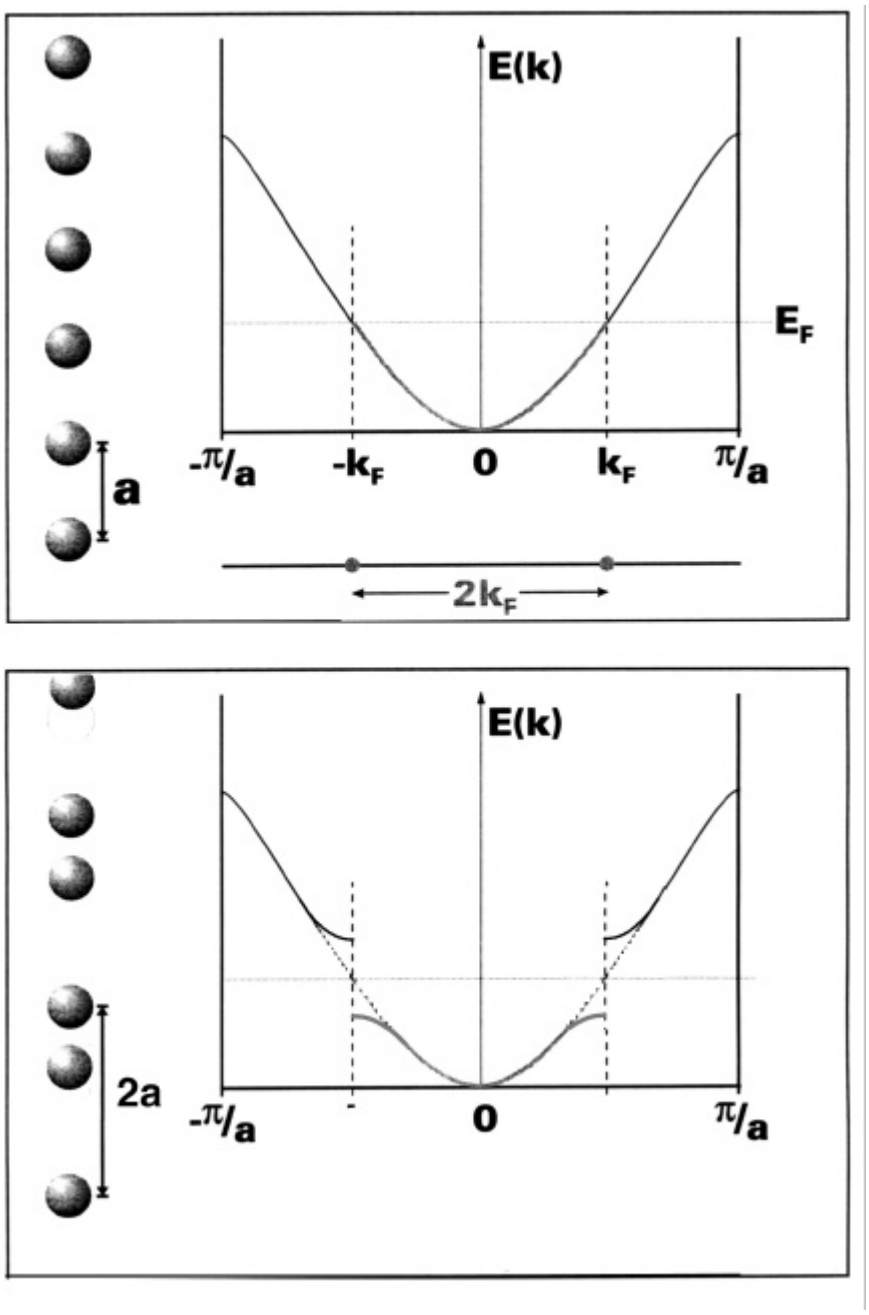

Figure 1.6 Peierls transition in one-dimensional metal

(top) One-dimensional crystal with free-electron band structure. E_F indicates Fermi energy
(bottom) One-dimensional crystal with double unit cell. A band gap appears and total electronic energy is lowered

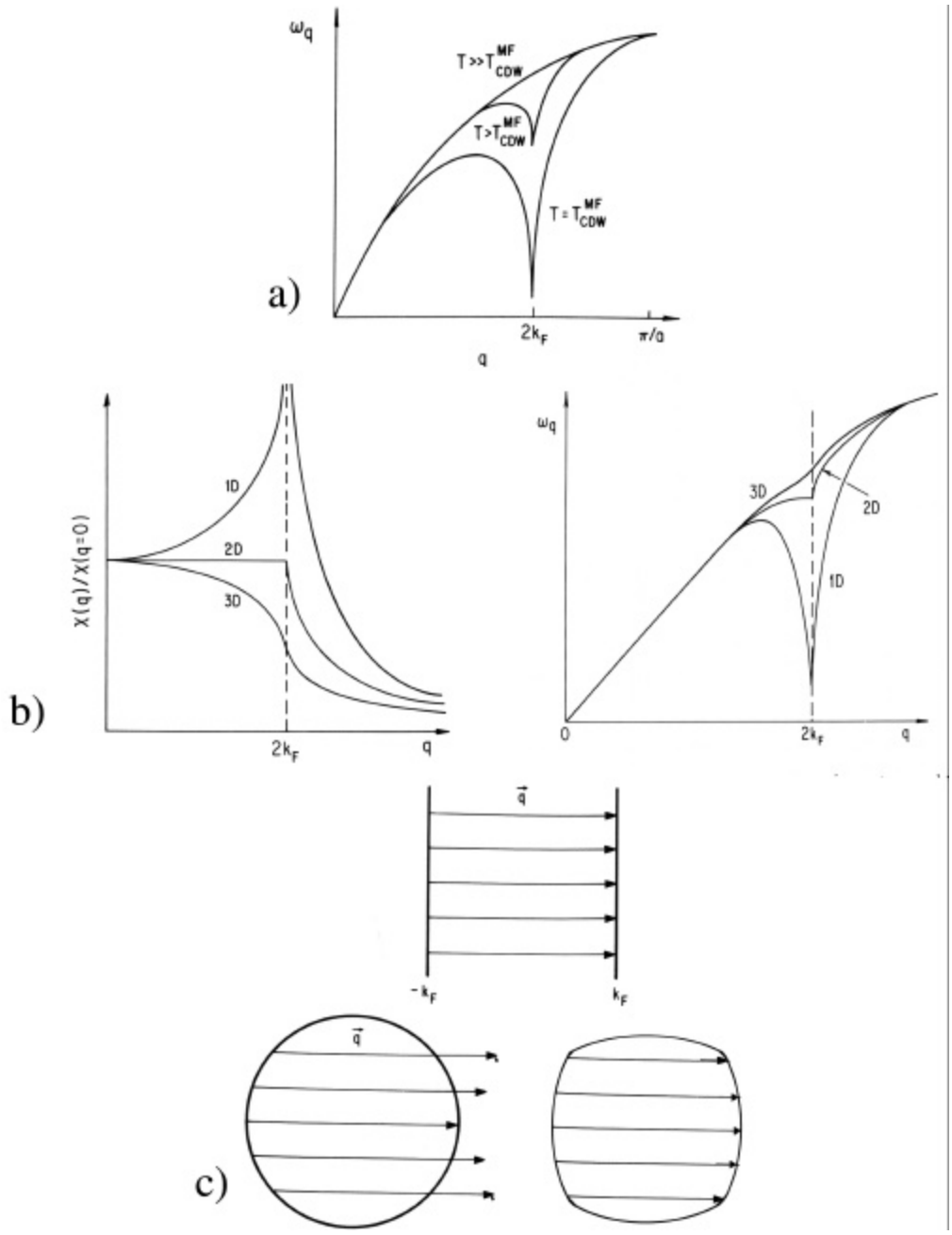

Figure 1.7 Kohn anomaly, response function, and Fermi surface nesting

a) Acoustic phonon dispersion relation of a one-dimensional metal at various temperatures above the transition temperature

b) (left) Wavevector dependent Lindhard response function for a one-, two-, and three-dimensional free electron gas at zero temperature. (right) Acoustic phonon dispersion relations of one-, two, and three-dimensional metals.

c) Fermi surface topology for a 1D and 2D free electron gas. The arrows indicated pairs of states, one full and one empty, differing by the wavevector $q=2k_F$.

temperature.

The reason for efficient screening at $2k_F$ lies in the divergent response of the electron gas in low dimensional system. Screening occurs when electrons react to counter any perturbation of the crystal. When electrons scatter from one portion of the band structure to another, a change in both energy and momentum can be involved. At T=0 the Pauli exclusion principle forbids many transitions. The transitions with a large difference in energy between initial and final states are much less likely to occur than the ones with a small difference. Therefore, the dominant transitions involve electrons right at the Fermi energy (E_F). An electron at E_F can be scattered from $-k_F$ to $+k_F$ with only small change in energy in the range of kT. These transition involves a large momentum shift $\Delta k=2k_F$. Thus any perturbation that incorporates a momentum of $2k_F$ will be efficiently screened. The Lindhard response function is a measure of how strongly a material will respond to a perturbation with momentum q. The dependence of the Lindhard response function

$$c(\vec{q}) = \int..\int \frac{d^d k}{(2p)^d} \frac{f_k - f_{k+q}}{E_k - E_{k+q}} \qquad (1.4)$$

for one-, two- , and three-dimensional free electron gas at zero temperature is shown in Fig. 1.7b along with acoustic phonon dispersion relations. In Eq. 1.4, d is the dimensionality, $f_k=f(E_k)$ is the Fermi function. Below the temperature at which the phonon frequency goes to zero a new phase with a periodic static lattice distortion and charge modulation with a wavelength $\lambda=2\pi/2k_F$ is formed. In its turn periodic lattice distortion leads to an energy gap, turning the material into insulator.

The reason for 3D and 2D materials to behave like 1D materials, that have a divergent electronic response function at $q=2k_F$ (Fig. 1.7b, left), lies in the topology of the Fermi surface, called nesting. The most significant contributions to the integral in Eq. 1.4 come from pairs of states – one full, one empty – which differ by $q=2k_F$ and have the energy close to E_F, thus giving a divergent contribution to $\chi(q)$. However, in higher dimensions the number of such states is significantly reduced as shown in Fig. 1.7c (left panel). For 2D anisotropy in the band structure can lead to the Fermi surface with areas that can be connected by one k-vector that is called spanning or nesting vector (Fig. 1.7c, right panel). This will cause the behavior analogous to 1D material.

The formation of CDW was proposed as an explanation for the symmetry lowering phase transition in Sn/Ge(111) and Pb/Ge(111) discussed in the next Chapter. The measurements and calculation have been focused on the main features that could identify CDW: Fermi surface nesting, metal-insulator transition (formation of a band gap), and periodic lattice distortion. Measurement of the temperature dependence of the phonon spectrum has not been reported yet.

1.4. Two Important Examples of 2D Phase Transitions

The phase transitions discussed in this section serve three purposes. The first is to show the universality of the problem investigated in this Thesis, the second is to point out the general role defects, and the third is to introduce some essential concepts such as displacive and order-disorder phase transitions. The origin of these symmetry lowering 2D phase transitions remain controversial.

1.4.1 (1×1) →(√2×√2)R45° phase transition in W(100)

The drama surrounding the phase transition in W(001) reminds one a lot the history of study of Sn/Ge(111) system, discussed in the next Chapter, except it was started years earlier. The main argument is about whether this phase transition is displacive or order-disorder type. The low temperature phase structure consists of tungsten atoms displaced from their ideal positions by a small amount to form zig-zag chains (Fig. 1.8). A Landau-Lifshtz symmetry analysis indicates that this transition can be continuous and this appears to be the case experimentally (Wendelken 1985). There are two possible scenarios for this transition.

Displacive transition scenario

An appealing picture of the phase transition presumes that the frequency of the phonon mode mentioned above becomes 'soft', i.e., approaches zero as the temperature drops. The crystal spontaneously distorts when the mode frequency reaches zero at Tc. The atomic displacements that transform the ideal surface into the reconstructed geometry correspond to a longitudinal phonon mode with wave vector $\mathbf{q}=\pi/a(1,1)$, where a is the lattice constant.

Order-disorder transition scenario

However, it is also possible that the surface tungsten atoms are displaced above T_c as well – but in random directions. At sufficiently low temperature, surface interactions favor an ordering of the displacements patterns into the observed structure. At present, available experiments do not unambiguously favor one mechanism over the other and it is unclear which one actually prevails.

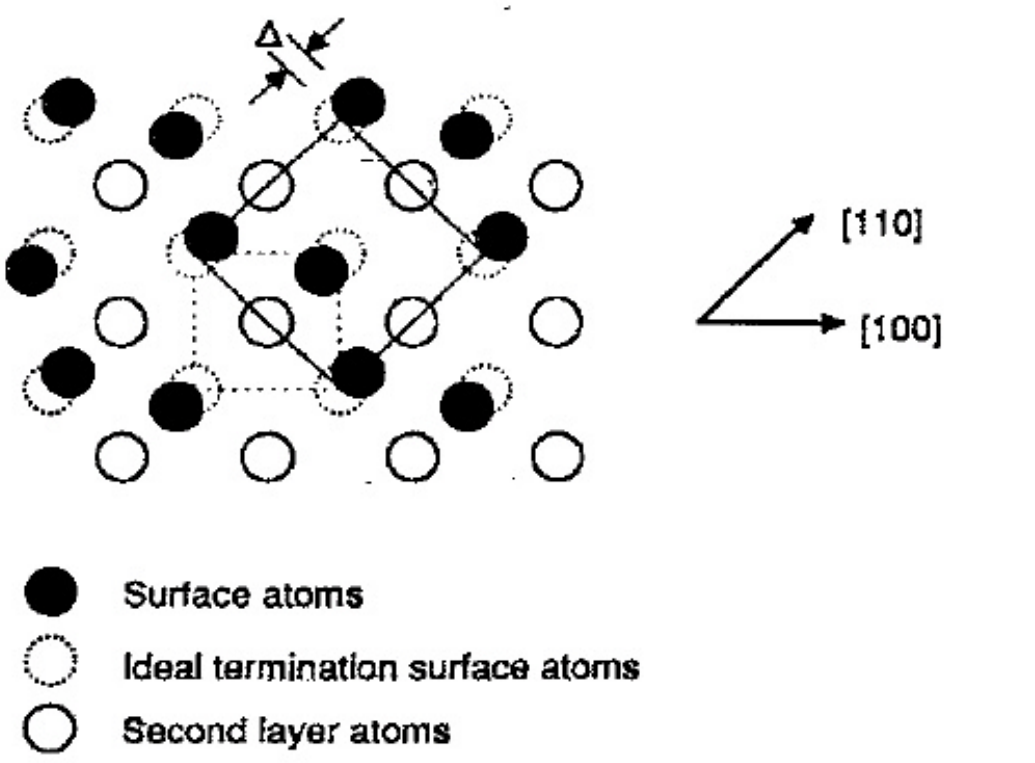

Figure 1.8 Debe-King model for the low-temperature W(001) surface reconstruction.
High temperature 1×1 phase is represented by open circles and low temperature $\sqrt{2}\times\sqrt{2}R45°$ is represented by closed circles. (Adopted from (Lee 1995))

Displacive versus Order-disorder

The differences in the surface dynamics for the order-disorder and displacive phase transitions are illustrated in the Fig. 1.9 (Ernst 1992). It shows a simple Hamiltonian describing the energetics of a one-dimensional system undergoing a structural phase transition. Each first-layer atom resides in an effective double-well potential which is centered at the ideal lattice sites. At low temperatures all atoms are located in the left or the right well (inside one domain). But when the temperature increased different situations can arise, depending on the local potential-well depth or central barrier height U, the strength of the 'springs' and the critical thermal energy kT_c. In case of order-disorder transition, the critical thermal energy is small compared to the local potential-well depth, and therefore above T_c each atom resides at one or the other potential minimum, away from the high-symmetry site. In this case the symmetrized single-particle probability distribution function would exhibit a double-peak structure at all temperatures below and above Tc.

In the displacive transition, on the other hand, the critical thermal energy kT_c is much larger than the well depth of the double-well potential. At high temperatures, the dynamics is determined by "strong" springs between the atoms which are no longer localized at the minima of the double-well potential and vibrate nearly harmonically about the high-symmetry sites. Thus the single-particle probability distribution function gradually develops from a double-peaked structure centered around the high-symmetry site into a single-peaked structure for $T>T_c$.

This is the good place to introduce the possible role of the defects in this transition. The defect will further break the symmetry by making the two minima of the

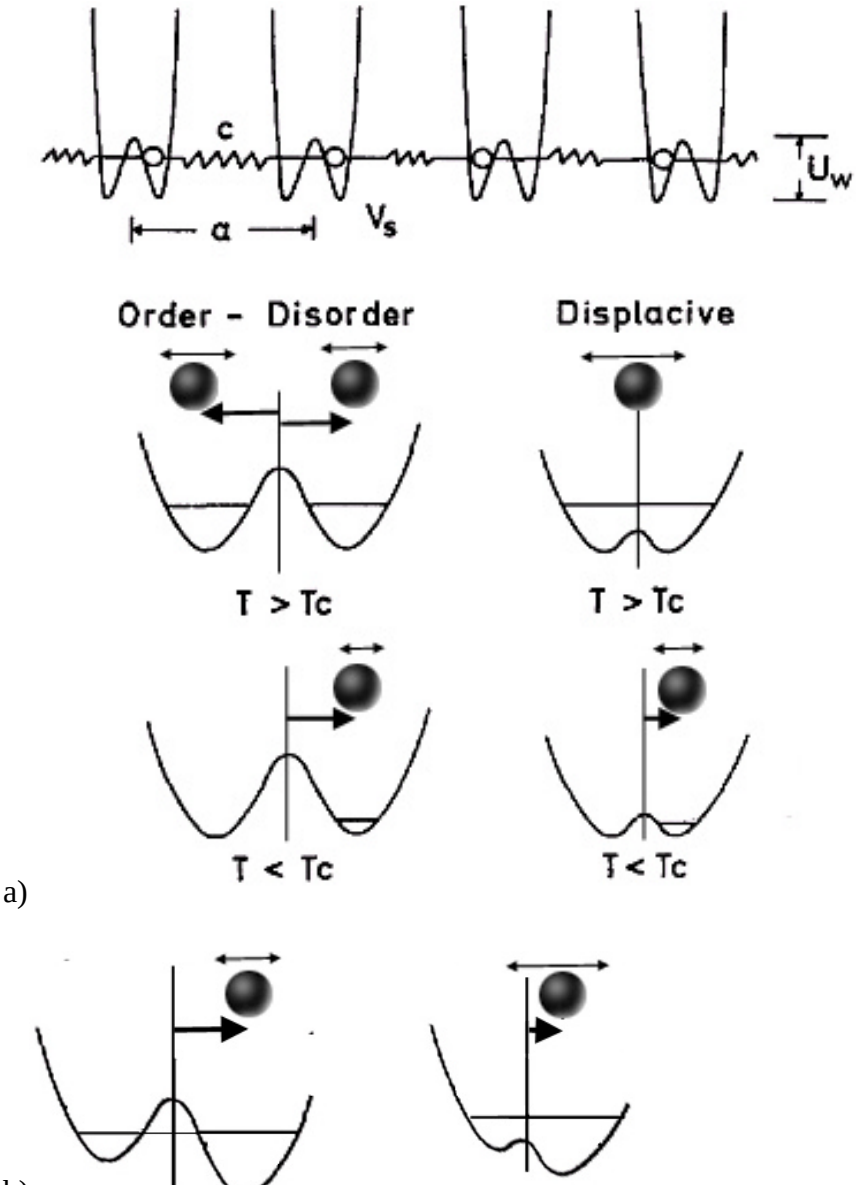

Figure 1.9 Schematic representation of a system undergoing a structural transition. Comparison of order-disorder to displacive phase transition.

a) The "springs" connect neighboring first-layer atoms by harmonic forces. The double-well potential represents the interaction with the underlying lattice and all intralayer interactions which are not included in the "springs". The relative strength of these interactions leads to different behavior of the system at high temperatures. Adopted from (Ernst 1992)
b) Defect-induced asymmetry of the double well potential.

double well potential inequivalent (Fig. 1.9b). At low temperature in both cases this would determine whether the atoms are going to be in the left or in the right minimum. At temperatures above Tc in case of order-disorder transition that would change the distribution of probabilities between too peaks. In case of displacive transition that would mean that the peak of the probability distribution function would shift off the high symmetry site.

The picture presented above was drawn assuming that the double well potential doesn't change with temperature. What authors haven't considered is that if this transition is driven, for example, by Charge Density Wave instability this assumption would be erroneous. In that case when the temperature is changed the electron-phonon coupling will affect "spring constants". In analogous simplified view (Fig 1.10), at high temperature the potential will have only one minimum and atoms will be positioned on the high symmetry sites (undistorted state), while when temperature is lowered two minima will appear and atoms will shift from the high symmetry sites (distorted state).

Returning to W(001) it should be noted that the structure of the (1×1) high temperature phase and the nature of the phase transition remain controversial issue. Existing experimental studies have supported either an order-disorder (Barker 1981; Wendelken 1985; Robinson 1989; Stensgaard 1989; Lee 1995) or displacive (Debe 1977b; Debe 1977a; Debe 1979; Ernst 1992). Extensive theoretical work has focused on the possible underlying driving forces leading to the LT structure and the statistical mechanics of the phase transition. Mechanisms considered include (short range) Jahn-Teller like driven reconstruction, (long range) Charge Density Wave and Fermi surface/surface-state models.

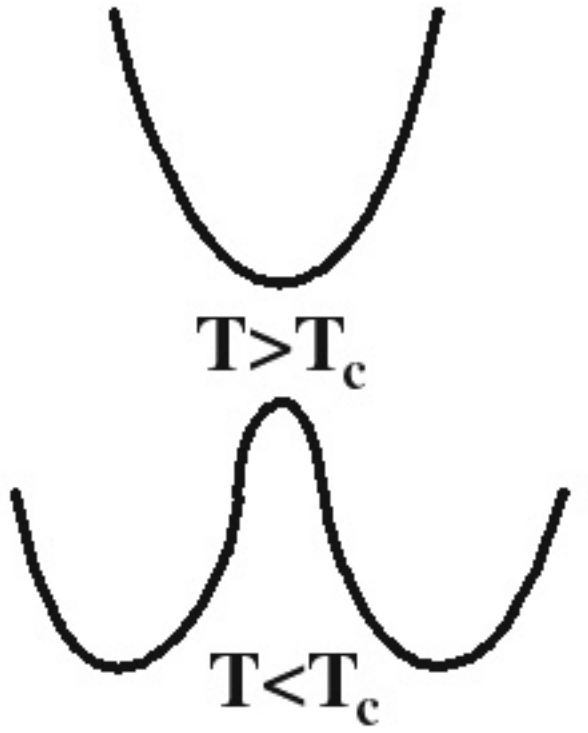

Figure 1.10 Schematic representation of temperature dependent potential for a simplified model of structural transition. (by analogy with Fig. 1.9)
This picture seems to be more appropriate to illustrate CDW transition than Fig. 1.9.

The number of STM measurements on this surface is quite limited. Wengelnik et al. studied this surface below transition temperature (80 K) (Wengelnik 1994). They found at LT a line pattern forming two domains (Fig. 1.11), which is in agreement with the Debe-King model. The dark spots were identified as H impurities. At room temperature the rows of clean W atoms could be weakly resolved for clean W(100). In general, they note that the noise in tunneling current drastically changes after H exposure both at low and room temperature, which could be related to the changes of the vibrational properties of the surface after H coverage.

It is possible that further work using an STM can clarify the role of defects on this surface and will help to understand this phase transition.

1.4.2 Nature of Si(001) (2×1)→c(2×4) phase transition

The surface of Si(001) is probably one of the most studied in the world according to the number of publications (>4000). It is for a large part due to its technological importance, though a very significant portion of the literature is devoted to scientific aspects. One of the reasons of such interest is the temperature induced symmetry lowering phase transition from (2×1) to c(2×4) structure. In this case as in case of W(001) and Sn/Ge(111) there is a battle about whether this is a displacive or order-disorder transition. The ones that prefer the latter are currently winning. But the matter is far from being resolved, as recent experiments infer that the c(2×4) is not a ground state.

The theoretical studies and experimental results have revealed the surface to be

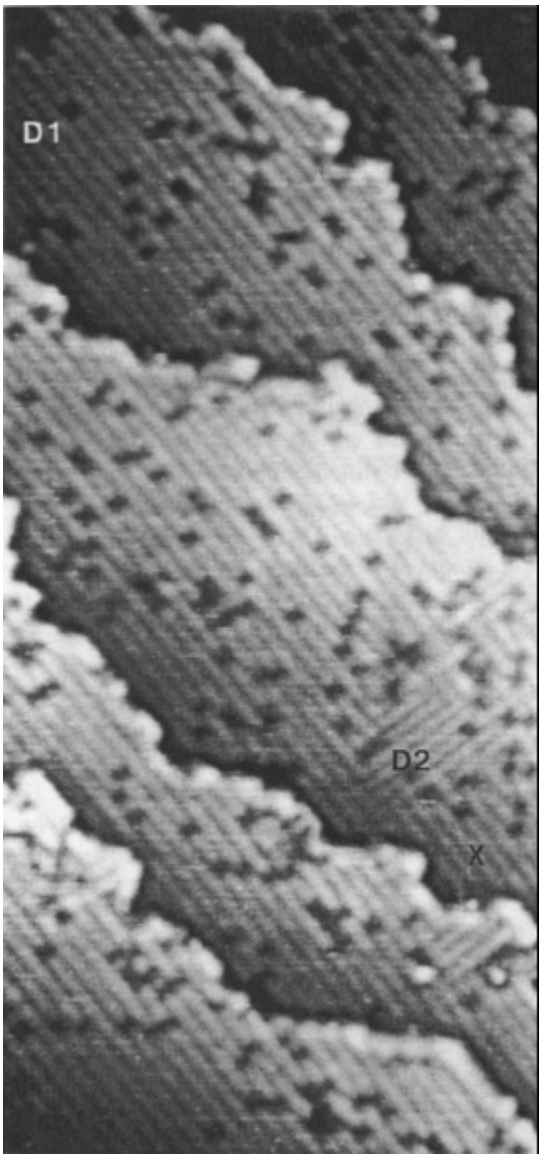

Figure 1.11 Constant current STM image of W(100)c(2×2) at 80 K.
It is acquired 30 min after a high-temperature flash. U=0.1V, I=0.5 nA, the area is 175×340 $Å^2$. The corrugation perpendicular to the lines is 0.15Å, the holes measured with a depth varying between 0.5 and 1.2 Å. Adopted from (Wengelnik 1994)

Point defects that were identified as mostly adsorbed H atoms have a sizable population, though their influence was usually ignored.

reconstructed to a (2×1) dimer structure above room temperature (Schlier 1959; Chadi 1979; Tromp 1985; Hamers 1986). Controversy has surrounded the topic of the exact nature of the dimers. Theoretical studies have lent support to two different models of the surface dimers, namely, the symmetric and asymmetric models. Experimental investigations have also attempted to verify one or the other model. STM images have shown symmetric-appearing dimers at RT except in the vicinity of defects and step edges where buckled dimers are observed (Fig. 1.12) (Tromp 1985; Hamers 1986). A variable temperature LEED measurement has shown that the surface undergoes a reversible phase transition around 200 K (Tabata 1987). The first low-temperature STM images showed that at LTs the surface is indeed largely composed of buckled dimers (Wolkow 1991; Wolkow 1992). However, a fair amount of symmetric-appearing dimers remain.

Below $T_c \approx 200K$, the 2×1 structure is transformed to a c(4×2) structure, which has the antiphase arrangement $\alpha\beta\alpha\beta$, as shown in the Fig. 1.13a. The buckled dimer, a fundamental unit of this reconstruction, is displayed in the Fig. 1.13b. The dimers of the 2×1 structure appear symmetric in STM images at room temperature; this is believed to be attributed to the time average of the flip-flop motion of the buckled dimers. Therefore, the phase transition from (2×1) to a c(4×2) structure is considered to be the order-disorder transition of the buckled dimers (Ihm 1983; Saxena 1985; Tabata 1987; Kubota 1994; Terakura 1995). At RT, some types of defects prevent dimers from oscillating that give rise to buckled appearance in the vicinity of defects.

There are some questions that raise a dark cloud over this nice picture. For example Smith at al. observed that at certain configurations of defects forming chains (2×n)

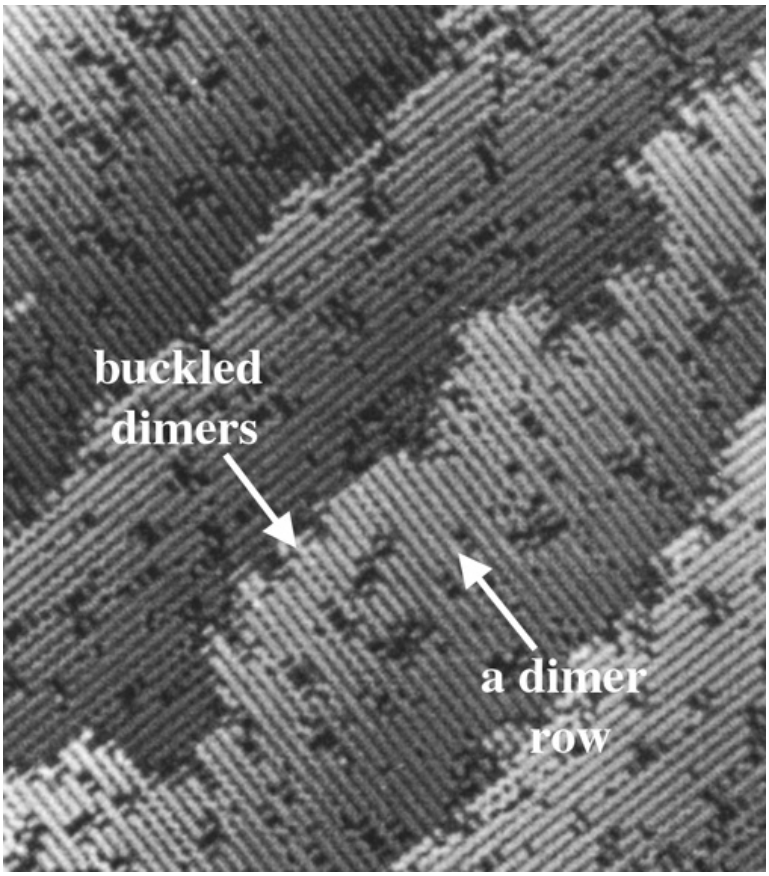

Figure 1.12 Filled state STM image of the 2×1 reconstructed Si(001) surface.
Most of the dimer rows consists of symmetric dimers. Some of the dimers appear buckled. (Adopted from (Demuth 1990))

a)

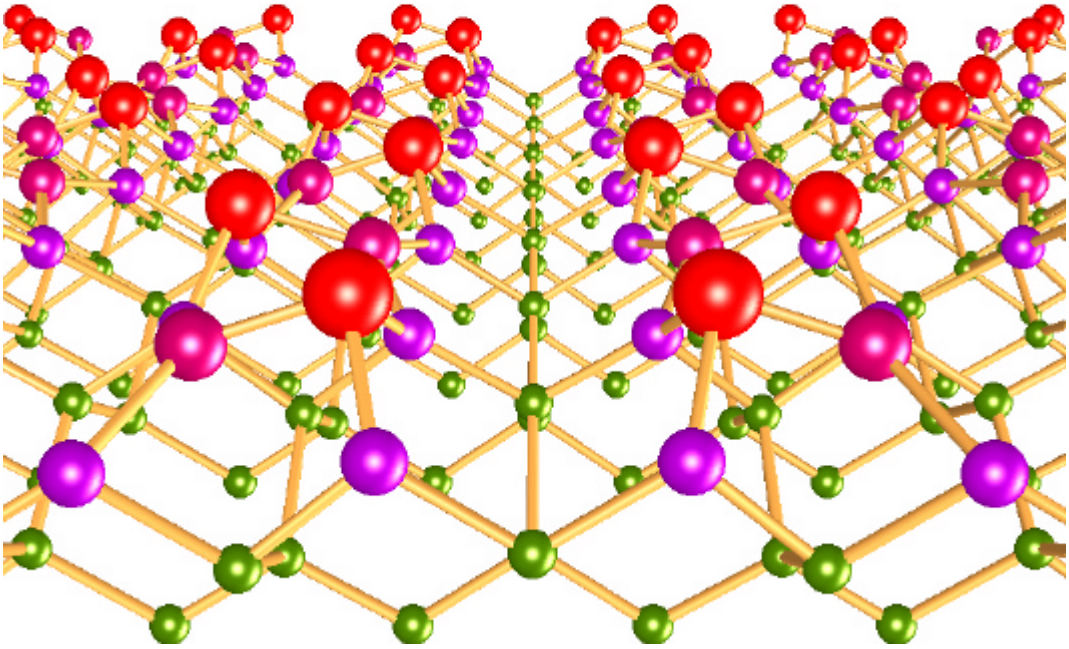

b)

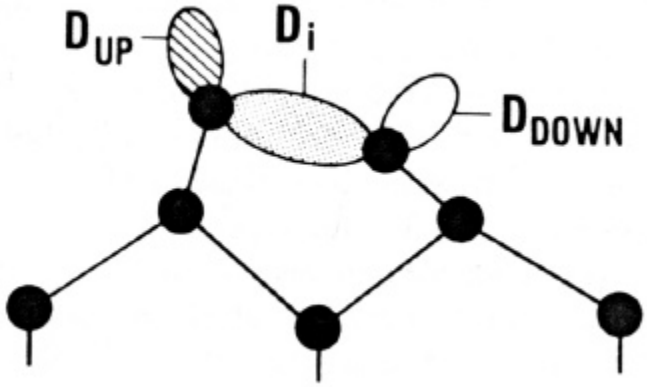

Figure 1.13 Structure of Si(001) surface

a) A perspective view of buckled dimer model for the c(4×2) structure of Si(001). (from (Terakura 2000))

b) Diagram of a buckled dimmer viewed from within the surface plane. The dimer bond, D_i, is represented by the region with dots. The buckling causes some charge transfer, so the state associated with the higher dimer atom is mostly filled, and the state associated with the lower atom is mostly empty. (Adopted from (Kubby 1987))

structure there is no buckling at 190 K (Smith 1996). And the fair question they asked was “Does this mean that dimers on the 2×n surface for some reason will not stop oscillating at LT?” Apparently, this is one of the many questions related to what defects do to this surface and to this phase transition. If fact, in that work they had set a goal to determine whether this is a second or first order phase transition by counting the number of buckled dimers at different temperatures. No conclusion was made but statement that further studies at different defect densities are necessary. The role of defects in appearance of symmetric dimers was further studied very recently by Hata et al. at a lower temperature, 80 K (Hata 2000b).

What is the role of defects in this phase transition?

A LEED study found that the phase transition took place over fairly broad temperature range (Tabata 1987). Thus the authors concluded that this is a second order order-disorder transition. However, their result lacked a quantification of the defect type and concentration on the surface. In 1994 (Inoue 1994) it was predicted that as little as 1% defect concentration could reduce the order parameter by 75%, resulting in a smearing out of the transition over a fairly broad temperature range. Based on this prediction, it would then appear that since the best Si(001) surface reported so far have ½%-1% defects, it may not be possible to ever remove their influence on the phase transition. Thus the difficulty to identify the true nature of the phase transition in a defect free system remains.

One of the ways to clarify the role of the defects is to eliminate them. Hata et al. developed a method to prepare almost defect free (defect density of 0.1%) surfaces and they observed that at 80 K the surface was perfectly buckled (Fig. 1.14a) (Hata 2000a).

a) 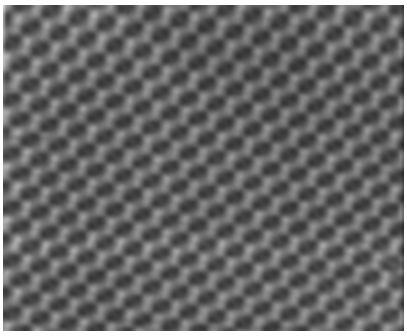 b) 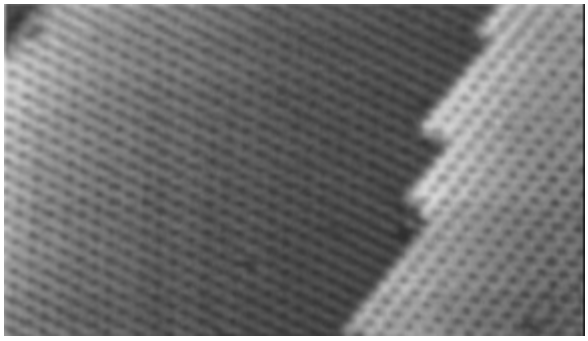

c) 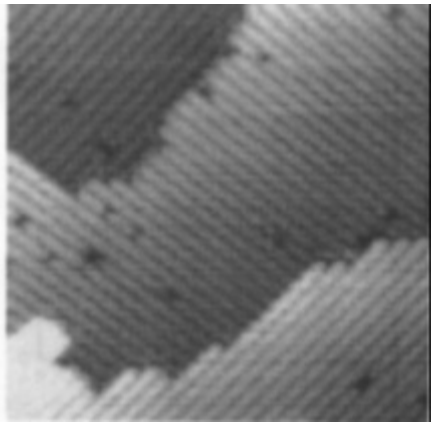

Figure 1.14 STM images of Si(001) surface at low temperatures.

a) empty state STM image of the defect free Si(001) surface at 80 K. (+0.6 V, 1 nA); (from (Hata 2000a))

b) filled state STM image of the Si(001) surface at 63 K, dimers are asymmetric (32×32 nm^2, -1.0 V, 0.1 nA);

c) filled state STM image of the Si(001) surface at 5 K. Dimers appear symmetric, even though some blurred asymmetry is noticeable.

(b and c are from (Yokoyama 2000))

This result indicated that the ground state of the defect free surface was 2×4. Though in the beginning of a new millennium even this conclusion was put to doubt. (Kondo 2000; Yokoyama 2000). It was found that when the temperature is lowered below 20 K the dimers appear symmetric, except the ones located near defects. (Fig. 1.14c). All calculations that claim that buckled dimers was a ground state must be questioned. Currently two scenarios contend for the explanation.

Yokoyama at al. speculate that their STM/STS measurements indicate that the dimers are flipping at 5 K (Yokoyama 2000). They suggest that the flipping reappears at lower temperature because of the reduction of the barrier height for the dimer flipping. Although the mechanism is not clear at present, a possible origin seems to be the effect of an anharmonic potential.

An alternative scenario is the following (Kondo 2000). The symmetric dimers are stabilized at low temperatures because of an antiferromagnetic coupling (or the electronic correlation) between dimers. With increasing temperature, the antiferromagnetic order (or the the electronic correlation) is thermally destroyed and then the asymmetric dimers become more stable than the symmetric ones. A further increase of temperature (above 100 K) leads to thermal excitations of moving phase defects, which change the phase of the asymmetry (Shigekawa 1997). Again, apparently symmetric dimers dominate the surface at room temperature.

Clearly, even though this problem has been studied by almost every possible method, the complexity of it still keeps us from complete understanding of the nature of this phase transition. And undoubtedly, defects are responsible for a large part of this complexity.

1.5. Atomic and electronic structure of α-phases of metals on semiconductors.

1.5.1 Substrates: Si(111) and Ge(111)

Germanium and silicon crystallizes in the diamond structure (Fig. 1.15a). All atoms are tetrahedrally bonded to four other atoms. The (111) planes (shown by gray area in Fig. 1.15a) of Si and Ge consist of double layers which are attached by bonds, one per atom, perpendicular to the layers (Fig.1.15b). Within the double layer a mesh of tetrahedral bonds, the remaining three per atom rigidly connect two double-layers. There is one broken (unsatisfied or dangling) bond per atom, i.e., bulk-like surface unit cell in the top double-layer. These dangling bonds are highly energetic and the clean surface seeks to rearrange in such a way as to reduce their number.

Cleaved Si(111) and Ge(111) surfaces exhibit (2×1) reconstruction. The reconstruction involves rearranging atoms from the hexagonal rings (normally six per ring) to form alternating rings with five and seven atoms. This arrangement buckles the surface, and does not reduce the number of dangling bonds, but chains the top-layer atoms near to each other allowing a π-bonding interaction. Thus, the surface energy is lowered, but the number of atoms is conserved.

Heat treatments of cleaved silicon and germanium surfaces cause the (111) –(2×1) cleavage structures to convert to the 7×7 and the c(2×8) structures, respectively.

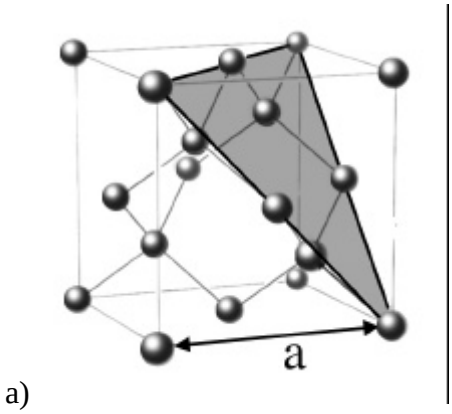

a)

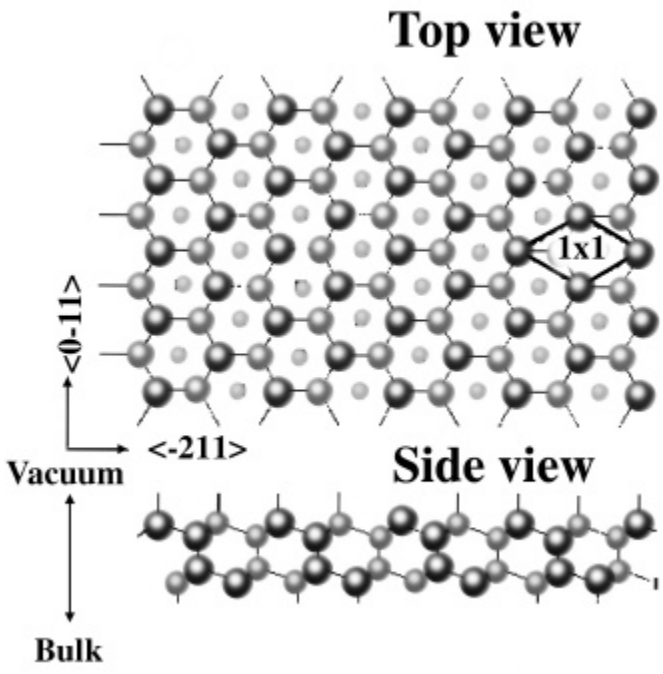

b)

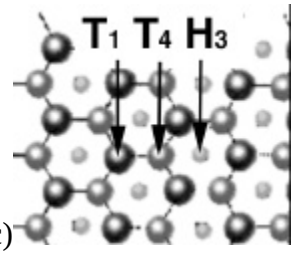

c)

Figure 1.15 Diamond crystal structure and its (111) surface

a) Conventional cubic cell of the diamond lattice. Nearest-neighbor bonds are shown. The four nearest neighbors of each point form the vertices of a rectangular tetrahedron. The shaded area indicates orientation of (111) surface
b) Model of the ideal surface for Ge(111) 1×1 (or Si). Dangling (unsatisfied) bonds are seen in the side view.
c) Nomenclature of the chemisorption sites at the (111) surface of crystals with diamond structure

1.5.2 (√3×√3)R30° of Sn and Pb on Si(111) and Ge(111)

Si(111) and Ge(111) dangling-bonds may be satisfied by the addition or removal of dangling bond electrons in the surface region. This is most easily accomplished by adsorbing foreign elements on a surface to which Si or Ge atoms can bond. Most metals adsorbed on Si(111) and Ge(111), at less than approximately 1 monolayer (ML), will form some superstructure. Submonolayer coverages of Sn on clean Ge(111) c(2×8) surfaces can induce (2×2), (5×5), (7×7) or (√3×√3)R30° phases. Such rearrangements are strongly dependent on adsorbate type, substrate temperature, coverage, annealing temperature and so on.

The most common reconstruction or superstructure is the (√3×√3)R30° formed with 1/3 of a monolayer (ML) of metal atoms. Atoms of group-III (B, Al, Ga, In), group IV (Si, Ge, Sn, Pb), group-V (Sn, Bi), noble metals (Ag, Au), alkali metals (Li,Cs) and others (Ce,Mg) have been reported to form (√3×√3)R30° structures on Si(111). Some of them are known to form (√3×√3)R30° structures on Ge(111). Description of all these phases goes well beyond the scope of this thesis.

Only isoelectronic systems of Sn/Ge(111), Pb/Ge(111), Sn/Si(111) and Pb/Si(111) will be discussed in this thesis (Fig. 1.16). Si, Ge, Sn and Pb all have the same valency of four. The α-phase of Pb or Sn on Ge(111) consists of 1/3 monolayer of equivalent Pb adatoms spaced ~7 Å apart in a hexagonal array of T_4 sites (Fig. 1.15c) atop the bulk-truncated germanium lattice, forming the (√3×√3)R30° arrangement shown in Fig. 1.17. For Sn and Pb on Si(111) the spacing between adatoms is 6.67 Å.

On semiconductor surfaces electronic states hybridize, and then overlap, so that

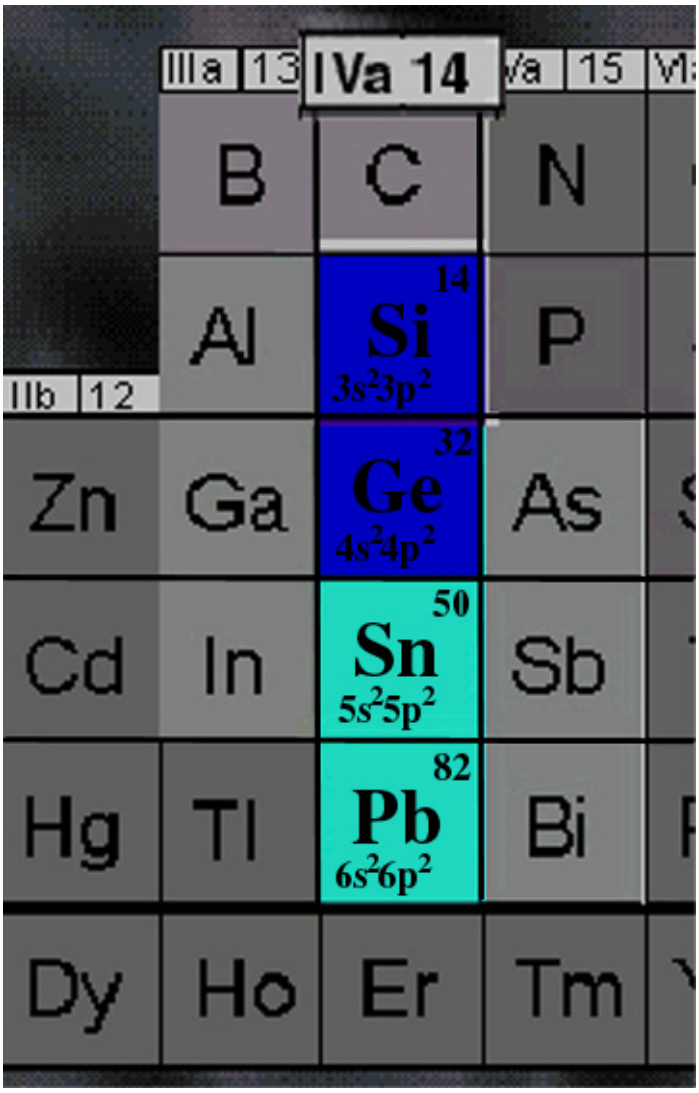

Figure 1.16 IVth column of Periodic Table of Elements
All of the highlighted elements have the same number of valence electrons (4). These are the elements that have an odd number of electrons in the $(\sqrt{3}\times\sqrt{3})R30°$ structure, providing a necessary condition for metallicity of Sn/Ge(111), Pb/Ge(111), Sn/Si(111) and Pb/Si(111) $(\sqrt{3}\times\sqrt{3})R30°$ surfaces. The neighboring elements in columns III and V would have an even number of electrons in $(\sqrt{3}\times\sqrt{3})R30°$ structures and thus should form insulating surfaces.

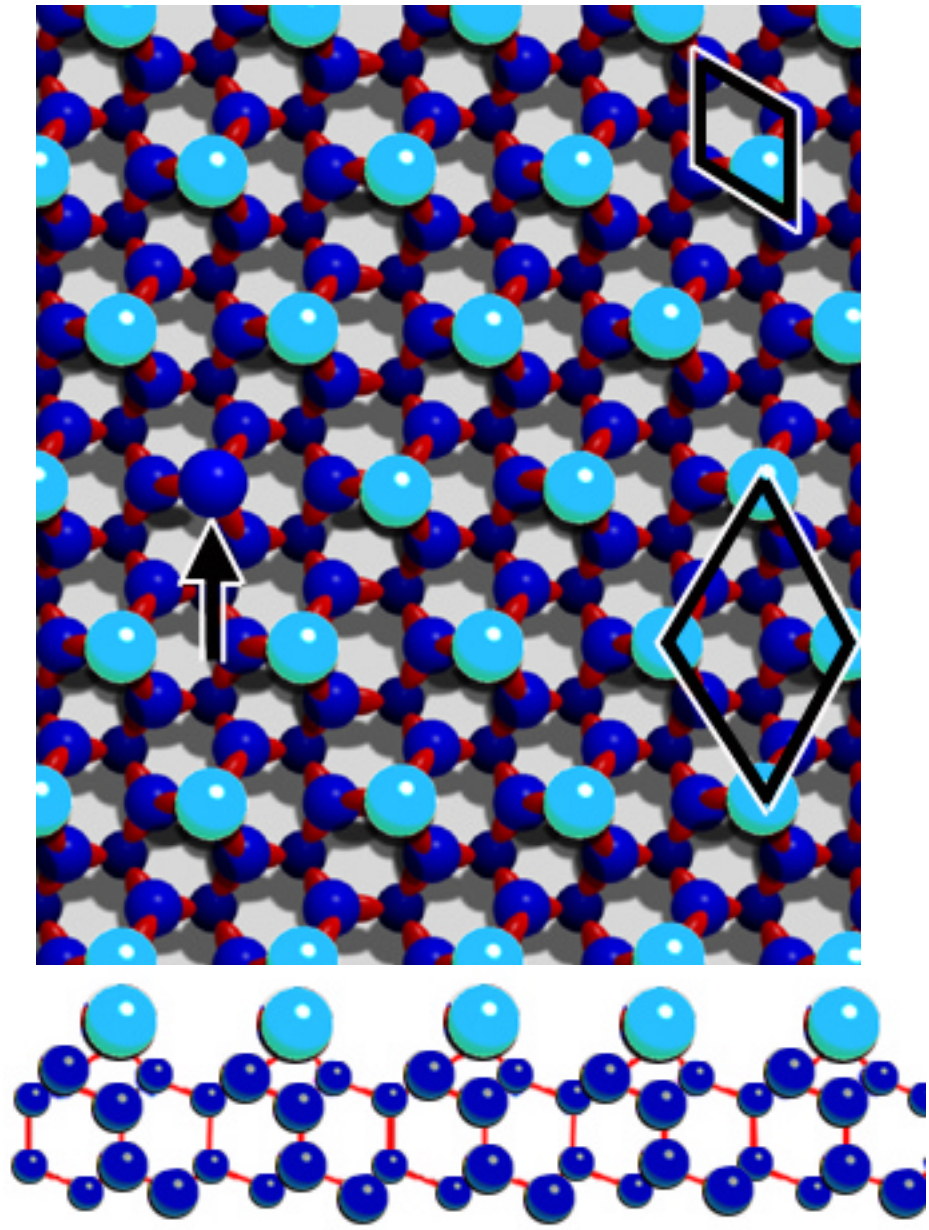

Figure 1.17 A ball model of Sn/Ge(111) ($\sqrt{3}\times\sqrt{3}$)*R*30° surface (and similar)
Sn atoms are represented by light blue balls, while Ge atoms by dark blue balls. The bonds are drawn as red ovals (dangling bonds are not shown). The diamond on the top is a (1×1) unit cell. The diamond on the bottom indicates a ($\sqrt{3}\times\sqrt{3}$)*R*30° unit cell. The arrow points to a substitutional Ge atom (called Ge defect in the text)

filled states correspond to bonds, and empty states to antibonds, with an energy gap in between. At the surface, hybrid orbitals pointing outwards remain as dangling bonds, with energy at mid-gap, as appropriate for a collapse between bonds and antibonds. The dangling bonds constitute therefore sharp surface states (they fall in the bulk energy gap), and are only half-filled (they cross the Fermi level). Surfaces of α-phase of Sn/Ge(111) and similar have one dangling bond per unit cell which should give rise to a half-filled surface state. The half-filling comes from the electron counting arguments. The $\sqrt{3}\times\sqrt{3}$ unit cell contains one Sn atom (or Pb) with valency 4 (Fig. 1.17) and 3 outer layer Ge (Si) atoms each with one unpaired electron and that give 7 electrons valence electrons in total (4e (Sn) + 3×1e (Ge) = 7e). By the same argument the $(\sqrt{3}\times\sqrt{3})R30°$ surfaces formed by elements from columns III or V (Fig. 1.16) can be insulating.

In 1974 Tosatti and Anderson indicated that these metallic surfaces are unstable to formation of CDW. They showed that such two-dimensional metals might have Fermi surface with flat portions, allowing nesting and large density of states at the Fermi energy, thus leading to a quasi- 1D dimensional electron dynamics (Tosatti 1974). Their calculations indicated that such systems should be unstable and surface phase transitions to an insulating state should follow. The insulating state can be either a magnetically ordered (Spin Density Wave) or a "Peierls superlattice" (Charge Density Wave), depending on the relative strength of the electron-hole and electron-phonon interaction.

1.6 (√3×√3)*R*30°↔(3×3) phase transition in Sn/Ge(111)

Recently discovered symmetry lowering phase transitions in Pb/Ge(111) and Sn/Ge(111) have been intensively investigated by different techniques. The experimental results and theoretical calculations are presented in more detail in Part2. This section contains a synopsis of the Part2 with sufficient information for understanding results presented in this thesis (Parts 3,4,5,6).

At room temperature, one third of a monolayer (ML) of Sn is arranged to a (√3×√3)*R*30° structure on Ge(111), with the Sn atoms occupying the T_4 sites (Fig. 1.15c) of the Ge(111) substrate (See Section 1.5) (Gothelid 1992). When the temperature is lowered, additional diffraction spots appear in the low-energy electron diffraction pattern and indicate a different (3×3) symmetry of the surface. The filled and empty state STM images display (3×3) hexagonal and honeycomb patterns of bright atoms, respectively (Carpinelli 1997). The complimentarity of the STM images at low temperature (LT) taken at opposite biases was interpreted as a characteristic feature of CDW. Electron Energy Loss Spectroscopy (EELS) showed that this system remains metallic below the phase transition temperature, while band gap formation usually accompanies CDW (It was detected in Pb/Ge(111)). Structure determination measurements using X-ray Diffraction and LEED –I/V indicated that lattice is distorted so that one out of three Sn atoms in the (3×3) unit cell is displaced out of plane (up) and two others into the plane (down), with the amplitude of the distortion of about 0.3 Å. The analysis of the XRD data also showed that the lattice is undistorted above the transition temperature. Photoemission spectroscopy was employed to elucidate the electronic structure of this

surface. Unfortunately the results were not consistent between different experimental groups. While some showed that the surface state bands crossing the Fermi level both above and below phase transition (confirming absence of band gap), others showed that the band gap does form all around (3×3) Brillouin zone (Avila 1999; Kidd 2000). Probably the most of the controversy was in the measurements of 4d core levels and their interpretations. It was found that the shape of 4d core level is too wide at room temperature for undistorted ($\sqrt{3}\times\sqrt{3}$)*R*30° structure (Gothelid 1995). This fact was interpreted as an indication that Sn atoms are not equivalent as they supposed to be according to the simple model that the Sn atoms are located at the T_4 sites (Fig. 1.17). Thus it was suggested that dynamical fluctuations were involved. In this picture the Sn atoms are flipping between two stable positions. Since STM is a time averaging technique the Sn atoms appear all equivalent because they fluctuate much faster than the acquisition time. Theoretical calculations also do not give us a consistent picture. While some first-principle calculations do not predict that (3×3) is the ground state of the system and suggest that electron-correlation effects not properly accounted in Local Density Approximation (LDA) are responsible for its stability, others do predict (3×3) as a stable structure (Carpinelli 1996; Carpinelli 1997; Avila 1999; Santoro 1999). The calculated shape of the Fermi surface does not allow for nesting usually necessary for electron-phonon mechanism of CDW formation.

In most of these works it was assumed that the system is free form any defects. The results presented in this Thesis clearly show that defects are very important in this system and their influence has to be accounted. The knowledge of the role of defects on

the properties of the system is a new and necessary step in understanding phase transitions in two-dimensional systems.

1.7. Summary

New phenomena emerge when the dimensionality is reduced. Phase transitions are very complex and dramatic phenomena that still lack precise microscopic description. It is generally believed that they are affected by defects and impurities. Such influence becomes even stronger in 1D and 2D systems. There is no such thing as “pure” system from the experimental point of view. Unfortunately “impure” crystals are very difficult to treat theoretically, and k-space techniques give an average picture that must totally misguide if the influence of inhomogeneities is ignored. Real space measurements with atomic resolution should be done to reach an understanding. The purpose of this Thesis is to give a new “real space” atomistic view on the 2D symmetry lowering phase transitions.

In the next PartI will present the knowledge that has been obtained in the recent years on phase transitions in Sn/Ge(111) and Pb/Ge(111) presented in historical perspective. Part3 is devoted to the description of experimental techniques and details of experimental procedures. In Part4 I present my results on the influence of defects in $\sqrt{3}\times\sqrt{3}\leftrightarrow 3\times 3$ phase transition in Sn/Ge(111) that are published in (Melechko 1999; Weitering 1999; Melechko 2000). Two new models for defect ordering phase transition and for CDW phase transitions are presented in Part5. Part6 deals with experimental observation of unexpected symmetry lowering transition in Sn/Si(111).

References for Part 1

Avila, J., Mascaraque A., Michel E. G., Asensio M. C., LeLay G., Ortega J., Perez R. and Flores F. (1999). "Dynamical fluctuations as the origin of a surface phase transition in Sn/Ge(III)." Physical Review Letters **82**(2): 442-445.

Axe, J. D., Grubel G. and Lander G. H. (1994). "Structure and Phase-Transformations in Uranium Metal." Journal of Alloys and Compounds **213**: 262-267.

Bardeen, J., Cooper L. N. and Scrieffer J. R. (1957). Physical Review **108**: 1175.

Barker, R. A. and Estrup P. J. (1981). "Surface-Structures and Phase-Diagram for the H-W(001) Chemisorption System." Journal of Chemical Physics **74**(2): 1442-1452.

Bennet, J. C. and Boswell F. W. (1999). Charge Density Waves phase transitions and microstructures in the TaTe4-NbTe4 system. Advances in the Crystallographic and Microstructural Analysis of Charge Density Wave Modulated Crystals. F. W. Boswell and J. C. Bennet. Dordrecht, Kluwer Academic Publishers**:** 69-120.

Binning, G., Rohrer H., Gerber C. and Weibel E. (1982). Appl. Phys. Lett. **40**: 15.

Boswell, F. W. and Bennet J. C., Eds. (1999). Advances in the Crystallographic and Microstructural Analysis of Charge Density Wave Modulated Crystals. Physics and Chemistry of Materials with Low-Dimensional Structures. Dordrecht, Kluwer.

Carpinelli, J. M., Weitering H. H., Barkowiak M., Stumpf R. and Plummer E. W. (1997). "Surface charge ordering transition: alpha phase of Sn/Ge(111)." Physical Review Letters **79**(15): 2859-2862.

Carpinelli, J. M., Weitering H. H., Plummer E. W. and Stumpf R. (1996). "Direct observation of a surface charge density wave." Nature **381**: 398.

Chadi, D. J. (1979). "Atomic and Electronic-Structures of Reconstructed Si(100) Surfaces." Physical Review Letters **43**(1): 43-47.

Chaikin, P. M. and Lubensky T. C. (1995). Principles of condensed matter physics, Cambridge University Press.

Comes, R., Shapiro S. M., Shirane G. and Heeger A. J. (1975). Physical Review Letters **35**: 1518.

Debe, M. K. and King D. A. (1977a). "New Evidence for a Clean Thermally Induced C(2x2) Surface- Structure on W[100]." Journal of Physics C-Solid State Physics **10**(11): L303-L308.

Debe, M. K. and King D. A. (1977b). "Space-Group Determination of Low-Temperature W(001)(Square Root 2x Square Root 2) Surface-Structure by Low-Energy-Electron Diffraction." Physical Review Letters **39**(11): 708-711.

Debe, M. K. and King D. A. (1979). "Clean Thermally Induced W[001](1x1)-](Square-Root 2xsquare-Root 2) R-45-Degrees Surface-Structure Transition and Its Crystallography." Surface Science **81**(1): 193-237.

Demuth, J. E., Koehler U. and Hamers R. J. (1990). "Surface Diffractometry and Lattice Imaging of Scanning Tunneling Microscopy Images." Journal of Vacuum Science & Technology a-Vacuum Surfaces and Films **8**(1): 214-217.

Dubiel, S. M. and Cieslak J. (1995). "Influence of Crystalline Boundaries on Spin-Density and Charge- Density Waves in Chromium." Physical Review B-Condensed Matter **51**(14): 9341-9344.

Ernst, H. J., Hulpke E. and Toennies J. P. (1992). "Helium-Atom-Scattering Study of the Structure and Phonon Dynamics of the W(001) Surface between 200-K and 1900-K." Physical Review B-Condensed Matter **46**(24): 16081-16105.

Gehring, G. A. and Gehring K. A. (1975). "Cooperative Jahn-Teller Effects." Reports on Progress in Physics **38**(1): 1-&.

Gothelid, M., Bjorkqvist M., Grehk T. M., Lelay G. and Karlsson U. O. (1995). "Metal-Semiconductor Fluctuation in the Sn Adatoms in the Si(111)-Sn and Ge(111)-Sn (Root-3x-Root-3)R30-Degrees Reconstructions." Physical Review B-Condensed Matter **52**(20): 14352-14355.

Gothelid, M., Hammar M., Tornevik C., Karlsson U. O., Nilsson N. G. and Flodstrom S. A. (1992). "Sn-Induced Surface Reconstructions on the Ge(111) Surface Studied with Scanning Tunneling Microscopy." Surface Science **271**(3): L357-L361.

Gruner, G. (1994). Density waves in solids. Reading MA, Addison-Wesley.

Hamers, R. J., Tromp R. M. and Demuth J. E. (1986). "Scanning Tunneling Microscopy of Si(001)." Physical Review B-Condensed Matter **34**(8): 5343-5357.

Hata, K., Kimura T., Ozawa S. and Shigekawa H. (2000a). "How to fabricate a defect free Si(001) surface." Journal of Vacuum Science & Technology a-Vacuum Surfaces and Films **18**(4): 1933-1936.

Hata, K., Kimura T., Takeuchi O. and Shigekawa H. (2000b). "Origin, cause, and electronic structure of the symmetric dimers of Si(100) at 80 K." Japanese Journal of Applied Physics Part 1-Regular Papers Short Notes & Review Papers **39**(6B): 3811-3814.

Hwang, C. M., Meichle M., Salamon M. B. and Wayman C. M. (1983a). "Transformation Behavior of a Ti50ni47fe3 Alloy .2. Subsequent Premartensitic Behavior and the Commensurate Phase." Philosophical Magazine a-Physics of Condensed Matter Structure Defects and Mechanical Properties **47**(1): 31-62.

Hwang, C. M. and Wayman C. M. (1983b). "Compositional Dependence of Transformation Temperatures in Ternary Tinial and Tinife Alloys." Scripta Metallurgica **17**(3): 381-384.

Ihm, J., Lee D. H., Joannopoulos J. D. and Xiong J. J. (1983). "Structural Phase-Diagrams for the Surface of a Solid - a Total- Energy, Renormalization-Group Approach." Physical Review Letters **51**(20): 1872-1875.

Inoue, K., Morikawa Y., Terakura K. and Nakayama M. (1994). "Order-Disorder Phase-Transition on the Si(001) Surface - Critical Role of Dimer Defects." Physical Review B-Condensed Matter **49**(20): 14774-14777.

Kidd, T. E., Miller T., Chou M. Y. and Chiang T. C. (2000). "Nature of the Sn/Ge(111) Surface-Charge-Density-Wave Phase Transtion." Physical Review Letters **85**(17).

Kohn, W. (1959). Physical Review Letters **2**: 393.

Kondo, Y., Amakusa T., Iwatsuki M. and Tokumoto H. (2000). "Phase transition of the Si(001) surface below 100 K." Surface Science **453**(1-3): L318-L322.

Kosterlitz, J. M. and Thouless D. J. (1973). "Ordering, Metastability and Phase-Transitions in 2 Dimensional Systems." Journal of Physics C-Solid State Physics **6**(7): 1181-1203.

Kubby, J. A., Griffith J. E., Becker R. S. and Vickers J. S. (1987). "Tunneling Microscopy of Ge(001)." Physical Review B-Condensed Matter **36**(11): 6079-6093.

Kubota, M. and Murata Y. (1994). "Streak Patterns in Low-Energy-Electron Diffraction on Si(001)." Physical Review B-Condensed Matter **49**(7): 4810-4814.

Landau, D. L. and Lifshitz E. M. (1970). Statistical Physics. New York, Pergamon.

Lee, J., Huang D. J. and Erskine J. L. (1995). "Forward-Electron-Scattering Study of the Surface-Structure and Phase-Transition on W(001)." Physical Review B-Condensed Matter **51**(19): 13824-13827.

Melechko, A. V., Braun J., Weitering H. H. and Plummer E. W. (1999). "Two-dimensional phase transition mediated by extrinsic defects." Physical Review Letters **83**(5): 999-1002.

Melechko, A. V., Braun J., Weitering H. H. and Plummer E. W. (2000). "Role of defects in two-dimensional phase transitions: An STM study of the Sn/Ge(111) system." Physical Review B **61**(3): 2235-2245.

Nelson, D. R. (1983). Defect-Mediated Phase Transtions. Phase Transitions and Critical Phenomena. C. Domb and J. L. Lebowitz. London, Academic Press. **7:** 1-99.

Orr, R. L. and Chipman J. (1967). Trans. Metall. Soc. AIME **239**: 630.

Overhauser, A. W. (1968). "Exchange and correlation instabilities of simple metals." Physical Review **167**(3): 691.

Peierls, R. E. (1955). Quantum Theory of Solids, Oxford University Press.

Robinson, I. K., Macdowell A. A., Altman M. S., Estrup P. J., Evanslutterodt K., Brock J. D. and Birgeneau R. J. (1989). "Order-Disorder Transition of the W(001) Surface." Physical Review Letters **62**(11): 1294-1297.

Santoro, G., Scandolo S. and Tosatti E. (1999). "Charge-density waves and surface Mott insulators for adlayer structures on semiconductors: Extended Hubbard modeling." Physical Review B-Condensed Matter **59**(3): 1891-1901.

Saxena, A., Gawlinski E. T. and Gunton J. D. (1985). "Structural Phase-Transitions on the Si(100) Surface." Surface Science **160**(2): 618-640.

Schlenker, C., Ed. (1989). Low-Dimensional Electronic Properties of Molibdenum Bronzes and Oxides, Kluwer.

Schlier, R. E. and Farnsworth H. E. (1959). J. Chem. Phys. **30**: 917.

Shigekawa, H., Hata K., Miyake K., Ishida M. and Ozawa S. (1997). "Origin of the symmetric dimers in the Si(100) surface." Physical Review B-Condensed Matter **55**(23): 15448-15451.

Smith, A. R., Men F. K., Chao K. J. and Shih C. K. (1996). "Variable low-temperature scanning tunneling microscopy study of Si(001): Nature of the 2x1->c(2x4) phase transition." Journal of Vacuum Science & Technology B **14**(2): 914-917.

Stensgaard, I., Purcell K. G. and King D. A. (1989). "Evidence for a Temperature-Induced Order-Disorder Phase- Transition on W(100)." Physical Review B-Condensed Matter **39**(1): 897-900.

Tabata, T., Aruga T. and Murata Y. (1987). "Order-Disorder Transition on Si(001)-C(4x2)to(2x1)." Surface Science **179**(1): L63-L70.

Terakura, K. (2000).

Terakura, K., Yamasaki T. and Morikawa Y. (1995). "Structural phase transition on Si(001) and Ge(001) surfaces." Phase Transitions **53**(2-4): 143-163.

Tosatti, E. (1995). Surface states, surface metal-insulator, and surface insulator-metal transitions. Electronic surface and interface states on metallic systems. Bertel and Donath. Singapore, World Scientific.

Tosatti, E. and Anderson P. W. (1974). "Charge and spin density waves on semiconductor surface." Japan. J. Appl. Phys. **Suppl. 2**: 381.

Tromp, R. M., Hamers R. J. and Demuth J. E. (1985). "Si(001) Dimer Structure Observed with Scanning Tunneling Microscopy." Physical Review Letters **55**(12): 1303-1306.

Tsuei, C. C. and Lilienthal H. (1976). "Magnetization Distribution in an Amorphous Ferromagnet." Physical Review B-Condensed Matter **13**(11): 4899-4906.

Weitering, H. H., Carpinelli J. M., Melechko A. P., Zhang J. D., Bartkowiak M. and Plummer E. W. (1999). "Defect-mediated condensation of a charge density wave." Science **285**(5436): 2107-2110.

Wendelken, J. F. and Wang G. C. (1985). "Finite-Size Effects on the W(001) Low-Temperature Phase- Transition." Physical Review B-Condensed Matter **32**(11): 7542-7544.

Wengelnik, H., Badt D. and Neddermeyer H. (1994). "Scanning-Tunneling-Microscopy on W(100) at 80-K and Room- Temperature." Surface Science **309**: 619-624.

White, R. M. and Geballe T. H. (1979). Long range order in solids, Academic Press.

Wolkow, R. A. (1991). “Ordered Buckled Dimer Configurations on Si(100) Observed with a New Variable Temperature Stm.” Abstracts of Papers of the American Chemical Society **202**: 185-PHYS.

Wolkow, R. A. (1992). “Direct Observation of an Increase in Buckled Dimers on Si(001) at Low-Temperature.” Physical Review Letters **68**(17): 2636-2639.

Yokoyama, T. and Takayanagi K. (2000). “Anomalous flipping motions of buckled dimers on the Si(001) surface at 5 K.” Physical Review B **61**(8): R5078-R5081.

Part 2

History

The study of the Sn/Ge(111), Pb/Ge(111) and similar systems began in 1981 (Ichikawa 1981). But it was not until 1996, when Carpinelli cooled down Pb/Ge(111), that the history of the symmetry lowering phase transition ($\sqrt{3}\times\sqrt{3}$)R30°$\leftrightarrow$(3×3) began. It is amazing that it took ~15 years for someone to cool down a system that is inherently unstable (See Part 1). Carpinelli et al. reported that α-phase of Pb/Ge(111) undergoes a phase transition from normal metal to Charge Density Wave state when the temperature was reduced (Carpinelli 1996). Later on they also reported that α-phase of Sn/Ge(111) exhibits a similar phenomenon (Carpinelli 1997). These observations attracted a lot of attention. The objective of this Part of the Dissertation is to present the observations on these systems scattered in many papers. Section 2.1 is devoted to the two papers of Carpinelli et al. that introduced the subject. In the next sections I present a review of works on Sn/Ge(111) that followed, beginning with results on atomic structure (Section 2.2), following with electronic structure measurements (Section 2.3) and finishing with theory developed for these surfaces (Section 2.4).

2.1. Discovery of Charge Density Wave phase transition in Pb/Ge(111) and Sn/Ge(111)

2.1.1 ($\sqrt{3}\times\sqrt{3}$)R30°$\leftrightarrow$(3×3) phase transition in Pb/Ge(111)

In an article in Nature Carpinelli et al. reported that α-phase of Pb/Ge(111) ($\sqrt{3}\times\sqrt{3}$)R30° exhibits a reversible, temperature-induced Charge Density Wave (CDW) localized at the surface (Carpinelli 1996). Their experimental observation showed that the formation of this new low temperature (LT) phase is accompanied by:

1) significant periodic valence-charge redistribution;

2) a pronounced lattice distortion and

3) a metal-nonmetal transition.

Pb/Ge(111): Experimental results at Room Temperature

Low Energy Electron Diffraction (LEED) data (Fig. 2.1a, left) show sharp diffraction spots, characteristic of the $(\sqrt{3}\times\sqrt{3})R30°$ surface symmetry displayed in Fig.1.14. Electron Energy Loss Spectroscopy (EELS) (Fig.2.1a, right) indicate that the RT α-phase is metallic. The direction of this measurement in k-space is shown in the inset of the Fig. 2.1a. The metallicity of this surface is indicated by

1. the presence of a broad, slowly decreasing Drude tail, produced when electrons at the Fermi level are excited into the adjacent continuum of empty states, and
2. the absence of a discrete energy loss onset.

Figure 2.2a presents RT STM data acquired at the same scan by at different bias voltages. In both the filled state and empty state, a hexagonal array of identical protrusions: all Pb atoms appear the same at RT in STM images.

Pb/Ge(111): Experimental results at Low Temperature

The LT LEED pattern shows the presence of extra spots (Fig. 2.1b), characteristic of a new (3x3) symmetry indicating considerable lattice distortion. In the EELS spectra there is no continuum of low energy losses; whereas the RT α-phase is metallic, a small gap ($E_g \leq$ 65 meV at 100 K) evolves as temperature is lowered. LT filled- and empty-state images of α-phase are shown in Fig.2.2b. Unlike the RT results, Pb adatoms no longer appear equivalent, and a new (3×3) symmetry found in LT LEED data can be seen. This is not the result of a rippled topography. Rather, it reflects the sensitivity of the STM

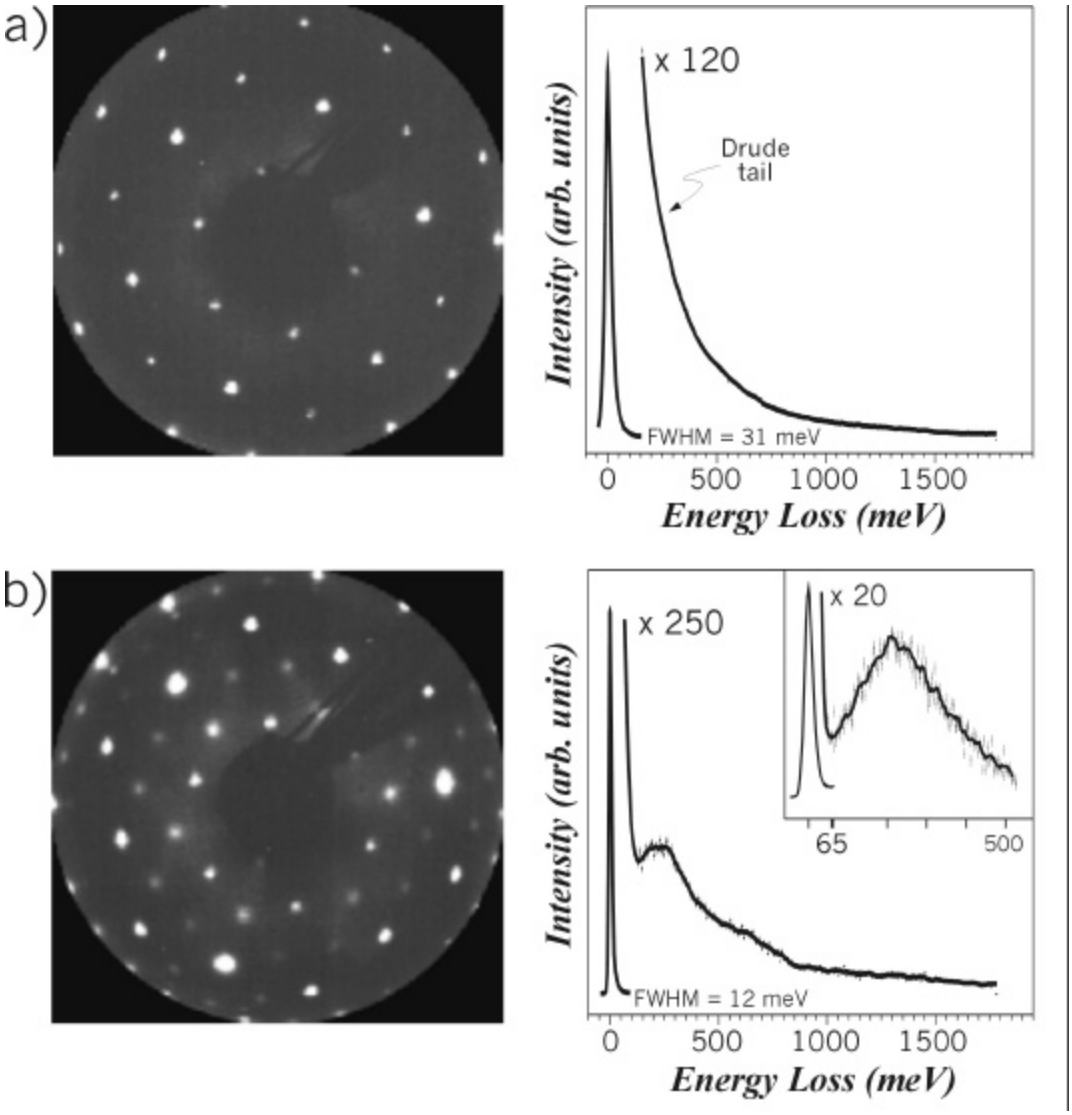

Figure 2.1 LEED and EELS data of the (√3×√3)*R*30°↔(3×3) phase transition in Pb/Ge(111)

RT (a) and LT (b;T≈100K) LEED (left) and EELS (right) data from the α-phase; beam energy for LEED was 48.6V.

In LEED, the change in symmetry from the room-temperature (√3×√3)R30° structure to the low-temperature (3x3) structure is highlighted by the emergence of many new diffraction maxima.

At RT, EELS indicates that α-phase is metallic. The discrete onset in the low-temperature spectrum indicates a surface band gap. The energy onset of such a loss spectrum corresponds to the gap magnitude E_g. Inset, off-specular data (non-zero parallel momentum transfer) inicating that the ground state band gap is no more than 65 meV. (Adopted from (Carpinelli 1996))

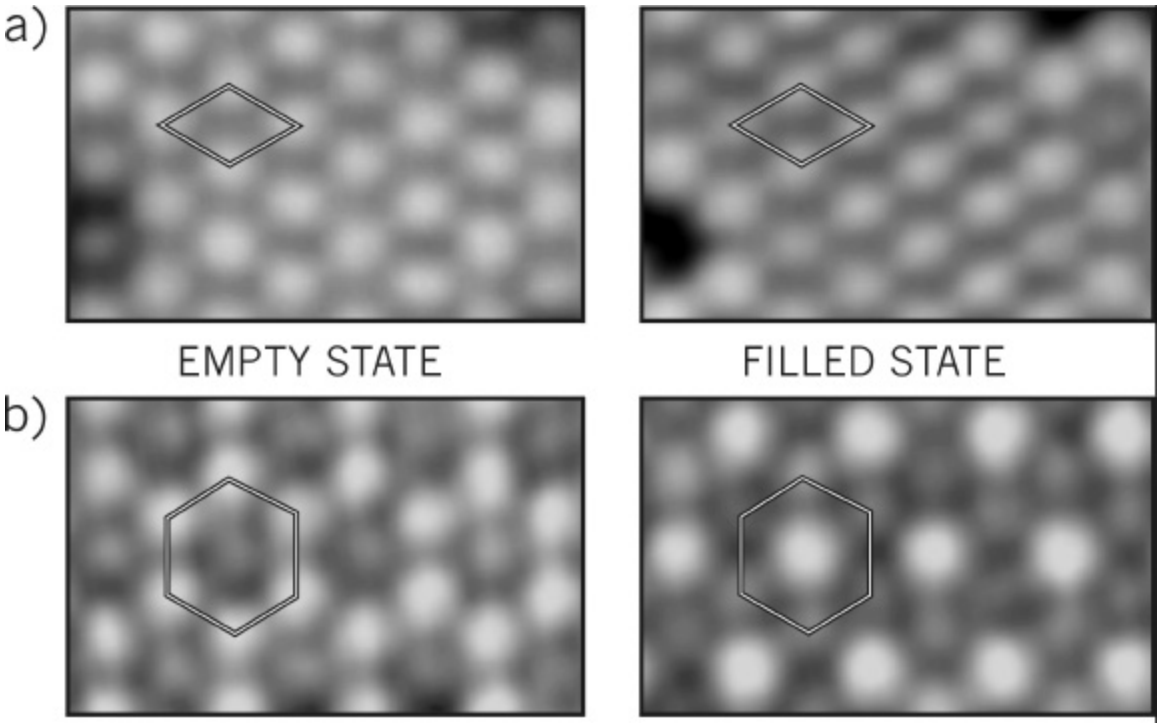

Figure 2.2 STM images of Pb/Ge(111) at RT and 60 K
(a) room temperature and (b) low temperature (T≈60K) STM data from the α-phase. (V_s=+1 V (left) and –1V (right) (Adopted from (Carpinelli 1996))

technique to the spatial profile of occupied (filled-state image) and unoccupied (empty-state image) electronic states. One out of three Pb adatoms now possess an enhanced concentration of filled states and appears brighter in the filled-state image. This same atom also possesses a diminished concentration of empty states and appears darker in the empty-state image. In other words, there is an excess charge on one Pb atom and depletion of charge on the other two Pb atoms in (3×3) unit cell. The result is the honeycomb-patterned charge superstructure commensurate with the underlying lattice.

The major inconsistency with the simple Surface Charge Density Wave (SCDW) picture results from electron counting. The new LT (3x3) unit cell is three times as large as the RT (√3×√3)R30° cell, containing 3 Pb and 9 Ge atoms and, therefore 21 valence electrons (3×4e (Pb) + 9e (Ge) = 21e). This requires this surface to be metallic in a band picture, in stark contradiction to the semiconducting ground state inferred from the EELS data.

Pb/Ge(111): Theoretical results

To identify the driving force for stabilization of a SCDW, Carpinelli et al. performed first-principle density functional calculations for this system using local density approximation (LDA). The calculations confirmed that the RT phase should be metallic with a half-filled band of surface states positioned in the gap region of the Ge substrate. In Fig. 2.3a, the wavy black line inside the (√3×√3)R30° surface Brillouin zone (the outer hexagon) depicts the shape and location of the calculated two-dimensional Fermi surface. A vector of constant momentum transfer connecting parallel segments of Fermi surface, called a nesting vector, was identified. The electronic response function of a nested Fermi surface would strongly peak at twice the Fermi wavevector ($2k_F$), which

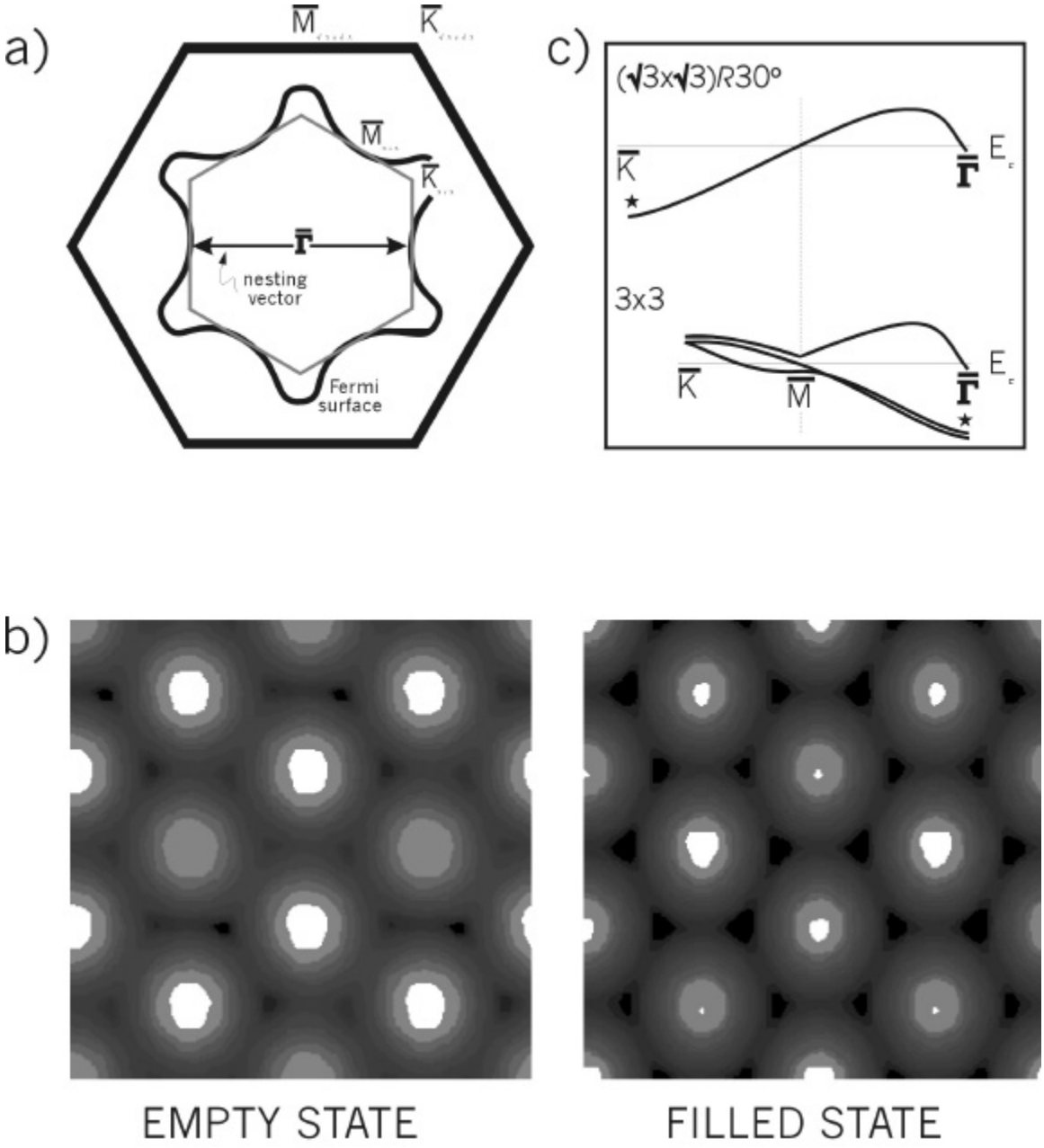

Figure 2.3 Calculations of electronic structure for Pb/Ge(111)

a) The wavy black line inside the outer hexagon (first Brillouin zone) is a curve drawn through calculated Fermi surface for the $(\sqrt{3}\times\sqrt{3})R30°$ structure.

b) Calculated contours of constant integrated local density of states (between E_F and +1V or –1V), simulating STM images.

c) Calculated band structure along high-symmetry directions for both the $(\sqrt{3}\times\sqrt{3})R30°$ and (3×3) structures

would facilitate enhanced electronic screening of phonons with momentum $2k_F$. This screening would result in a soft phonon at $2k_F$, a Kohn anomaly. If the nesting (and hence the screening) is strong enough, a static lattice distortion occurs, incorporating the symmetry of the nesting vector. As seen in Fig. 2.3a, the predicted nesting vectors almost match the symmetry of the observed (3x3) ground state (inner hexagon, Fig. 2.3a). Therefore, Carpinelli et al. concluded that Fermi-surface nesting, or consequently, electron-phonon coupling, drives this transition.

Ground state calculations showed that Pb and surface Ge atoms rearrange themselves to a (3x3) structure, reducing the total energy by about 0.020 eV per $(\sqrt{3}\times\sqrt{3})R30°$ unit cell. The corrugation of the lead adlayer was predicted to be ~0.05Å. Two simulated STM images for this structure (Fig. 2.3b) show qualitative agreement with the experimental data. Figure 2.3c shows the calculated band structure near the Fermi energy for both $(\sqrt{3}\times\sqrt{3})R30°$ and (3x3) structures. At RT, a single half-filled band (with strong p_z character) crosses the Fermi energy. Owing to the reduced symmetry, three bands exist in this region at low temperature: one crosses the Fermi energy (metallic) as before, but the other two show the effect of the new SCDW periodicity, opening up a small gap at the new (3×3) zone boundary ($\overline{M}$).

However, problems exist:

1) the calculated distortion (0.05 Å) of the lead atoms is not large enough to account for the intensity of the fractional-order LEED spots.
2) the theoretical (3x3) surface is metallic, contrary to the EELS data.

From those discrepancies Carpinelli et al. inferred that electron-electron interactions (not properly accounted for in the local density approximation) result in larger-than-predicted

lattice displacements, as well as the formation of a surface band gap (a Mott insulator) which further stabilizes the low-temperature phase. This could be a reasonable inference, as calculated charge density plots for Pb/Ge(111) indicate the states involved with Fermi surface nesting are localized, a necessary precursor to the onset of significant correlation effects.

The importance of the connection between the localization and electron-electron interaction was studied later on by Santoro et al. (Santoro 1999). The width W of the surface state band is relatively small: W≈0.5 eV for Pb and Sn/Ge(111), W≈0.3 eV for SiC(0001). Moreover, this band is half filled. These facts call for a careful consideration of electron-electron interactions, as well as of electron-phonon interactions, as possible sources of instability. The importance of electron-electron interaction is underlined by the different phenomenology of SiC(0001) and K/Si(111):B with respect to Pb/Ge(111). The stronger insulating character of the former surfaces parallels closely their stronger electron-electron repulsions, connected both with more localized surface Wannier functions (see Section 2.4 for details), and with reduced screening, due to larger bulk semiconducting gaps. An order of magnitude estimate for U, an effective repulsion (Hubbard U) for two electrons on the same adatom Wannier orbital, is U=0.6 eV for Si, the corresponding value would be smaller for Ge(111), in view of a very similar dispersion and of a ratio of about 4/3 between the dielectric constants of Ge and Si. The role of electron correlation in 3D CDW formation and stability was first discussed by Overhauser (Overhauser 1968).

2.1.2 (√3×√3)R30°↔(3×3) phase transition in Sn/Ge(111)

Carpinelli et al. showed that similar phenomena occur in an isoelectronic system α-Sn/Ge(111) (Carpinelli 1997). The change in LEED pattern indicated a structural transition from RT (√3×√3)R30° to LT (3×3) symmetry. They observed that such a change happens at appreciably lower temperature (-60°C for Sn/Ge(111) versus -20°C for Pb/Ge(111)). STM images acquired at RT and LT (~ 60 K) also show a change of symmetry (Fig. 2.4). At RT, all adatoms appear with equal brightness. When temperature is lowered adatoms no longer appear equivalent, and a new (3×3) unit cell can be identified. The bottom panel of the Fig.2.4 is a sum of LT filled and empty state images. It demonstrates the complimentarity between the filled state and empty state, which in its turn "guarantees these data indicate a real valence charge rearrangement and do not contain significant information about accompanying periodic lattice distortion." EELS spectra are shown in the Fig. 2.5 indicate that both RT and LT phases of Sn/Ge(111) are metallic at this specific q. Density-functional theory calculations were performed to understand the nature of the (3×3) phase of the Sn/Ge(111). It was found that that in this case (3×3) phase was not the ground state. Moreover, the calculated Fermi surface doesn't show any significant nesting in (3×3) direction and it was suggested that it doesn't play a role in this phase transition.

The calculated ground-state band structure around the Fermi energy is shown in the Fig. 2.6a. The large dots indicate the Sn-p_z-like surface band (S1) that causes the (√3×√3)*R*30° structure to be metallic. The inset of the Fig. 2.6b shows the calculated overlayer Fermi surface centered on Gamma-bar. This shape resembles that of the Pb

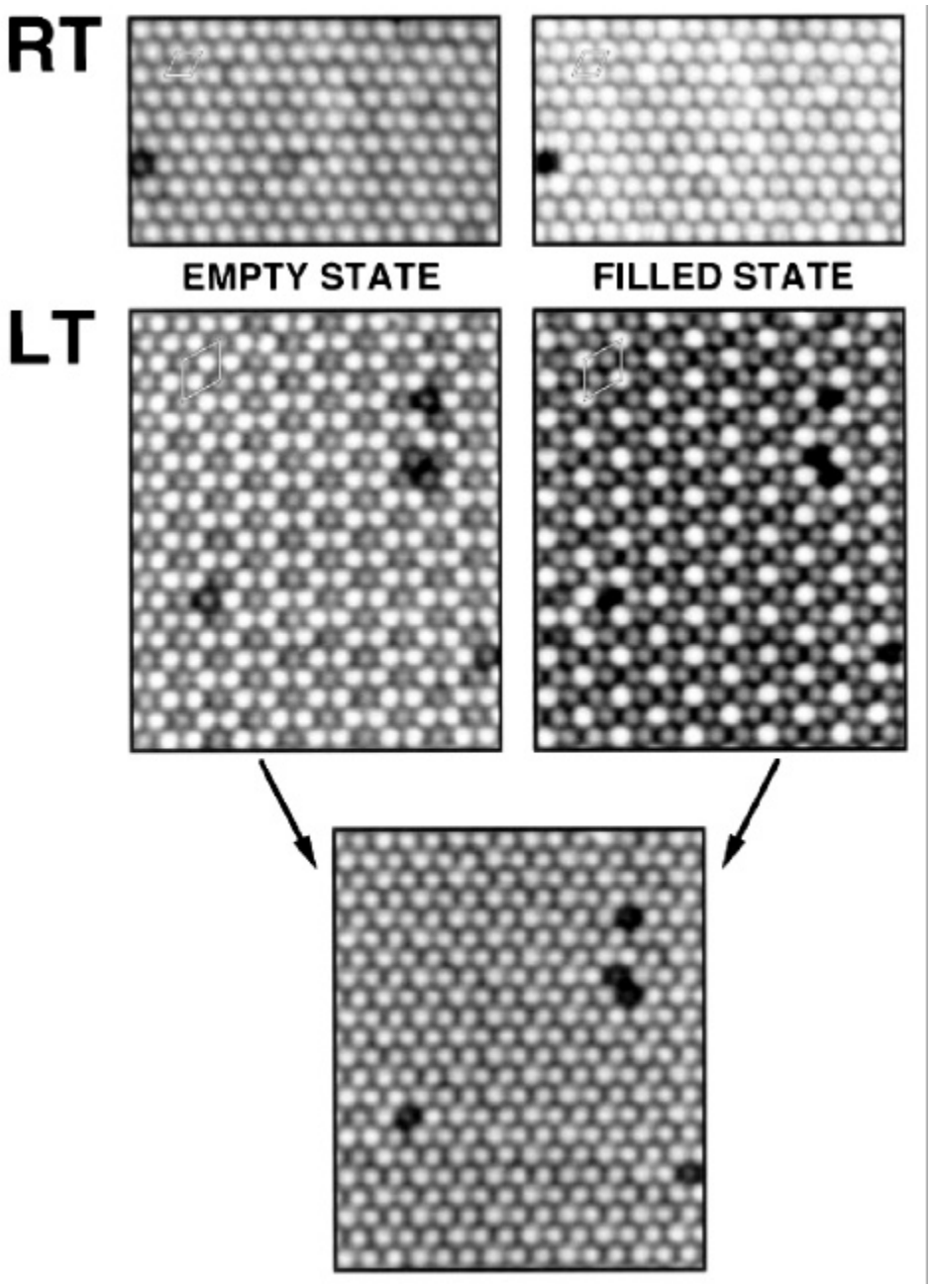

Figure 2.4 STM images of Sn/Ge(111) acquired at RT and LT (60 K).
Registry aligned 105×60 $Å^2$ STM images showing atomically resolved map of the Sn overlayer's unoccupied (V=+1.0V, left) and occupied (V=-1.0V, right) LDOS. An average of the two LT images is shown at the bottom to demonstrate complimentarity (a feature of CDW). (from (Carpinelli 1997))

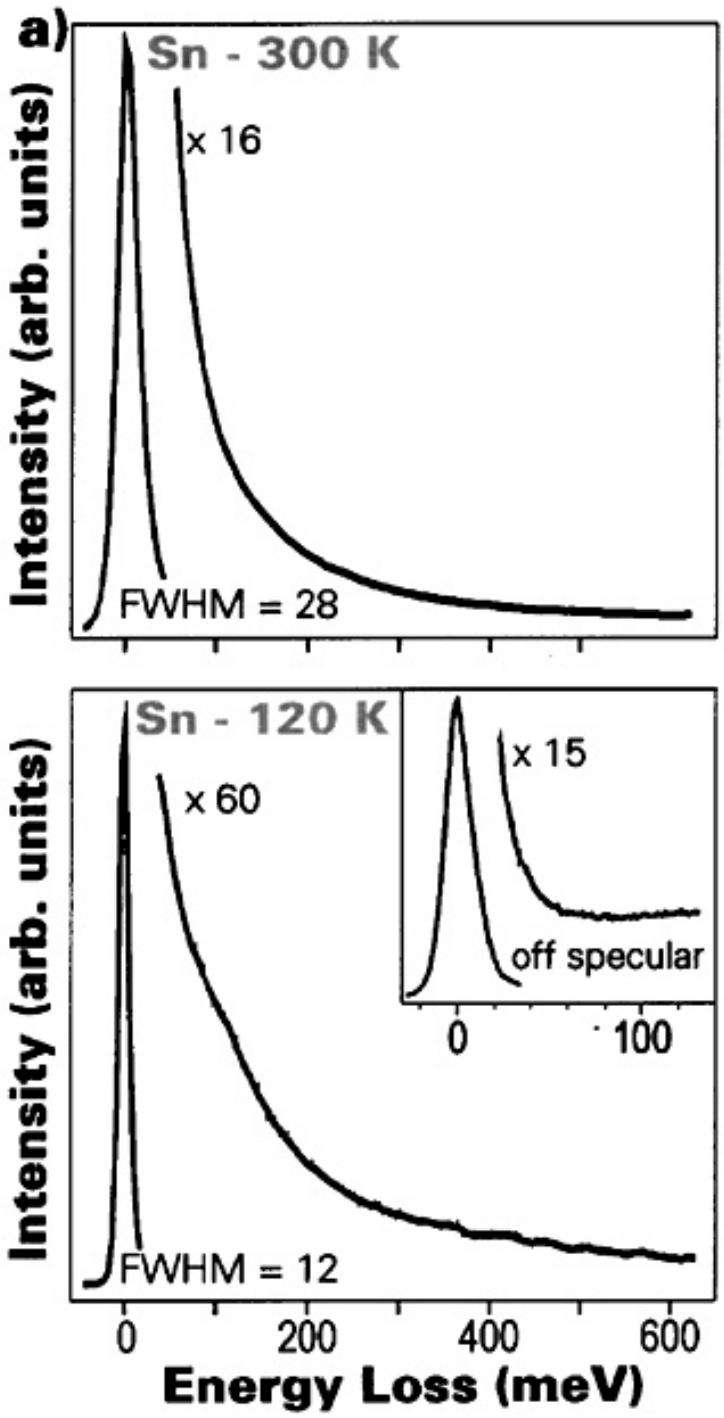

Figure 2.5 EELS data of the RT and LT Sn/Ge(111).
Specular EELS data of the RT and LT Sn/Ge(111) (impact energy =7 eV; inset =5° off specular). Drude tail indicates a metallic character of the surface both at RT and at LT. No metal-insulator transition was observed that would be expected if the CDW is formed.

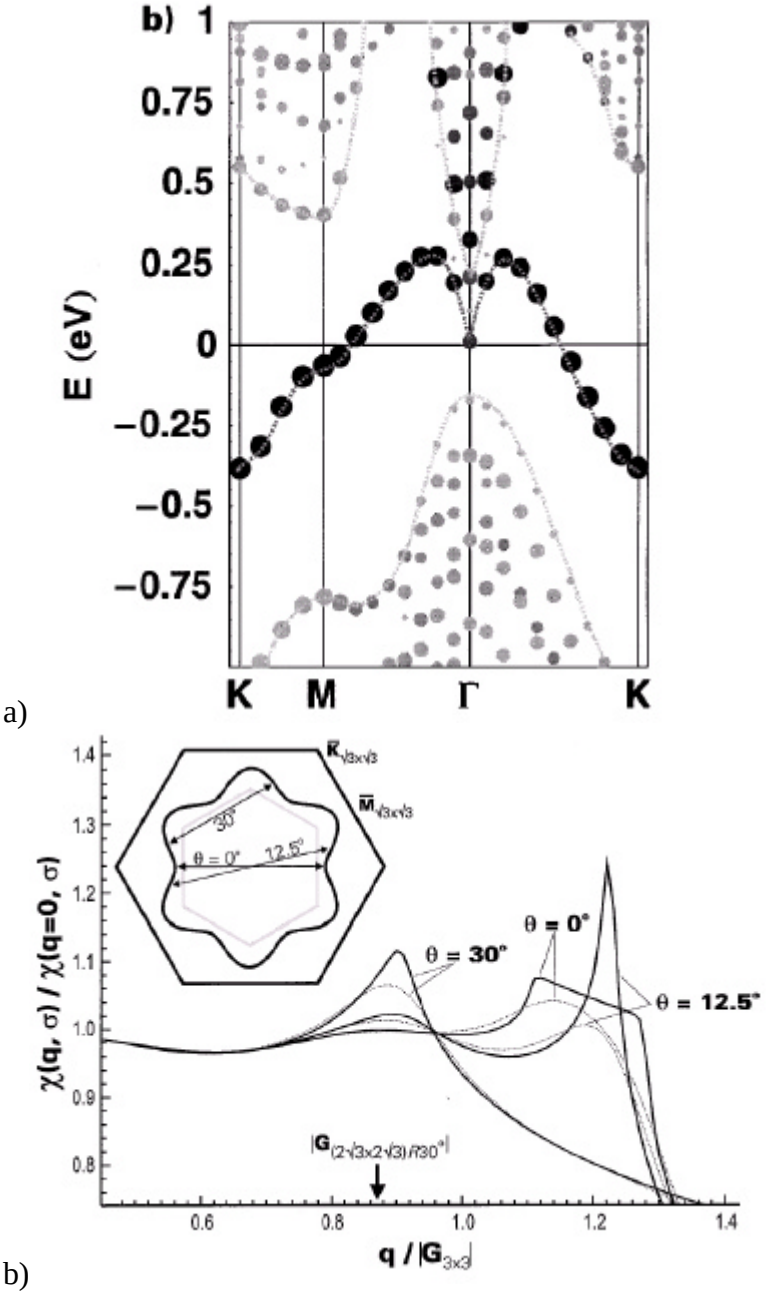

Figure 2.6 Electronic structure of the Sn/Ge(111) its calculated Lindhard response function

(a) Calculated ground-state band structure of the Sn-alpha phase; gray level indicates Sn-p_z character (black is highest)

(b) Angle specific T~0 (solid) and RT (dashed) normalized Lindhard response functions based on the calculated FS. Inset shows the Ge(111) (√3×√3) R30° surface Brillouin zone (outer hexagon) containing the calculated Fermi contour for the Sn overlayer.

(from (Carpinelli 1997))

Fermi surface (see Fig. 2.3a). It is not well nested along 0°. This is illustrated by calculating the momentum-resolved Lindhard function or the dielectric response (Fig. 2.6b) of a pseudo-free-electron band with angular-dependent effective mass appropriately chosen to exactly yield the calculated FS. The cusp along θ=0° is 11% off commensurate (~$1.11G_{3\times3}$). Thus it should not result in a Kohn anomaly. Instead, one would expect the broad peak along θ=30° to bring about a $(2\sqrt{3}\times2\sqrt{3})R30°$ distortion because it is only 4% off commensurate (~$1.04G_{(2\sqrt{3}\times2\sqrt{3})R30°}$). I will return to this very important observation in Part 6, where Sn/Si(111) system is discussed and $2\sqrt{3}$-symmetry was found.

2.2. Atomic structure of Sn/Ge(111)

One of the keys to understanding the origin of the CDW transition in the Sn/Ge(111) system is the structure of the periodic lattice distortion accompanying the electronic transition. Such investigations have been conducted using Surface X-ray Diffraction (SXRD) (Pedersen 1987; Baddorf 1998; Bunk 1999) and Low Energy Electron Diffraction (LEED I/V) (Zhang 1999). The measurements were done at room temperature and at “low temperature”. The “low temperature” was assumed to be the temperature bellow critical temperature reported by Carpinelli (Carpinelli 1997). Unfortunately it is not possible to build a complete picture based on these data for a couple of reasons: there is no actual variable temperature measurements so that the size of the PLD would be determined across the phase transition temperature, the “low temperature” was different in different papers so that the direct quantitative comparison has to be done carefully.

The structural model of the Sn/Ge(111) ($\sqrt{3}\times\sqrt{3}$)R30° determined by SXRD is presented in the Fig. 2.7. The bottom picture is a side view showing the Sn overlayer and three bilayers of Ge. Both of these diagrams show Ge atoms in the bulk positions associated with a (1×1) LEED pattern. The arrows indicate the direction of the distortion of Ge atoms induced by the presence of Sn atoms on the surface. Structural parameter values are given in Table 2.1. The LEED/SXRD structure (Zhang 1999) gives a Sn-Ge bond length of 2.86 Å, with a "pinching" in the three Ge atoms in the surface plane by 0.05 Å (Fig. 2.7). Within experimental error all Ge-Ge bond length are the same as the bulk value of 2.45 Å. This structure does have an angular distortion in the Ge-Ge bond compared to the ideal sp^3 hybridization. SXRD results from (Bunk 1999) show that the Ge-Ge bond lengths deviate less than 3% from the bulk value of 2.45 Å. The Ge-Sn bonds with 2.83 Å are slightly larger than the sum of the tetrahedral covalent radii for germanium and white tin (2.74 Å/ 2.82 Å) and larger than the value expected for grey tin (α-Sn) and germanium (2.63 Å). The Sn bond angle is 82.0°. The in-plane displacement of the first layer Ge atoms is 0.17 Å.

When the temperature is reduced the surface reduces its symmetry to lower its energy. This occurs through a vertical rippling of the Sn layer which induces distortion in the Ge first bilayer (See Fig. 2.8a and Table 2.2). All of the resulting distortion results in changes in bond angles trying to minimize any changes in the bond lengths. Consider first the structural changes associated with Sn(B). The outward displacement of Sn(B) accompanied by inward and upward motion of the Ge(2B) atoms creates an appreciable increase in the tetrahedral bond angle (Sn-Ge(2)-Ge(4)), from 65.5° for the $\sqrt{3}$ phase to 77.1° for the (3×3) phase. There is also a change in the Ge tetrahedral bond angle defined

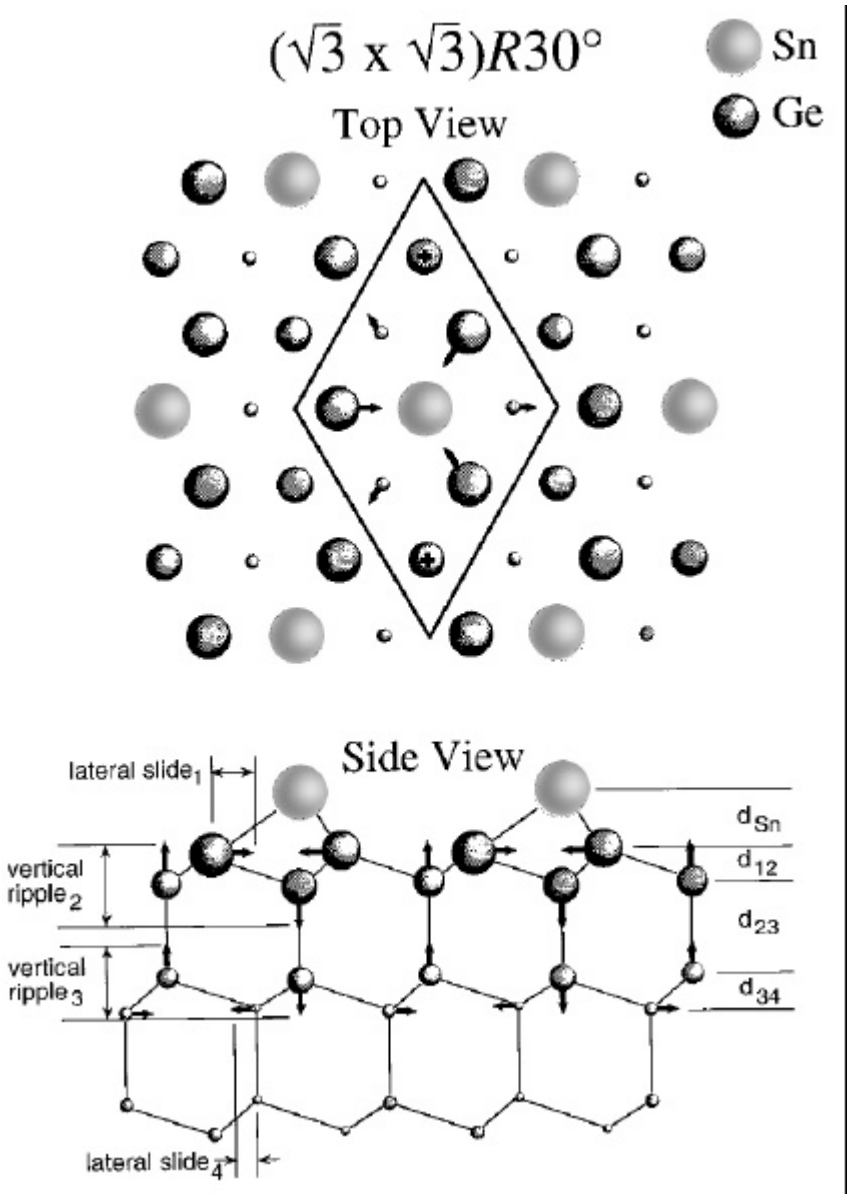

Figure 2.7 Structural model of Ge(111)-(√3×√3)R30°- Sn.
The top is a view from above the structure and the bottom is a side view. Ge atoms are drawn in bulk-truncated positions, with arrows to show the direction of distortions induced by Sn; plus signs indicate motion out of plane of the figure. Arrow lengths are not to scale (from (Baddorf 1998))

Table 2.1 Structural parameters for Sn/Ge(111) (√3×√3)*R*30° determined by LEED and XRD

Δd_i is the vertical distance of the *i*th plane with respect to the position of an ideally bulk truncated surface. d_{Sn} is the vertical distance of the Sn from the first Ge layer. The geometry of this surface is shown in Fig. 2.8.

Parameteres (Å)	SXRD (Pedersen 1987)	SXRD (Baddorf 1998)	LEED I/V (Zhang 1999)	LEED/SXRD (Zhang 1999)	SXRD (Bunk 1999)
d_{Sn}	1.72 Å	1.91 Å	1.75 Å	1.75 Å	1.84 Å
lateral slide$_1$	0.204 Å	0.05	0.03	0.05	0.17 Å
vertical ripple$_2$	0.58	0.61	0.562	0.556	0.53
vertical ripple$_3$	0.58	0.40	0.463	0.426	0.38
lateral slide$_4$	0.106	0.04	0.182	0.04	0.07
Δd_1		0.088	-0.024	-0.018	-0.01
Δd_2		0.028	-0.042	-0.030	
Δd_3		0.085	-0.067	-0.059	
Δd_4		0.052	-0.027	-0.030	

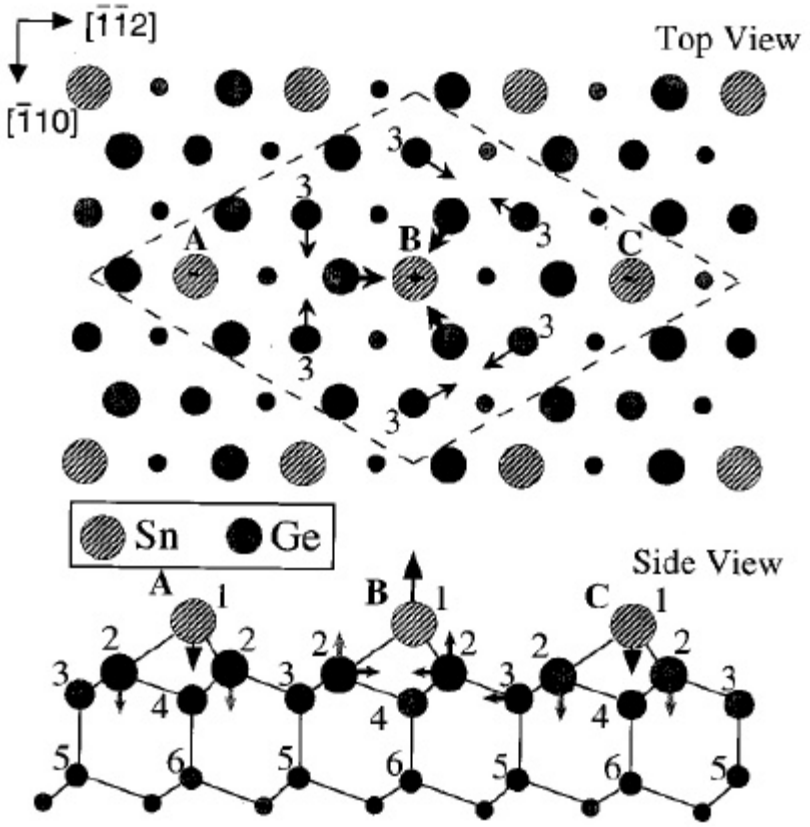

a)

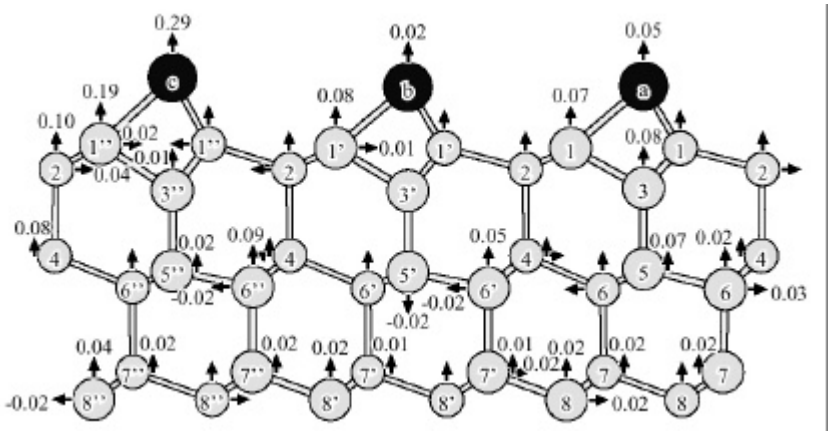

b)

Figure 2.8 Structural model of Sn/Ge(111) (3×3) LT phase.

a) (from (Zhang 1999)) The arrows show the direction of the distortion-induced charge ordering transition with respect to the (√3×√3)*R*30° RT phase, i.e., the difference between the (3×3) and (√3×√3)*R*30° structures.

b) (from (Bunk 1999)) Here the displacements relative to the room temperature (√3×√3)*R*30° phase are given in Å. For clarity the displacements of symmetry equivalent atoms are shown only once.

Table 2.2 Structural distortion for the low-temperature (3×3) phase compared to the room-temperature (√3×√3)*R*30° phase.
The geometry of the surface is shown in Fig. 2.8

Parameter	LEED I/V	LEED/SXRD (Zhang 1999)	SXRD (Bunk 1999)
ΔSn (A and C)	(A) –0.101 (C) –0.061	-0.015	0.05 0.02
ΔSn (B)	+0.294	0.355	0.29
Δd_1(A and C)		-0.036	0.07 0.08
Δd_1(B)		+0.134	0.19
Lateral 1-B		0.117	
Lateral 3		0.148	

by Ge(2B)-Ge(4B)-Ge(6B), from 118° for the √3 to 122° for the (3×3). Therefore, the bonding of the Sn to the Ge in the B site becomes more s-p_z like (Harrison 1980). The downward motion of Ge atoms 2A and 2C causes a slight increase in the distortion in the tetrahedral formed by Ge(2A)-Ge(3A)-Ge(5A), driving Sn atoms A and C to be more p_x-p_y bonded. The tetrahedral formed by the three Ge(2) atoms, the second-layer Ge(3) atom, and the third-layer The Ge(3)-Ge(5) axis is tilted by 3.5° with respect to the surface normal. The three Ge(3)-Ge(5) axis. The azimuth bond angles in the plane perpendicular to the 3-5 axis are not identical, distorted to 127°, 115°, and 118°, with respect to ideal value of 120°.

The interplay between the electronic structure, the geometrical structure, and the lattice dynamics can now be understood, at least qualitatively. The system lowers its electronic energy by lowering the symmetry and the price paid in bond-angle distortions is less than the energy gained (Harrison 1980). The physics is nearly ideal case of a band Jahn-Teller distortion, discussed by Friedel (Friedel 1977).

There are several important features to be noted (Bunk 1999):

(i) One Sn atom is displaced out of the surface plane by 0.29 Å; this Sn atom is at a vertical position 0.26 Å higher than the average position of the two lower Sn atoms.

(ii) The three nearest-neighbor Ge atoms partially follow this relaxation, mainly in the z direction and not in-plane.

(iii) The average layer spacing between the first and second Ge double layer is expanded relative to the room-temperature phase. For the room-temperature phase this distance is 1.004 and from the second and the third double layer 0.993 in

lattice coordinates, i.e. and expansion and a contraction relative to the bulk value of 1.000. However, for the LT phase the first to second double-layer distance is 1.026 and the second to third layer distance is 1.002, i.e., a considerable expansion in the upper two double layers.

(iv) The outwards displaced Sn atom has a very anisotropic atomic displacement parameter (adp) with an amplitude 10 times large in the z direction than in-plane. This means that either the atom is performing a very anisotropic motion with a large amplitude or, as is more likely at LT, there is some disorder in the z position of this atom. The adp's for the nearest-neighbor Ge atoms are also larger than at RT, again indicative of disorder. This is not surprising since the position of these atoms must at least partially follow the Sn atoms.

(v) Their analysis showed that if the if there is more than one site for the Sn atoms in the $(\sqrt{3}\times\sqrt{3})R30°$ structure the height difference is much less than that observed in the (3×3) phase. The fact that the adp of the surface layer Ge atoms are similar in both phases is strong evidence against an order/disorder phase transition.

2.3. Electronic structure of Sn/Ge(111)

Angle-resolved ultraviolet photoemission spectroscopy (ARUPS) was used to investigate in detail the electronic structure of the valence band and the core levels of Sn/Ge(111). It is mainly due to the discrepancy in the results obtained by different groups that we owe the existence of several models for the PT in Sn/Ge(111).

2.3.1 Core level spectra

The stabilization of a 3×3 reconstruction from the RT α√3 unit cell means that inequivalent Sn atoms must appear at LT. One suitable tool to analyze this should be core level photoemission spectroscopy. In this technique, the inner core levels are measured. The existence of components with different binding energies is related to a different chemical environment (initial state effect). Different screening properties may also affect the binding energy (final state). The 4d core levels at RT has been one of the major issues debated in the literature (Gothelid 1995a; Gothelid 1995b; Le Lay 1998; Uhrberg 1998; Avila 1999b; Kidd 1999; Uhrberg 2000). The Sn atoms are known to occupy the T_4 adsroption site at RT and should give rise to a single core level component. Yet the observed Sn core level line shape at RT is too broad, indicating a splitting into multiple components.

In the ideal (√3×√3)*R*30° Sn/Ge(111) structure all Sn atoms are equivalent thus this should give only one component in core level spectra (Fig. 2.9). In the (3×3) phase of Sn/Ge(111) observed at LT there are three Sn atoms per unit cell. The measurements of the atomic structure showed that one Sn atom is displaced up (out of the surface) and two of the other two are displaced down (toward bulk). At low temperatures, a charge transfer occurs resulting in two different charge states, one positive and the other negative, relative to the initial "neutral" state (Fig. 2.9b). The negative would correspond to the bright atom in the filled state STM image and correspondingly to one "up" atom as determined by LEED I/V and XRD. As shown in the Fig. 2.9b, there are as twice as many positive atoms as the negative atoms in LT phase (one up and two down); thus, the

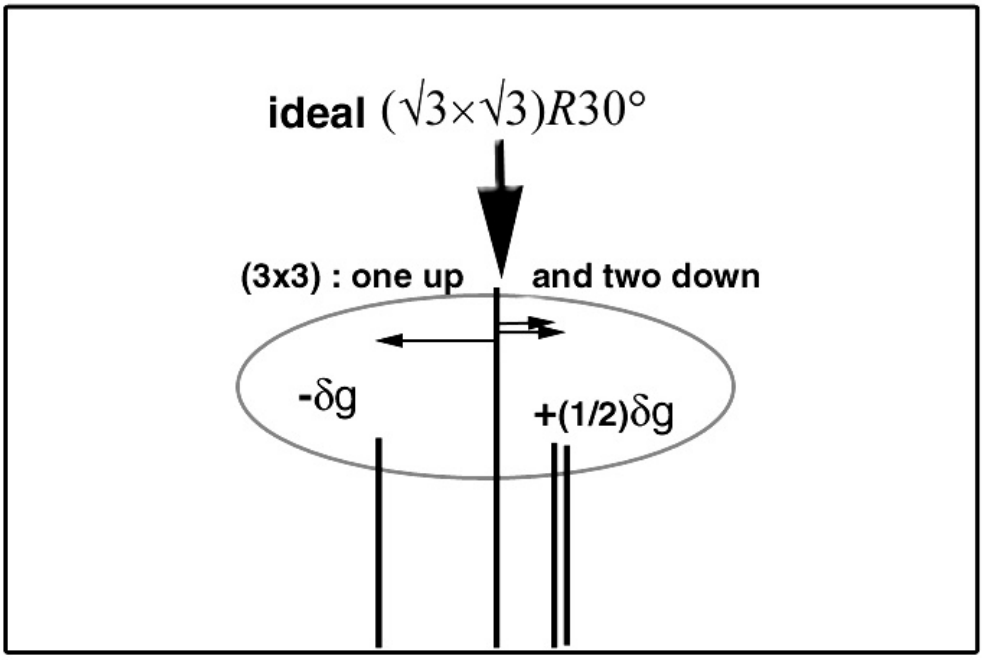

a)

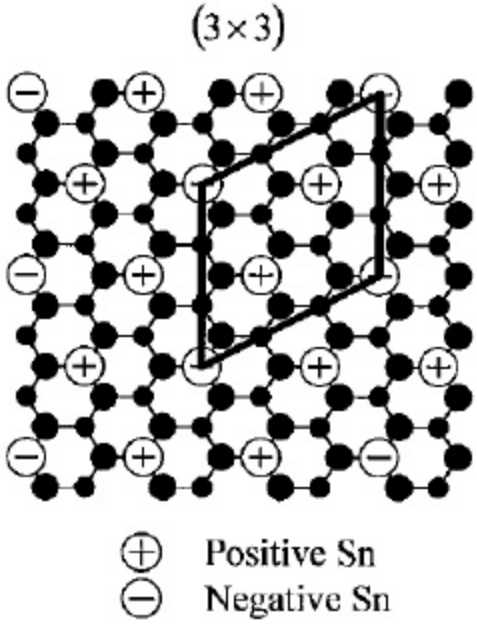

b)

Figure 2.9 Diagram of energy shifts for (3x3) with respect to ($\sqrt{3}\times\sqrt{3}$)*R*30°

a) diagram of core level shifts

charge redistribution in (3×3) Sn/Ge(111) phase

extra charge on the negative atoms is roughly twice as much as that for the positive atoms.

From their RT measurements (Fig. 2.10a) Avila et al. assumed that two components with intensity ratio of 1:2 give a sufficiently good fit (Avila 1999b). The influence of defects was discarded because “the line shape was the same for many preparations”, though I would assume from that only that the number of defects was constant in their experiments. They also found that at the LT 3×3 phase, both components were preserved, and there was only a small change of their relative intensities Thus, it was concluded that “the existence of two distinct components in the core level at LT means that two inequivalent kinds of atoms exist at the surface in the 3×3 reconstruction, as expected, but surprisingly the two kinds of atoms subsist at RT.”. This observation along with their density functional (DFT) and molecular dynamics (MD) calculations (see Section 2.4 below) lead them to the picture that “Sn atoms fluctuate at RT between two positions and are stabilized in a 3×3 structure at LT.

The results of Kidd et al., in contrast, do show temperature dependence of the line shape (Kidd 1999). They interpreted the broad RT core level spectra (Fig. 2.10b) as a result of three components: one from normal state and the other two associated with CDW (Kidd 1999). The presence of the CDW components in the RT phase was assumed to be related to the defect induced effects. Their interpretation has been made to agree with our STM observations that I present in Part 4, hence I would like to discuss their results in more detail. This charge transfer is expected to cause a splitting of the Sn core level from the initial neutral position to one at a lower (higher) binding energy for the negatively (positively) charged atoms in the CDW phase. The Sn 4d core level spectra

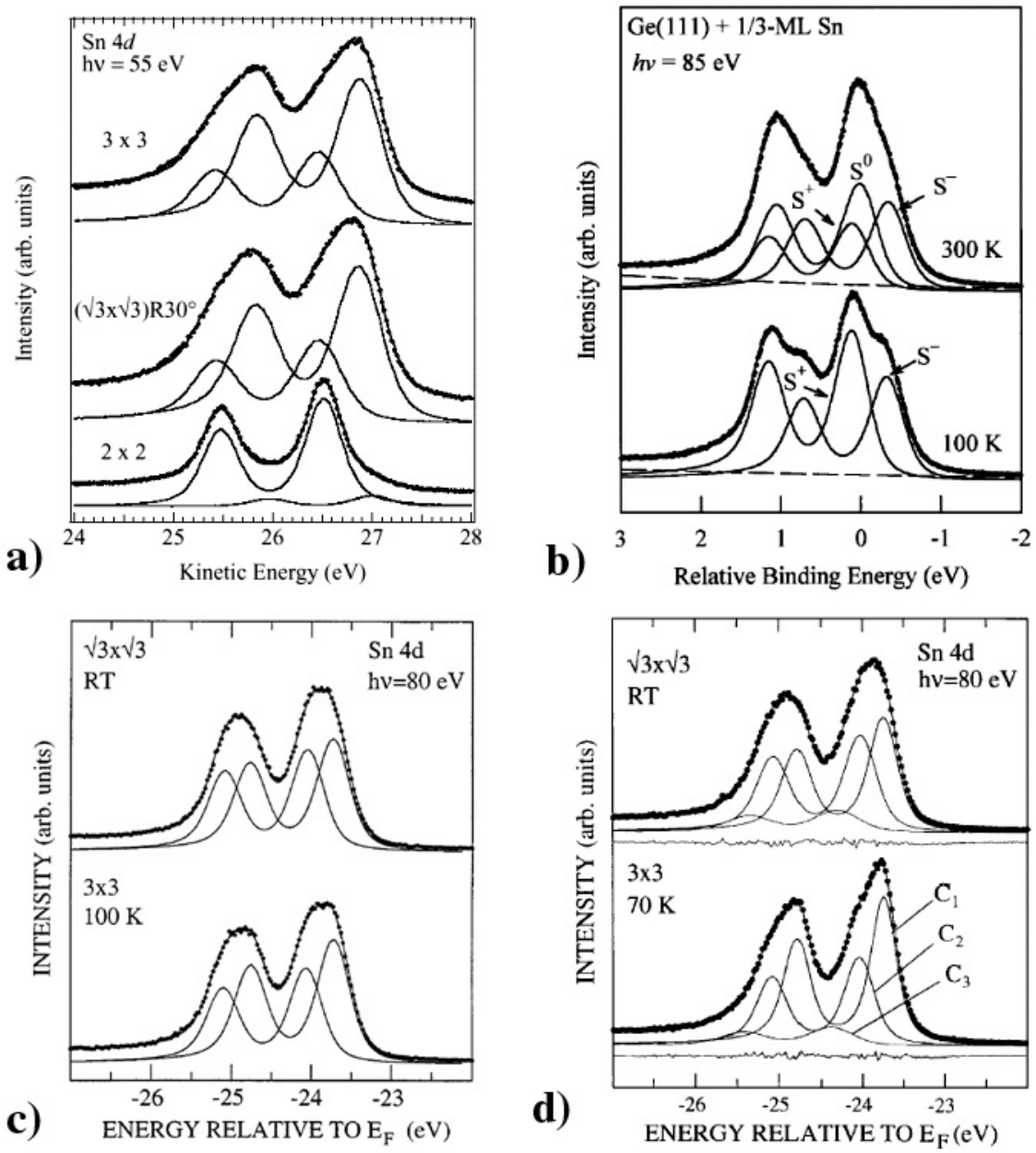

Figure 2.10 4d core level spectra for Sn/Ge(111) at RT and LT.

a) Sn 4d core level for different surface reconstructions From bottom to top, the core levels found for the 2×2, α√3, and 3×3 reconstructions (from (Avila 1999b).

b) from (Kidd 1999)

c) from (Uhrberg 1998)

d) (Uhrberg 2000)

obtained by Kidd et al. are displayed in Fig. 2.10b. They stated that their spectra were temperature dependent in contrast to other's. At 100 K only two components, labeled S^+ and S^-, were sufficient to fit. The intensity ratio between these two components was found to be 1.5. The difference from the expected value of 2 could be explained by the presence of defects and will be discussed later. At RT the line shape was broad with a shoulder on the lower binding energy side that indicated more than one component. An attempt to fit this spectrum as well as other spectra taken at temperatures above 100 K with just two components was found to be unsuccessful – the peak positions shifted by up to 80 meV and the quality of the fit was poor. With peak the addition of a third component, the parameters for peak widths and positions all were within experimental accuracy (10 meV). This new component has a binding energy in between the S^+ and S^- and is closer to the S^+ component. It is reasonable to associate this new component with the neutral Sn atoms in the normal phase. Figure 2.11a shows the binding energies of these three components as a function of temperature. The explanation for the LT behavior was presented above. What is puzzling is the persistence of the S+ and S- at higher temperatures. The analysis of the STM images offers an explanation for this effect. Ge substitutional defect induces perturbation around it with negatively and positively charged atoms. Even though the shape of this perturbation (Fig. 2.11b) suggested by Kidd et al. is not exactly what was observed by STM (see Part 4), the idea in general is very appealing. Quantitatively there are more negatively charge atoms around defect that positively charged atoms, this is why the S- component has a bigger intensity at RT than the S+ component.

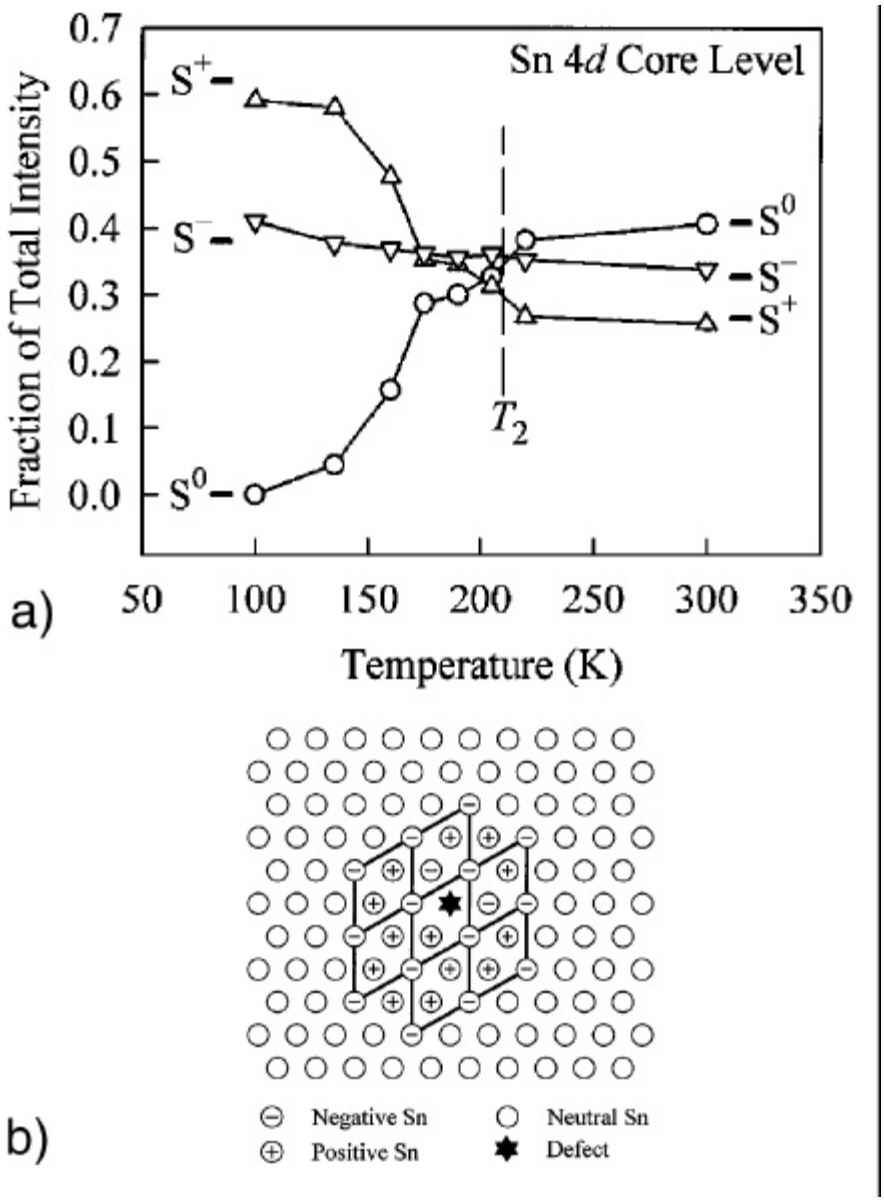

Figure 2.11 Temperature dependence of the intensities of the three Sn 4d core level components according to Kidd (Kidd 1999)

a) Temperature dependence of the intensities of the three Sn 4*d* core level components S_1 , S_0 , and S_2 normalized to the total intensity taken at a photon energy of 85 eV. The curves are straight-line segments connecting the data points. The upper transition temperature T_2 at about 210 K is indicated by a vertical dashed line. The short horizontal line segments near the two ends of each curve indicate the expected limiting values based on their model.

b) Charge distribution around Ge defect at RT assumed to account for Sn 4d core level splitting

Unfortunately the ambiguity of the peak fitting procedure and the complexity of the sample preparation does not allow us to call this matter closed. It is not possible to obtain truly unique fits to each spectrum, and any comparison, especially when it comes to intensities, will be subject to a significant uncertainty. The issue of sample preparation (see Part 3) was addressed by Uhrberg et al. in their recent work (Uhrberg 2000). The core level spectra obtained by this group after careful analysis of the dependence on the Sn coverage are shown in the Fig. 2.12d along with their previous results (Fig. 2.12c) (Uhrberg 1998). The LEED pictures presented in the Fig. 2.12a are obtained at LT (70-100K) for different Sn coverages. The lowest coverage results in a strong "2×2" diffraction which does not form normal circular spots on the LEED screen. Instead they have a rectangular shape similar to what can be observed on a disordered c(2×8) surface. When the coverage is increased they observed a mixed 2×2 and 3×3 phases for the cooled samples in the coverage range 0.20-0.25 ML (See also Fig. 3.9 and 3.10 of this Thesis). At higher coverages the 2×2 disappears and only 3×3 is observed. Sn 4d spectra corresponding to the different LEED pictures are shown in the Fig. 2.12b. From this comparison they concluded that results obtained by Kidd et al. correspond to the Sn coverage in the range between 0.20 and the 0.22 ML spectra, while others reported results for the 1/3 ML.

Two conclusions can be made from what was presented above. First, the sample preparation is crucial to reproducibility of results. Second, the core level spectroscopy as well as LEED are area averaging techniques and the interpretation of the results has to be done very carefully, taking special care to the differentiating between different reconstructions coexisting at this surface at all times (see Part 3). The nature of the RT

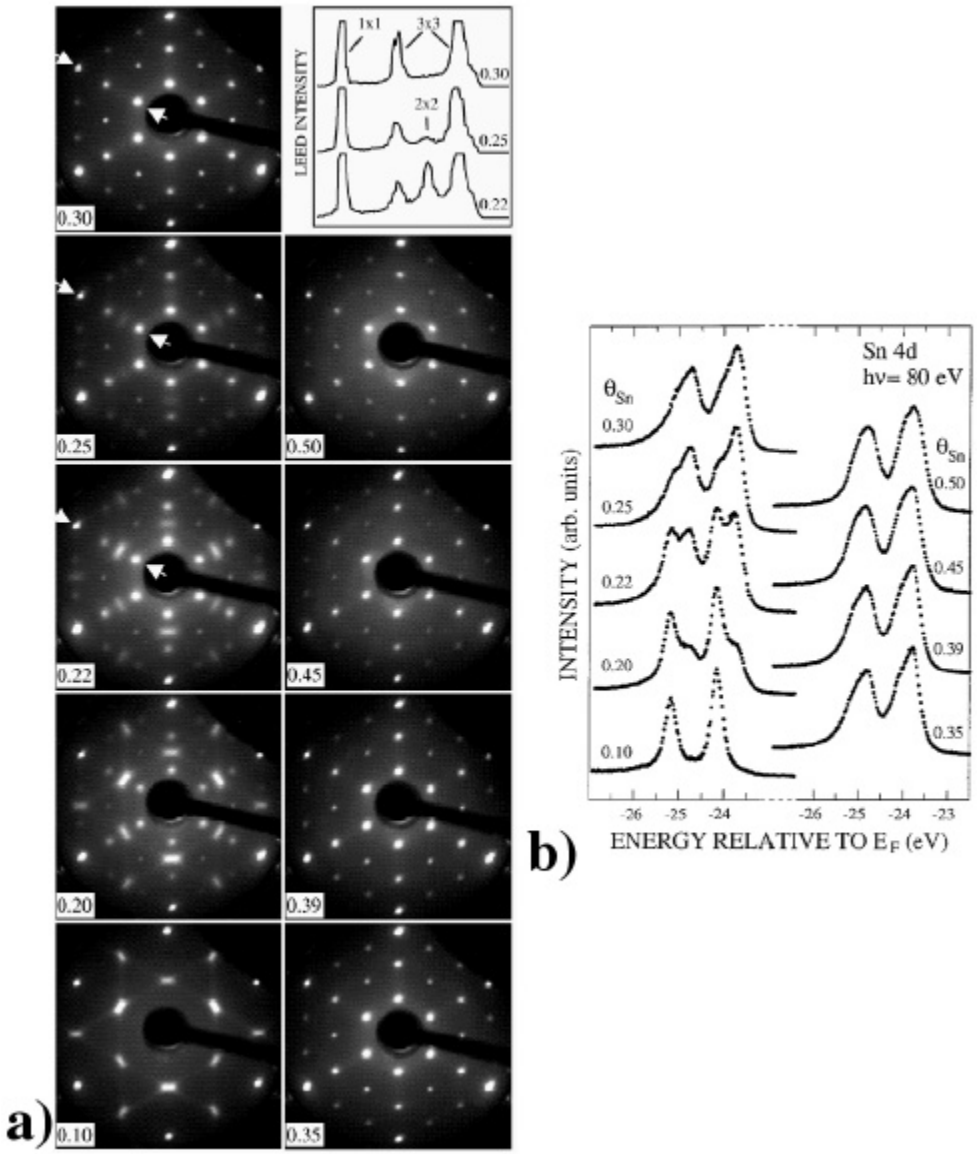

Figure 2.12 LEED patterns and Sn 4d core level spectra at different coverages of Sn on Ge(111).

a) LEED patterns (37 eV electron energy) from Sn/Ge(111) surface with different Sn coverage as indicated in each frame. The graph shows the LEED intensity between the arrows for the 0.22, 0.25, and 0.30 ML coverages. Both 0.22 and the 0.25 ML surfaces show 2×2 diffraction while the 0.30ML surface shows only 3×3 diffraction.

b) Sn 4d core-level spectra taken at low temperature (70-100 K) from surfaces corresponding to the LEED patterns in a). The 0.10 ML spectrum was recorded at RT. The spectra are displayed with the same peak height.

and LT phase of Sn/Ge(111) can not be determined based solely on core level spectra.

2.3.1 Valence band photoemission spectra

The results for the valence structure of Sn/Ge(111) have been as diverse as core level results. Four of them are presented in Fig. 2.13 in chronological order (Goldoni 1997; Uhrberg 1998; Avila 1999a; Kidd 2000). The same results are shown in the Fig. 2.14 rescaled for comparison.

Goldoni and Modesti observed a dispersive peak in the normal phase transforming into a nondispersive peak in the CDW phase accompanied by a depletion of the density of states near the Fermi level (Fig. 2.13a). These observations were taken as evidence for strong electron correlation effects. Uhrberg and Balasubramanian rejected this interpretation based on their results (Fig. 2.13b). Their photoemission data showed that the $\sqrt{3}\times\sqrt{3}$ and the 3×3 surfaces have almost identical surface band structures with two dispersive bands, one of which crosses the Fermi level. The close resemblance between the electronic structures suggests a common atomic structure. Taking also into account that the Sn 4d core level spectra they obtained do not change with temperature and are split into two components they concluded that $(\sqrt{3}\times\sqrt{3})R30°$ phase was just a structurally disordered state of the (3×3) phase. Avila at al. came to similar conclusions (Fig. 2.13c), except they suggested the dynamic fluctuations as such source of disorder. In the above-mentioned works the influence of defects was totally disregarded. The ARPES measurements by Kidd et al. (Fig. 2.13d) of the valence structure of Sn/Ge(111) were done with focus on the (3×3) zone boundary in order to track changes near the Fermi level that can be correlated with the phase transition. Despite the lack of nesting, a

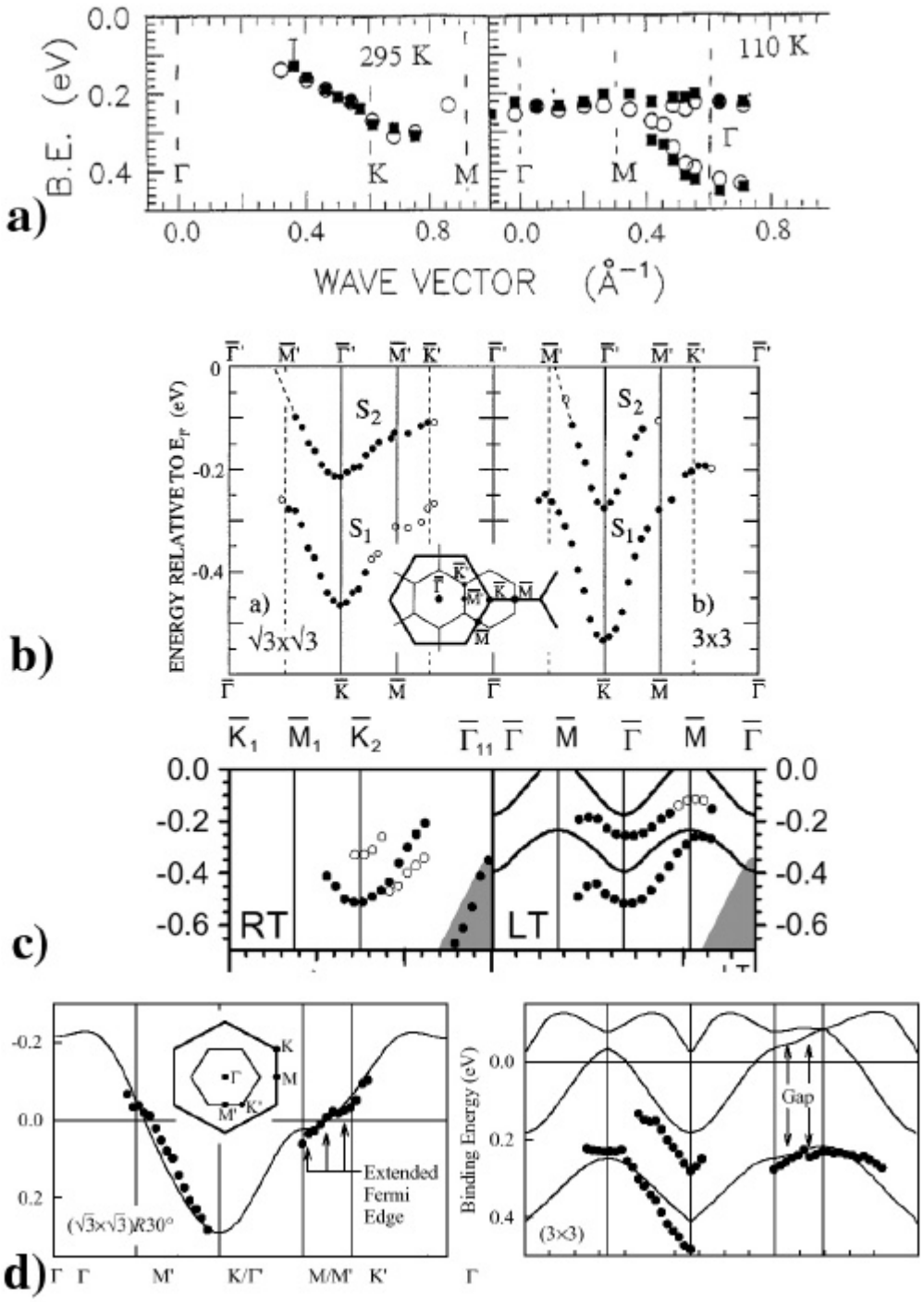

Figure 2.13 Valence band structure of Sn/Ge(111) determined by ARUPS
a) (from (Goldoni 1997)) b) from ((Uhrberg 1998)), c) (from (Avila 1999a)), d) (from (Kidd 2000))

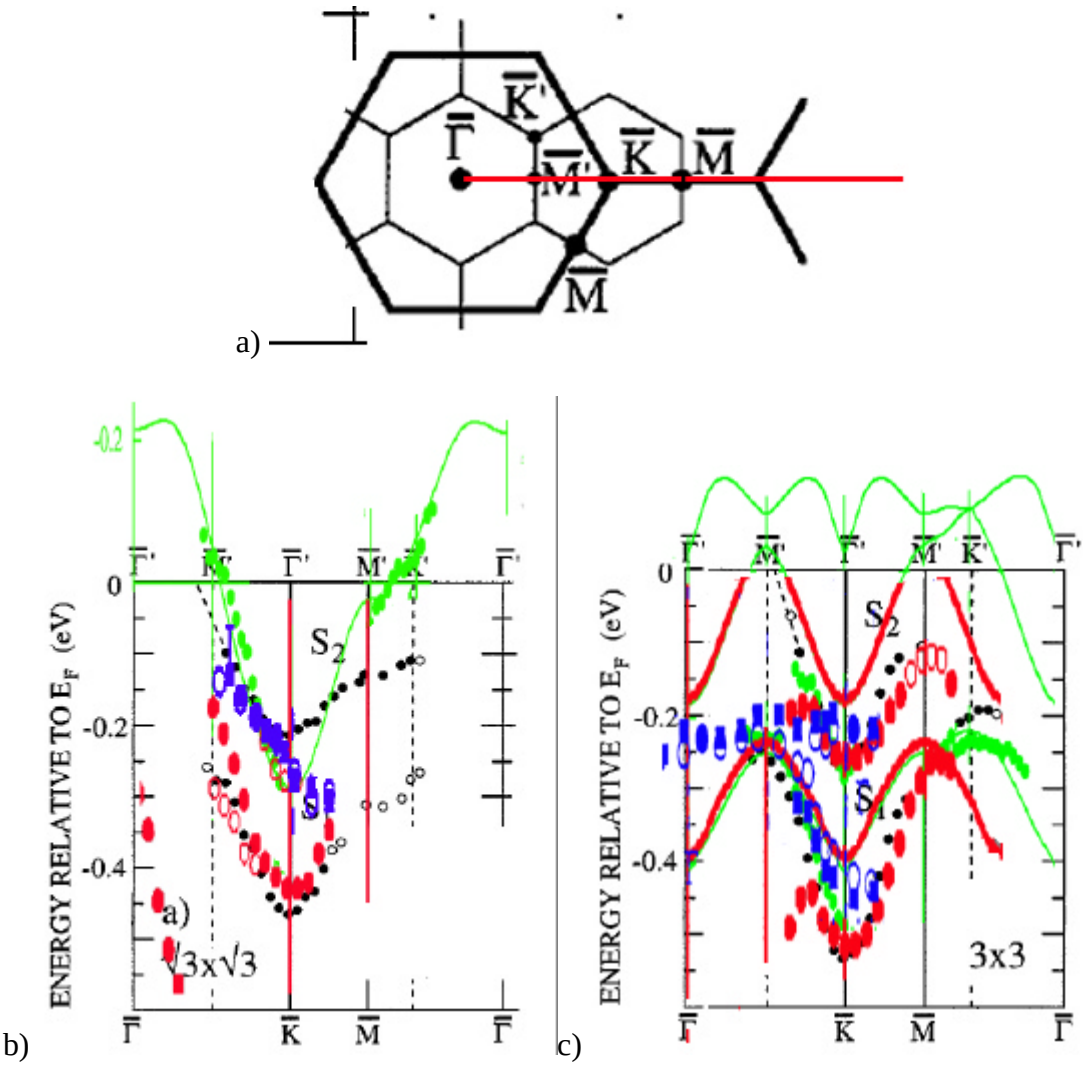

Figure 2.14 Valence band structure of Sn/Ge(111) determined by ARUPS

a) The notations of directions in the BZ of (√3×√3)*R*30° (bold lines) and (3x3) (thin lines). Red line indicates the direction shown in (b).
b) Valence band structure of Sn/Ge(111) at RT
c) Valence band structure of Sn/Ge(111) at LT

The bands are rescaled from Fig. 2.13, where blue is from (Goldoni 1997), black is from(Uhrberg 1998), red is from (Avila 1999a), and green is from (Kidd 2000)

gap opening was observed around the (3×3) zone boundary. Influenced by the results presented in this Thesis (Part 4), the role of defects was carefully considered. They took into account that at RT the defects induce (3×3) perturbation or as they call it "mixed phase". This way their results yield band dispersions in excellent agreement with theory (Santoro 1999). The key new concept here was that a slight change in state occupancy due to defect doping leads to large changes in electronic response, resulting in a Peierls-like (3×3) instability (see Section 2.4). The phase transition was concluded to be defect-mediated as was proposed in (Melechko 1999).

The observation of the gap opening by Kidd et al. is illustrated in the Fig. 2.15. The bottom spectra, taken at normal emission (Γ), are nearly identical for the two phases. The other three sets of spectra were taken with polar emission angles 17, 22, and 26° along the Γ-M azimuth, and correspond to K', midway between K' and M', and M' on the (3×3) zone boundary, respectively. These are representative of what happens around the (3×3) zone boundary – a well-developed Fermi edge at RT is replaced by a gap at 80K.

The band structure determined by Kidd et al. is shown in the Fig. 2.13d. At RT (left panel) the half-filled band crosses the Fermi level. The Fermi surface does not mesh with the (3×3) zone, yet the RT spectra indicate a Fermi edge all around the (3×3) zone boundary. This region of "extended Fermi edge" is indicated in the figure. The dispersion lies within just several tens of meV within the Fermi level. The finite peak width and the low dispersion along K'-M' conspire to give rise to the extended Fermi edge.

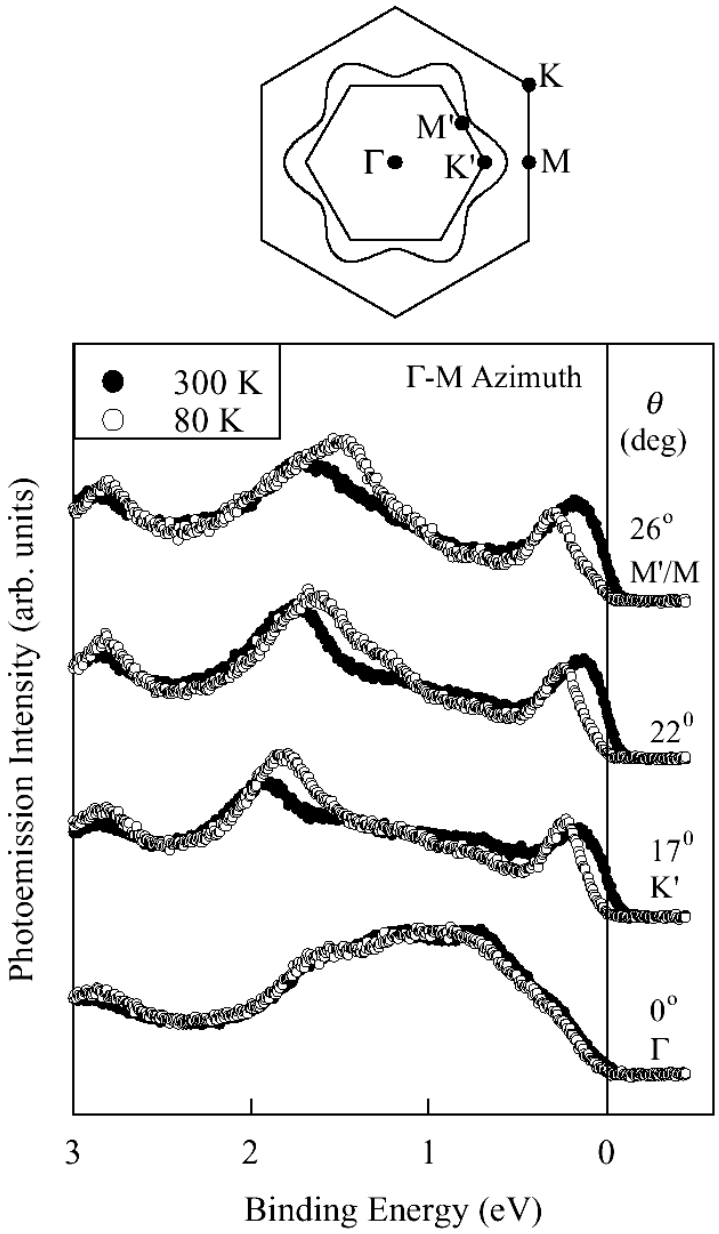

Figure 2.15 Comparison of photoemission spectra taken at 80 and 300 K by (Kidd 2000)

The spectra shown are for polar emission angles of 0, 17, 22, and 26º along the Γ-M azimuth. They correspond to Γ, K', midway between K' and M', and M' in the Brillouin zone. The inset shows the $(\sqrt{3}\times\sqrt{3})R30°$ Brillouin zone (large hexagon), the (3×3) Brillouin zone (small hexagon), and the $(\sqrt{3}\times\sqrt{3})R30°$ Fermi surface (curve).

The change in spectra next to the Fermi energy indicates a band gap opening at LT.

The measured band dispersions for the (3×3) phase is displayed on the right panel of Fig. 2.13d. It shows that, between M' and Γ', the single band for the $(\sqrt{3}\times\sqrt{3})R30°$ phase is split into three bands in the (3×3) phase. The lower two bands are observed by photoemission, and the highest band is unoccupied and therefore not observed. Between M' and K', the $(\sqrt{3}\times\sqrt{3})R30°$ band also spits into three bands in the (3×3) phase. Only the lowest band is occupied, and its energy is much lower than the corresponding $(\sqrt{3}\times\sqrt{3})R30°$ band near the Fermi level. This energy shift accounts for the apparent gap opening in the spectra around the (3×3) zone boundary.

From their results they concluded (see Section 2.4):

1. The bands remain dispersive below the transition, ruling out strong correlation as the driving mechanism (as in metal-insulator transitions).
2. Dynamic fluctuation can also be ruled out, as the band dispersions for the two phases are different.
3. The hybridization hypothesis is invalid, since the surface band does not overlap with other bands.

In a recent work Avila et al. (Avila 2000) used a new procedure to determine the Fermi surface in Sn/Ge(111). Figure 2.16a present a full plot of the distribution of the photoelectron intensity at E_F, which is a graphical representation of the Fermi surface of the Sn/Ge(111) $(\sqrt{3}\times\sqrt{3})R30°$ phase. It correspond to the integrated intensity in the window between $E_F \pm 0.05$ eV as a function of the parallel momentum. Straub et al. (Straub 1997) proposed a new method, which allows extracting from the experimental images of the intensity at E_F vs. $k_{||}$, the values of k_F. The procedure involves the

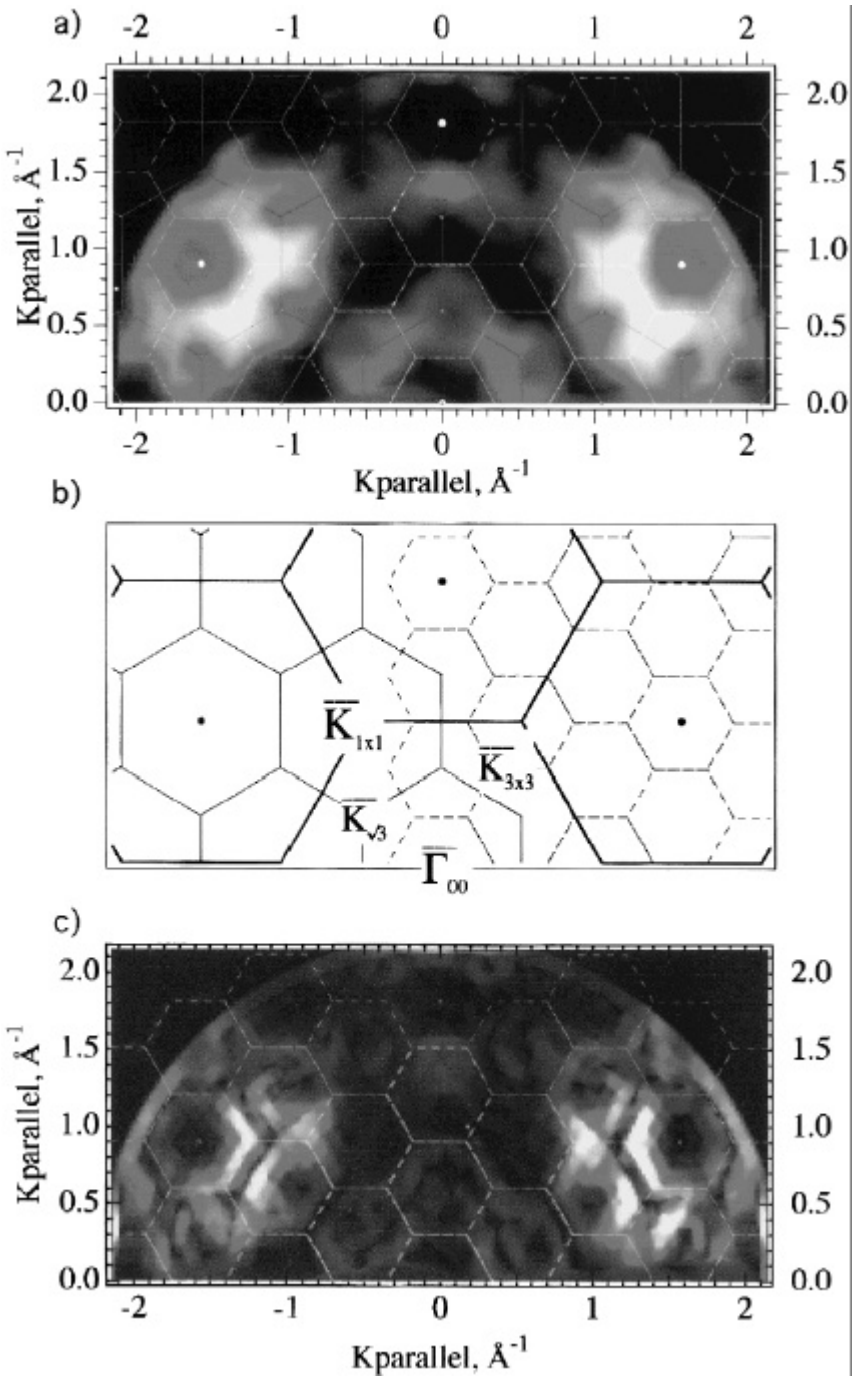

Figure 2.16 Fermi surface of Sn/Ge(111)-(√3×√3)*R*30° (Avila 2000)

a) Photoelectron intensity at E_F as a function of parallel momentum.
b) Schematically the bold, solid and dashed lines depict the Brillouin zones for the (1×1), (√3×√3)*R*30°, and (3×3) unit cells, respectively.
c) The gradient of the intensity at E_F as a function of the parallel momentum is depicted.

calculation of the gradient of the photoemission intensity at F_F with respect $k_{||}$ experimentally determined. This treatment produces two maxima out of each maximum in the original Fermi surface image. It was found that the one on the side of the unoccupied states accurately reflects the value of $k_{||}$. This procedure was applied the data in Fig. 2.16a and the result is presented in the Fig. 2.16c. In order to determine the complete shape of the Fermi surface in the reduced Brillouin zone, the maxima in the gradient-Fermi surface image has been analyzed in the whole k space. Figure 2.17 shows the contour of the Fermi surface they obtained in the result. The Fermi vector is 10% shorter than the value requested to be coupled by the wave vector of the 3×3 phase. The Fermi surface they obtained disagree with the predicted theoretical values (Carpinelli 1997) and the experimentally estimated one (Goldoni 1997), which are larger than the reciprocal lattice vector of the 3×3 phase. Hence, they concluded, the topology of the Fermi surface they measured this way rules out the formation of the commensurate CDW induced by electron-phonon coupling.

2.4. Theoretical models

The results of the theoretical calculations of the ground state were already presented in the Section 2.1. Carpinelli et al. concluded that:

1) LDA predicts (3×3) ground state for Pb/Ge(111) but fails to do so for Sn/Ge(111).

2) Fermi surface nesting is poor to account for the formation of CDW.

In this section I am presenting a review of the subsequent attempts to address these problems made by different groups.

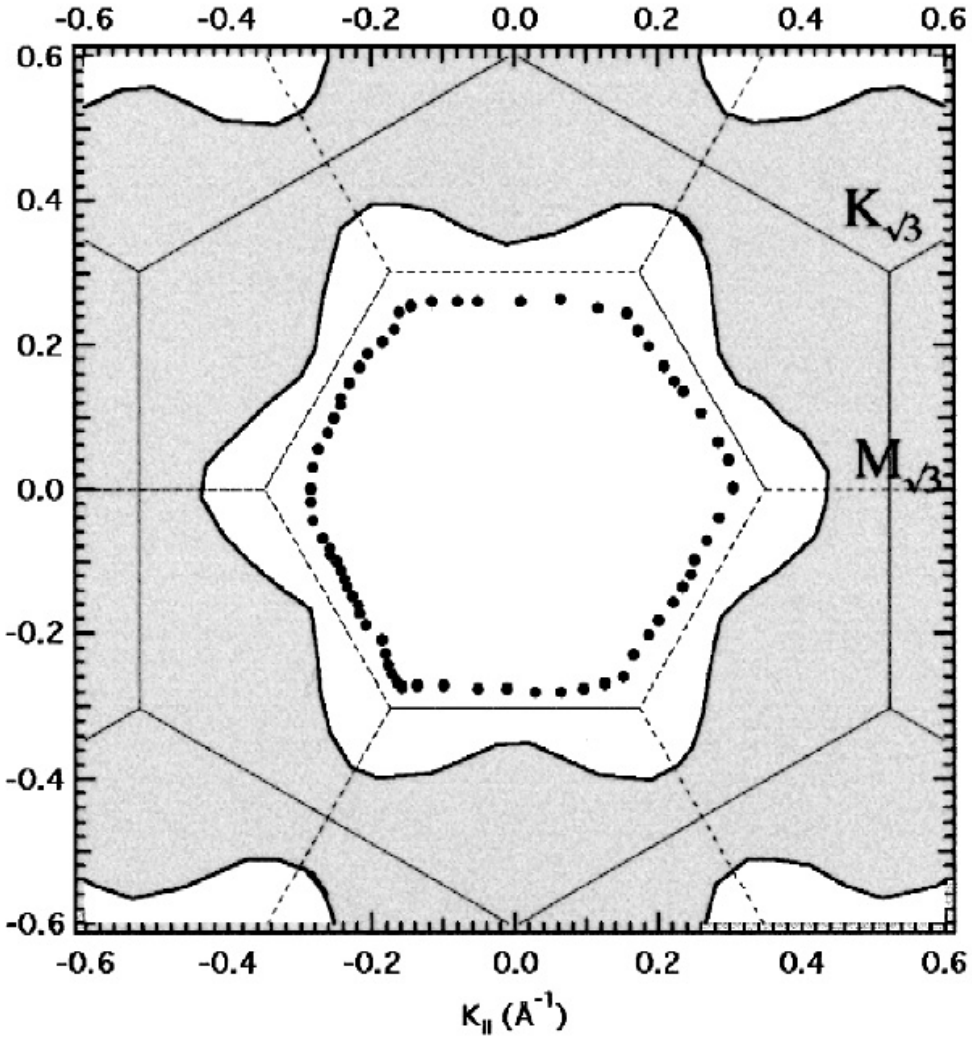

Figure 2.17 Schematic representation of the experimental Fermi surface of Sn/Ge(111).
It was derived by Avila et al derived from gradient Fermi surface image (Fig. 2.16) .(Avila 2000) compared to the theoretical Fermi surface obtained by Carpinelli et al. (Carpinelli 1997).

Electron-phonon coupling enhanced by Fermi surface nesting usually drives CDW transitions. In Sn/Ge(111) Fermi surface for a half-filled band in the $(\sqrt{3}\times\sqrt{3})R30°$ zone encloses ½of the zone area, which is too large for nesting with the (3×3) zone of area only 1/3 of the original zone. The lack of nesting was confirmed by band calculations (Santoro 1999; Ortega 2000), has fueled a lot of controversy. Several alternative models have been proposed:

a) rehybridization mechanism (Le Lay 1998)

b) an order-disorder transition (Uhrberg 1998)

c) a dynamical fluctuations model (Avila 1999b)

d) strong electron correlation (Goldoni 1997)

Different theoretical models were used for the explanation of the different experimental results.

Extended Hubbard modeling (Santoro 1999)

LDA calculations cannot properly account for electron-electron correlation effects. This drawback sometime can be overcome by using so called "LDA+U" or Extended Hubbard modeling. It doesn't allow to determine the stability of a $(\sqrt{3}\times\sqrt{3})R30°$ phase with respect to competing, structurally different phases. This can be addressed only by a full *ab initio* calculation. However, it can be made more realistic by using parameters extracted from first-principles calculations, and could be very helpful in clarifying the possible scenarios as a function of the strength of electron-electron interaction.

The basic starting point was the quantitatively accurate surface-state band dispersion E(k) which one calculates in gradient-corrected LDA (Carpinelli 1996; Scandolo 1998). The result of such calculation is shown in Figure 2.18 for the case of

a)

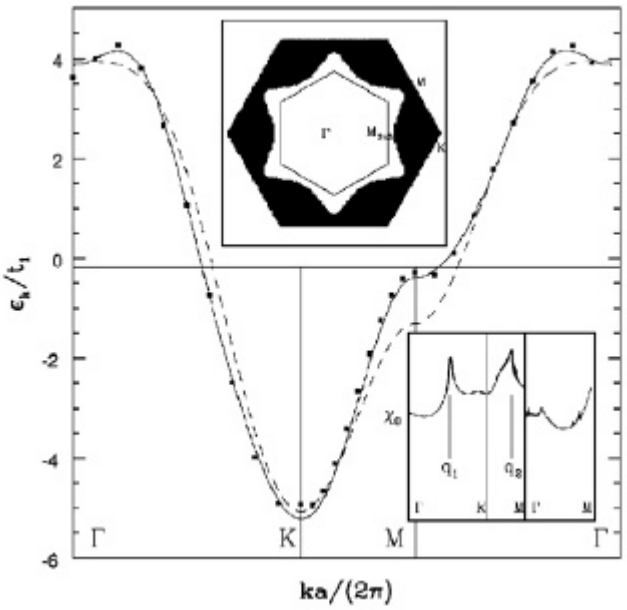

a)

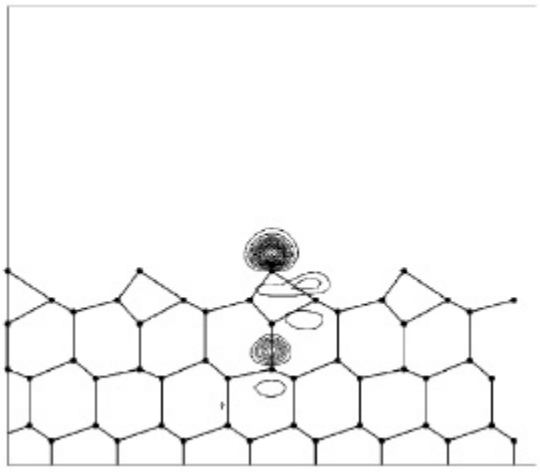

Figure 2.18 Electronic structure of Si/Si(111) obtained from LDA (Santoro 1999)

a) Surface-state dispersion for hypothetical Si/Si(111), as obtained from gradient corrected LDA (solid squares). A very similar band is obtained for Pb/Ge(111) and Sn/Ge(111). The solid line is a tight-binding fit. Upper inset: The Fermi surface of the half-filled surface band. The outer hexagon is the BZ of the $(\sqrt{3}\times\sqrt{3})R30°$ phase, and the inner hexagon in the BZ of the (3×3) phase. Notice the poor nesting at the BZ corner wave vector $\mathbf{k}=(4\pi,0)$, joining two opposite $M_{3\times3}$ points. Lower inset: The zero temperature Lindhard response function for the half-filled surface band. Notice the two peaks at $q_1=0.53\mathbf{k}$ and $q_2=1.3\mathbf{k}$, and no feature at **k**, indicating poor nesting.

b) Density contours of the Wannier function associated with the Si/Si(111) surface band, calculated with gradient-corrected LDA; dots correspond to atomic positions.

Si/Si(111), a model system convenient for calculations. Next they associate to every adatom a Wannier orbital (Fig. 2.18b) and write the effective Hamiltonian for the surface band as follows:

$$H = \sum_{k}^{BZ} \sum_{s} E(k) c_{k,s}^{+} c_{k,s} + H_{ph} + H_{e-ph} + H_{\text{int}}$$

H_{int} includes correlation effects, which are not correctly accounted for within LDA, which can be parametrize as follows:

$$H_{\text{int}} = U \sum_{r} n_{r,\uparrow} n_{r,\downarrow} + \frac{1}{2} \sum_{r \neq r'} V_{r-r'} (n_r - 1)(n_{r'} - 1)$$

b) Here, U is an effective repulsion (Hubburd U) for two electrons on the same adatom Wanier orbital, and $V_{r\text{-}r'}$ is the direct Coulomb interaction between different sites r and r'. The LDA estimates of the bare Coulomb repulsion U0 and V0 between two electrons, respectively, on the same and on neighboring Wannier orbitals are – for the test case of Si/Si(111) – of about 3.6 and 1.8 eV, respectively. Screening effects by the underlying bulk are expected to reduce very substantially these repulsive energies. An order of magnitude estimate for U and V is obtained by dividing their bare values by the image-charge screening factor, $(\varepsilon+1)/2 \approx 6$, yielding, for Si, U=0.6 eV, and V=0.3 eV. Corresponding values would be somewhat smaller for Ge(111), in view of a very similar dispersion and a ratio of about 4/3 between the dielectric constants of Ge and Si.

It would take too much space to repeat all their calculations here. I would like to present here only some relevant conclusions:

1. If U and V are ignored, there is no electron-phonon driven 3×3 CDW surface instability. However, any phase involving a CDW, for example, as a secondary

order parameter attached to a primary Spin Density Wave (SDW), can take advantage and gain some extra stabilization energy from a small surface lattice distortion, via electron-phonon coupling.

2. Electron-electron repulsion and the two-dimensional Fermi surface are capable of driving transitions of the undistorted metallic surface to a variety of states, that are either insulating or in any case less metallic, some possessing the 3×3 periodicity.
3. This can occur via two different mechanisms: a) the intersite repulsion V can stabilize insulating or semimetallic CDW's, without a crucial involvement of spin degrees of freedom; b) the on-site repulsion U can produce essentially magnetic insulators with or without a weak accompanying 3×3 CDW, as required by symmetry.
4. For U moderate of order W (surface state bandwidth) and for smaller V, an interesting state is realized, with a large SDW and a small accompanying CDW. The state is either a small-gap insulator, or a semimetal, and may or may not be associated with a net overall magnetization, depending on the nature of the leading SDW.
5. For U and V both small but finite, a metallic CDW without any magnetism is obtained. The same phase can also be stabilized for larger values of U by the presence of a substantial electron-phonon coupling. In this case, V is the coupling responsible for the 3×3 symmetry of the unit cell, whereas the role of the electron-phonon coupling is that of destroying magnetism by effectively decreasing U. Electron-phonon coupling alone is not sufficient to justify a commensurate 3×3 CDW.

Either or the phases in 4) and 5) could be natural candidates for explaining the weak 3×3 CDW seen experimentally in Sn/Ge(111) and Pb/Ge(111)

Dynamical Fluctuations Model of the Surface Phase Transition in Sn/Ge(111)

Avila et al. have proposed a dynamical fluctuations model to account for their experimental results obtained by core level and valence band photoemission spectroscopies (Avila 1999b). They determined that, both above and below the transition, two different components in the Sn 4d core level and a band splitting in the surface state crossing the Fermi energy. Their theoretical results indicate that these two effects are due to existence of two structurally different kinds of Sn atoms that fluctuate at RT between two positions and are stabilized in a (3×3) structure at LT (Fig.2.19). This was done by means of a combination of local-orbital and plane-wave (PW) DFT methods. First, they explored the geometry of the (3×3) surface using a molecular-dynamics (MD) technique base of a local-orbital self-consistent DFT approach.

The ground state 3×3 geometry was found with this method presents a unit cell with one Sn atom displaced upwards and the other two Sn atoms displaced downwards, with a total vertical distortion ~0.35 Å. The corresponding vertical distortion of the Ge last layer atoms is ~0.20Å, the Sn-Ge distance being quite similar (2.68-2.74 Å) for both types of Sn atoms. In these calculations the 3×3 reconstruction is lower in energy than $\alpha\sqrt{3}$ by 40 meV per Sn atom. The accuracy of these results has been checked using the more rigorous PW DFT method. Both the local density approximation and the generalized gradient approximation have been used, and they provide very similar results for the geometries and for the total energy differences between the $(\sqrt{3}\times\sqrt{3})R30°$ and 3×3

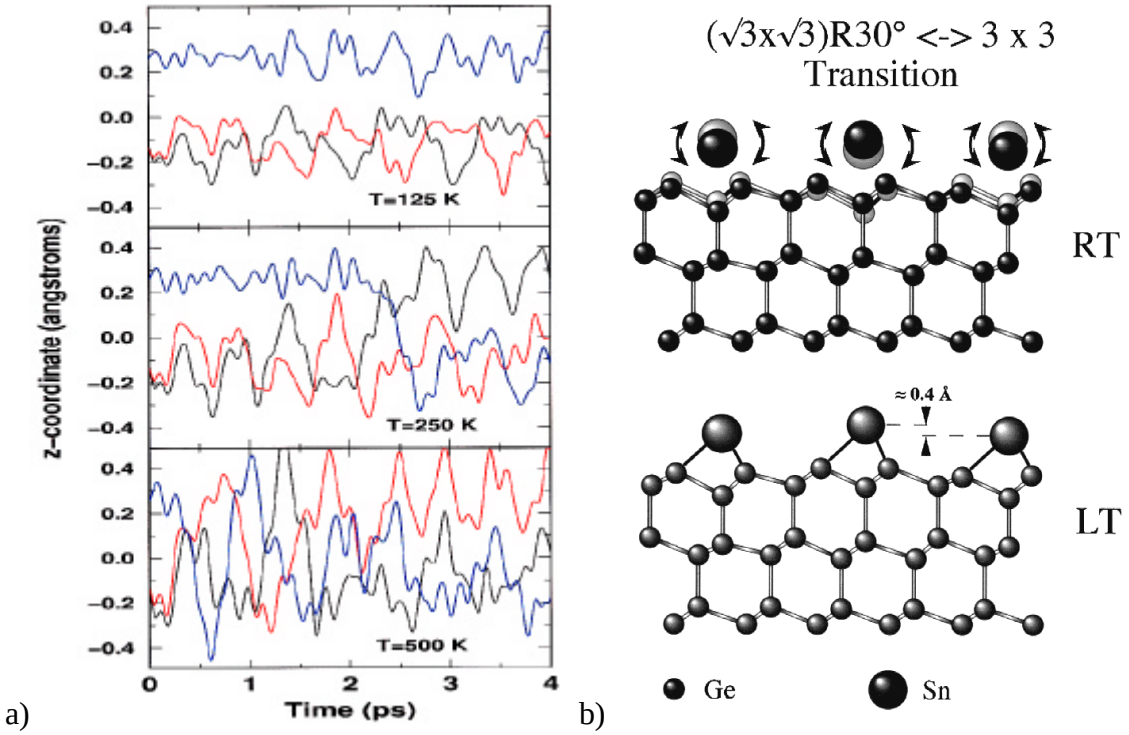

Figure 2.19 Dynamical fluctuations model

a) Time evolution of the z coordinate (perpendicular to the surface) of the three Sn atoms (blue, red, and black lines) in the (3×3) unit cell for the temperatures T~125, 250, and 500 K in the Molecular Dynamics simulations

b) Structural model: Sn atoms are flipping between stable positions at RT and are frozen at LT.

reconstructions. The PW confirm the local-orbital results. Both structures are local minima of the total energy and their geometries, in particular, the vertical distortion of the Sn atoms, are very similar to the ones found by the local-orbital method. The 3×3 structure is the most stable one, although the absolute energy minimum for it is found only 5 meV per Sn atom below the energy minimum of the $(\sqrt{3}\times\sqrt{3})R30°$ reconstruction.

Their LDA calculation for the occupied surface bands is shown in the Fig. 2.13c along with photoemission data. Another empty band, not shown in the figure appears 0.15 eV above E_F. The experimental bands are shifted by 0.2 eV. Their calculation reproduces the band splitting and they find for the 3×3 reconstruction a surface band crossing E_F along $\overline{\Gamma}\overline{M}$ line. The atomic origin of the surface bands can be traced back to the corresponding Sn dangling bonds. The band with higher binding energy, filled with two electrons, is mainly weighted on the Sn atom displaced upwards, while the other two surface bands with lower binding energy, occupied by one electron, are associated with the other two Sn atoms displaced downwards.

As a next step they performed molecular dynamics simulations. To do that they started with the atoms in the same 3×3 ground state positions, but with random velocities chosen, in each case, from a different Maxwell-Boltzmann distribution. Then, they followed the time evolution of the system using LDA forces. This time evolution of z coordinated of the three St atoms in the 3×3 unit cell for the temperatures T~125, 250, and 500 K is displayed in the Fig. 2.19a. For T~125 K, the Sn atoms fluctuate around their equilibrium positions, one at higher z and two at lower z. For T~250 K an upper atom and one of the two lower Sn atoms exchange heights. For T~ 500K the system fluctuates very quickly, with the Sn atoms exchanging between the upper and lower

heights. This model describes the behavior very similar to the suggested for the analogous case of Si(001) along the c(4×2) →(2×1) phase transition (see Part 1).

Defect-mediated phase transition

One of the models that appeared recently as a response to our claim that defects are very important in this phase transition (Melechko 1999; Weitering 1999; Melechko 2000) exploits the fact that the electronic response is highly sensitive to doping by defects (Kidd 2000). The LDA-Hubbard calculation (Ortega 2000) shows that the $(\sqrt{3} \times \sqrt{3})R30°$ and (3×3) phase have nearly the same energy, with a difference of just a few meV per Sn atom. Thus, it is not surprising that seemingly minor perturbations caused by surface defects can induce the phase transition locally at RT as we have observed.

The model has the following assumptions. The defects, being electron donors can cause an upward shift of the local Fermi level relative to the band in the surrounding area. Shown in the Fig. 2.20 are calculated Lindhard response functions $\chi(k)$, presented as two-dimensional green-scale maps, using the band dispersion in (Santoro 1999). In each map, the hexagonal $(\sqrt{3} \times \sqrt{3})R30°$ Brillouin zone is indicated. The intensity level at each k corresponds to the value of χ, and the conversion between intensity and χ is indicated by the linear green scale bar to the right. The map on the left, labeled $\Delta E_F=0$ (unshited Fermi level), shows no particular features at the hexagon corners (K), in agreement with earlier calculations indicating poor nesting (Santoro 1999). The map on the right is for a small upward shift of the Fermi level by 50 meV. The χ function now looks dramatically different, and is dominated by six peaks at the K points. Since ΓK equals a (3×3)

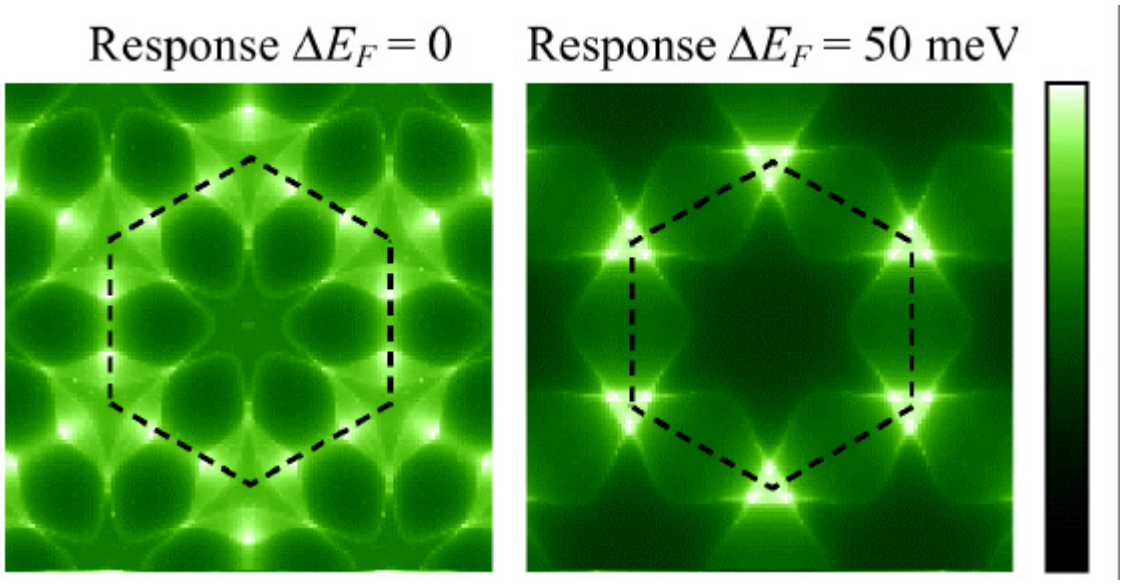

Figure 2.20 Lindhard response function for (√3×√3)*R*30° Sn/Ge(111)
The gray scale maps represent Lindhard response functions for the ideal (√3×√3)*R*30° phase (left) and the same with the Fermi level shifted upward by 50 meV relative to the band. The dashed hexagons indicated the (√3×√3)*R*30° Brillouin zone.
(from (Kidd 2000))

reciprocal lattice vector, this strong peaking at K can lead to a (3×3) response. Detailed calculations show that this peaking at K is already evident, although less pronounced, at a mere ~10 meV shift of the Fermi level. This high sensitivity of the electronic response to a small perturbation is a consequence of the proximity of a saddle point near the Fermi level resulting in a low band dispersion along M'-K' (See Fig. 2.13d). The same band dispersion is also responsible for the "extended Fermi edge" discussed in their paper. Thus, they concluded that the basic mechanism for the phase transition is the same as in traditional Peierls CDW materials, except that defect doping is the source of the instability.

As the temperature is lowered, the surface regions affected by the defects grow, and eventually overlap to form a fully-developed (3×3) phase below ~100 K as shown in this Thesis (Part 4).

2.5. Summary and conclusions

The α-phase of Sn/Ge(111) undergoes a symmetry lowering phase transition from (√3×√3)*R*30° to (3×3) when the temperature is reduced. The STM observations indicated that this is a result of a transition to a Charge Density Wave state. This transition is accompanied by a periodic lattice distortion as was measured by LEED and XRD. Some of the LDA calculations failed to predict the stability of the (3×3) ground state, so the electro-electron correlation effects were believed to be involved. Calculations of the Fermi surface showed absence of good nesting that is usually a condition of the electron-phonon mechanism of CDW formation. XPS measurements of the 4d Sn core level spectra brought about an alternative model in which Sn atoms are flipping between two

stable positions at high temperature and are frozen at low temperatures. Irreproducibility of the results of the photoemission measurements done by very good experimentalists suggests that the mechanism of this phase transition is very complex. The results of this thesis will demonstrate the complexity of the Sn/Ge(111) system. Ge defects that are usually ignored play a very important role in this transition and must be taken into account.

References for Part 2

Avila, J., Huttel Y., Le Lay G. and Asensio M. C. (2000). "Dynamical fluctuation and surface phase transition at the Sn/Ge(111) root 3 x root 3R30 degrees-alpha interface." Applied Surface Science **162**: 48-55.

Avila, J., Huttel Y., Mascaraque A., Le Lay G., Michel E. G. and Asensio M. C. (1999a). "Electronic instabilities of the two-dimensional Sn/Ge(111) alpha-phase." Surface Science **435**: 327-331.

Avila, J., Mascaraque A., Michel E. G., Asensio M. C., LeLay G., Ortega J., Perez R. and Flores F. (1999b). "Dynamical fluctuations as the origin of a surface phase transition in Sn/Ge(III)." Physical Review Letters **82**(2): 442-445.

Baddorf, A. P., Jahns V., Zhang J. D., Carpinelli J. M. and Plummer E. W. (1998). "Periodic lattice distortion accompanying the (3x3) charge- density-wave phase of Sn/Ge(111)." Physical Review B-Condensed Matter **57**(8): 4579-4583.

Bunk, O., Zeysing J. H., Falkenberg G., Johnson R. L., Nielsen M., Nielsen M. M. and Feidenhans R. (1999). "Phase transitions in two dimensions: The case of Sn adsorbed on Ge(111) surfaces." Physical Review Letters **83**(11): 2226-2229.

Carpinelli, J. M., Weitering H. H., Barkowiak M., Stumpf R. and Plummer E. W. (1997). "Surface charge ordering transition: alpha phase of Sn/Ge(111)." Physical Review Letters **79**(15): 2859-2862.

Carpinelli, J. M., Weitering H. H., Plummer E. W. and Stumpf R. (1996). "Direct observation of a surface charge density wave." Nature **381**: 398.

Friedel, J. (1977). Electron-Phonon Interactions and Phase Transitions. T. Riste. New York, Plenum**:** 1-49.

Goldoni, A. and Modesti S. (1997). "Strong correlation effects in the (3 x 3) charge density wave phase of Sn/Ge(111)." Physical Review Letters **79**(17): 3266-3269.

Gothelid, M., Bjorkqvist M., Grehk T. M., Lelay G. and Karlsson U. O. (1995a). "Metal-Semiconductor Fluctuation in the Sn Adatoms in the Si(111)-Sn and Ge(111)-Sn (Root-3x-Root-3)R30-Degrees Reconstructions." Physical Review B-Condensed Matter **52**(20): 14352-14355.

Gothelid, M., Grehk T. M., Hammar M., Karlsson U. O. and Flodstrom S. A. (1995b). "Adsorption of Tin on the Ge(111)-C(2x8) Surface Studied with Scanning-Tunneling-Microscopy and Photoelectron-Spectroscopy." Surface Science **328**(1-2): 80-94.

Harrison, W. A. (1980). Electronic Structure and the Properties of Solids, The Physics of the Chemical Bond. San Francisco, Freeman.

Ichikawa, T. and Ino S. (1981). "Structural Study of Sn-Induced Superstructures on Ge(111) Surfaces by Rheed." Surface Science **105**(2-3): 395-428.

Kidd, T. E., Miller T. and Chiang T. C. (1999). "Core level analysis of the surface charge density wave transition in Sn/Ge(111)." Physical Review Letters **83**(14): 2789-2792.

Kidd, T. E., Miller T., Chou M. Y. and Chiang T. C. (2000). "Nature of the Sn/Ge(111) Surface-Charge-Density-Wave Phase Transtion." Physical Review Letters **85**(17).

Le Lay, G., Aristov V. Y., Bostrom O., Layet J. M., Asensio M. C., Avila J., Huttel Y. and Cricenti A. (1998). "Surface charge density waves at Sn/Ge(111)?" Applied Surface Science **123**: 440-444.

Melechko, A. V., Braun J., Weitering H. H. and Plummer E. W. (1999). "Two-dimensional phase transition mediated by extrinsic defects." Physical Review Letters **83**(5): 999-1002.

Melechko, A. V., Braun J., Weitering H. H. and Plummer E. W. (2000). "Role of defects in two-dimensional phase transitions: An STM study of the Sn/Ge(111) system." Physical Review B **61**(3): 2235-2245.

Ortega, J., Perez R. and Flores F. (2000). "A theoretical case study: the Sn/Ge(111)-(3 x 3) surface." Journal of Physics-Condensed Matter **12**(1): L21-L27.

Overhauser, A. W. (1968). "Exchange and correlation instabilities of simple metals." Physical Review **167**(3): 691.

Pedersen, J. S., Feidenhans'l R., Nielsen M., Kjaer K., Grey F. and Johnson R. L. (1987). Surface Science **189/190**: 3266.

Santoro, G., Scandolo S. and Tosatti E. (1999). "Charge-density waves and surface Mott insulators for adlayer structures on semiconductors: Extended Hubbard modeling." Physical Review B-Condensed Matter **59**(3): 1891-1901.

Scandolo, S., Ancilotto F., Chiarotti G. L., Santoro G., Serra S. and Tosatti E. (1998). "First principles calculations of charge and spin density waves of root 3-adsorbates on semiconductors." Surface Science **404**(1-3): 808-812.

Straub, T., Claessen R., Steiner P., Hufner S., Eyert V., Friemelt K. and Bucher E. (1997). “Many-body definition of a Fermi surface: Application to angle- resolved photoemission.” Physical Review B-Condensed Matter **55**(20): 13473-13478.

Uhrberg, R. I. G. and Balasubramanian T. (1998). “Electronic sructure of the root 3x root 3-alpha and 3x3 periodicities of Sn/Ge(111).” Physical Review Letters **81**(10): 2108-2111.

Uhrberg, R. I. G., Zhang H. M. and Balasubramanian T. (2000). “Determination of the Sn 4d line shape of the Sn/Ge(111) root 3 x root 3 and 3 x 3 surfaces.” Physical Review Letters **85**(5): 1036-1039.

Weitering, H. H., Carpinelli J. M., Melechko A. P., Zhang J. D., Bartkowiak M. and Plummer E. W. (1999). “Defect-mediated condensation of a charge density wave.” Science **285**(5436): 2107-2110.

Zhang, J. D., Ismail, Rous P. J., Baddorf A. P. and Plummer E. W. (1999). “Periodic lattice distortion accompanying the charge-density- wave transition for Sn/Ge(111).” Physical Review B-Condensed Matter **60**(4): 2860-2863.

PART 3

Analytical Techniques and Experimental Details

In Part III I will present a description of techniques I have used and some experimental details, which were not appropriated for other Parts (devoted to the main subject of the Thesis). Most of my results were obtained using Scanning Tunneling Microscope. Here I give some basics on principles of operation of an STM. For more detailed information the reader should consult review books by Chen (Chen 1993) and Wiesendanger (Wiesendanger 1994) and user manuals. The description of experimental details is usually brief in scientific publications, which does not reflect the percentage of time spent making the instrument perform properly or understanding what has been recorded. In Surface Science it is especially true due to necessity to use Ultra High Vacuum (UHV) equipment. The best way to learn basic practices of UHV is usually from experienced colleague, though a book by O'Hanlon is recommended (O'Hanlon 1989). Since most of the equipment I used was produced commercially, reading manuals was one of the main sources of information (if your favorite 'experienced colleague' is not available). Finally, it is not possible to obtain a complete picture of a phenomena using one technique. Nowadays a whole arsenal of tools is available to the surface scientist. A comprehensive review on different techniques can be found in Woodruff's 1994 book. (Woodruff 1994).

3.1. Scanning Tunneling Microscopy

3.1.1. Introduction: simple picture

The Scanning Tunneling Microscope (STM) was invented ~1981 by Binning and Rohrer, who received the Nobel Prize in physics in 1986. It was implemented by Binning, Rohrer, Gerber, and Weibel (Binning 1982). Figure 3.1 schematically shows its

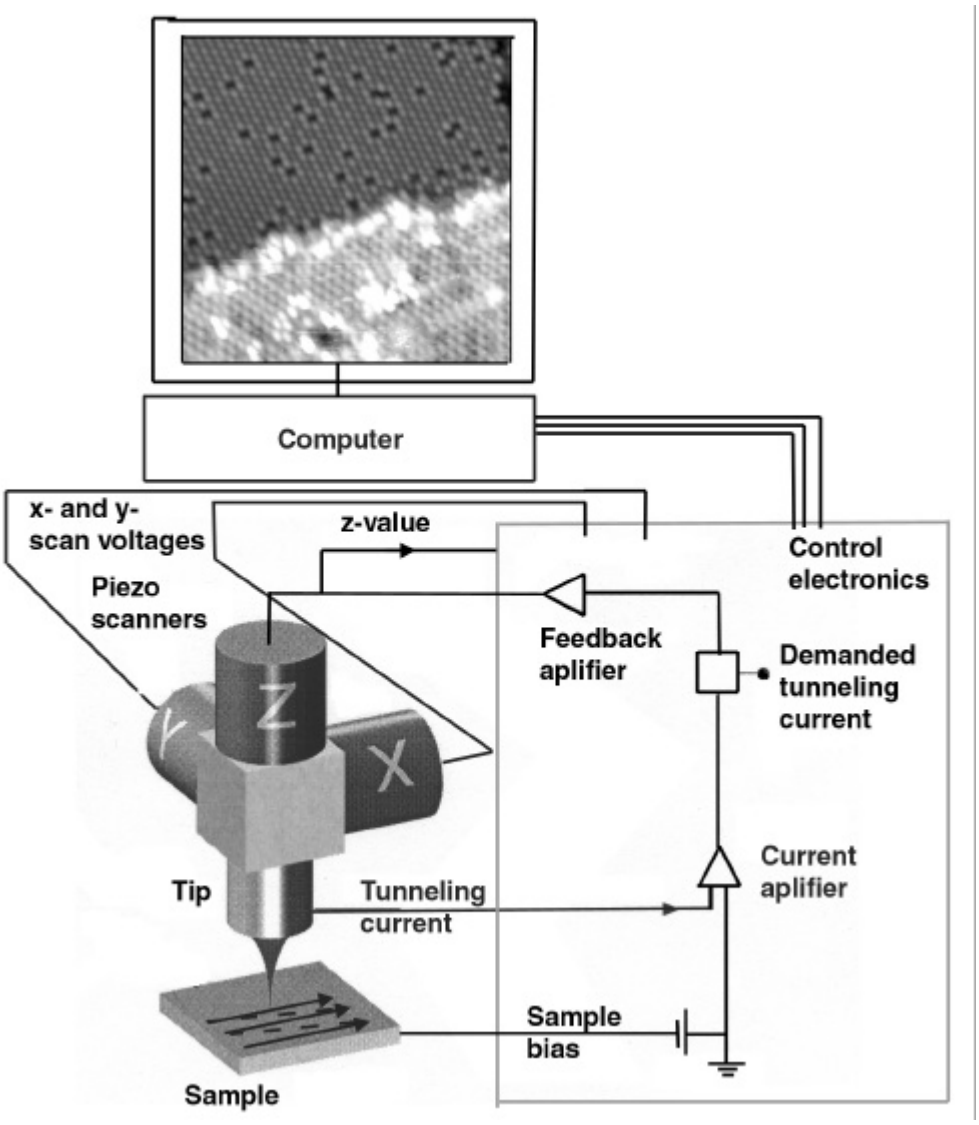

Figure 3.1 Schematics of STM

constituent parts. The general principle of STM is very simple. In STM a bias voltage is applied between a sharp metal tip and a conducting sample. After bringing the tip and sample surface within a separation of only a few Ångströms (10^{-10} m), a tunneling current can flow due to the quantum mechanical tunneling effect.

Consider a potential barrier and a microscopic particle, with energy smaller than the barrier height (Fig. 3.2). From the point of view of classical physics, this particle will never penetrate the barrier. In quantum physics it is possible due to the wave-particle dualism. An electron impinging upon a potential energy barrier can be found on another side of the barrier with finite probability. This phenomenon is called tunneling. The tunneling current can be used to probe physical properties locally at the sample surface as well as to control the separation between tip and sample surface. The distance control based on tunneling is very sensitive to small changes in separation between the two electrodes because the tunneling current is strongly (exponentially) dependent on this separation. By scanning the tip over the sample surface while keeping the tunneling current constant via a feedback loop, we can follow the surface contours with the tip. By monitoring the vertical position z of the tip as a function of the lateral position (x,y), we can get a three-dimensional image z(x,y) of the sample surface. Motion of the tip both laterally and vertically with respect to the surface can be realized with sub-atomic precision using piezoelectric drives.

3.1.2. Theory of STM

One of the first theories that gave a reasonably complete explanation of the physics of the STM is the modified Transfer Hamiltonian approach, which is based on Bardeen's work

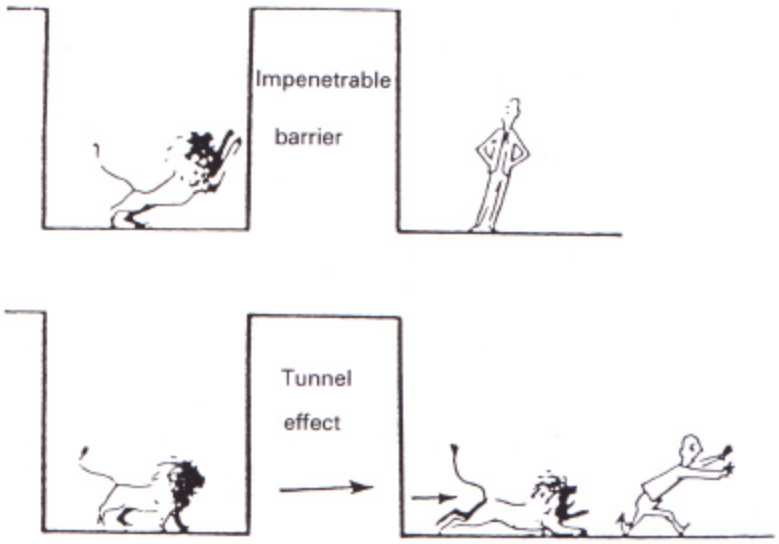

Figure 3.2 Quantum tunneling: classical and quantum lions in a well.

The difference between classical theory and quantum theory, illustrating tunneling through a potential barrier (Bleaney 1984)

(Bardeen 1961). Although restricted, this approach gives a useful conceptual understanding and pictorial view of how the STM works. Bardeen considered two independent wavefunctions of the tip and the sample (Fig. 3.3) for which the current can be expressed as:

$$I = \frac{2pe}{\hbar} \sum_{m,n} \left[f(E_n) - f(E_m) \right] \left| M_{mn} \right|^2 d(E_n + eV - E_m) \qquad (3.1)$$

where f(E) is the Fermi distribution function. Note that Eq. (3.1) resembles the Fermi golden rule but it is formally different in that the wavefunctions ψ_ν and ψ_μ are eigenstates of different Hamiltonians of the tip and the sample. In the limit of small voltage Eq. 3.1 reduces to

$$I = \frac{2p}{\hbar} e^2 V \sum_{m,n} \left| M_{mn} \right|^2 d(E_n - E_F) d(E_m - E_F) \qquad (3.2)$$

where the tunneling matrix element can be expressed as the quantum mechanical current operator.

$$M_{mn} = \frac{\hbar^2}{2p} \int d\vec{S} \cdot (y_m^* \nabla y_n - y_n \nabla y_m^*) \qquad (3.3)$$

To evaluate the current, the wavefunctions of the tip and the sample have to be known. This can be difficult for the tip states since the geometry of the probe is generally unknown.

Tersoff and Hamman approximated the tip wavefunction with an *s* wave (quantum number l=0) which led them to the result that(Tersoff 1983):

$$I \propto \sum \left| y_n(\vec{r}_0) \right|^2 d(E_n - E_F) \equiv r(\vec{r}_0, E) \qquad (3.4)$$

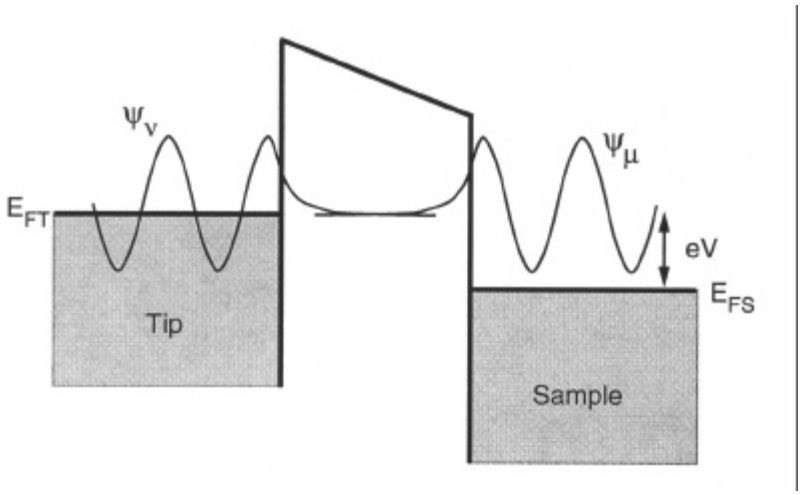

Figure 3.3 Schematic energy level diagram illustrating the overlap of the tip and sample wavefunctions in the tunnel region

This result shows that what we observe with STM is the surface local density of states (LDOS) at E_F evaluated at the center $\mathbf{r_o}$ of the tip. The tunneling current at the probe is thus proportional to the surface LDOS so that a constant current topograph is essentially a contour map of constant surface LDOS, i.e. the charge density of the states at E_F.

This theory was successful in explaining the early results obtained on Au(110) (Binnig 1983) and also predicting the voltage dependent imaging of the GaAs(110) surface later observed by Feenstra and Stroscio (Feenstra 1987a). However, the restrictions to low biases and the demand for an explicit knowledge about the wavefunctions involved makes the application of this theory limited.

At finite bias, STM records more than the sample's LDOS at E_F. This is illustrated in Fig. 3.3, which includes schematic energy level diagrams of the tip and sample. When the two are brought within tunneling range, their Fermi levels line up. A bias voltage V applied between them exposes the filled states of one to the empty states of the other, allowing for significant elastic tunneling. As the bias voltage magnitude is increased, more states will gain the ability to tunnel without violating the Pauli exclusion principle. Therefore, the tunnel current at finite bias is a measure of the integrated sample LDOS (evaluated at the tip position) between E_F and $E_F \pm V$ (depending on bias polarity):

$$I \sim \int_{E_F}^{E_F \pm V} dE\, r(r_o, E) \tag{3.5}$$

with

$$r(r_o, E) = r(r_o) e^{-2s\sqrt{\frac{2m}{\hbar^2}(f_s + f_t - 2E + eV) + k_{\parallel}^2}} \tag{3.6}$$

where ϕ represents the tip/sample workfunction and $k_{||}$ is the surface state's momentum parallel to the surface. This, however, requires the assumption that the tip's LDOS is featureless.

This brings us to a conclusion that STM is a spectroscopic tool. It allows us to obtain information about density of filled as well as empty states (for metals that would be states below and above the Fermi level). Moreover voltage dependent STM measurements give us the information about spatial distribution of different states. All that it needed is to take a derivative of the tunneling current with respect to bias voltage.

There is no convention on how the polarity of the bias is presented in publications: some researches give it as a voltage on the sample with respect to the tip, some the other way around. This is very confusing because you can't tell if filled or empty state images are presented. I developed a mental picture for myself that is illustrated in the cartoon in the Fig. 3.4. Electrons fill the energy levels ("buckets") from the bottom up. If the bias is applied the electrons are spilled from the negative "bucked" to the positive one. If the top "bucket" (negative end) is empty (no filled states at this position), or the bottom bucket is full (no place to spill) there is no current.

3.1.3 Basics of operation

Tip preparation

One of the prerequisites of obtaining atomic resolution is manufacturing of the STM tip. A tip has to be rigid to remain stationary during scanning, chemically inactive, and should have a featureless density of states, not to forget that it has to be conducting. Most

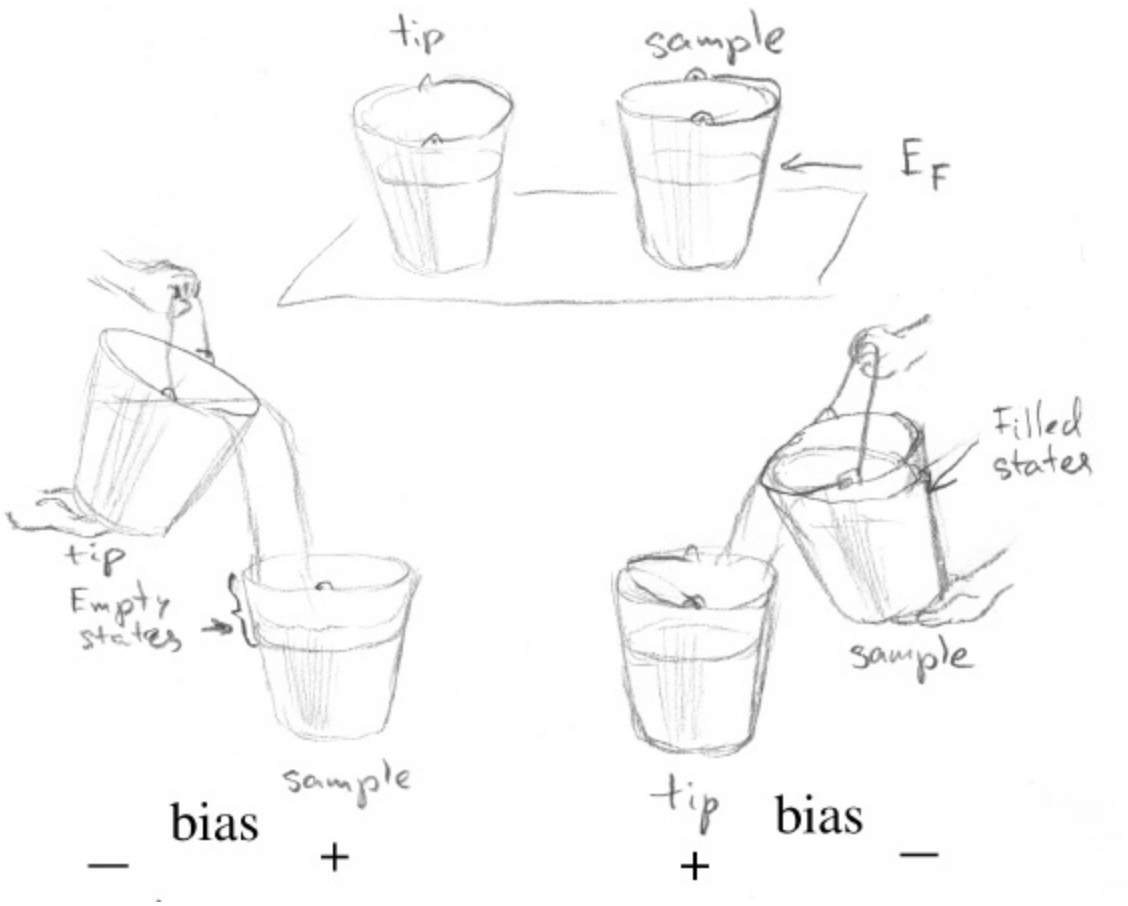

Figure 3.4 "Buckets-of-water" representation of EMPTY (left) and FILLED (right) STM images

often W or PtIr probes are utilized. Several different methods of tip preparation exist (Melmed 1991): etching, pulling, cutting wires etc. Even though those methods could be quite sophisticated, they are more art than technology. (The tip resembling a hook after being bumped into the sample, scraped across it and bumped again can give beautiful results for months, while a nice and sharp tip can fail completely).

The technique mainly used in our group to prepare tips is based on the chemical etching. This method originated in 60's for the purposes of Field Ion Microscopy (Muller 1960). Figure 3.5 (top) displays schematics of the tip making apparatus. . A 10 mil W wire is placed in the middle of a Pt ring (5 mm in diameter) that rest atop of a bath of 2N NaOH solution so that it pulls up the solution surface due to the surface tension. A constant ~ 10 V bias voltage is applied between the wire and the ring. Such a geometry dictates a necessary etching pattern. A current, usually ~15 mA in the beginning, flows through the junction. As the wire is slowly etched away, the current slowly reduces down to ~ 5mA. When the necked region (Fig. 3.5 middle) finally is completely eroded away, the bottom part of the wire drops off, drastically reducing the current. A circuit placed in series with the power supply detects this current drop-off it shuts down the etching. This results in a very sharp tip, usually about 200-300 Å radius of curvature, on the wire (Fig. 3.5 bottom).

Additionally, tips can be treated *in situ* by either electron bombardment or field emission. To do the former the tip is placed in front of a hot filament and high bias is applied between them (500 V). The latter can be done when the tip is placed in front of a sample 10-20 Å away and then bias is set to 10 V and current to 50 nA. This usually produces a very drastic change of the tip (on nanometer scale). A more gentle way is to

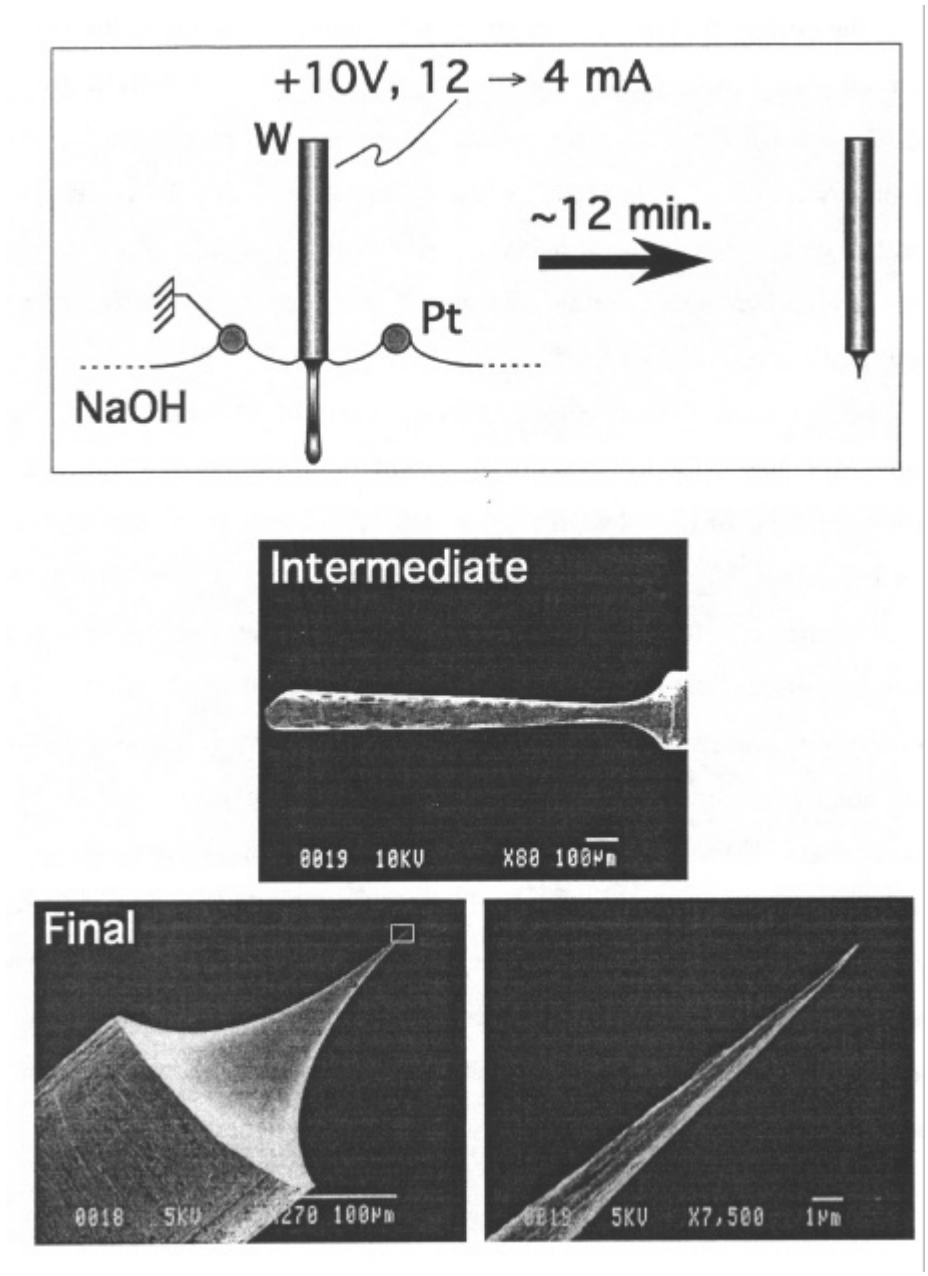

Figure 3.5 STM tip preparation

(top) Schematic view of a common tip-etching setup
(middle and bottom) Electron micrographs of a W wire in the intermediate and final stages of etch
(adopted from (Carpinelli 1997)

apply high voltage (5-10 V) during scanning for 1-2 seconds. This operation changes configuration of the atoms at the apex of the tip. On the instruments with inefficient vibration isolation such as JEOL, loud singing in a low tone can produce a desirable effect. If none of the above helps, a gentle crash of the tip into the sample can do the job. The list of voodoo tricks can be extended.

Constant current and constant height modes

Obtaining STM images is a very tedious work. It takes sometimes days to get the right parameters to achieve atomic resolution. Sometimes it takes minutes. There is no general recipe for that. There are different basic modes of data acquisition. The most often used is a constant current mode. It is illustrated in the Fig. 3.6a. A feedback loop adjusts the height of the tip during scanning so that the tunneling current flowing between tip and sample is kept constant. The height (z), controlled by the voltage on the Z-piezo drive is recorded then as a function of x and y. The contour map z(x,y) is often referred to as the 'topographic image' of the surface, though it is determined not only by arrangement of atoms. A quick-response feedback loop is used for constant current imaging. In the constant height mode the tunneling current is recorded while the tip-height distance is kept more or less stationary (Fig. 3.6b). The constant height imaging uses a slow-response feedback loop to maintain only a constant time-averaged current.

Constant-current imaging (CCI) is important for acquiring spectroscopic information. A near-zero bias constant current image approximately maps out a contour of constant sample LDOS at E_F. At higher bias CCI represent a constant integrated sample LDOS from E_F to E_F+V. For example, if the sample is biased positive, the bright

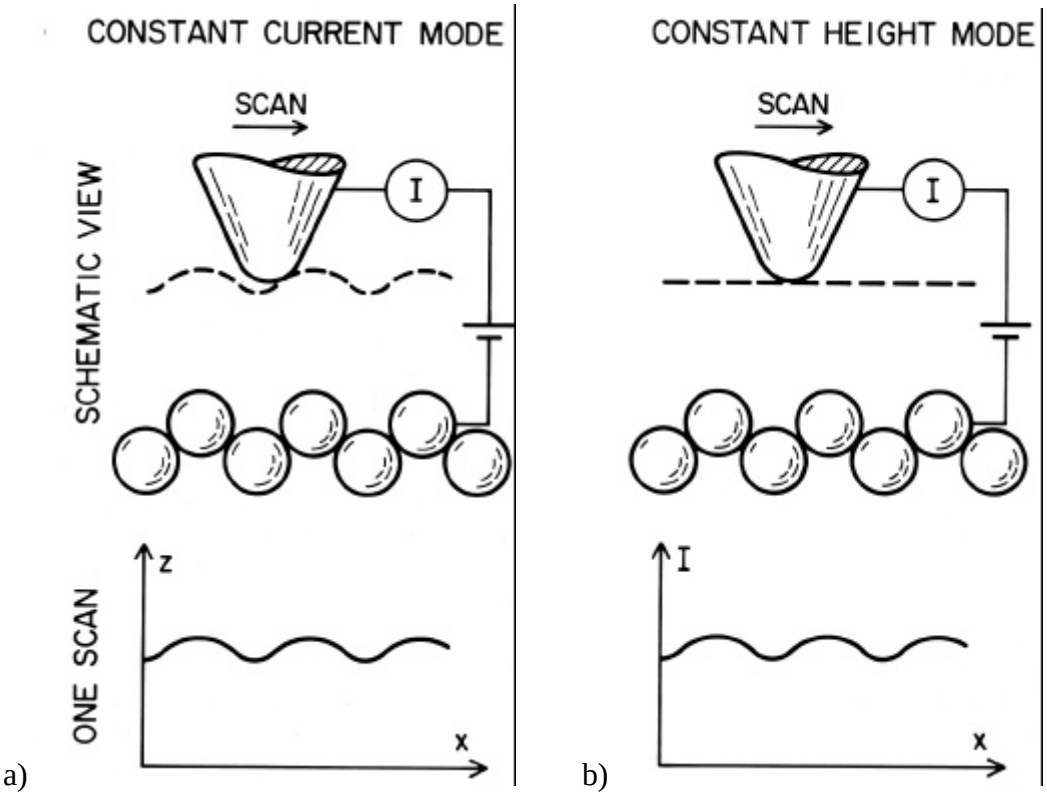

Figure 3.6 Constant current and constant height STM imaging modes
(from (Binnig 1987; Hansma 1987))

regions in the image represent areas with a high total density of holes (empty states); while if the sample is biased negative, the bright regions in the image are the areas with a high total density of electrons (filled states) (Tersoff 1983).

Constant-height imaging (CHI) allows higher acquisition rates since it is not limited by the response time of the feedback loop. The faster scan rates with CHI make possible a variety of measurements of the dynamical processes at a surface.

Scanning Tunneling Spectroscopy

The variation of a tunneling current as a function of applied voltage reveals spectroscopic information about the electronic structure of solids. In combination with STM it become possible to obtain spectroscopic data with atomic resolution, information that is unobtainable using other methods. The simplest way to obtain spectroscopic information with the STM is to acquire constant current topographs at different voltages on the same part of the surface, so called voltage dependent imaging. Differences in the LDOS at different energies can be identified from such images. For example, the complimentarity of the CCI obtained at +1V and –1V (Fig. 2.2 for Pb/Ge(111) and 2.4 for Sn/Ge(111) indicated the presence of the Charge Density Wave. Another important example is determination of different species as described in Part 4 where the Ge defects were identified by different appearance at opposite biases.

One of the frequently used spectroscopic modes is current image tunneling spectroscopy (CITS) (Hamers 1986). In CITS the feedback loop is disabled for a short time at each measurement point during a topography scan. The bias is then ramped through a range of voltages and the tunneling current is measured for each of them before

the feedback loop is turned on again. The feedback loop's off time is so short that the tip remains in approximately the same position during the voltage ramp. Thus an I-V curve is measured for each pixel. A constant current topograph is acquired simultaneously, making it possible to directly relate I-V characteristics to topographic features. The current images, which map the current measured for constant voltage, are particularly useful in determining the lateral distribution of features seen is the spectroscopy.

Although the Transfer Hamiltonian theory gives valuable contributions to the understanding of the STM, spectroscopy measurements usually violate the low bias approximation on which it depends. However, a general approximation to the total current can be obtained by integrating over all the states which are allowed to tunnel by the Pauli Exlusion principle.

$$I \sim \int_0^{eV} dE\, r_s(r,E)\, r_t(r,E-eV)\, T(E,eV,r) \qquad (3.7)$$

where $r_s(r,E)$ and $r_t(r,E)$ are the density of states of the sample and the tip at location r and with an energy E, measured with respect to their individual Fermi levels. The tunneling transmission probability $T(E,eV,r)$ for electrons with energy E and applied bias voltage V can be obtained using Transfer Hamiltonian matrix elements. An intuitive picture can be gained by considering the case of simple planar electrodes, for which we find:

$$T(E,eV,r) = \exp(-2d\sqrt{\frac{2m}{\hbar^2}(\Phi + \frac{eV}{2} - E)}) \qquad (3.8)$$

where Φ is the average barrier height, usually expressed as the mean of the tip and the sample workfunctions.

Eq. 3.7 implies that the contour followed by the tip at constant tunneling current is a rather complicated function of the density of states of the tip and the sample and the transmission probability.

Changing the applied bias will change the number of states allowed to tunnel by the Pauli exclusion principle, and it might be expected that structure in dI/dV would give information about the surface density of states. However, since the transmission probability is approximately exponentially dependent on the bias voltage (Eq. 3.8) the tunneling probability is always largest for electrons at the Fermi level of whichever electrode is negatively biased, and this tends to dominate over the density of state effects. Feenstra et al (Feenstra 1987b) suggested the following expression for the surface DOS:

$$\frac{dI/dV}{I/V} \propto r_z(eV) \qquad (3.9)$$

This normalization procedure divides the differential conductivity by the total conductivity, and essentially removes the dependence on the transmission probability. An example of how this emphasizes density of states features is given in Fig. 3.7 (Johansson 1997). DOS features seen with other spectroscopic techniques are often reproduced well, peak widths and lineshapes though tend to vary from tip to tip and so cannot be used quatitatively. It should be stressed out that the true strength of the STM lies in its ability to measure spectroscopic features as a function of position, not as a function of energy. In practical terms, to validate the STS results it is necessary to do repeated experiments, using different tips and under different experimental conditions, e.g. by changing set point current and sample biases for imaging. Also, it is beneficial to compare STS with photoemission or other spectroscopies.

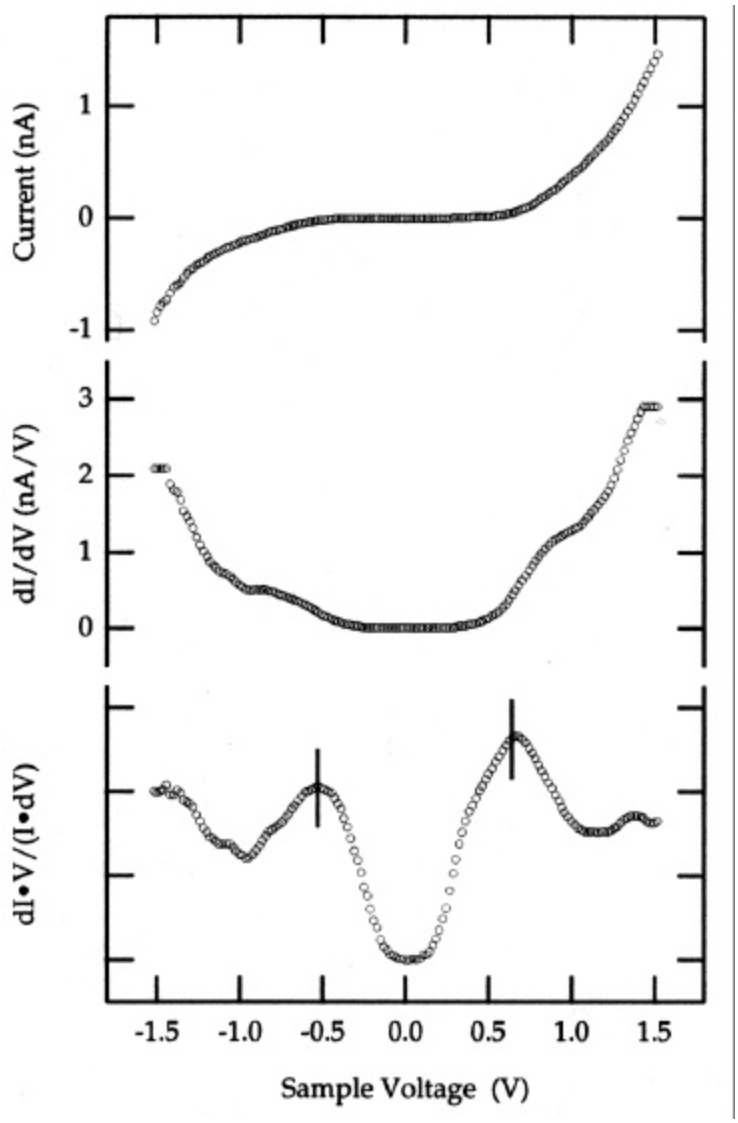

Figure 3.7 Area-averaged CITS obtained from the Si(001) -2×1 surface
(a) current
(b) differential conductivity,
(c) normalized conductivity
from (Johansson 1997)

Varying temperature

Study of phase transition with STM requires existence of capabilities to vary temperature of the sample. This is a very hard engineering challenge and the main reason why the cost of a commercial Variable Temperature (VT) STM is an order of magnitude higher than RT STM. In two designs I worked with, produced by JEOL and Omicron, the sample is brought in contact (clamped) to a copper block that is connected to a cryostat via flexible copper wires that provide vibration isolation. Any given temperature is then achieved by cooling using liquid helium (LHe) or liquid nitrogen (LN2) and counterheating using a resistive element at the end of the cryostat.

Even though the temperature can be stabilized with a very high precision, thermal drift is a significant problem. The solution to that could be an electronic drift compensation when additional bias applied to x and y piezo in order to trace the spot of interest. If the temperature is being changed it is practically impossible to trace the same area.

Art of image processing

In order to get the information out of the STM image usually noise filters are applied. The challenge is to remove noise and preserve all relevant information. There is also a danger of creating some artificial information that was not in the actual STM image. The usual sequence I used to process Constant Current images is the following. A sample original image is presented in the Fig. 3.8a. The area under considerations is inclined with respect to the plane of the image. This makes one part of the image very bright and another very dark in the grayscale map (orange). As a first step the average plane is subtracted from the values of z-coordinates. The result is presented in the Fig. 3.8b. Due

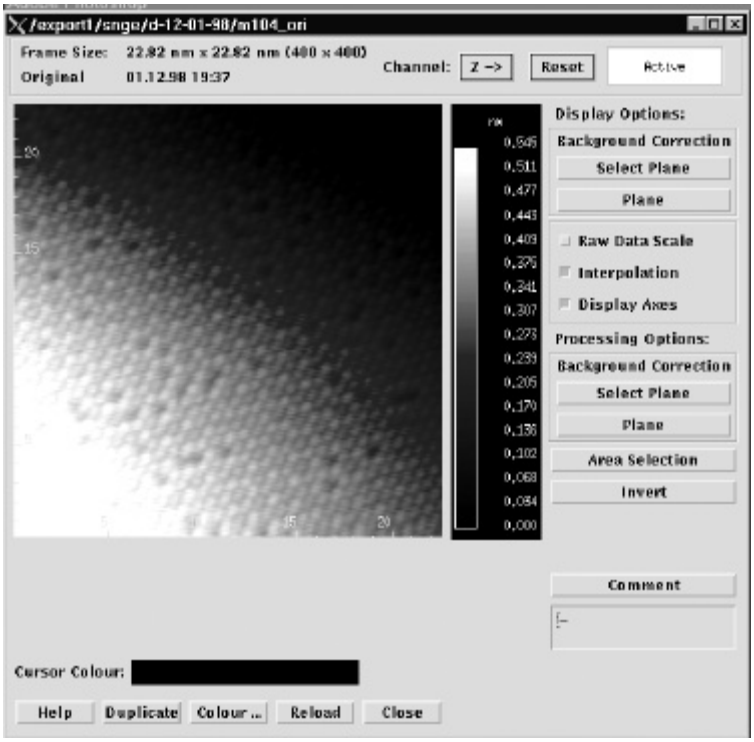

a)

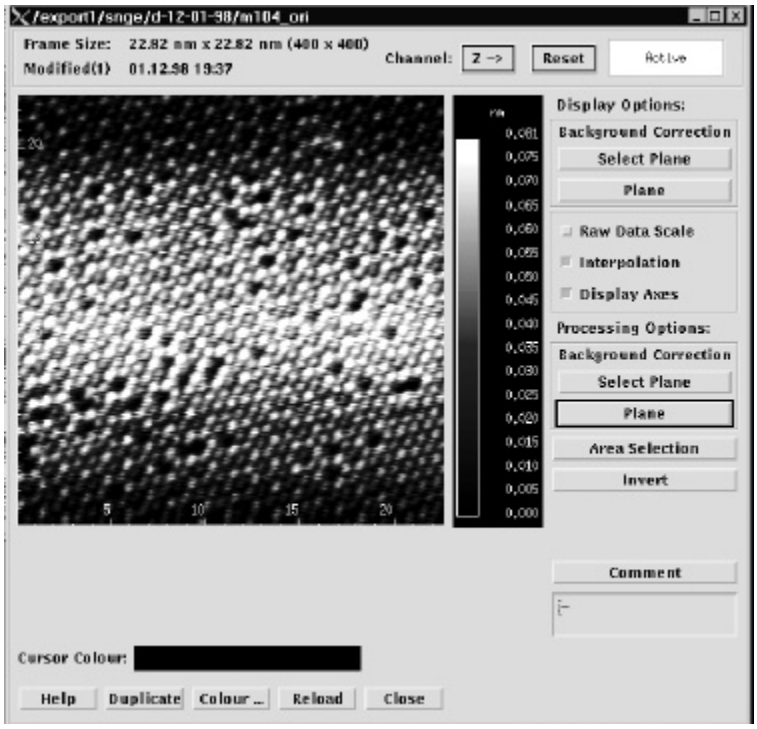

b)

Figure 3.8 Plane subtraction for background correction of an STM image

a) An original STM image

b) An image after plane subtraction

(Omicron SPM 2.2 interface)

to drift in the z-direction (thermal) the average brightness might vary perpendicular to the scanning direction. Hence, the next processing step is to calculate and subtract the average for each line. The result is shown in the Fig. 3.9a. This is usually applicable to the images of areas with small corrugation. If the area has features that are more than a nanometer high ("blobs") averaging will make a part of the image next such feature too dark thus distorting the image. In that case the data editing is applied. The undesired feature is cut out by setting the values to average z-value of the surrounding area of the interest.

After all this done the noise filtering procedures are applied. I found the most useful is to import an image in Adobe Photoshop and to subject it to "Gaussian blur" filter. The magnified image and the result of the Gaussian blur is presented in the Fig. 3.10a and b respectively. Gaussian blur smoothes the streaks that are result of the fluctuations in the measured parameters (tunneling current, bias and so on.). By controlling the radius of the blur it is possible to tune the size of the features you would like to preserve. Usually the size of the atoms in the image should be 10 times bigger that the radius of the blur. After application of the Gaussian blur the atoms appear as nice round balls. Slightly larger radius of blur can be used to enhance the features with a larger period. For example if the (3×3) perturbation is week at RT image it could be enhanced by Gaussian blur with subsequent contrast enhancement. This is actually how I came to realize that the defects induce (3×3) density waves in their vicinity.

Another important alternative filtering technique is Fourier filtering. First the Fourier transformation of an STM image is obtained, then it is modified by applying a variation of filters to remove some components, or enhance some with respect to the

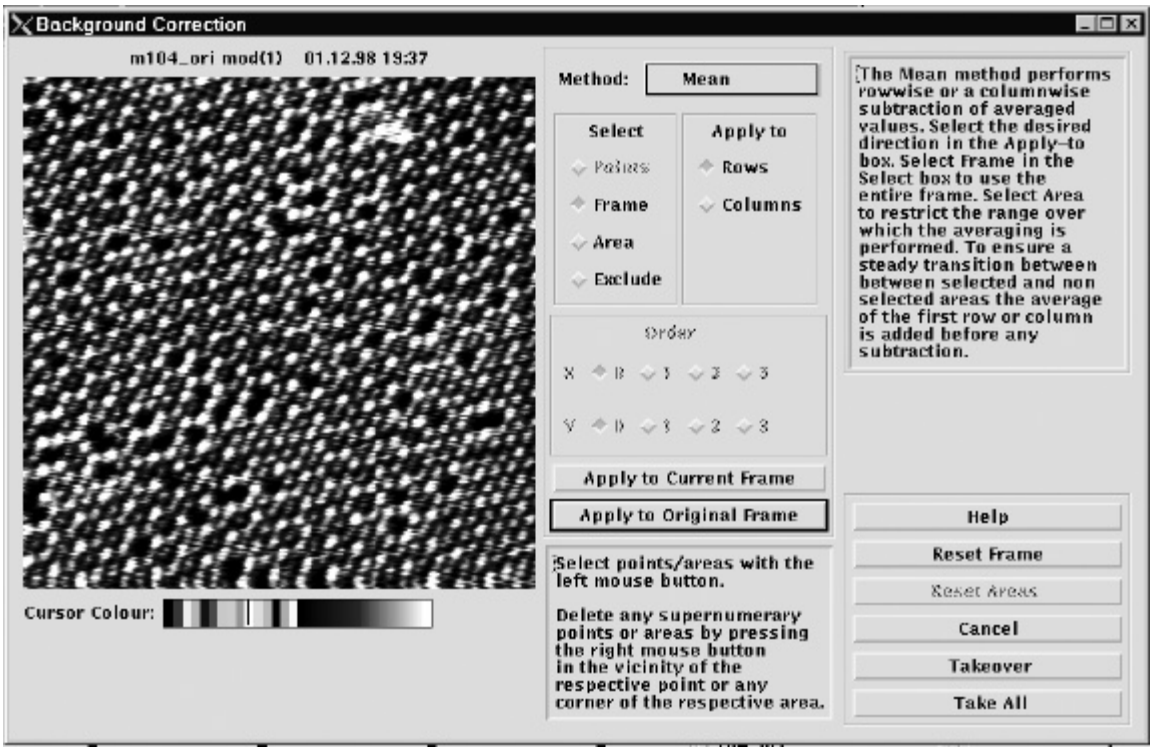

Figure 3.9 Mean method for background correction

(Omicron SPM 2.2 interface)

a)

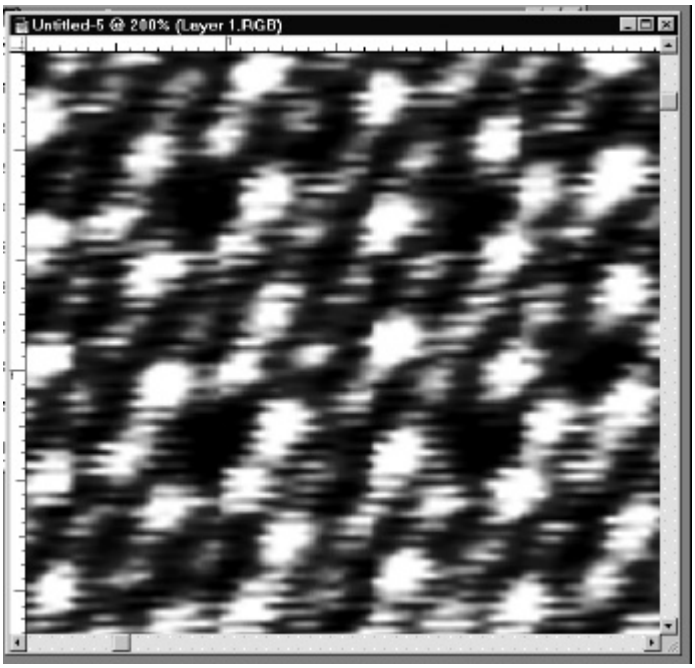

b)

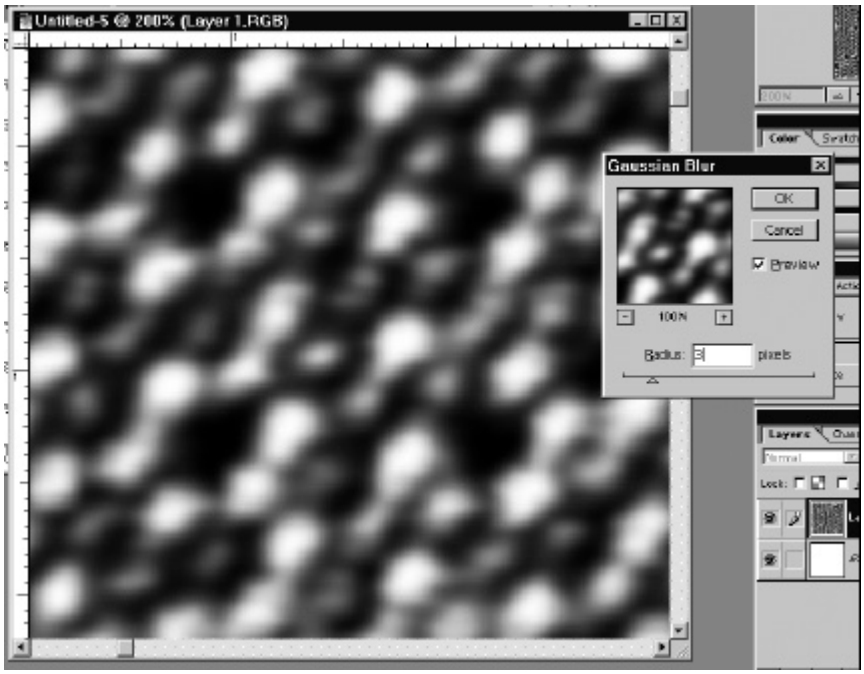

Figure 3.10 Gaussian blur noise filter

a) "Streaky" STM image
b) Gaussian blur filtered (a) using Adobe Photoshop.

other, and the last, the filtered image is obtained by inverse Fourier transformation. Figure 3.11a displays the original image and its Fourier transformation. Then the Butterworth low pass filter was applied (Fig. 3.11b). The white circle shows the cut off spatial frequency. After application of this procedure the “streaks” (shown in Fig. 3.10a with higher magnification) disappear. This also shows that the Gaussian blur is a way to cut off higher spatial frequency components. By extracting spots that correspond to the lattice it is possible to enhance the larger periodicity components. In example shown in Fig. 3.12a such subtraction creates an image with only (3×3) periodicity left. Such procedure was applied to LT STM image of Sn/Si(111) to enhance a new periodicity (Part 6). And finally if we cut the two components of the (3×3) lattice we can extract a “3×3” wave in one direction.

3.2. Low Energy Electron Diffraction

Low Energy Electron Diffraction gives information on the crystal surface symmetry. Electrons with energy range of 20-500 eV that are elastically backscattered from a crystal surface will form a Fraunhofer diffraction pattern that is the Fourier transform of the surface atom arrangement, if you are not concerned with intensitity. The first experiments were done by Davisson and Germer in 1927 (Davisson 1927). (Davisson was awarded Nobel Prize in Physics in 1937 for electron diffraction). In 60’s Germer guided the development of the modern LEED display system (Scheibner 1960).

Figure 3.13 illustrates a typical arrangement. Electrons enter from the left and some fraction of backscatter towards a hemispherical grid G1. A retarding potential difference between G1 and a second grid G2 allows only the elastically backscattered

a)

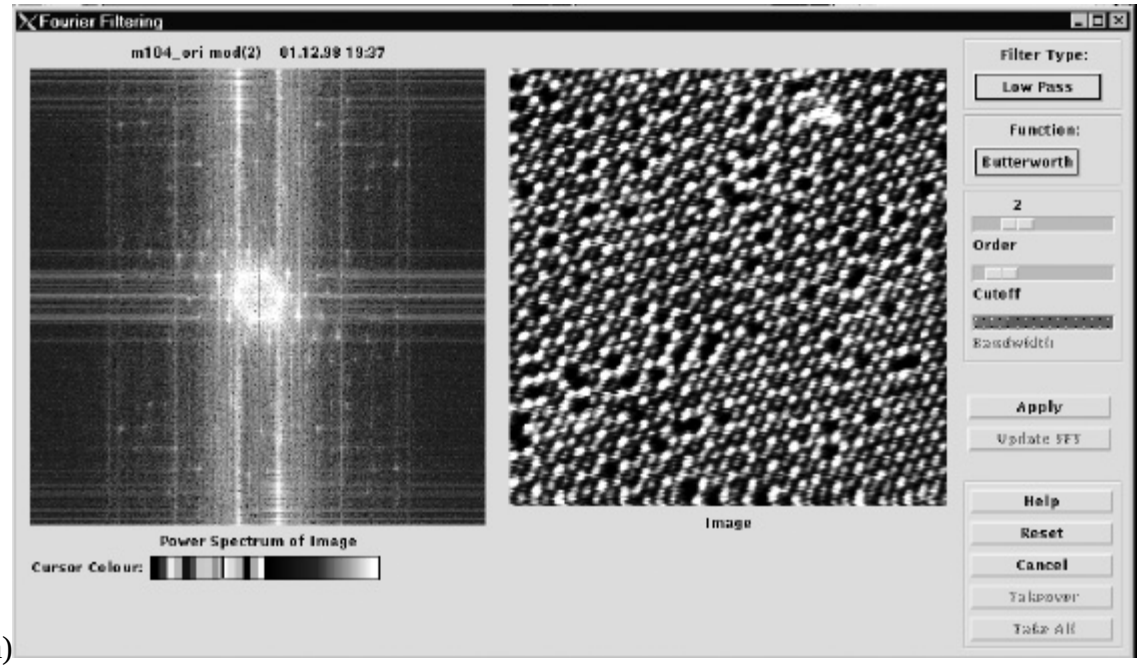

b)

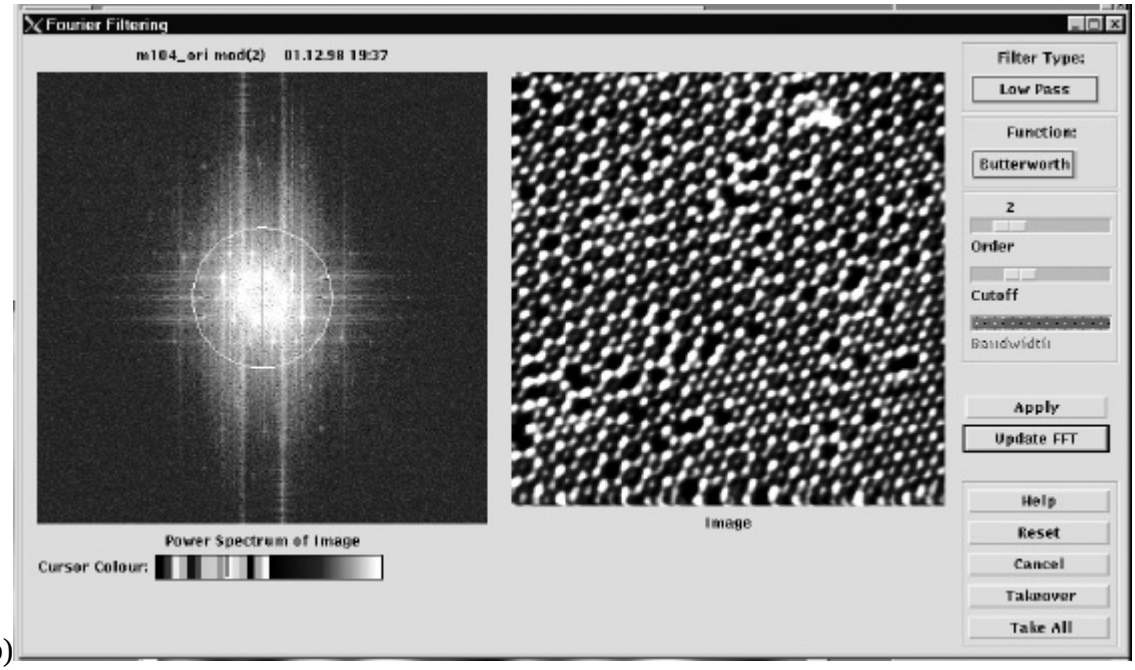

Figure 3.11 Fourier filtering

a) Fourier transformation (left) of the STM image (right)
b) Low pass Butterworth filter applied to (a)

a)

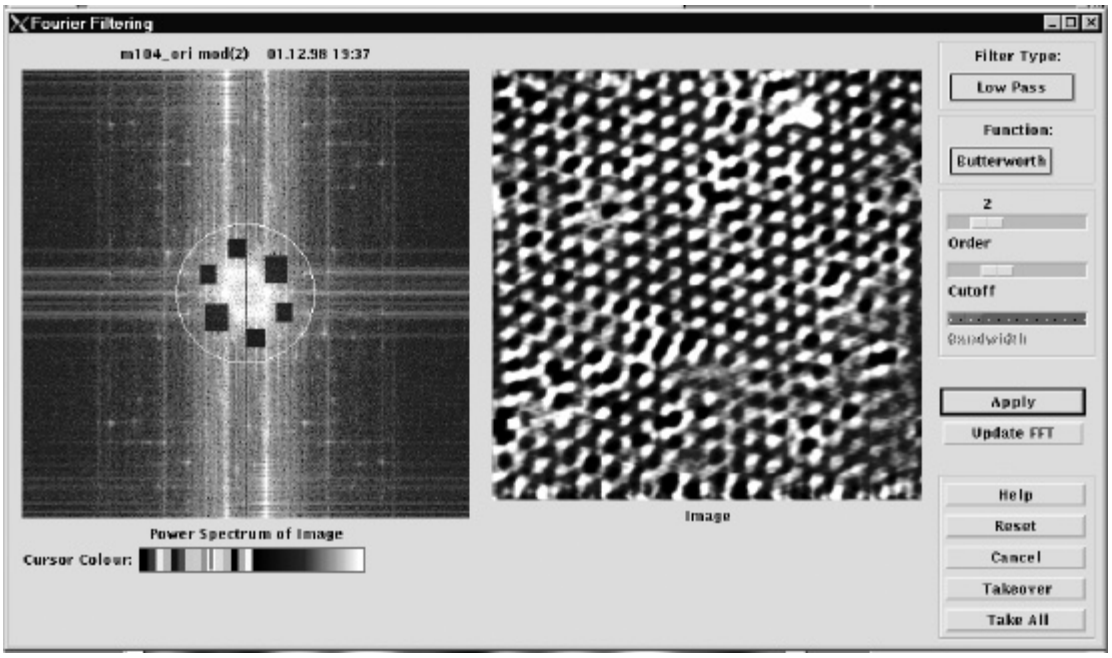

b)

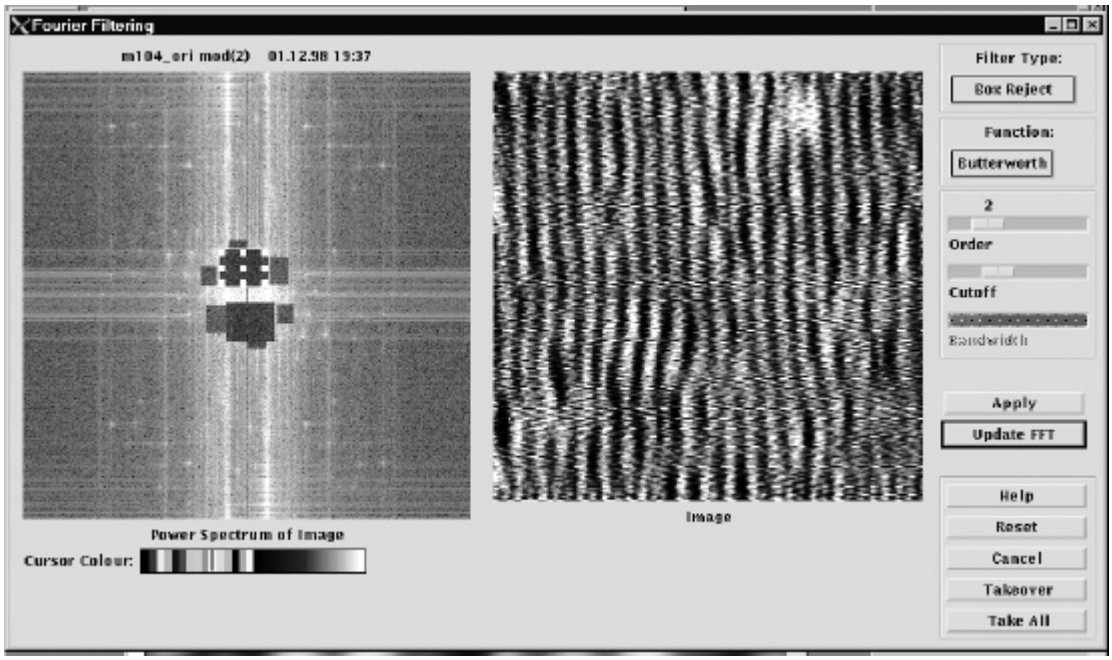

Figure 3.12 Lattice subtraction using Fourier filtering

a) Spots corresponding to $(\sqrt{3}\times\sqrt{3})R30°$ periodicity are cut off (left) and the image is inverse Fourier transformed (right)
b) Same as a) but all spots except two are removed.

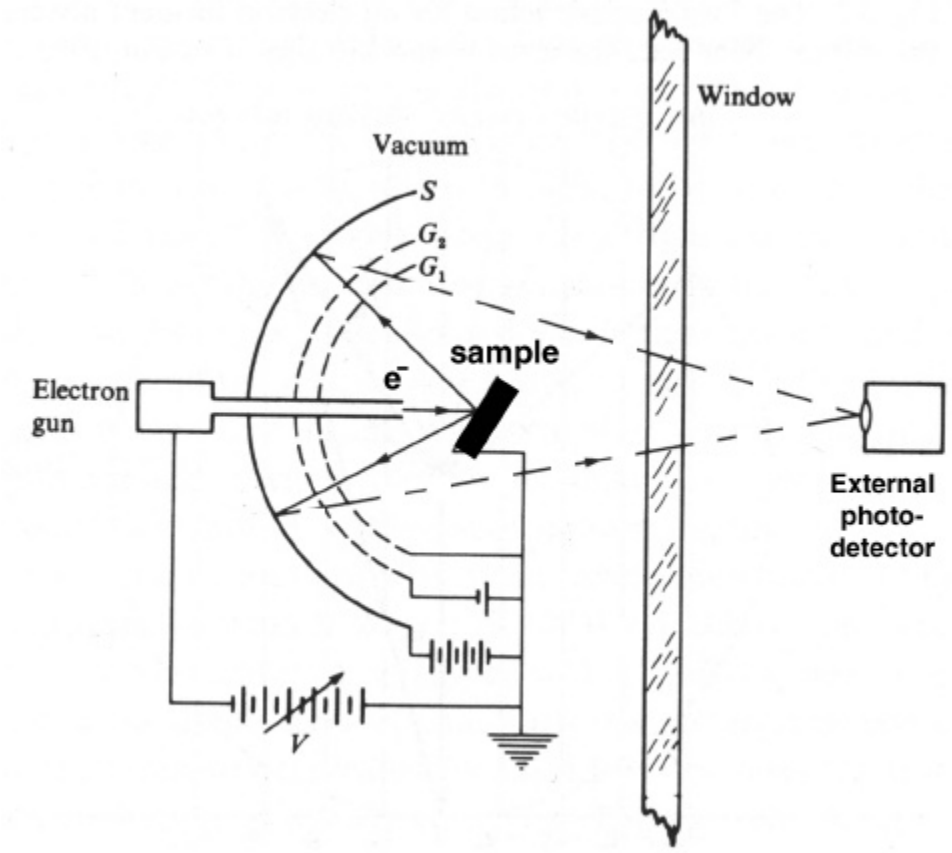

Figure 3.13 A display-type LEED system (Clarke 1985)

electrons (about 1% of the total yield) to reach G2. A fluorescent screen S is held at a large positive potential so that the electrons accelerate and excite screen phosphors upon impact. A still (or better video) camera records the image of the diffraction "spot pattern".

3.3. Sample preparation and experimental details

3.3.1 Sn/Ge(111)

The experiments were carried out in a commercial Ultra-High Vacuum (UHV) VT STM. The n-type Ge(111) substrate (Sb doped, 0.18 V cm, 5×10 mm^2) was cleaned *in situ* by Ne^+ sputtering (1 KeV, 10 min, 20 $\mu A/cm^2$) and annealing cycles (~15 min at 800 K, measured with an IR pyrometer). Between three and five cycles are required to obtain a well-ordered surface. STM images recorded from the prepared Ge(111) surface at room temperature revealed average terrace widths of about 700 Å. Figure 3.14 displays filled and empty state STM images of the clean c(2x8) reconstructed surface of Ge(111) (a) and b), respectively). Figure 3.14c is the LEED pattern acquired at 55 eV.

Sn (purity 99.9999%) was deposited for 5 to 10 min with an evaporation rate of approximately 0.04 ML/min from a commercial Knudsen cell surrounded by a water-cooled shield. The temperature of the Knudsen cell was stabilized at 1000 °C, and the sample was held at room temperature during deposition. After Sn is dosed on the sample, fuzzy (2×2) diffraction spots are visible in the LEED pattern. In order to form the (√3×√3) structure, the sample was annealed at 500 K for approximately 25 min and subsequently cooled to room temperature. Sharp (√3×√3) patterns were obtained after this procedure. (√3×√3)-spots were most intense at a beam energy of 43 eV. The sample was then transferred to the STM stage. Close inspection of STM images recorded at room

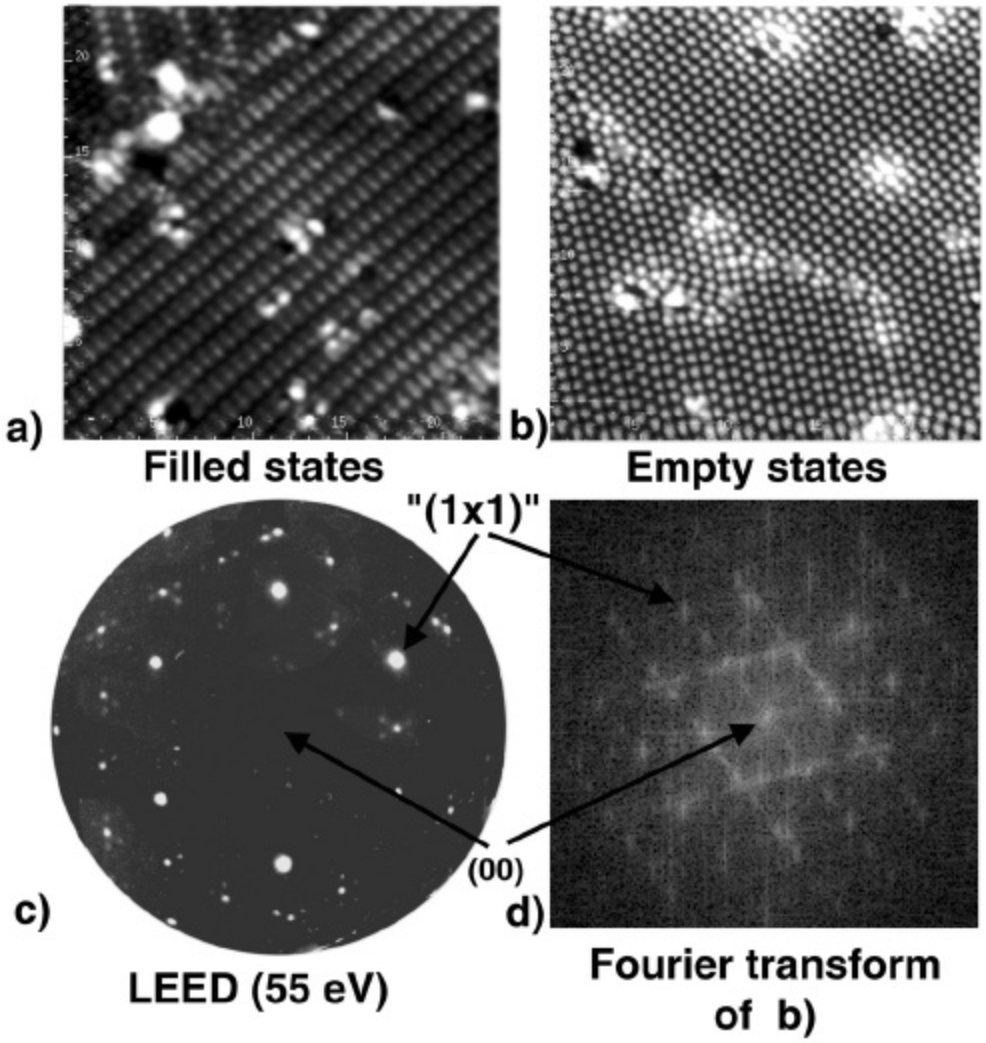

Figure 3.14 STM and LEED data from clean c(2×8) reconstructed surface of Ge(111)

a) Filled state (-1V) STM image of Ge(111) c(2×8) reconstructed surface
b) Empty state (+1 V) STM image of Ge(111) c(2×8) surface
c) LEED pattern from Ge(111) c(2×8)
d) Fourier transform of (b)

temperature shows that the (√3×√3) phase always coexists with small regions of other Sn sub-monolayer structures on Ge(111), such as (7×7) and (5×5) reconstructions (Fig. 3.15) (Gothelid 1992; Gothelid 1995) as well as (2×2) patches (Fig. 3.16) (Le Lay 1998). The nature of the surface before annealing depended upon the coverage (deposition time). For low coverage (5 min deposition time), the surface would consist of (√3×√3) and (2×2) reconstructed terraces, while a higher coverage (10 min) produced (√3×√3) areas surrounded by disordered Sn. The (√3×√3) areas seemed to be the same for different coverages. For example, the defect density discussed below does not appear to depend upon the initial coverage. Annealing time and temperature were optimized to give maximum (√3×√3) reconstructed surface. High annealing temperature leads to the stable (5×5) and (7×7) reconstructions Fig. (5x5and7x7), and too low of an annealing temperature does not produce a sufficiently ordered surface.

3.3.2 Temperature control

On the STM stage, the sample was cooled using a continuous flow cryostat at an average rate of 4 K/min. During the experiments, the temperature T_b of the clamping block of the STM stage was measured and stabilized in the range between 20 K and 300 K with 0.1 K precision. T_b is slightly lower than the actual temperature at the sample, T. T was measured and calibrated to T_b in separate runs both prior to and after the experiments using a chromel-constantan thermocouple attached to the sample. Later on I refer only to the actual temperature of the sample T, which was reproducible within 5 K.

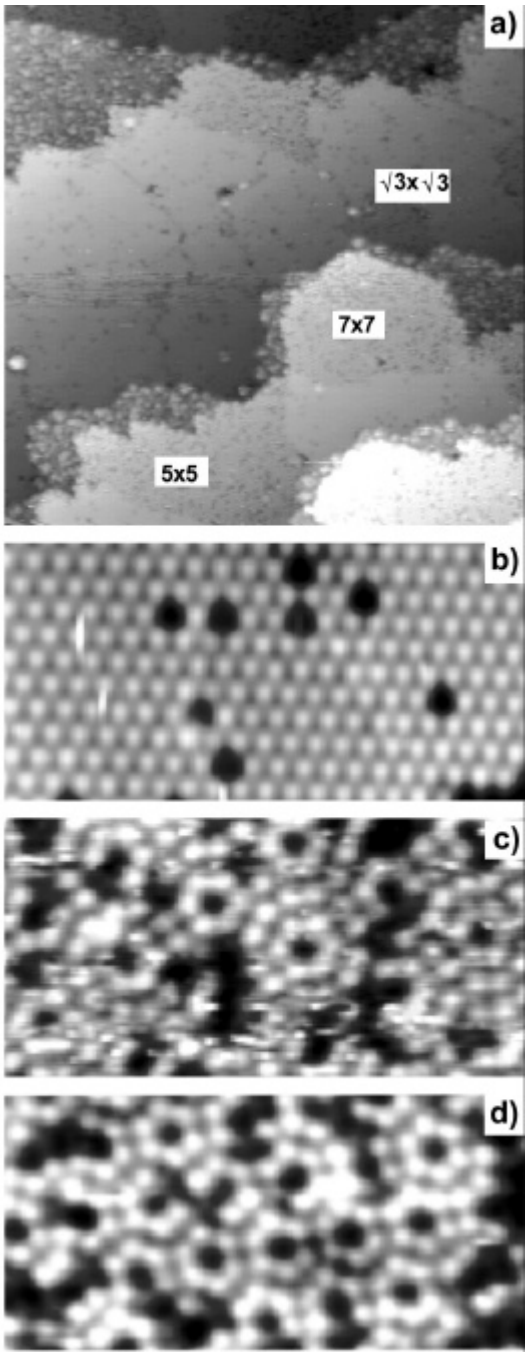

Figure 3.15 Coexisting phases of (√3×√3)*R*30°, (7×7) and (5×5) reconstruction possible after Sn is deposited on top of clean Ge(111) and annealed

a) Large scale STM image (700Å×700Å)
b) (√3×√3)*R*30° reconstruction (empty state)
c) (7×7) reconstruction (empty state)
d) (5×5) reconstruction (empty state)

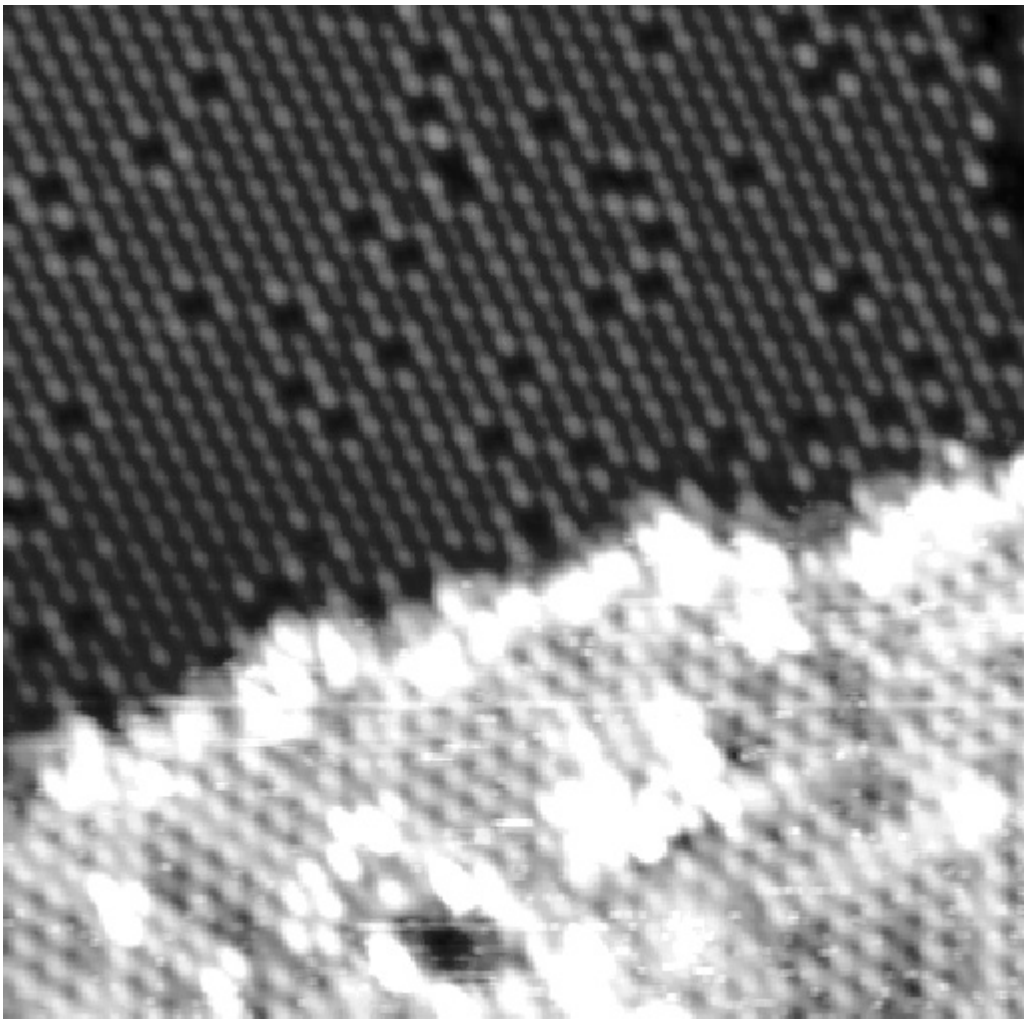

Figure 3.16 Coexisting ($\sqrt{3}\times\sqrt{3}$)*R*30° and (2×2) for coverages slightly lower than 1/3 ML of Sn on Ge(111)

References for Part 3

Bardeen, J. (1961). Physical Review Letters **6**: 57.

Binnig, G. and Rohrer H. (1987). "Scanning Tunneling Microscopy - from Birth to Adolescence." Reviews of Modern Physics **59**(3): 615-625.

Binnig, G., Rohrer H., Gerber C. and Weibel E. (1983). "(111) Facets as the Origin of Reconstructed Au(110) Surfaces." Surface Science **131**(1): L379-L384.

Binning, G., Rohrer H., Gerber C. and Weibel E. (1982). Appl. Phys. Lett. **40**: 15.

Bleaney, B. (1984). "Microwave Spectroscopy in Oxford - the 1st Decade .1. Microwave Gas-Spectroscopy." Contemporary Physics **25**(4): 315-329.

Carpinelli, J. M. (1997). Charge-Ordering Transition in Ultrathin Metal Films. Department of Physics, University of Pennsylvania.

Chen, C. J. (1993). Introduction to Scanning Tunneling Microscopy. New York, Oxford University Press.

Clarke, L. J. (1985). Surface Crystallorgraphy. New York, Wiley.

Davisson, C. J. and Germer L. H. (1927). "Diffraction of electrons by a crystal of nickel." Physical Review **30**: 705.

Feenstra, R. M. and Stroscio J. A. (1987a). "Tunneling Spectroscopy of the Gaas(110) Surface." Journal of Vacuum Science & Technology B **5**(4): 923-929.

Feenstra, R. M., Stroscio J. A. and Fein A. P. (1987b). "Tunneling Spectroscopy of the Si(111)2x1 Surface." Surface Science **181**(1-2): 295-306.

Gothelid, M., Grehk T. M., Hammar M., Karlsson U. O. and Flodstrom S. A. (1995). "Adsorption of Tin on the Ge(111)-C(2x8) Surface Studied with Scanning-

Tunneling-Microscopy and Photoelectron-Spectroscopy." Surface Science **328**(1-2): 80-94.

Gothelid, M., Hammar M., Tornevik C., Karlsson U. O., Nilsson N. G. and Flodstrom S. A. (1992). "Sn-Induced Surface Reconstructions on the Ge(111) Surface Studied with Scanning Tunneling Microscopy." Surface Science **271**(3): L357-L361.

Hamers, R. J., Tromp R. M. and Demuth J. E. (1986). "Surface Electronic-Structure of Si(111)-(7 X 7) Resolved in Real Space." Physical Review Letters **56**(18): 1972-1975.

Hansma, P. K. and Tersoff J. (1987). "Scanning Tunneling Microscopy." Journal of Applied Physics **61**(2): R1-R23.

Johansson, M. (1997). Scanning Tunneling Microscopy and Spectroscopy of Adsorbates on Aluminum and Silicon. Department of Synchrotron Radiation Research, Institute of Physics. Lund, Sweden, Lund University.

Le Lay, G., Aristov V. Y., Bostrom O., Layet J. M., Asensio M. C., Avila J., Huttel Y. and Cricenti A. (1998). "Surface charge density waves at Sn/Ge(111)?" Applied Surface Science **123**: 440-444.

Melmed, A. J. (1991). "The Art and Science and Other Aspects of Making Sharp Tips." Journal of Vacuum Science & Technology B **9**(2): 601-608.

Muller, E. W. (1960). Adv. in Elect. and Electron Phys. **13**: 83.

O'Hanlon, J. F. (1989). A user's guide to vacuum technology. New York, Wiley.

Scheibner, E. J., Germer L. H. and Hartman C. D. (1960). Rev. of Sci. Inst. **31**: 112.

Tersoff, J. and Hamann D. R. (1983). "Theory and Application for the Scanning Tunneling Microscope." Physical Review Letters **50**(25): 1998-2001.

Wiesendanger, R. (1994). Scanning probe microscopy and spectroscopy : methods and applications. Cambridge, New York, Cambridge University Press.

Woodruff, D. P. and Delchar T. A. (1994). Modern Techniques of Surface Science. Cambridge, Cambridge University Press.

Part 4

Role of defects in two-dimensional phase transitions:

An STM study of the Sn/Ge (111) system

In this Part, I present my experimental observations on the influence of Ge substitutional defects and vacancies on the ($\sqrt{3}\times\sqrt{3}$) $\leftrightarrow$ (3×3) Charge Density Wave phase transition in the α-phase of Sn on Ge(111). Briefly, above ~100 K, Ge substitutional defects stabilize regions with (3×3) symmetry that grow with decreasing temperature and the STM images can be described by a superposition of exponentially damped waves. The range of these waves, represented by a decay length, diverges at a temperature $T_{c1}\approx 70$ K. Below this temperature the surface consists of (3×3) domains separated by abrupt domain walls. Additionally, at temperatures below $T_{c2}\approx 105$ K defect-defect density-wave-mediated interactions force an alignment of the defects onto a honeycomb sublattice that supports the low-temperature (3×3) phase. This defect-mediated phase transition is completely reversible. The length scale involved in this defect-defect interaction dictate the domain size (~10^4 Å^2).

4.1. Room-temperature α-phase of Sn/Ge(111)

Figure 4.1(a) is a large area filled state STM image of the ($\sqrt{3}\times\sqrt{3}$) structure showing several terraces, with an average terrace width of ≈700 Å. The size of the ($\sqrt{3}\times\sqrt{3}$) domains is dictated by the terrace width and line defects marked by the arrows in Fig. 4.1(a). The resulting area is on average $\approx 5\times10^5$ Å^2. Several point defects are visible in the filled and empty state images of Figs. 4.1(b) and (c), respectively. About 90% of those defects are substitutional Ge atoms. They will be referred to just as Ge defects. Ge defects can be identified because they appear as black spots surrounded by six bright Sn

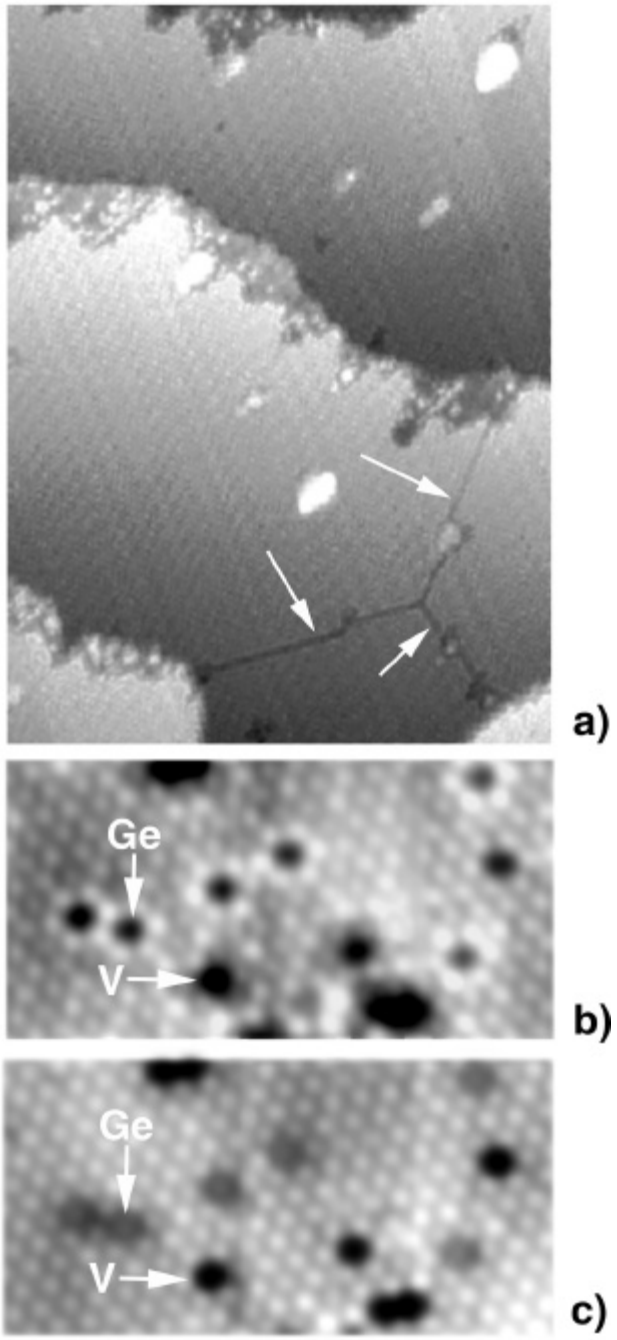

Figure 4.1. STM images of the (3x 3) phase recorded a t T= 295 K.

(a) Filled state overview image (600x1000 Å^2. U_G = -1.3 V, I_T=0.1 nA). Line defects in the (3x 3) terraces are marked b arrows.

(b) Close up filled state image (146x72 Å^2. U_G=-1.0 V, I_T=0.4 nA).

(c) Same as (b) but empty state image (U_G=+1.0V).

atoms in filled state images, indicating charge transfer from defects to neighboring atoms (Stumpf 1999). Vacancies account for the remaining 10% of defects in α-Sn/Ge(111). They appear as black spots surrounded by six dark nearest-neighbor Sn atoms and six bright second nearest neighbors in the filled state image. Ge defects and vacancies can also be distinguished in the empty state image, where Ge defects appear as gray and vacancies appear as black spots. The identification of Ge substitutional and vacancy defects has been discussed in detail (Carpinelli 1998). One Ge defect and one vacancy are labeled in Figs. 4.1(b) and 4.1(c). The presence of substitutional atoms from the substrate is a feature common to the α-phases of Pb/Ge(111) (Carpinelli 1998) and Sn/Si(111) (Tornevik 1994). The average concentration of point defects is 3±1% (corresponding to $(6\pm2)\times10^{-4}$ defects/Å^2). The defect density did not vary significantly with Sn coverage. An analysis of the STM image in Fig. 3(b) of (Gothelid 1995) ($(\sqrt{3}\times\sqrt{3})$ surface, θ =0.4 ML) yields a defect density of about $4\text{x}10^{-4}$ defects/Å^2 (2%) in agreement with our result. Figure 4.1(c) presents an empty state STM image of the same region of the surface as shown in Fig. 4.1(b). Here Ge defects appear as gray spots surrounded by a ring of Sn atoms that are slightly darker than Sn atoms in perfect (3x 3) regions. Vacancies are dark in both empty and filled state images because they do not provide any orbital. (Carpinelli 1998)

4.2.Low-temperature phase of α-Sn/Ge(111) and correlation of defects

As the temperature is lowered, the room-temperature ($\sqrt{3}\times\sqrt{3}$) phase gradually converts to an ordered (3×3) phase (Weitering 1999), (Carpinelli 1997a). The details of the temperature dependence of this transition will be discussed in the next section. Here I

describe the stable configuration that is seen below ~100 K. The filled and empty state STM images of this (3×3) configuration are complementary, with bright protrusions forming a hexagonal and honeycomb pattern, respectively (Carpinelli 1997b). The structure of this phase has been determined for both Sn (Zhang 1999) and Pb (Mascaraque 1999) and is very similar. One of the three Sn atoms in the (3×3) unit cells moves up by ≈0.35 Å while the other two move down by ≈0.02 Å. The vertical rippling of the Sn atoms is accompanied by a small perpendicular (0.17 Å) and parallel (0.12 Å) distortion of the first layer of Ge atoms. In Fig. 4.2(b), moving atom A up and atoms B and C down can produce this structure. Note that the lattice distortion is localized to the surface region. The creation of a (3×3) sublattice from the original (√3×√3) lattice with the local structure described above is not unique, because three different (3×3) domains exist. It is easy to see how this happens from the structural model shown in Fig. 4.2(b). There are three Sn atoms in the (3x3) unit cell, which have been labeled as A, B, and C. If atom A moves up then B and C move down, so that atom A forms a (3×3) hexagonal sublattice as seen in the STM filled state images. But it is equally probable that atom B (C) moves up and atoms A and C (A and B) move down, again forming a (3x3) hexagonal sublattice of B (C) atoms. Figure 3(a) illustrates the three different hexagonal sublattices (black grid (a), dashed grid (b), and white grid (c)), which cover the (√3×√3) lattice (gray balls) completely. Let us assume that the atoms on the sub-lattice a move up and become bright in the STM image. The observed bright hexagonal sublattice is shown in Fig. 4.3(b). A combination of the atoms on sublattices b and c form the honeycomb sublattice of dark atoms seen in the filled state image is reproduced in Fig. 4.3(c).

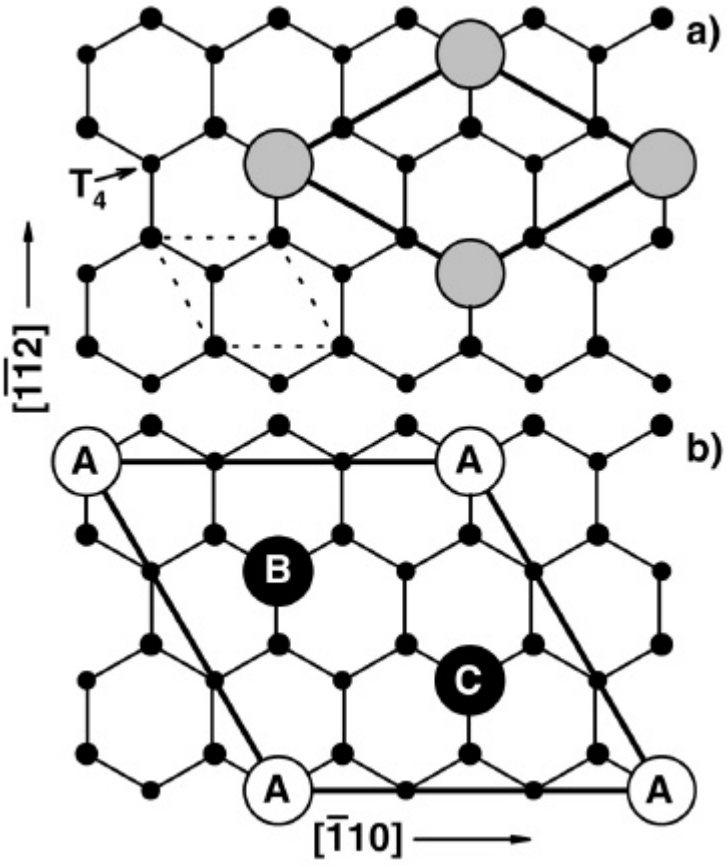

Figure 4.2 Ball model of the two structures of Sn on Ge.

(a) (3x 3) unit cell formed by Sn on Ge(111) at room temperature (α phase). The gray, small black and circles correspond to Sn atoms at the corner of and inside the unit cell, respectively.

(b) The three different Sn atoms in the unit cell are labeled A, B, and C. In the (3x3) phase, one Sn atom moves up ant the other two down.

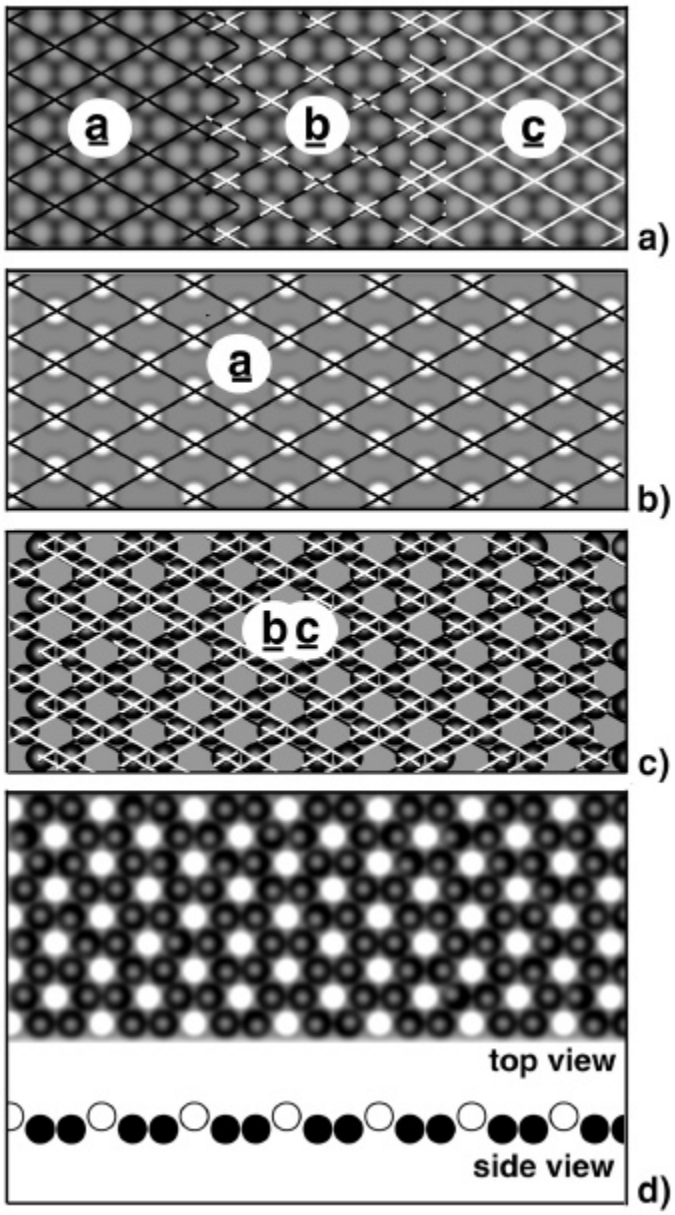

Figure 4.3 (3×3) sublattices

(a) Three different possibilities to lay (3x3) grids over a $(\sqrt{3} \times \sqrt{3})$ lattice are represented by gray circles. Grids a, b, and c, are illustrated by black, dashed, and white lines, respectively.

(b) Hexagonal sublattice of corner atoms of the (3x3) structure coinciding with grid a in (a), called sublattice "A".

(c) Honeycomb sublattice formed by sublattices b and c combined.

(d) Combination of (b) and (c) results in a lattice that resembles the observed filled state low-temperature STM images. The side view illustrates the vertical rippling of the structure.

Finally, the combination of the bright hexagonal sublattice formed by sublattice a and the honeycomb sublattice of dark atoms formed from the combination of sublattices b and c is shown in Fig. 4.3(d), representing the filled state image. Making the atoms in sublattices b and c bright and a dark can reproduce an empty state image. Obviously, we can form three different domains of a hexagonal sublattice by starting with sublattice a, b, or c.

Figure 4.4(a) is a filled state STM image of the (3×3) phase at 30 K showing the coexistence of two of the three possible domains. The domain on the left is labeled ''A'' (black grid) and the one on the right ''B'' (dashed grid). In the ''A'' domain atoms on sublattice a are bright whereas atoms on sublattices b and c are dark. In domain ''B'' atoms on sublattice b are bright whereas atoms on sublattices a and c are dark. The domain boundary is very abrupt, only a few Å wide. The (3×3) domains have various shapes and sizes but are appreciably smaller than the original $(\sqrt{3} \times \sqrt{3})$ domains. Inspection of many STM images gives an average area for the (3×3) domains of 10^4 Å^2 compared to the average size of the $(\sqrt{3} \times \sqrt{3})$ domains of 5×10^5 Å^2 . The filled state STM image presented in Fig. 4.5 shows a larger image than Fig. 4.4, where all three domains labeled ''A,'' ''B,'' and ''C'' can be seen. White lines highlight the domain boundaries. In general, the domain walls are sharp and parallel to the <112> direction except when there are special configurations of defects such as the regions between the wiggly white lines. These special regions will be discussed later. The ''B'' domain is one of the largest observed with an area of 3.4×10^4 Å^2, containing ≈800 Sn atoms. There are 40 Ge defects in the ''B'' domain marked by a, b, or c depending upon which sublattice they are

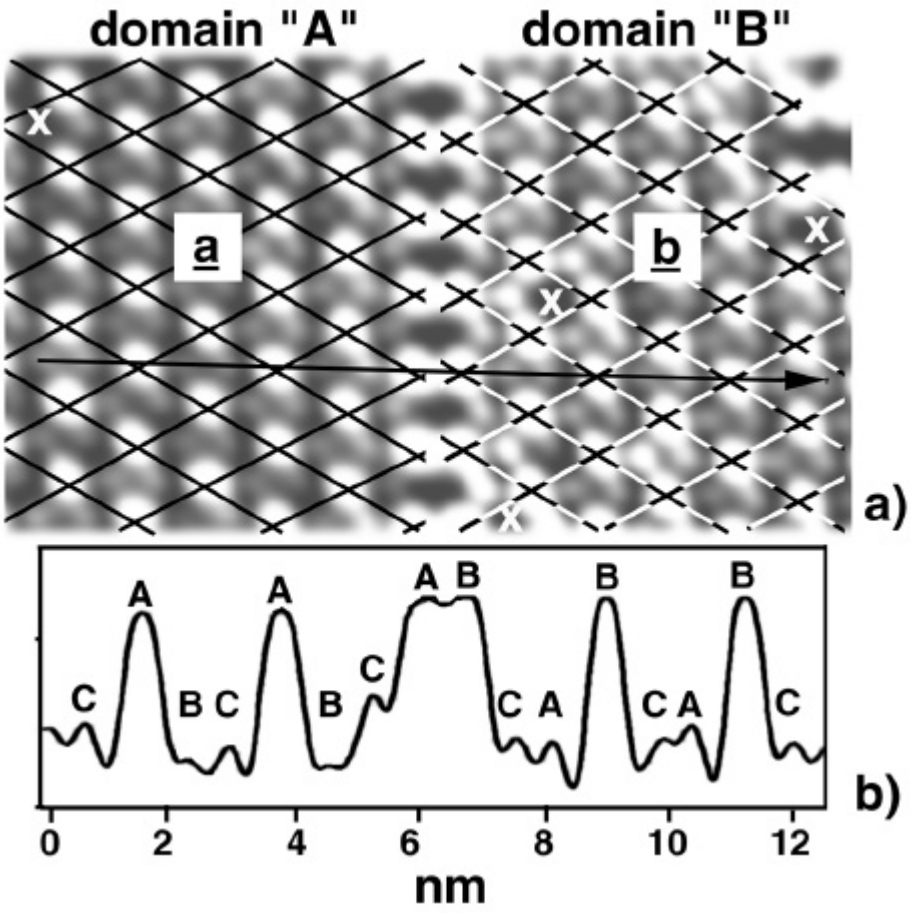

Figure 4.4 Boundary between two (3×3) domains

(a) Filled state STM image (140×42) Å, U_G=-1 V, I_T=0.1 nA) recorded at T=30 K. Two different (3×3) domains are marked by different colored grids. Four Ge defects are highlighted by white crosses. A black arrow indicates the position and direction of a line scan shown in (b).

(b) Average line scan along the <112> direction starting in domain “A”.

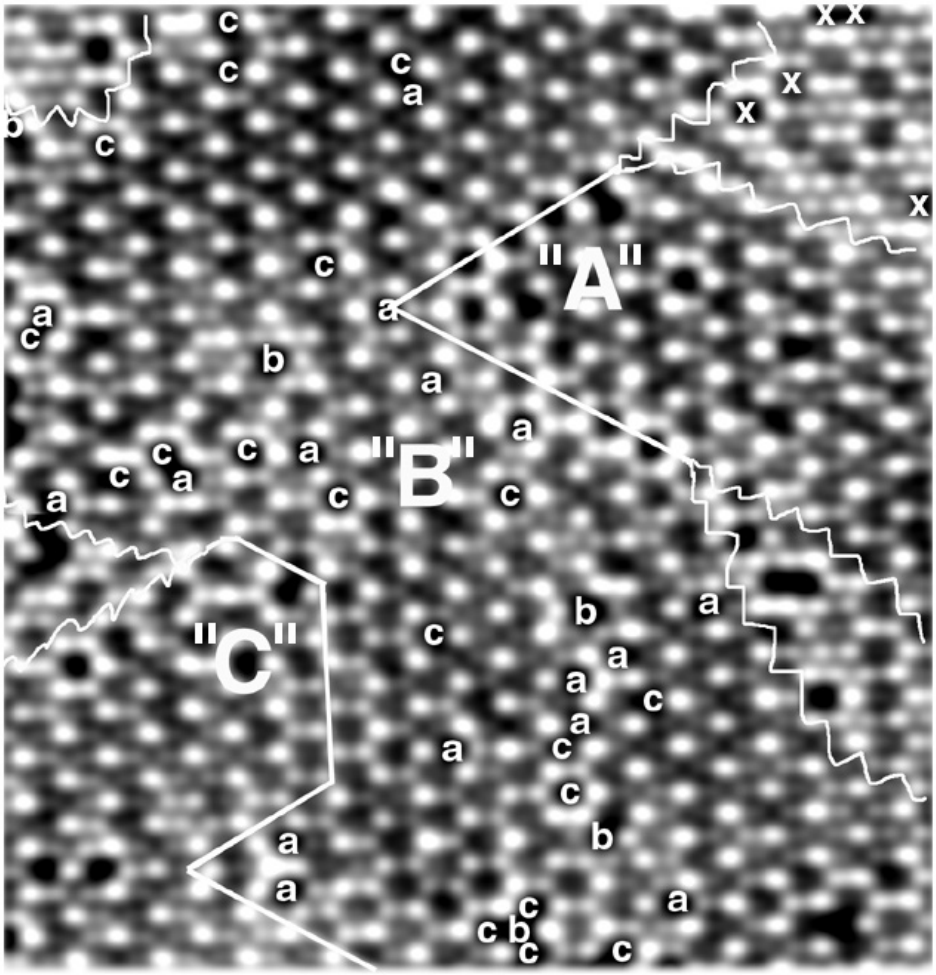

Figure 4.5 Filled state image (220×230) Å^2, U_G-1 V, I_T=0.1 nA) obtained at T=50 K. Three different (3×3) domains are denoted by "A", "B", and "C". White lines highlight domain boundaries. Ge defects are indicated by a, b, and c in domain B according to their lattice position. Outside of domain B Ge defects are indicated by ×.

located. Amazingly, only five Ge defects are located on the b sublattice where the charge density is maximum. Sixteen defects are on sublattice a and 19 on sublattice c, the preferred sites for Ge defects where the charge density has a minimum. Statistically, we find that within each (3×3) domain ≈90% of the Ge defects are positioned on the charge minimum sites forming a honeycomb sublattice. There is no measurable ordering of the defects within the honeycomb lattice; they populate equally the two equivalent hexagonal sublattices that make up this honeycomb structure. A statistical analysis of the location of the defects at room temperature (165 K, 105 K, and 50 K) was performed and described in the Section 4.4. At room temperature and at 165 K, Ge defects are randomly distributed on all three sublattices. Upon cooling to 50 K and 105 K, 90% of Ge defects are positioned on the honeycomb sublattice of charge minima within each domain (compare this to 67% for a random distribution).

Finally, let's discuss the regions between domains shown in Fig. 4.5. The presence of Ge defects on charge maximum sites has interesting consequences. For example, the straight domain boundary running from about the center of the image in Fig. 4.5 to its upper-right corner is suddenly interrupted by an inhomogeneous region stabilized by Ge defects positioned in between domain A and B. Here three Ge defects are located on the charge maximum sites of domain A. There are approximately 70 Sn atoms in this region. Fading of the boundary between A and B can also be seen in the middle right part of the image. This region includes four defects, two on sublattice b and two on sublattices a and c, again stabilizing an inhomogeneous structure.

Analysis of the low-temperature STM images of the (3×3) phase have thus produced three surprising observations.

(i) Small (3×3) domains are formed inside of what was a large (3×3) domain. On average there are 40 (3×3) domains contained within an original (3×3) domain.

(ii) Almost all Ge defects in the low-temperature (3×3) phase are aligned on the charge minimum honeycomb sub-lattice.

(iii) Small inhomogeneous regions are stabilized by defects in the walls between (3×3) domains.

These observations raise intriguing questions. Why should the large (3×3) domains (see Fig. 4.1(a)) not be converted into one uniform (3×3) domain? Why does the system apparently prefer many energetically costly domain walls (white lines in Fig. 4.5) over a large (3×3) domain? Observations (ii) and (iii) suggest that Ge defects provide the key for understanding the formation of the structure of the low-temperature phase. The role of defects in the transition from the (3×3) $\rightarrow$(3×3) phase will be described in detail in the following section.

4.3. The transition from (3×3) to (3×3)

STM images become quite complex as the temperature is reduced from room temperature. Damped oscillatory density waves, (3×3) in character, are generated by every defect where the extent of the density wave is characterized by a temperature-dependent decay length, l(T). At temperatures between 300 K and 105 K, images are comprised of these interfering density waves, forming complex arrays of bright

hexagonal, bright honeycomb, and (3×3) coexisting structures. Based on our observations, an ansatz for the density waves was proposed,

$$I(r) = f_{\sqrt{3}\times\sqrt{3}}(r) + \sum A_n e^{-\frac{|r-r_n|}{l(T)}} \sum \cos\left[k_i(r-r_n) + f_n\right] \qquad (4.3.1)$$

I(r) is the brightness of an atom in the filled state image at a position r; $f_{3\times3}$ models the (3×3) periodicity of the STM images with no defects present. The second term on the right side of Eq. (4.3.1) consists of a sum over all attenuated waves induced by N defects with coordinates r_n and phases ϕ_n . It appears sufficient to consider the amplitude A_n as a constant for all defects. Damping is taken into account by introducing the exponential factor with a decay length l(T). Each defect contributes three cosine waves with wave vectors along the three <112> directions (see Fig. 4.2(b)). The outcome of this fitting procedure is reproduced in Fig. 4.6, showing that the inverse decay length decreases monotonically in the temperature range between 300 K and 120 K. The horizontal line in Fig. 4.6, labeled $1/l_{av}$, marks the average Ge defect-defect separation of l_{av} =45 Å.

Since defects play such a crucial role in the phase transition, it is appropriate to begin with an analysis of the STM images of defects at room temperature. Figure 4.7 displays four different filled state images of Ge defects and vacancies recorded at room temperature. In panel (a) a single Ge defect appears as a dark spot. (Seehofer 1993; Carpinelli 1998). The six nearest-neighbor Sn atoms are appreciably brighter than all other Sn atoms in the (3×3) structure. The grid on this image shows th at a density wave with honeycomb symmetry is created by the Ge defect even at room temperature.

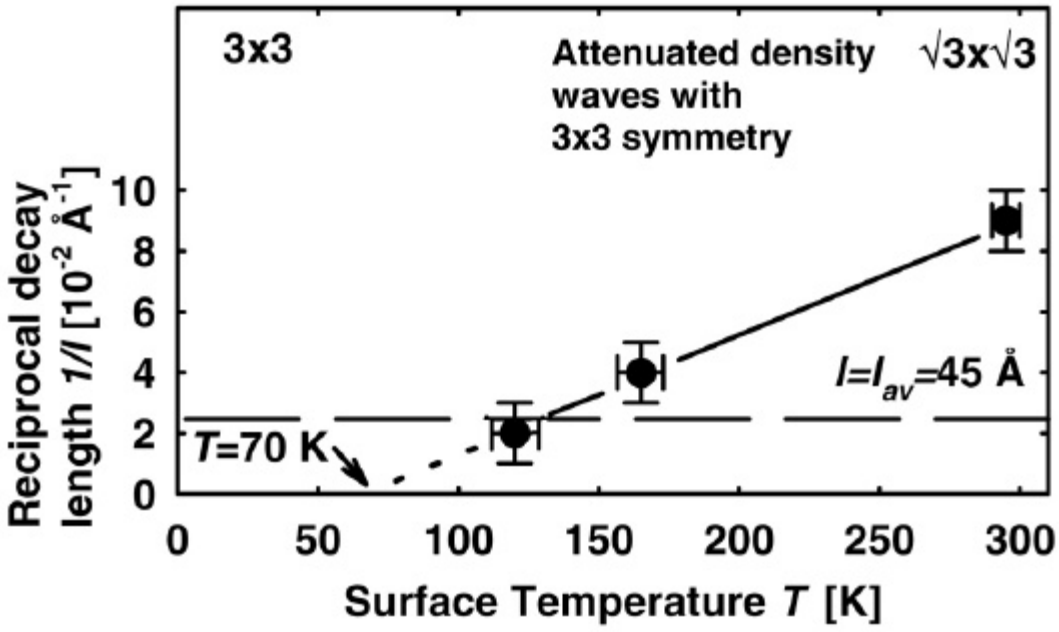

Figure 4.6 Temperature dependence of the reciprocal decay length 1/l(T).

The horizontal dashed line corresponds to an average defect-distance of 45 Å (Ref (Gothelid 1992)). l(T) diverges at T=70 K.

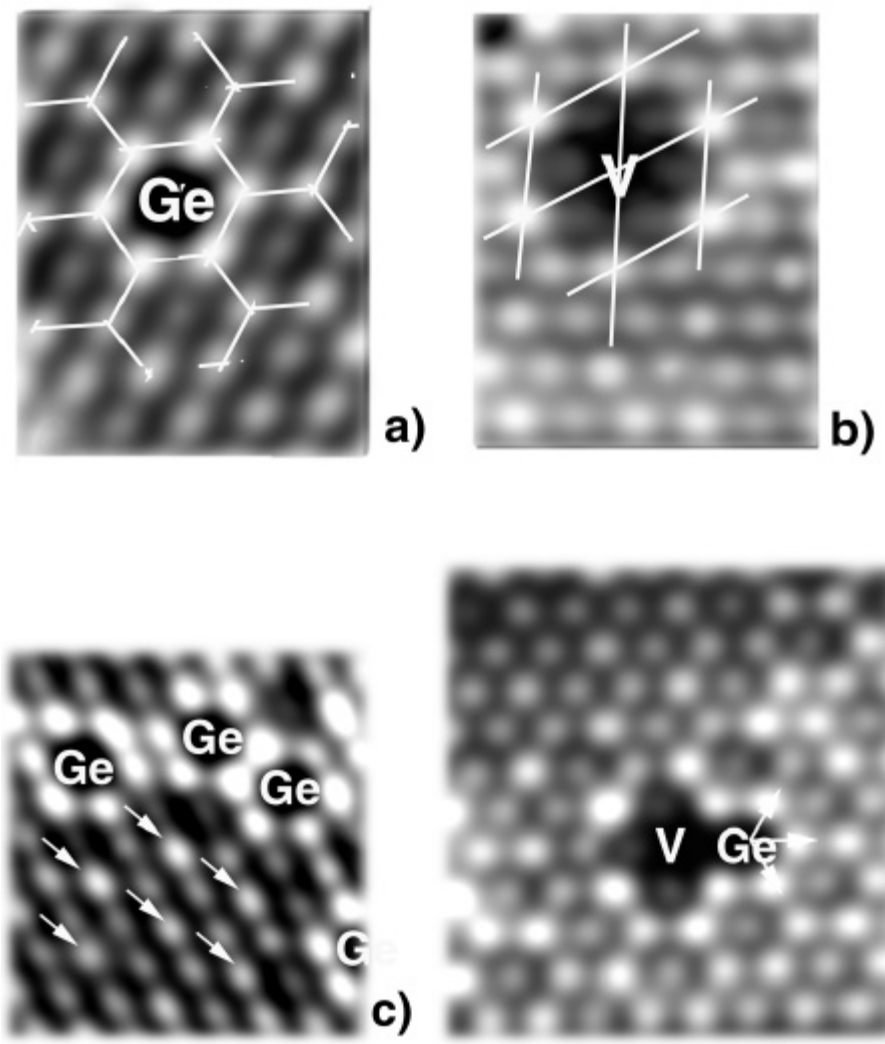

Figure 4.7 Filled state STM images (U_G=-1 V, I_T=0.1 nA) of defects at room temperature.

(a) A single Ge defect with a grid showing the beginning of a honeycomb structure surrounding the defect.
(b) A single vacancy defect with the (3×3) hexagonal grid indicated.
(c) Four Ge defects.
(d) A Ge defect and a vacancy on adjacent sites (65×68 Å^2). The three equivalent <112> directions of the wave vectors, k_i (I=1,2,3), in the model, Eq. (4.1), are marked by white arrows.

Panel (b) shows a single vacancy that creates quite a different density wave. The nearest-neighbor Sn atoms are now dark, and the symmetry of the density wave being set up is similar to the (3×3) hexagonal sublattice. These observations allow for a definitive choice of the phase ϕ_n in Eq. (4.1): $\phi_n=0$ for a vacancy and $\phi_n=\pi$ for a Ge defect. Panel (c) shows a region where the Ge defects are close together but on different sublattices. The two Ge defects on the top right are on the same sublattice, which we label a, but the one on the left and the one on the right edge of the image are on the c sublattice. This gives a complex interference pattern of bright and dark atoms that can be seen as far as 3-4 atoms away from the defects. The bright Sn atoms on the lower part of the image resemble a (3×3) hexagonal structure (marked by arrows as a visual aid). Panel (d) shows a vacancy and Ge defect on nearest-neighbor sites. As the temperature decreases, the extent of the defect perturbation grows since l(T) increases (Eq. (4.1)) and a complicated interference pattern results. Before showing a comparison of experimental data and simulations from Eq. (4.1) (computer code is presented in Appendix A) with 70–100 defects present, it is illustrative to discuss model simulations involving only a few Ge defects.

Figure 4.8 is a set of simulations for different arrays of Ge defects. In panels (a)–(c), the decay length was chosen to be 11 Å, simulating a room-temperature experiment. In panel (a), two Ge defects on different sublattices a and b produce a hexagonal-like pattern on sublattice c. This is a consequence of the superposition of two honeycomb patterns from each Ge defect (as in Fig. 4.7a). In panel (b), three Ge defects occupy sites on the same sublattice (a). Superposition of waves from these ordered Ge defects yields a honeycomb pattern. Panels (c) and (d) illustrate the influence of the exponential factor in Eq. (4.1). Here three Ge defects are placed on three different (3×3) sublattices. Ge defects

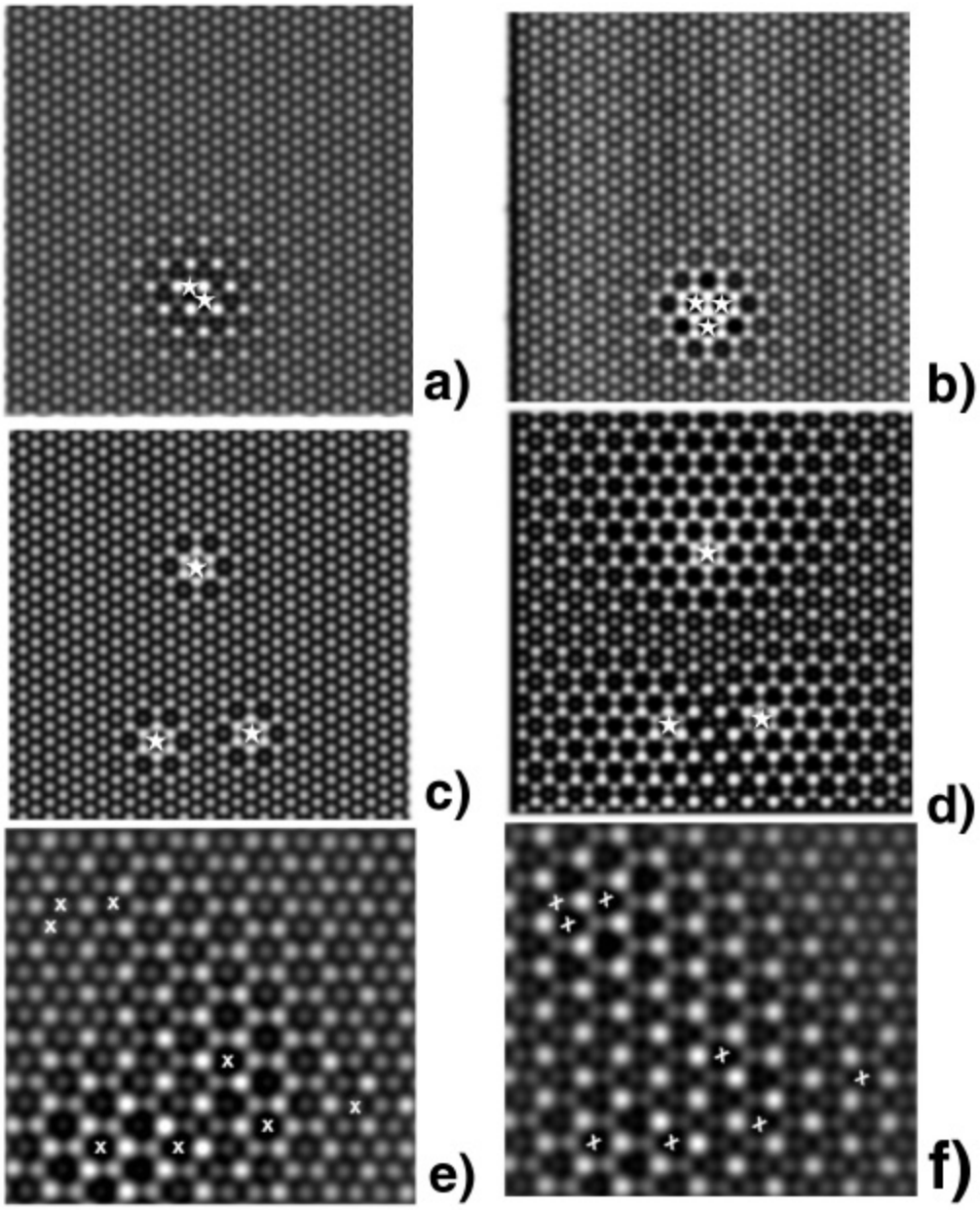

Figure 4.8 Simulation for different configurations of Ge defects
(labeled by their sublattice position).

(a) Two Ge defects on a and b sublattice with l=11 Å.
(b) Three Ge defects all on a (l =11 Å).
(c) Three Ge defects on a, b, and c (l =11 Å).
(d) Same three Ge defects as in panel (c) but l =100 Å.
(e) Eight defects randomly distributed, a, b, and c (l =100 Å).
Eight defects aligned on two sublattices a and b (l =100 Å).

on a and b are closer to each other (bottom) than to the Ge defect at the top (c). When the decay length is only 11 Å (panel (c)), Ge defects produce honeycomb patterns, decaying before they would interfere. If the decay length l(T) is increased to 100 Å (simulating a temperature of ≈100 K), a complex pattern is obtained (panel (d)). Above the Ge defect at the top, the honeycomb pattern expected from a single Ge defect is observed. In between the two Ge defects at the bottom is a hexagonal pattern, while to the right or left of these Ge defects are honeycomb patterns on different sublattices. One important fact is that in between the top and bottom defects a region of $(\sqrt{3} \times \sqrt{3})$ is created as a result of destructive interference. Simulations with eight defects and a decay length of l= 100 Å are presented in panels (e) and (f). Defects in panel (e) are randomly distributed on all three sublattices (Fig. 4.3), three defects on a and b, and two on c. The resulting superposition pattern does not resemble a uniform lattice (i.e., it is neither purely honeycomb nor purely hexagonal). In panel (f) we have shifted the two c sublattice defects, one to sublattice a and the other to sublattice b. The superposition yields a nearly perfect hexagonal sublattice with bright atoms occupying sublattice c. Sublattices a and b become dark, (i.e., all defects sit on dark sites (charge-density minima)). This simulation answers the question of how Ge defects, which on their own generate a honeycomb density wave, can produce a hexagonal pattern at low temperature as seen in Figs. 4.4 and 4.5. They align themselves on any two of the three possible sublattices (Fig. 4.3). The interference pattern from Ge defects randomly distributed on two sublattices, say a and b, produces a hexagonal pattern on the third sublattice c. This is in agreement with images recorded at T<~100 K, as shown, for example, in Figs. 4.4 and 4.5.

Now it is possible to explain how we determined the value of l(T) from experimental data. In principle, it should be quite easy to determine the extent of the density wave from a single Ge defect as a function of temperature. In practice, interference patterns between density waves from nearby Ge defects makes this procedure impossible. Panel (a) of Fig. 4.9 shows such a complex interference pattern in a filled state image taken at 165 K. In the simulations, defect sites and type are taken from the experimental image. The best-fit simulation is shown in panel (b), with an inverse decay length 1/l (165 K)=0.04 $Å^{-1}$. Panels (c) and (d) show the simulations where the inverse decay length is slightly larger, 1/l =0.05 $Å^{-1}$, and slightly smaller 1/l =0.03 $Å^{-1}$. Our definition of a good fit was that the complex interference patterns between defects seen in the experiment were reproduced in the simulated image. The two regions circled in the experimental image illustrate this procedure. There are no defects inside either the white or black circle, but the effects of defects are quite different. The image inside the white circle is (3×3) while a bright hexagonal pattern is created by defects inside of the black circle. The best-fit simulation shown in panel (b) reproduces both of the structures. If the decay length is shortened as it is in panel (c), the (3×3) pattern in the white circle is correct, but the image in the black circle is (3×3) instead of (3×3) hexagonal as seen in the image. On the other hand, if the decay length is increased too much (panel (d)), a (3×3) hexagonal pattern is created inside the white circle. The decay length used in (b) reproduces the interference patterns in the experimental data, while the decay lengths in (c) and (d) are incorrect. This procedure was used to determine l (T) and the error bars in Fig. 4.6. At temperatures between 300 K and 120 K, the surface structure is very complex as reflected in the STM

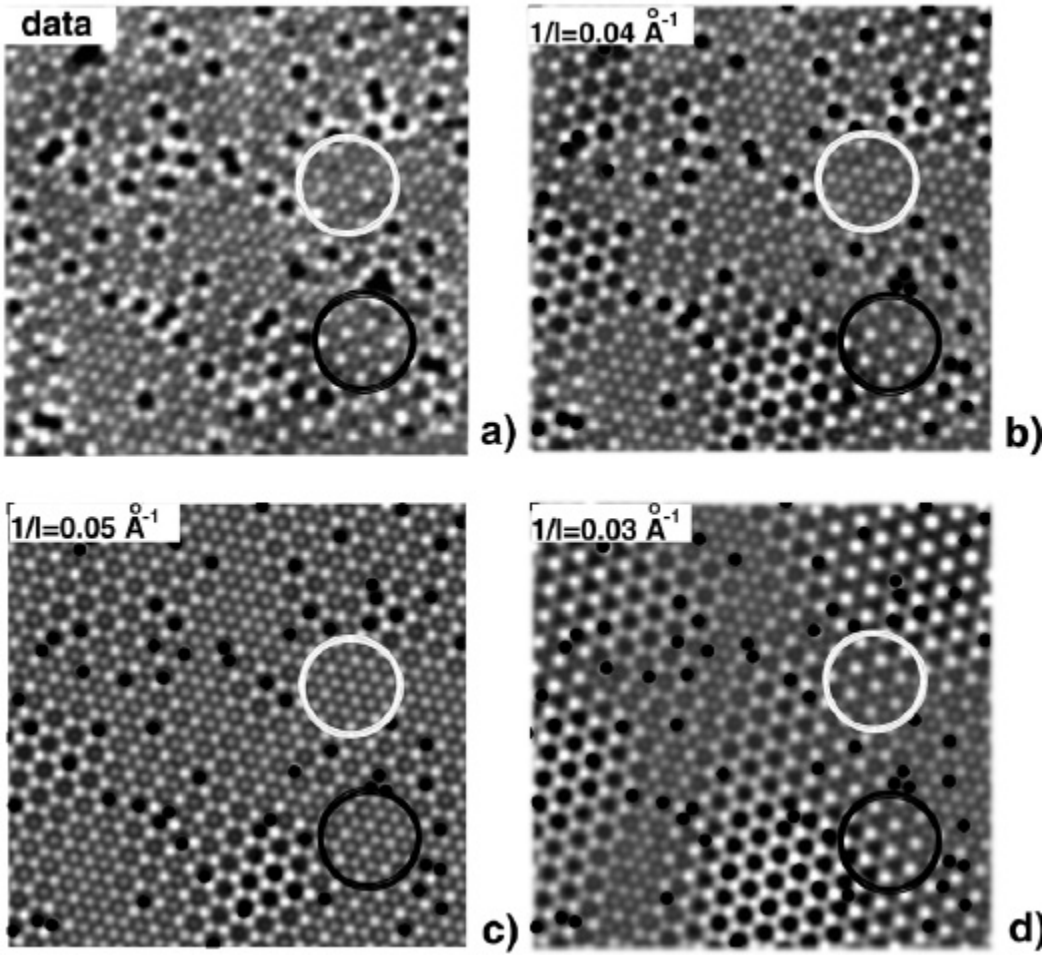

Figure 4.9 Comparison of an STM image and simulations for fitting.

(a) Filled state STM image (175×180 Å^2, U_G=-1 V, I_T=0.1nA), recorded at T =165 K.
(b) Simulation for 1/ *l* (T)=0.04 Å^{-1} (best agreement).
(c) Simulation for 1/ *l* (T)=0.05 Å^{-1} (too large).
(d) Simulation for 1/ *l* (T)=0.03 Å^{-1} (too small)

The two circles are regions where the interference pattern is very sensitive to the decay length. Inside the white circle the experimental image is (3×3) while inside the black it is (3x3) hexagonal.

images.

Even though a (3×3) LEED pattern appears at 210 K, a (3×3) phase for pure system would appear in STM images only below 70 K, according to our measurements of the decay length. The proof of this statement will be presented in detail in Part 5**.** At intermediate temperatures, the surface is comprised of an inhomogeneous mixture of hexagonal, honeycomb, and (3×3) patches. Even within a region that has a given symmetry, say a (3×3) hexagonal, the intensity of ‘‘like’’ atoms is not uniform. This implies that the structure within this region is not uniform and not the same as the structure determined at 60 K (Mascaraque 1999; Zhang 1999). A simple illustration of the intricacy of this temperature regime can be given by counting the number of bright, dark, and gray atoms in a large set of images as a function of temperature. This procedure is slightly subjective, but inspection of Figs. 4.1, 4.5, 4.7, and 4.9(a) shows that it is not difficult to classify all atoms into one of the three categories (defects are not counted). Figure 4.10 is such a plot with data for four different temperatures. The simplest model would have only gray (‘‘normal’’) atoms from the (3×3) structure at room temperature and a ratio of 33% bright and 67% dark at low temperature from the hexagonal (3×3) structure. As the temperature is decreased from room temperature, the fraction of gray atoms should go to zero and the bright and dark should increase from zero, but always with a 1:2 ratio. Obviously this picture does not reproduce the data in Fig. 4.10 because we have ignored the Ge defects. At room temperature, there are about 3±1% Ge defects with six bright atoms surrounding each defect, so we would anticipate ≈18±6% bright atoms. The superposition of waves from defects close together makes some second- and

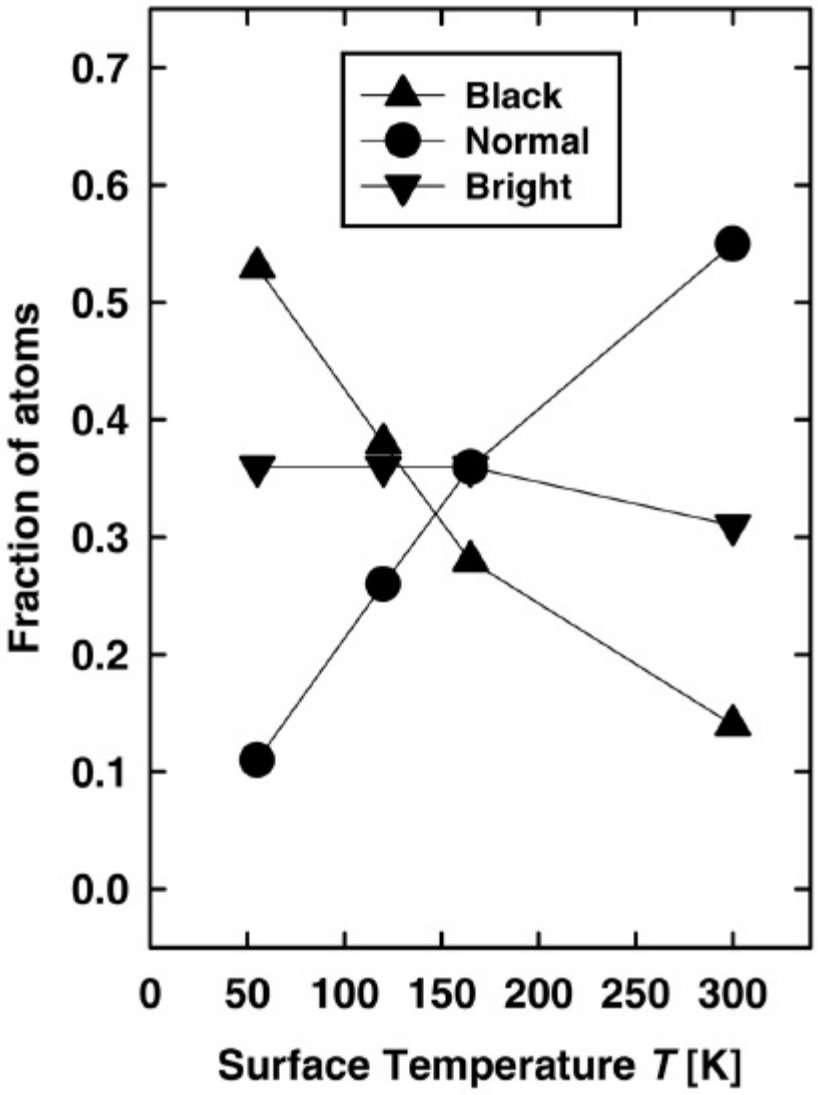

Figure 4.10 Fractions of bright, dark, and normal atoms in filled state STM images as a function of temperature.

The fractions were determined from averaging over about ten 250×250 Å^2 images for each temperature. "Normal" refers to atoms that look like atoms in undistorted regions of filled state images recorded from the room-temperature (3×3) phase.

third-nearest neighbors bright and some first-nearest neighbors dark, giving the experimental number of 30% (see Fig. 4.7(c)). At low temperature the perfect ratio of one bright for two dark is perturbed by the domain walls as shown in Fig. 4.5. The branching ratios for bright, dark, and gray at intermediate temperatures is not something that could have been predicted. For example, the fact that the fraction of bright atoms is almost constant is a consequence of the details of the interference patterns. This plot indicates how complicated interpretation of core-level spectra can be without the aid of an STM (Kidd 1999). Interpretation of the STM images in its turn is not straightforward as well. First of all, the acquisition time of one scan is of the order of 1 msec or more. Thus the STM image is a time average of the local density of states and possible dynamical processes such as flip-flop motion of atoms are not detectable. Again, STM gives information of the local density of states and the actual charge on atom can be only inferred from the calculations or other measurements (such as core level spectroscopy).

The complex images obtained at intermediate temperature showing both hexagonal and honeycomb structures also exhibit contrast reversal when the bias is changed. This complementarity in the imaging is a key feature of the low-temperature STM image ($T<105$ K) (Carpinelli 1996; Carpinelli 1997b). Figure 4.11 reveals more details of the bias dependence of (3×3) structures above 70 K. These STM images taken at $T=120$ K show a region of the surface where both a hexagonal and honeycomb-like structure exist. The filled state image is shown in (a) and the empty state image in (b). The bright atoms in the empty state image are dark in the filled state image and vice versa. We obtain complementary filled and empty state images at all temperatures. The line scan in Fig. 4.11(c) taken at the left part of the images demonstrates that we have two

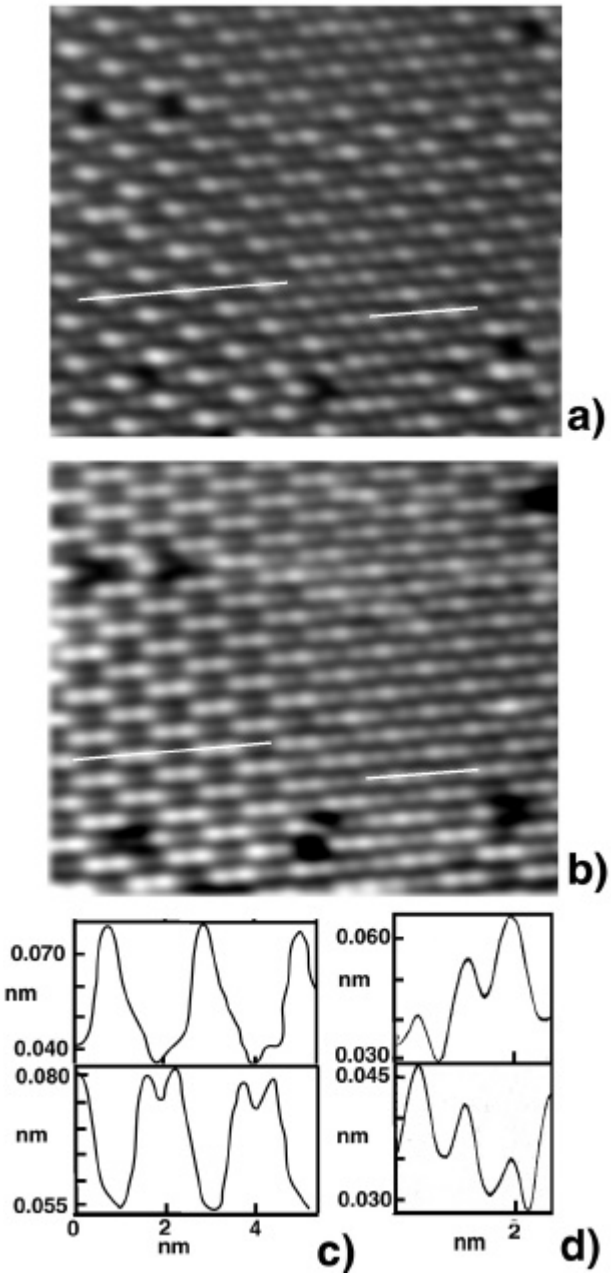

Figure 4.11 Complimentarity of filled and empty state images (180×180 Å^2, I_T=0.13 nA) at T=120K.

(a) Filled state STM image (U_G= -1 V).

(b) Empty state STM image (U_G=+1 V) of the same surface area. A honeycomb pattern is clearly visible in the center portion of this image. The image is fully complimentary to (a).

(c) and (d) Line profiles taken along the lines indicated in the left portion of images (a) and (b).

dark and one bright atom in the (3×3) unit cell in the filled state image (hexagonal) and two bright and one dark in the empty state image (honeycomb). This is the behavior for the low temperature (3×3) first reported at T<60 K by Carpinelli et al. (Carpinelli 1997b). The structure of this configuration is one Sn atom up and two Sn atoms down in a (3×3) cell. The right part of the images in Fig. 4.11, however, includes an example in which all three atoms of a unit cell appear different. This is corroborated by line scans presented in Fig. 11(d), showing that the two images are still complementary. It is reason-able to assume that differences in brightness of the atoms are associated with rearrangement of charge accompanied by a vertical distortion of the Sn atoms. If this assumption is correct, then there are regions of this image (center portion) where the (3×3) structure consists of two atoms up and one atom down. Recent work on structure determination of (3×3) phase using XRD showed this type of structure (two up and one down).(Avila) We have obtained many STM images similar to Fig. 4.11 for temperatures ranging from 120 K to 200 K. Surfaces such as shown in Fig. 11 undoubtedly give rise to strong diffraction spots with (3×3) symmetry. However, different regions of the surface will contribute different diffraction intensities due to the variations in the arrangement of atoms within (3×3) cells, rendering the determination of unit-cell structures ambiguous.

4.4. Motion and correlation of defects at low temperature

Ge defects rule the nature of the $(\sqrt{3} \times \sqrt{3}) \rightarrow (3\times3)$ phase transition in this system. They pin damped density wave distortions at temperatures below room temperature, interact with these waves, and align themselves onto the favorable charge minimum honeycomb

sublattice at low temperature. One remaining question to be answered is at what temperature they move. Two arguments can be presented that lead to different pictures of this process. The first picture is based on the premise that the divergence of the decay length l(T) is the critical parameter. In this model, independent of the defect concentration, there is a phase transition at ≈70 K that forces some of the Ge defects to move into favorable lattice sites on the honeycomb sublattice. The second picture is based upon the density of defects and the defect-defect density-wave-mediated interactions. In this picture, the phase transition happens when the interaction energy between the defects exceeds the activation energy to move the Ge defects. This length scale is represented by l_{av} shown in Fig. 4.6 and is approximately equal to 40 Å for this system. At a temperature where $l(T) \approx l_{av}$, the complex density waves mediate a defect-defect interaction.

To answer the question about the temperature at which Ge defects are aligned, a statistical analysis of STM images at various temperatures was performed.

Statistical Analysis of defect distributions

Our method of counting defects is illustrated in Fig. 4.12. Figure 4.12a shows a ball model of the $(\sqrt{3}\times\sqrt{3})R30°$ lattice. The white circles correspond to Sn atoms. About 10% of the Sn atoms are substituted by point defects (black circles). This model resembles typical STM images that were recorded at room temperature. A unit consisting of $12\times12=144$ atoms, which will be referred to as sampling area (SA), is highlighted in Fig. 4.12a. This particular SA contains seven defects. From each STM image of a series of 15 images ($N_I=15$) recorded at a temperature T, 25 SA's ($N_S=25$) were *randomly* selected and analyzed. The size of an SA (length of an edge: ≈80 Å) is slightly smaller

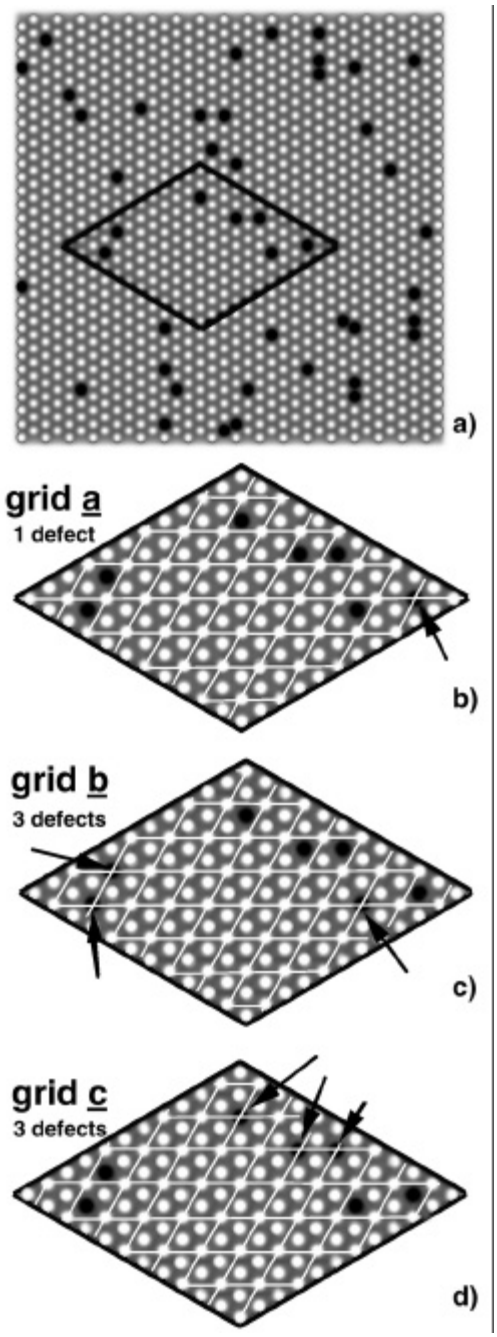

Figure 4.12 Sampling defect distribution

a) Ball model of a (3×3) surface with randomly distributed Ge defects. Open and black circles represent Sn atoms and Ge defects, respectively. A sampling area consisting of 12×12 atoms is highlighted (see text).

b)-d) Enlarged drawing of the sampling area showing in a). Three different possibilities to overlay a (3×3) grid on a ($(\sqrt{3}\times\sqrt{3})R30°$ structure (grids a, b, and c) are shown. Black arrows indicated defects that coincide with the (3×3) grid.

than the typical size of a (3×3) domain at low temperatures (diameter: $d_{3\times3} \approx 100$ Å). The steps of the analysis are demonstrated in Figs. 4.12b– 4.12d. In Fig. 4.12b, a hexagonal grid *a* (cf. Sec. 4.2 of Chapter 4) is laid over the SA. Only one of seven defects (marked by an arrow in Fig. 4.12b) coincides with sublattice *a*. The two other possibilities to overlay a (3×3) grid on a (√3×√3)*R*30° lattice, grids *b* and *c*, are illustrated in Figs. 4.12c and 4.12d, respectively. In either case, three defects (again marked by arrows) coincide with grids *b* and *c*, respectively. According to the observations presented in Sec. 4.2, the system prefers (3×3) domains with minimal amounts of Ge defects on charge maxima sites. Therefore, it is reasonable to assume that a (3×3) domain ''A'' (cf. Sec. 4.2) is formed in the SA of Fig. 4.12 because only one of seven defects (Fig. 4.12a) would coincide with a charge-density maximum. Thus, the fraction n_{il} of defects that would occupy charge maxima site of the *i*th SA taken from the *l*th image is

$$n_{il} = \frac{\min(N_a^{il}, N_b^{il}, N_c^{il})}{N_a^{il} + N_b^{il} + N_c^{il}}, \qquad i = 1,...,N_S, \quad l = 1,...,N_I \tag{4.4.1}$$

where $N_a^{il}, N_b^{il}, N_c^{il}$ are the numbers of defects coinciding with sublattices *a*, *b*, and *c*, respectively. For the SA shown in Fig. 4.12, we obtain $N_a^{il} = 1$, $N_b^{il} = N_c^{il} = 3$, and $n_{il} = 1/7 \approx 0.14$. It follows immediately from Eq. 4.4.1 that $0 \le n_{il} \le 0.\overline{3}\,\overline{3}$ for all *i* and *l*. The fractions n_{il} were calculated for each SA. Then, each SA was counted in one out of six bins labeled *j*, $j = 1,...,6$. Each bin represents a range of the width $0.\overline{3}\,\overline{3}/6 \approx 0.055$ of n_{il} values, i.e., the bin $j = 1$ covers all SA's with $0 \le n_{il} \le 0.055$, bin $j = 2$ covers all SA's with $0.055 \le n_{il} < 0.11$ and so on. The SA shown in Fig. 4.12 ($n_{il} \approx 0.14$)

contributes to bin $j=3$. Generally, the contribution p_j^{il} of the *i*th SA selected from image *l* to bin *j* can be written in the form

$$p_j^{il} = \begin{cases} 1 \text{ if } \dfrac{j-1}{6} \le 3n_{il} < \dfrac{j}{6} \\ \\ \qquad\qquad j = 1,...,6 \\ \\ 0 \text{ otherwise} \end{cases} \qquad (4.4.2)$$

Finally, the fraction *P(j)* of SA's in bin *j* is determined by summarizing over all p_j^{il},

$$P(j) = \frac{1}{N_I N_S} \sum_{i,l} p_j^{il} \qquad (4.4.3)$$

Note that $\sum_j P(j) = 1$. The case $j=1$ deserves particular attention since in SA's that contribute to bin $j=1$, the number of defects on one sublattice, is practically zero (i.e., the defects occupy two out of three sublattices). This corresponds to the alignment of defects found in (3×3) domains at $T \le 100K$ (Sec. 4.2). Therefore, $P(j=1)$ is called **correlation probability** P_C, $P_C = P(1)$.

The results of the analysis of STM images recorded at T=295 K and T=55 K, as well as computer-simulated images are compiled in Fig. 4.13. Computer-simulated images of different defect distributions (e.g., random on all three sublattices a, b, and c, or random on only two sublattices) were generated and analyzed to assist with the interpretation of the distributions *P(j)* determined from experimental STM images.

About 50% of the selected SA's from STM images at T=55 K contribute to bin $j=1$ as illustrated in Fig. 4.13a. This is in agreement with the observation that Ge defects in images recorded at T=55 K are located on the honeycomb sublattice formed by

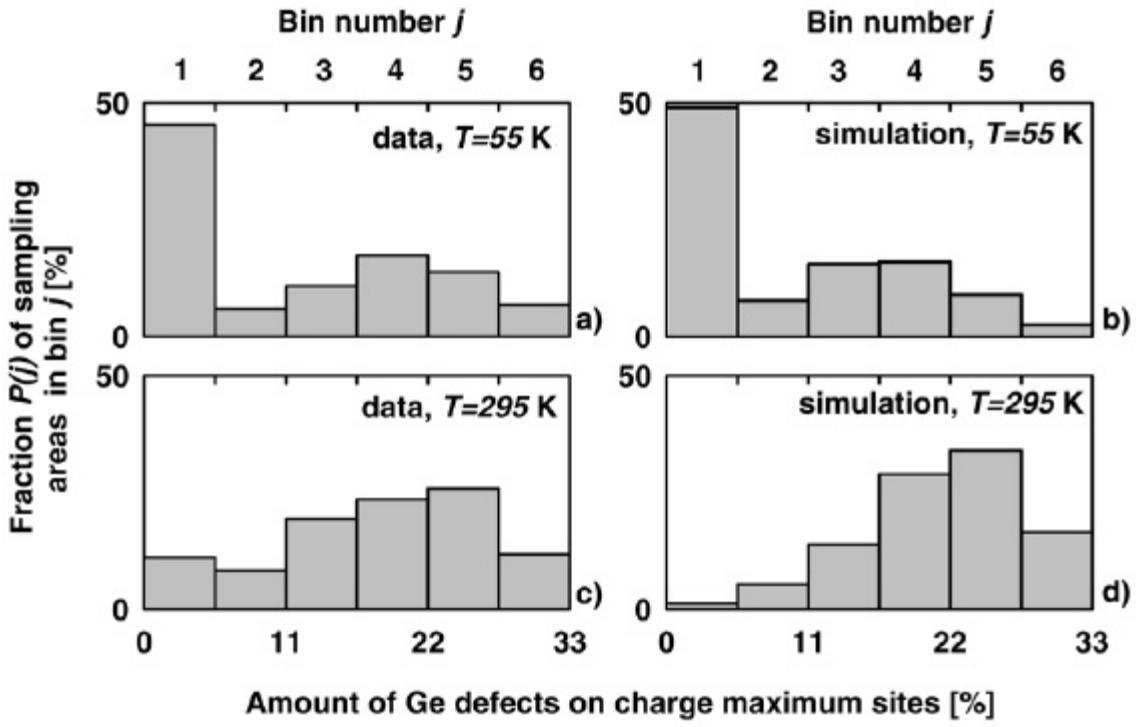

Figure 4.13 Probability of finding a certain amount of defects on (3×3) charge maximum sites deduced from a statistical analysis of STM images (see text)

a) Results for STM images recorded at T=55K (LT).
b) Distribution for a computer generated defect distribution which takes the existence of domain boundaries in the (3×3) phase into account.
c) Analysis of STM images recorded at T=295K (RT).
d) Results for computer generated images with a random defect distribution.

two out of three (3×3) sublattices. The small but not negligible fractions of SA's in bins $j > 1$ in Fig. 4.13a are due to situations where the SA lies in two (3×3) domains, for example, types A and B. Such cases are not unlikely as the size of the SA is only slightly smaller than the average domain diameter. To confirm these conclusions, a statistical analysis (Eqs. 4.4.1-4.4.3) of 15 computer-simulated low-temperature images was carried out. The simulated images were constructed from a (√3×√3)*R*30° lattice similar to the one shown in Fig. 4.12a. Each lattice was randomly divided in three or four domains. Each domain resembled a perfect (3×3) domain A, B, or C, as defects were randomly distributed only on two randomly chosen sublattices. The results of the analysis of simulated images are presented in Fig. 4.13b and are in good agreement with the results in Fig. 4.13a.

The analysis yields $P(j = 1) = 1$ and $P(j > 1) = 0$, if the existence of several domains in each simulated image is ignored and all defects are randomly distributed on only two sublattices (e.g., a and b).

A significantly different distribution P(j) is obtained if STM images are recorded at T=295 K. These are analyzed following the procedure described above. Figure 4.13c illustrates that in this case only 10% of the SA's belong to bin $(j = 1)$. To prove that Fig. 4.13c indeed reflects a random distribution of defects, 15 computer-simulated images with random defect distribution (cf. Fig. 4.12a) were analyzed. The results are shown in Fig. 4.13d and in fair agreement with Fig. 4.13c. Hence, the statistical analysis clearly proves that Ge defects are randomly distributed at room temperature and above 105 K.

The procedure and the definition of the correlation probability P_C are given above. The results are plotted in Fig. 4.14. Essentially, P_C is the probability to find an area of a given size with all defects located on two out of three sublattices. The filled circles in Fig. 4.14 represent the results of the analysis of the data recorded during a cooling cycle. The sample was prepared, the $(\sqrt{3} \times \sqrt{3})$ confirmed, and then the sample was cooled to the temperature T. The STM images were randomly sampled with a sampling area (SA), which was taken slightly smaller (80×80 $Å^2$) than the average size of the (3×3) domains at low temperature. The number of Ge defects on all three sublattices was recorded. P_C=0% if the Ge defects equally populated all three sublattices (a, b, and c); P_C=100% if all defects are distributed only on two sublattices, equally populating each of them. Because of the finite size of the images and existence of domain boundaries at low temperature, a statistical analysis of well-defined computer generated distributions was performed to facilitate the interpretation of experimental data. A statistical analysis of a computer generated random distribution of Ge defects on all three sublattices a, b, and c gives P_C =10%, compared to P_C ≈50% for computer generated distributions where the area was divided into sections (‘‘domains’’) with defects perfectly aligned on the honeycomb sublattice in that section (i.e., the defects are placed only on a and b inside section 1, and only on c and b in section 2, and so on). The correlation probability for the ‘‘aligned’’ distribution is P_C≈50%, P_C not 100% because the SA straddles the ‘‘domain’’ boundaries in the random sampling procedure. The result of the statistical analysis of experimental STM images obtained at different temperatures is shown in Fig. 4.12. It shows that the defects are randomly distributed for temperatures T >150 K. In stark contrast, the correlation probability is ≈50% for images taken at 50 K and 105 K.

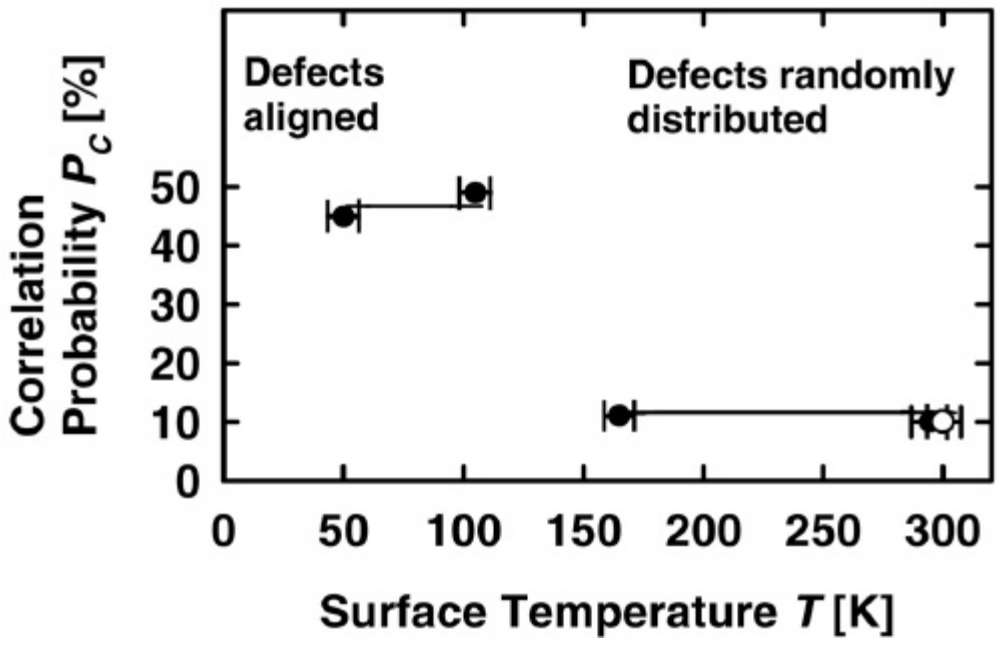

Figure 4.14 Temperature dependence of the correlation probability P_C (see text). Data points marked by filled circles were determined using the analysis described in the Appendix B after cooling the sample to temperature T. The open circle at T=300 K corresponds to an experiment where the sample was cooled to T=30 K and subsequently warmed up to room temperature.

Evidently, Ge defects align themselves at 105 K, a temperature above the projected transition temperature of 70 K based on a diverging decay length. Sufficient data have not been recorded at 120 K to perform the statistical analysis.Therefore, the transition temperature for this defect density is somewhere between 105 K and 120 K. The following experiment was conducted to investigate the reversibility of the $(\sqrt{3} \times \sqrt{3}) \rightarrow (3\times3)$ phase transition. After preparing a good $(\sqrt{3} \times \sqrt{3})$ structure, the sample was cooled to 40 K and held there for two hours producing the (3×3) domain structure described in Section 4.2. Subsequently, the sample was warmed up to room temperature, and a statistical analysis of the Ge-defect distribution was performed. Defects were distributed randomly on all three sublattices (open circle data point in Fig. 4.14). The phase transition is completely reversible.

Our picture implies a long-range density-wave-mediated interaction between defects. The consequence of this interaction has been directly observed in several STM images. Figure 4.15 shows two empty state STM images of the same area taken at T≈120 K, illustrating the effects caused by a change in the defect distribution. In panel (a) of Fig. 4.15 two different (3×3) regions are marked by black and white grids (sublattices). Since these are empty state images, the low-temperature (3×3) structure is now represented by a bright honeycomb sublattice. The image in panel (b) is from the same area, taken one minute later. Comparison of these images reveals a dramatic change in surface morphology associated with the appearance of a vacancy in Fig. 4.15(b) (denoted by a white arrow). As a consequence, another (3×3) reconstructed region shows up in the upper right part of Fig. 4.15(b) (white grid) while the other (3×3) region (black grid) is apparently pushed away from the vacancy. The circled protrusion is interpreted as the

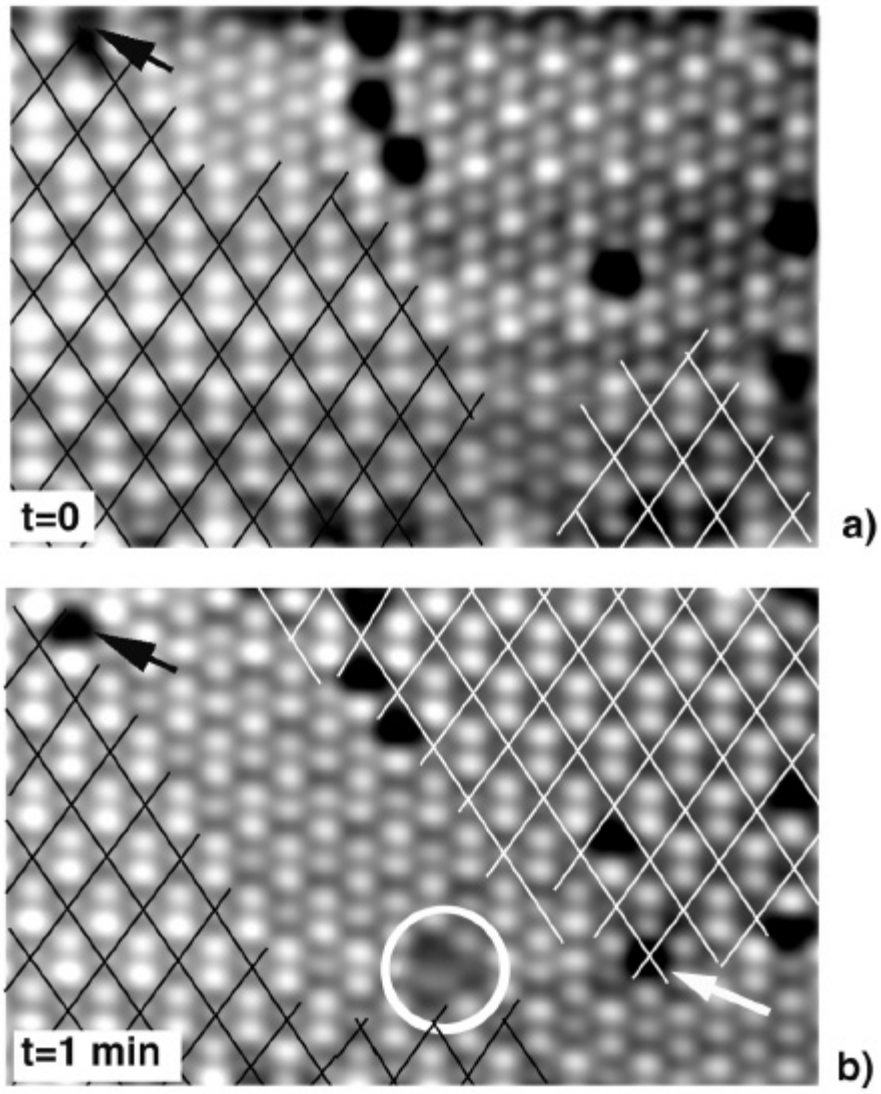

Figure 4.15 Empty state STM images at T=100 K (140×90 Å^2, U_G=1 V, I_T=0.1 nA) recorded 1 min apart.

Two different (3x3) regions (honeycomb pattern) are marked by black and white grids.

(a) The black arrow indicates a Ge defect.

(b) A new vacancy (see text) is labeled by a white arrow. Note the dramatic change in the (3x3) regions as a response to the appearance of the vacancy. The white circle marks the Sn atom, which has been removed from its original site. The Ge defect labeled by a black arrow has moved downwards by one lattice spacing.

image of the Sn atom, which was kicked out when the vacancy was formed. It has moved about 35 Å. Also the motion of a single Ge defect to an adjacent site can be seen in the upper left-hand corner (black arrow) of both panels. It is difficult to determine what created the vacancy, either thermal fluctuations or the tip, but these observations illustrate the effective long-range interaction between the density waves and the defects. Notice also that Fig. 4.15(a) again shows the coexistence of honeycomb, hexagonal, and $(\sqrt{3} \times \sqrt{3})$ patches. In summary we find that defect-defect density-wave-mediated interactions drive the phase transition to the (3×3) low-temperature structure. When a single defect moves under the influence of this force, it causes a domino effect, moving (aligning) other defects. The length scale of the defect-defect density-wave-mediated interaction dictates the domain size.

4.5. Summary and conclusions

The results presented in the paper show conclusively that the defect-defect density-wave-mediated interaction drives the $(\sqrt{3} \times \sqrt{3}) \rightarrow (3\times3)$ phase transition in α-Sn/Ge(111) system. When the temperature-dependent decay length l(T) becomes comparable to the average defect-defect spacing l_{av}=45 Å, Ge defects start to interact and realign onto the honeycomb sublattice.

The realignment of Ge defects locks in the (3×3) phase; l_{av}=45 Å dictates the domain size induced by density wave pattern. With the Ge-defect density present on this surface, the transition temperature is 105 K $\leq T_c \leq$120 K. This observation raises many interesting speculations and questions.

(i) What are the kinetics and energetics associated with defect motion and domain-wall formation?

(ii) What would happen if we could create a surface with only one Ge defect inside of a $(\sqrt{3} \times \sqrt{3})$ domain? There would be a transition to a honeycomb (3×3) sublattice (filled state image) at 70 K (Fig. 4.6). This (3×3) structure would be two Sn atoms up and one down. Likewise, if we could create only one vacancy in a $(\sqrt{3} \times \sqrt{3})$ domain, there would b e a transition to a hexagonal (3×3) structure at 70 K. This (3×3) structure would be one Sn atom up and two down.

(iii) Would there be a phase transition from $(\sqrt{3} \times \sqrt{3}) \rightarrow$(3×3) if the surface were defect free? If so, would the stable structure be hexagonal or honeycomb?

(iv) The data and interpretations suggest that if the defect density could be controlled then both the transition temperature 105 K$\leq T_C \leq$120 K and domain sizes could be tuned. If the defect density is decreased the transition temperature would decrease and the domain size increase.

References for Part 4

Avila, J., Mascaraque A., Le Lay G., Michel E. G., Gothelid M., Ascolani H., Alvarez J., Ferrer S. and Asensio M. C. "Order-disorder transition driven by dynamical effects between the Sn/Ge(111)-(3x3) and (root3xroot3)R30 phases." to be published.

Carpinelli, J. M. (1997a). Charge-Ordering Transition in Ultrathin Metal Films. Department of Physics, University of Pennsylvania.

Carpinelli, J. M., Weitering H. H., Barkowiak M., Stumpf R. and Plummer E. W. (1997b). "Surface charge ordering transition: alpha phase of Sn/Ge(111)." Physical Review Letters **79**(15): 2859-2862.

Carpinelli, J. M., Weitering H. H. and Plummer E. W. (1998). "Charge rearrangement in the GexPb1-x/Ge(111) interface." Surface Science **401**(3): L457-L463.

Carpinelli, J. M., Weitering H. H., Plummer E. W. and Stumpf R. (1996). "Direct observation of a surface charge density wave." Nature **381**: 398.

Gothelid, M., Bjorkqvist M., Grehk T. M., Lelay G. and Karlsson U. O. (1995). "Metal-Semiconductor Fluctuation in the Sn Adatoms in the Si(111)-Sn and Ge(111)-Sn (Root-3x-Root-3)R30-Degrees Reconstructions." Physical Review B-Condensed Matter **52**(20): 14352-14355.

Gothelid, M., Hammar M., Tornevik C., Karlsson U. O., Nilsson N. G. and Flodstrom S. A. (1992). "Sn-Induced Surface Reconstructions on the Ge(111) Surface Studied with Scanning Tunneling Microscopy." Surface Science **271**(3): L357-L361.

Kidd, T. E., Miller T. and Chiang T. C. (1999). “Core level analysis of the surface charge density wave transition in Sn/Ge(111).” Physical Review Letters **83**(14): 2789-2792.

Mascaraque, A., Avila J., Alvarez J., Asensio M. C., Ferrer S. and Michel E. G. (1999). “Nature of the low-temperature 3 x 3 surface phase of Pb/Ge(111).” Physical Review Letters **82**(12): 2524-2527.

Seehofer, L., Falkenberg G. and Johnson R. L. (1993). “Stm Study of the Structure and Phases of Pb on Ge(111).” Surface Science **290**(1-2): 15-25.

Stumpf, R. R., Carpinelli J. M. and Weitering H. H. (1999). “Apparent charge transfer at the GexPb1-x/Ge(111) interface.” Physical Review B-Condensed Matter **59**(24): 15779-15783.

Tornevik, C., Gothelid M., Hammar M., Karlsson U. O., Nilsson N. G., Flodstrom S. A., Wigren C. and Ostling M. (1994). “Adsorption of Sn on Si(111)7x7 - Reconstructions in the Monolayer Regime.” Surface Science **314**(2): 179-187.

Weitering, H. H., Carpinelli J. M., Melechko A. P., Zhang J. D., Bartkowiak M. and Plummer E. W. (1999). “Defect-mediated condensation of a charge density wave.” Science **285**(5436): 2107-2110.

Zhang, J. D., Ismail, Rous P. J., Baddorf A. P. and Plummer E. W. (1999). “Periodic lattice distortion accompanying the charge-density- wave transition for Sn/Ge(111).” Physical Review B-Condensed Matter **60**(4): 2860-2863.

Part 5

Models of CDW transition

in a 2D system

with defects

The symmetry lowering transition observed in α-phase of Sn/Ge(111) is a complex phenomenon that is comprised of two intertwined phase transitions. One is Charge Density Wave phase transition and the other is disorder-order phase transition in the defect distribution, which accompanies CDW transitions and is caused by the CDW-mediated interaction of mobile defects. To understand and illustrate both of them I have introduced two theoretical models of the evolution of these transitions with temperature.

The CDW transition can be described by a Charge Compensation Model. The framework of this model is based on the assumption that the electronic response of the system is such that charges on the nearest neighbors of a charged lattice node try to 'compensate' or screen it. This screening is temperature dependent and at certain temperature "overscreening" (Ashcroft 1976) leads to the formation of a Charge Density Wave state. Computer simulations based on this model can nicely reproduce experimental STM images of Sn/Ge(111) at all temperatures. The same calculations are done for a model system whose free energy is written as a certain function of order parameter, where the role of the order parameter is played by a charge on an atomic site. This dependence of free energy on the order parameters describes a classical second-order phase transitions in Landau theory. These two observations brings us to conclusion that CDW transition in Sn/Ge(111) is a CDW transition and it is of the second order. This is the first determination of the order of this phase transition.

The second phase transition that accompanies the CDW transition is of the first order order-disorder phase transition in the defect distribution. Defects create local CDW and they interact with each other via these local CDW. The range of the defect-induced CDWs grows when the temperature approaches CDW transition temperature. When it

reaches a certain value the interaction between defects acquires a collective character and they order.

5.1. Theoretical model of disorder-order phase transition in the defect distribution

The basic assumptions of this models comes from the experimental observations (presented in Part 4):

1. Defects induce local CDW. The range of defect-induced CDW is temperature dependent.
2. Defects interact with CDW: It is energetically favorable for a Ge defect to be located in the charge density minimum.
3. Ge defects are mobile and can exchange position with a nearest neighbor Sn if forced by the CDW. The force is proportional to the difference in charge density.
4. There is a finite threshold energy barrier that has to be overcome for defect to exchange its position with nearest neighbor Sn atom.

Defect-induced local CDW

I assume that one Ge defect creates a perturbation in a form of waves decaying with distance, with 3x3 symmetry and with a phase of these waves such that filled state STM image appears as a honeycomb pattern. The whole STM image is a result of the superposition of such waves from each defect. It was described in Part 4 in detail. Here I just repeat the equation:

$$I(\vec{r}) = f_{\sqrt{3}\times\sqrt{3}}(\vec{r}) + \sum_{n=1}^{N_{def}} \left(A \cdot e^{-(\frac{|\vec{r}-\vec{r}_n|}{l(T)}} \times (\sum_{i}^{3} \cos(\vec{k}_i \cdot (\vec{r}-\vec{r}_n) + f)) \right) \quad (5.1.1)$$

Here I(r) is the brightness of the STM image. For a given decay length, l(T) and random defect distribution at a given density, e.g. 5%, the result will look like the image displayed in Figure 5.1. We can assume that the brightness of the different atoms is proportional to charge density or vertical atomic displacement z. The black squares indicate the defects.

Defect interact with CDW

An experimental observation is that Ge defects avoid the charge density maxima lattice sites. Thus it is reasonable to assume that if a defect is located on charge density maximum there is a lateral force exerted on it toward minimum.

Threshold barrier

I assume, as an approximation, that the difference in energy for defect to be on one site versus its nearest neighboring site is proportional to the difference of the value of I(r) on these sites.

$$\Delta E \propto I(\vec{r}_{def}) - I(\vec{r}_{NN}) \quad (5.1.2)$$

And if this difference exceed a threshold value H, Ge defect exchanges it's position with neighboring Sn atom (Fig. 5.2). Figure 5.2a illustrates such an event. The defect indicated by an arrow is located on the charge maximum site on the left panel. Even though the nearest neighboring sites are energetically favorable the charge difference is less than the threshold value necessary to overcome the activation barrier. When the charge difference exceeds the threshold value defect exchanges its position with neighboring Sn atom. This

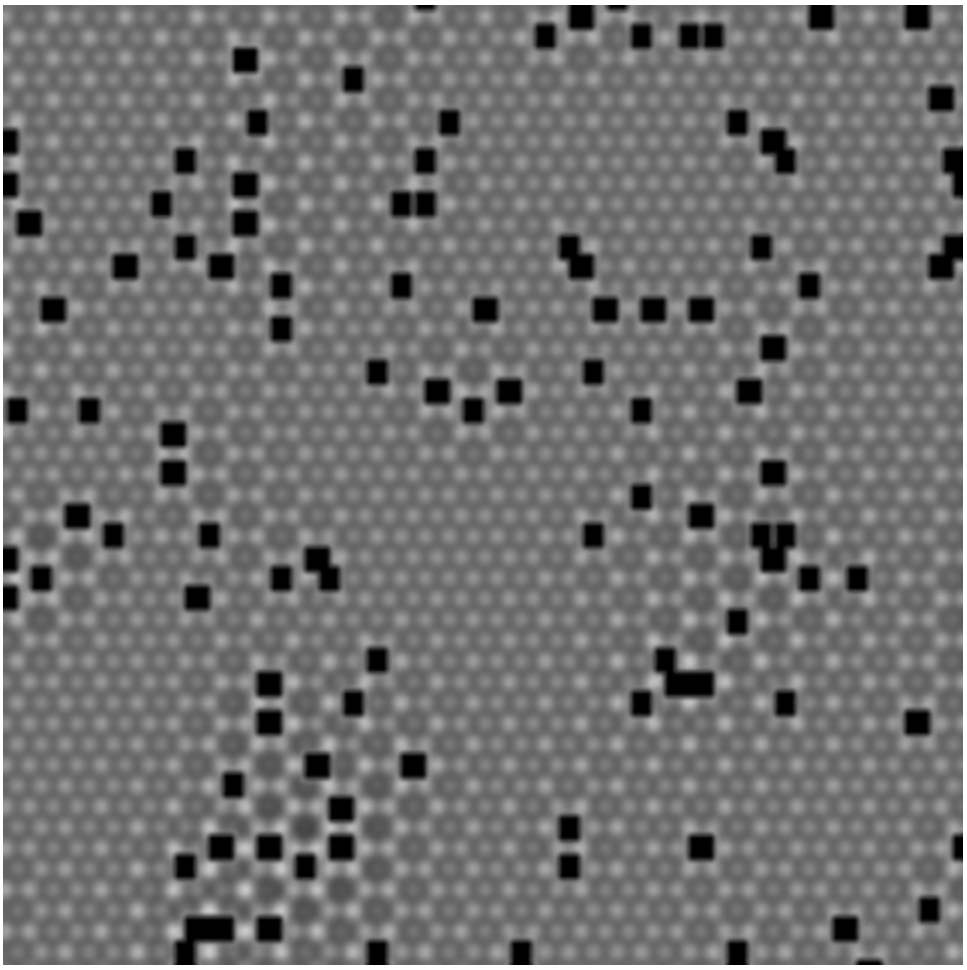

Figure 5.1 Simulated STM image with given defect distribution

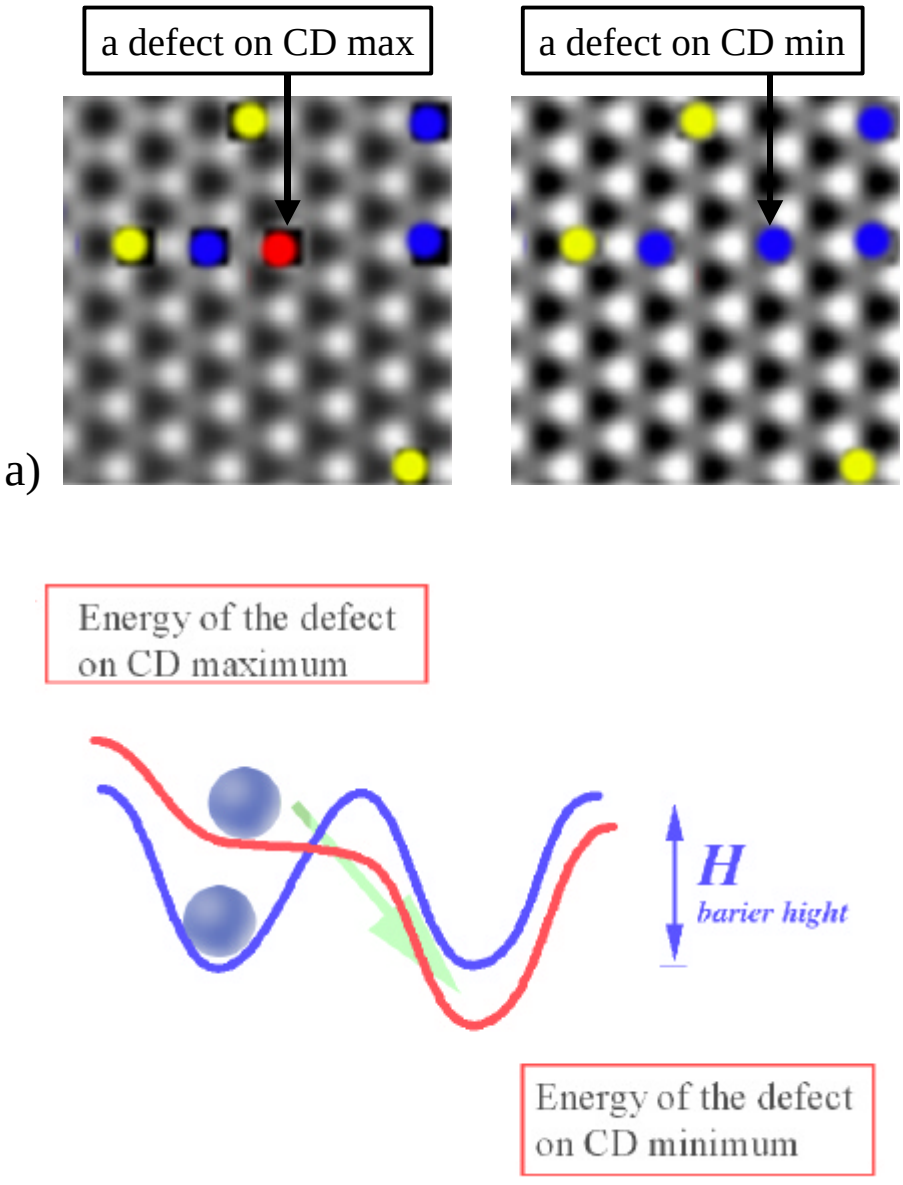

Figure 5.2 Density-wave-induced defect-defect interaction

is shown on the right panel of Fig. 5.2a. In this particular case the difference in charge increased compared to the situation on the left panel due to slight increase in the decay length l(T) so that more defect-induced waves contributed constructively to the interference pattern in the location of this particular defect.

Saturation

One of the drawbacks of using the ansatz is that it is a linear superposition of waves from every defect. If the extent of these waves is very large the amplitude would be proportional to the total number of defects. For example, if we had 500 defects on a surface aligned on one sublattice and the decay length would be close to infinity, the charge on one lattice site would 500 times the intensity of the CDW induced by one defects. It should be more difficult to add more and more charge to one lattice site. (This, unphysical artifact has been completely overcome in the theoretical model introduced in the section 5.2.) There is a simple way to avoid this problem by introducing saturation. After the amplitude I(r) is calculated it is saturated using a nonlinear function Sat(I). Sat(I) is assumed to be a linear function that has a slope equal to one for small values of the argument and approaches constant when the argument increases. An example of such a function is illustrated in the Fig. 5.3. The saturation procedure thus can be expressed by the equation:

$$I(\vec{r}) = Sat(I_{ansatz}(\vec{r})) \qquad (5.1.3)$$

Thus I(r) never exceeds a saturation value I_{sat} used here as a parameter.

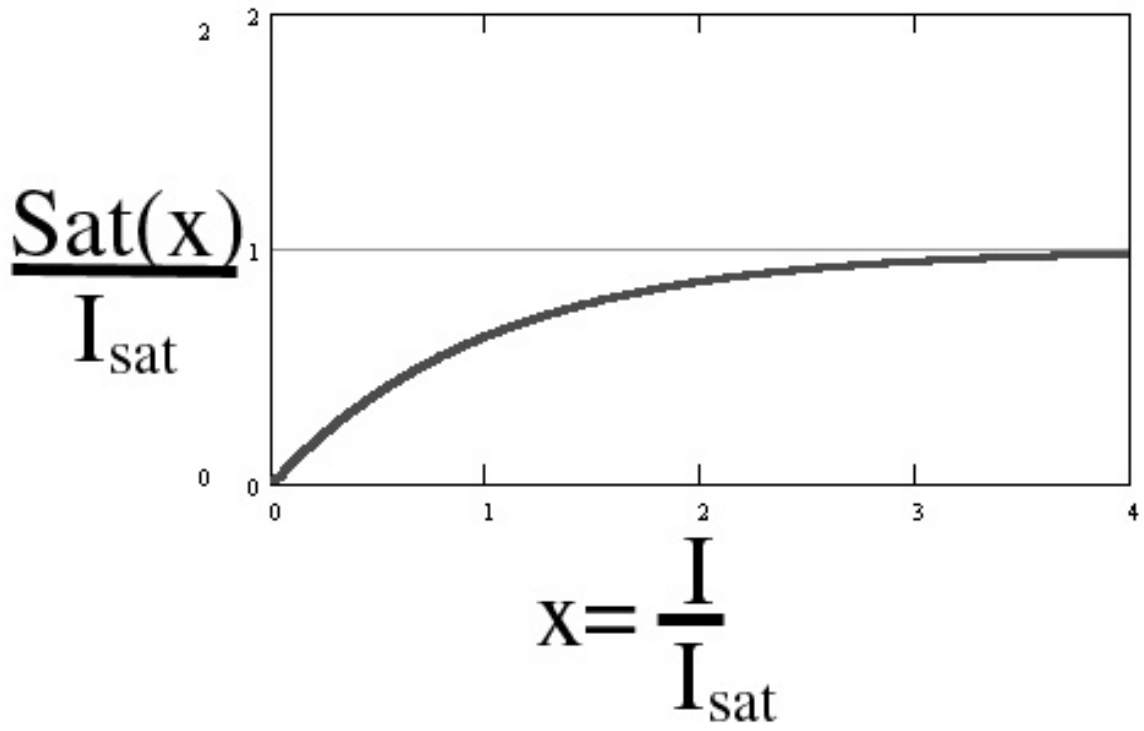

Figure 5.3 Saturation function

Temperature dependence

Temperature enters the problem in two ways:

1) Through temperature dependent decay length l(T).
2) Through random thermal motion of defects. It is reasonable to assume that besides hopping caused by CDW, defects can hope due to finite temperature. The experimental observation indicates that the distribution of defects returns to random when temperature is increased back to RT. Such a restoring force can be simulated by a simple Monte-Carlo procedure, which is described below.

The temperature dependence of the decay length l(T) is simply taken from experimental results for Sn/Ge(111) so that it is growing with lowering temperature and that its reciprocal value is linear with temperature:

$$\frac{1}{l(T)} = A \cdot T + B \qquad (5.1.4)$$

Parameters A and B are taken from the experiment.

Simulation

The predictions of this model were obtained using computer simulations. The following algorithm was used to perform the computations:

1) N defects (defect density as a free parameter) are positioned randomly on the 3x 3 lattice.
2) The intensity parameter I(r) is calculated using ansatz.
3) For each defect I(r) is compared at the defect site with I(r) at a nearest neighbor: If this difference bigger than a threshold value then this defect is moved. (The minimum out of 6NN is chosen, and it is checked that this NN is not a defect too.)

4) If the difference is smaller than a threshold value use Monte-Carlo procedure to decide whether to move or not.

   a) Random number between 0 and 1 is retrieved.

   b) Then this number is compared to the Boltzman factor: $b = e^{-\left[\frac{E}{k \cdot T}\right]}$.

   Where $E=(H-(I_{def}-I_{nn}))$, And $k = \alpha k_B$, is a product of Boltzman constant and a parameter accounting the mobility of defects (attempt frequency).

   c) If this random number is smaller than the Boltzman factor then the defect is moved to the nearest neighbor position.

The temperature is changed and the order in the distribution of defects is measured (P_C, the correlation probability (see Part 4). The number of repeats at each temperature point controls the simulation of the cooling/warming speed. In the simulations this number was varied from 1 to 1000 for each temperature step (usually 1 K). More repeats is used to approach equilibrium at each temperature. To determine the cooling speed that correspond to a particular simulation such parameters as an attempt frequency and activation barrier must be assessed by experimental measurements or by more basic calculations.

This model requires the following input parameters::

1) attempt frequency (mobility of defects)
2) density of defects
3) threshold barrier
4) temperature and decay length

Results

Figure 5.4 displays a result of a simulation with parameters chosen so that it resembles the experimental result of the Part 4. Temperature dependence of the decay length was taken from the experiment. A considerably large number of defects (5% in this case) was assumed to be randomly distributed on an area of (200×200) atoms. Decay length was slowly increased from the RT value simulating cooling process. The temperature step ΔT was 1K and number of repeats was 1 for each temperature. The threshold barrier was chosen slightly below the saturation value H. Correlation probability (see Part 4 and Appendix B for definition), the order parameter of this transition, increases only slightly down to the critical temperature (Fig.5.4a). In this case the interaction of defects is localized leading to short-range order. Figure 5.4b displays a distribution of defects slightly above the transition temperature. Defects located on different (3×3) sublattices (3 possibility) are colored red, blue and yellow. For better visualization when a defect moves from one position to the next nearest neighbor its color changes accordingly. The total number of defects was constant. Equal number of all colors in Fig. 5.4b is an indication of the fact that defects are randomly distributed. When the decay length reaches critical value a “domino effect” suddenly changes the distribution of defect from random to ordered one. Such an effect is a signature of a first order phase transition. In this case all defects located on “red” sublattice move to the “blue” and “yellow” (Fig. 5.4c). The correlation probability at this point becomes equal to one (Fig. 5.4a). It never becomes one in an experiment since a domain structure is formed. This model doesn’t account for domain formation.

a)

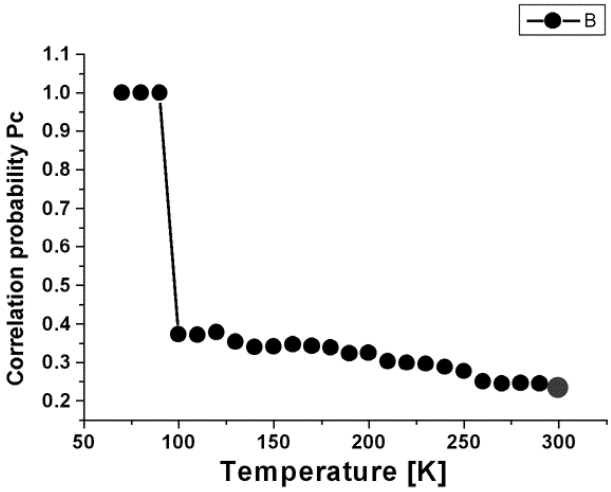

b)

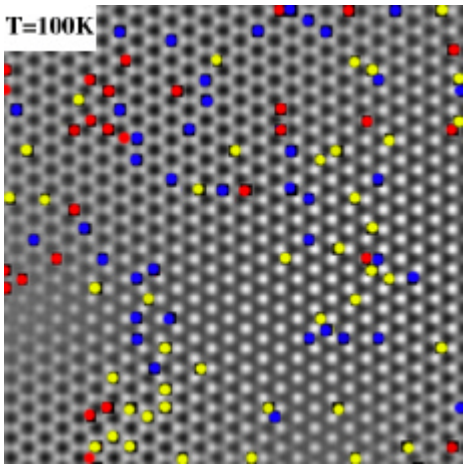

c)

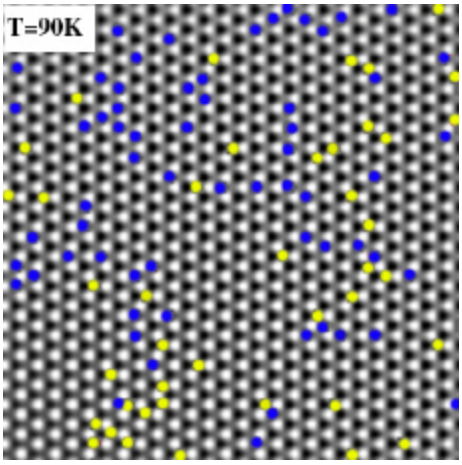

Figure 5.4 Computer-simulated defect ordering phase transition

a) Temperature dependence of correlation probability
b) A simulated STM image slightly above critical temperature
c) A simulated STM image below critical temperature

Full lattice is 200x200 atoms, 2000 defect (5%)

The result presented in the Fig. 5.4 tells us that this simple model presented above describes this order-disorder transition fairly well. I used several free parameters that must be calculated or measured before this model will have any predictive power. One of them is the threshold barrier H, or to be more correct, its ratio to the saturation value of I(r). In the simulation in the Fig. 5.4 H was only slightly smaller than I_{sat}. ($H > I_{sat}$ is not considered since defects would be locked in their position all the time.) If H is much smaller than I_{sat}, then defects align on one sublattice. Apparently, the state of defects ordered on two sublattices is a "metastable", since slow cooling (simulated by increased number of repetitions at each temperature step) will bring to them to alignment on one sublattice.

The driving force for the alignment of defects on one sublattice is in the symmetry of CDW induced by one defect. In this case each defect is producing a honeycomb perturbation and the ideal arrangement would be one honeycomb lattice with defects located in the centers of the honeycomb hexagons.

One trivial consequence of this model but very important to mention is the dependence of the critical temperature on the density of defects. It is illustrated in the Fig. 5.5. When the density of defects is increased the critical temperature is increased too. It is a reflection of the fact that collective interaction of defects begins when the decay length becomes comparable to the average distance between defects. The bigger density means the smaller the average defect-defect distance, and consequently the higher critical temperature is.

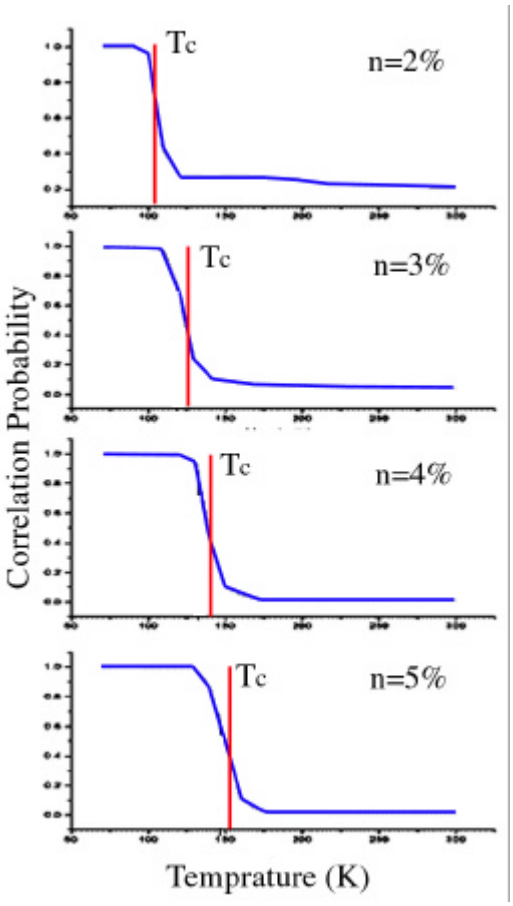

a)

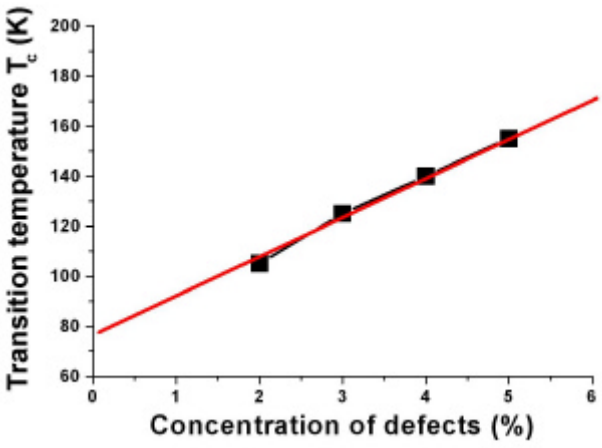

b)

Figure 5.5 Dependence of phase transition temperature on the density of defects

Clustering of defects

The fact that a defect-induced CDW decays (it is non-uniform) with the distance from a defect at temperatures above CDW phase transition temperature results in the attraction between two defects that interact via such CDWs. This phenomenon is illustrated in the Fig. 5.6. In this case a small number of defects was distributed on the lattice. The difference of the simulation presented in Fig. 5.6 from the one in Fig. 5.4 is that there are no defects outside the area shown. It means that there is no force to compensate an overall attraction in this group of defects. The simulation started from the randomly distributed defects and the short decay length (as at RT). Then the decay length is increased and defects are allowed to move around. This leads to their bunching (Figs. 5.6b and c). The shape of the cluster in Fig. 5.6b is dictated by the initial distribution. And finally, their ordering transition happens (Fig. 5.6d). The attractive force should decrease when the decay length increase. If the defects are easy to move in certain temperature range defects are expected to cluster.

5.2. Theoretical model of CDW phase transition

The sharp domain walls that appear at low temperatures couldn't be accounted by a simple model of superposition of defect-induced waves. It is impossible to obtain an interference pattern in which one (3x3) domain suddenly stops and the other one immediately begins by summing a finite number of gradually decaying cosine functions with a fixed periodicity even for ordered defects. Nonlinear effects have to be involved to create such "step-wise" features. To tackle this problem I have developed a model, which

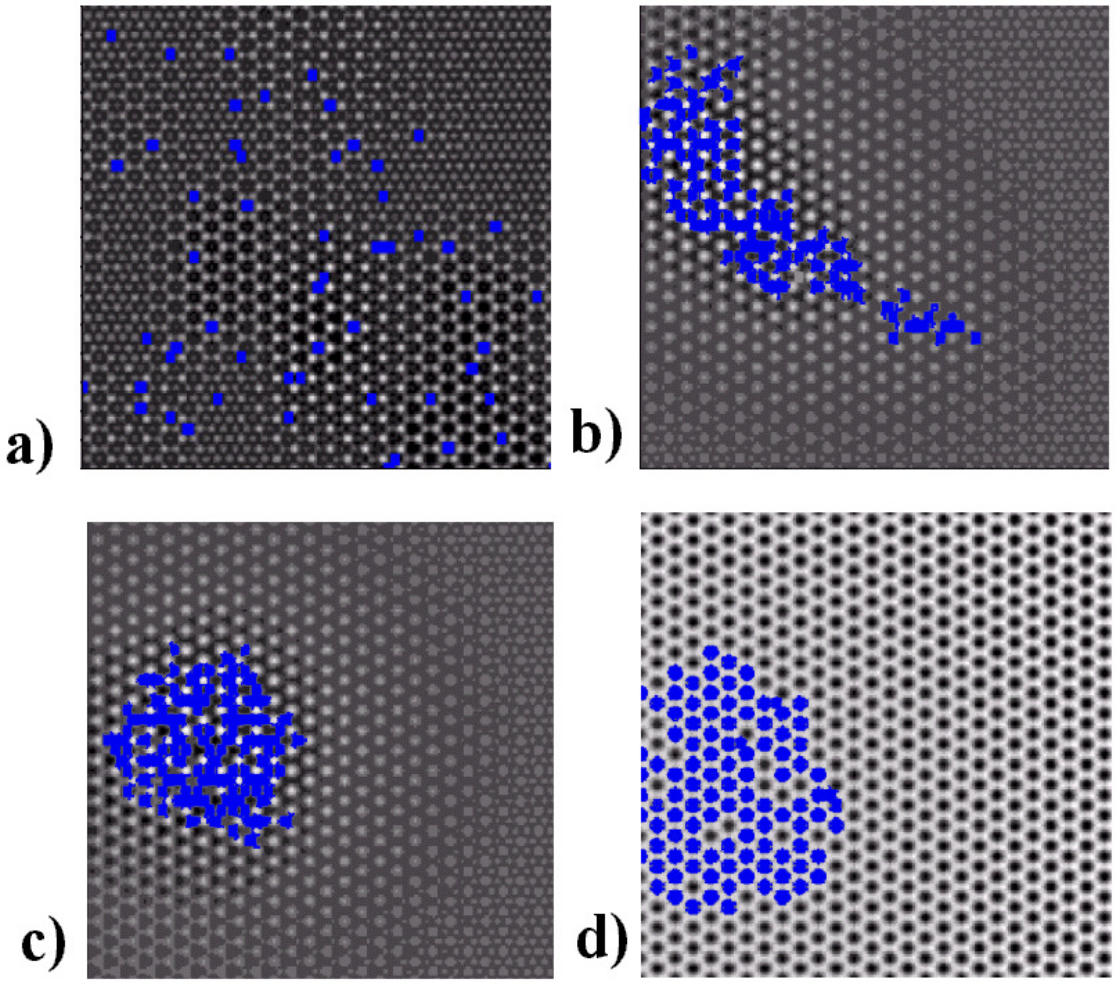

Figure 5.6 Demonstration of the attractive average force between defects.
An attractive interaction between defects leads to bunching of a high-density localized group of defects (blue squares)

I call Charge Compensation Model for the principle it is based upon. To my great surprise what we acquired this way was the theoretical model that describes the CDW phase transition. Now by varying a parameter we can calculate how STM image would look like at any temperature, both above and below the phase transition temperature for a given defect distribution.

Description of the model

Let's assume that a Sn atom on site ***i*** (Fig. 5.7) can take the "charge" q_i in response to "charges" on the nearest neighbors that can be calculated by Equation 5.2.1.

$$q_i = -R(T) \cdot \sum_{j}^{6NN} q_j \qquad (5.2.1)$$

Here R(T) is a "charge compensation factor", the free positive parameter that is monotonous function of temperature. Its temperature dependence will be discussed later. The summation goes over six nearest neighbors shown in the Fig. 5.7. In other words, when a charge is place on one of the atoms its nearest neighbors will try to screen or "compensate" it.

First we create some initial charge distribution, then the charge is calculated on one lattice site as a response to the charges on its nearest neighbors using (5.2.1). Then we proceed to the next atom and make the same calculation for it and so on for all atoms in a lattice. When lattice site is occupied by a defect the charge on it is taken to be constant. Thus defects are treated as a part of boundary conditions. To reach a self-consistent solution this procedure is repeated many times till the solution converges.

The idea for this model appeared from the following considerations. Previously Ge defects were treated as source of waves. Sn atoms are actually very similar

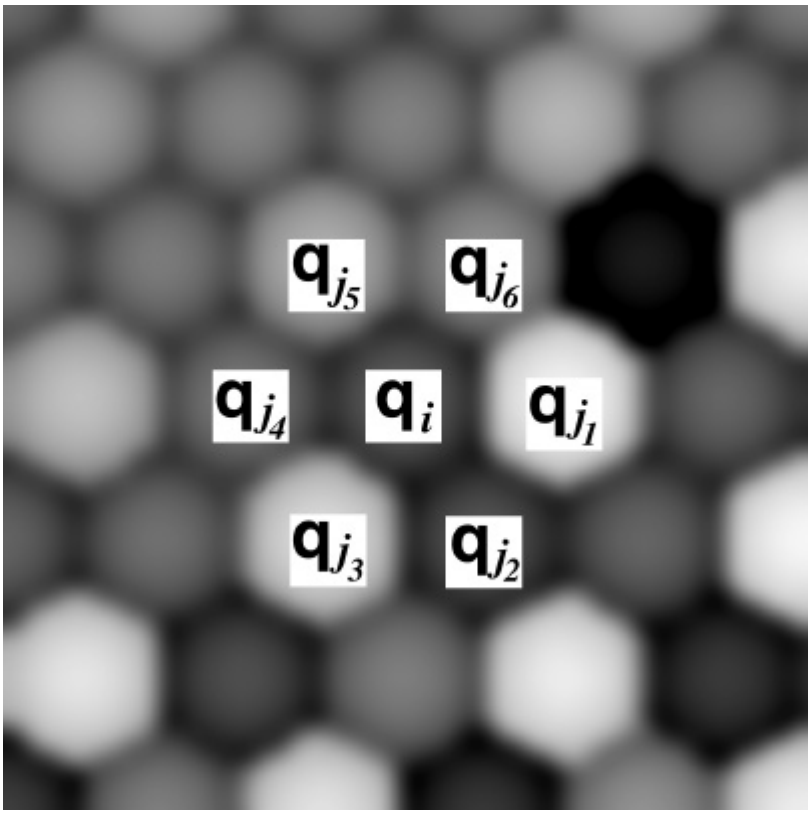

Figure 5.7 Schematics of the Charge Compensation Model calculation
Charge q_i on the site *i* "compensates" the sum of charges of its nearest neighbors. Brightness of balls is proportional to the calculated charge. The black ball in the right top corner is a Ge defect that has a fixed charge (usually –1 in calculations). The rest are Sn atoms with charge calculated self-consistently using Eqs. 5.2.1-5.2.3

to Ge atoms and it would be reasonable to treat them in a similar fashion. In this model Sn atoms are “secondary” sources of CDW. This is very similar to the Huygens principle used to calculate propagation of waves in optics: every point in space is a source of secondary waves.

To make this model more realistic we must include saturation effects. It should be increasingly more and more difficult to add charge to one atom. This in a simplest way can be accounted by adding a saturation term to (5.2.1):

$$q_i = -R(T) \cdot \sum_{j}^{6NN} q_j - s(q_i) \qquad (5.2.2)$$

where s(q) is must be an odd function of q_i. The first nonlinear term in the polynomial that can be used for this purpose is cubic.

$$s(q_i) = a_3 q_i^3 \qquad (5.2.3).$$

Here a_3 is a free parameter that is assumed small and positive. It is admissible to use higher order terms for finer adjustment to fit the experimental results. For our purposes (5.2.3) proved to be sufficient. The atomic sites that correspond Ge defects have a fixed charge.

$$q_{def} = const \qquad (5.2.4)$$

The solutions were obtained numerically by self-consistent iterations. (See the computer code in Appendix C for the details). The charges of the atoms outside the area were chosen to be zero. This is a reasonable approximation since the particular portion of the surface calculated this way was always far from boundaries and was surrounded and

included defects that completely controls the solution inside. As I mentioned before, defects plays a role of distributed boundary conditions.

Figure 5.8a displays the filled state STM image taken at 55 K. It consists of the (3x3) domains separated by sharp domain walls (indicated by lines). Such domain walls are impossible to obtain using a simple superposition model (Eq. 5.1.1). The observation showed that they do not appear at temperatures down to at least 120 K. In the following I show that sharp domain walls are characteristic only for temperatures below transition temperature. Figure 5.8b shows that image calculated using Charge Compensation Model (CCM) looks very similar to the STM image in the Fig. 5.8a. The most notable fact is that the domain walls have the same position and shape as in the real STM image. This image was calculated by taking coordinates of defects from the actual STM image. The value of Charge Compensation Factor R was 0.35. The sharp domain walls appear in the calculated image only if R is greater than the critical value R_c=1/3. The value of R was chosen to be 0.35±0.01 to obtain the best fit to the experimental image.

For the $R<R_c$ the CCM model gives the same results as the ansatz (or superposition model). Thus the STM images at temperatures above T_{c1} (Part 4 figure) can be reproduced. For example the Figure 5.8c shows the filled state image obtained at room temperature. The calculated image in Fig. 5.8d gives a very good fit to it if the coordinates of defects are taken the same and the value of R is equal to 0.30. The equivalence of two models for temperatures higher than T_{c1} can be illustrated by calculation for one defect. When we use ansatz to simulate STM images the perturbation is assumed to be in a form of exponentially damped waves (Fig. 5.9a), in CCM this comes out as a result of the self-consistent calculation (Fig. 5.9b). Figure 5.9c shows the

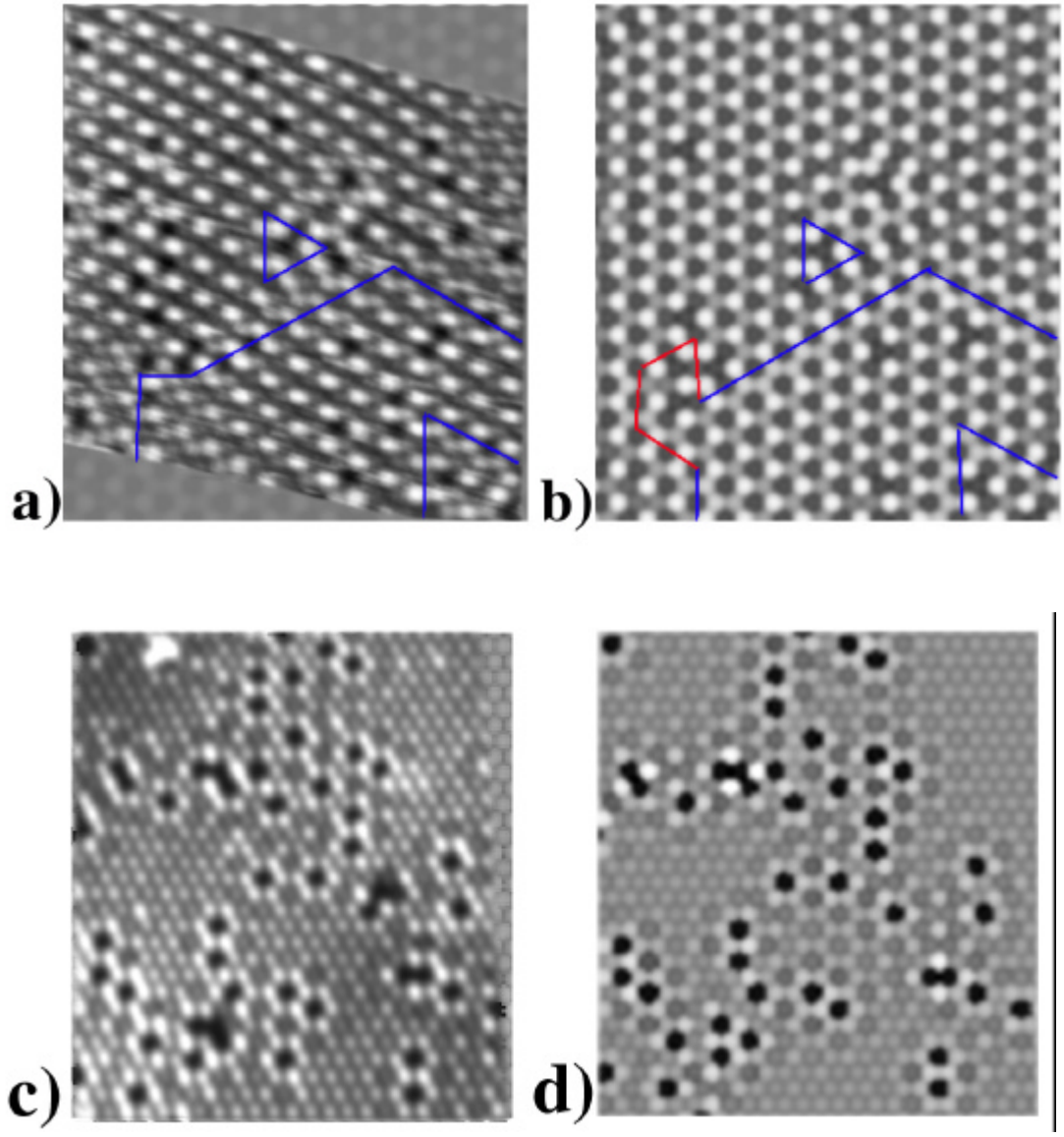

Figure 5.8 Comparison of experimental STM images and the ones calculated using Charge Compensation Model

a) Filled state STM image of Sn/Ge(111) acquired at 55 K. The surface consists of (3×3) domains with sharp domain walls indicated by blue lines. Black spots are Ge defects.
b) An image calculated using Charge Compensaiton model with R=0.35. The positions of defect were taken from the experimental image a). Domain structure is reproduced beautifully.
c) STM image at RT

Calculated STM image with R=0.30

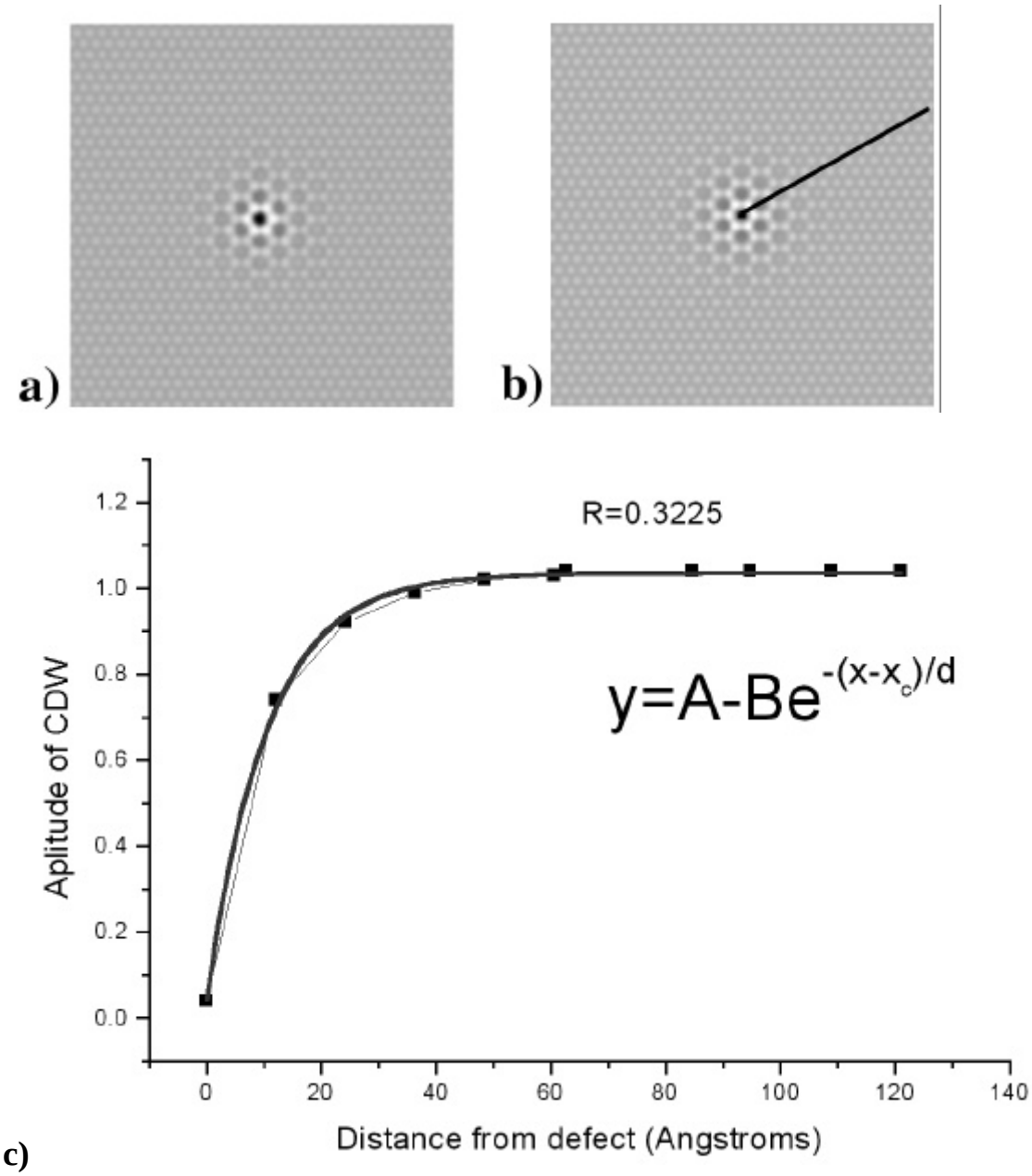

Figure 5.9 Exponentially decaying waves around a defect

a) At STM image is simulated using ansatz (Eq. 5.1)
b) A calculated STM image using Charge Compensation Model that gives exactly the same result
c) An exponential fit of the envelope function of the line profile along the black line in b), demonstrating that CCM does produce exponentially decaying wave as in experiment (Part 4)

fit of the line profile along the direction indicated in the Fig. 5.9b by a black line.

The decay length determined from the calculated images using CCM grows when R approaches 1/3 from below. This is illustrated in the Figure 5.10a. The best fit of this dependence is

$$l = A - \frac{B}{(R_c - R)^a} \qquad (5.2.4)$$

when the exponent *a* is ½and R_c is 1/3. Here d is the decay length. We can compare this dependence with temperature dependence of the decay length that was determined experimentally. It is plotted in the Fig. 5.10b and fitted with

$$l = A + \frac{B}{(T - T_c)^b} \qquad (5.2.5)$$

The exponent b was assumed to be equal to 1. Unfortunately, it is not possible to determine b exactly since the data set is very limited. If we know the value of b we could determine the temperature dependence of R. For example if we assume that b=1. Then

$$R_c - R \sim (T - T_c)^{1/2} \qquad (5.2.6)$$

All we can conclude by now is that R(T) is a monotonous function of temperature.

Ginzburg-Landau theory and Charge Compensation Model

Even though the Charge Compensation Model appeared from intuitive arguments it has a straightforward interpretation in the framework of Ginzburg-Landau theory of phase transitions. In fact, Landau theory had been applied to Charge Density Waves in transition-metal dichalcogenides (McMillan 1975) and later on applied for analysis of

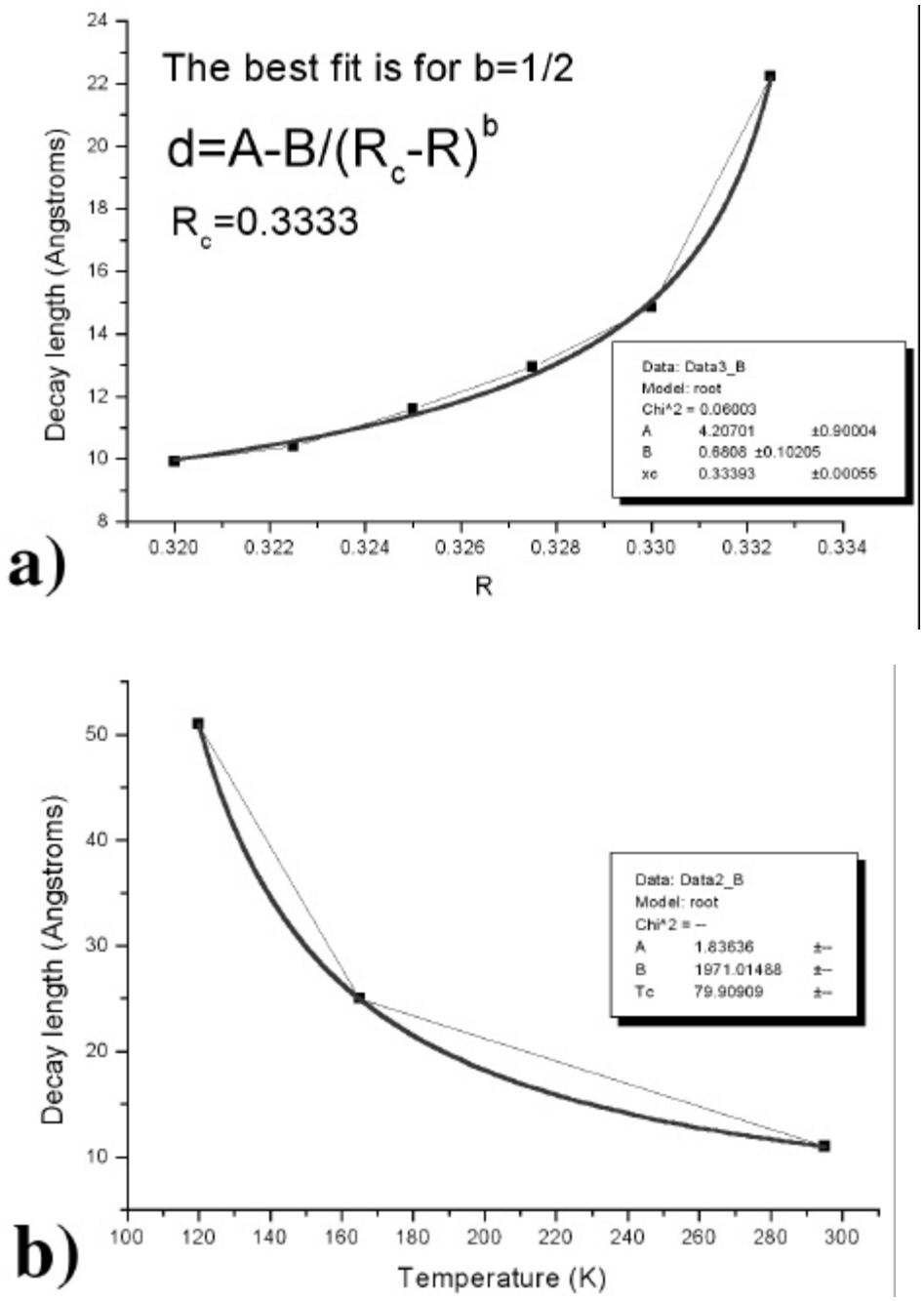

Figure 5.10 The decay length in model and experiment

a) Dependence of the decay length of the defect induced waves on the "charge compensation factor" R. The decay length diverges at R=1/3.

b) Temperature dependence of the experimentally determined decay length (see Part 4). The decay length diverges at 79 K.

STM images of CDW in layered materials. We can proceed by analogy with McMillan's work except all the calculation can be done on the discrete lattice since CDW in Sn/Ge(111) is always commensurate. So we don't have to switch to continuous formulation.

Let's consider a system that has the following free energy dependence on the order parameter $\{q_i\}$:

$$F = \sum_n (q_n^2 + R(T) q_n \sum_{i(NNN)} q_i + a_4 q_n^4) \ , \qquad (5.2.7)$$

where the order parameter q_n is a charge on a lattice site. The first summation goes over all atoms in the lattice. The internal sum runs over six next nearest neighbors to the n-th site. We proceed by solving for the order parameters q_n, which minimize the free energy. This can be done by solving a system of equations:

$$\frac{\partial F}{\partial q_n} = 2q_n + 2R(T) \sum_{i(NNN)} q_i + 4a_4 q_n^3 = 0 \qquad (5.2.8)$$

Essentially, the expressions (3.2) mean that the CCM that we described in the Section II is the minimization procedure for a free energy (3.1).

For a pure system the free energy (3.2.7) for a linear chain (1D) where each atom has two nearest neighbors the solution is very simple: the unit cell doubles and each atom has the same amount of charge but an opposite sign (Fig. 5.11a). For a square lattice the solution is also obvious because we can construct the superlattice in which every atom has a charge of opposite sign to its nearest neighbors (Fig. 5.11b). For a triangular lattice, as in case of a frustrated antiferromagnet such a solution is not possible. Instead as shown in Fig. 5.11c, the free energy (5.2.7) has a minimum when the system has three different

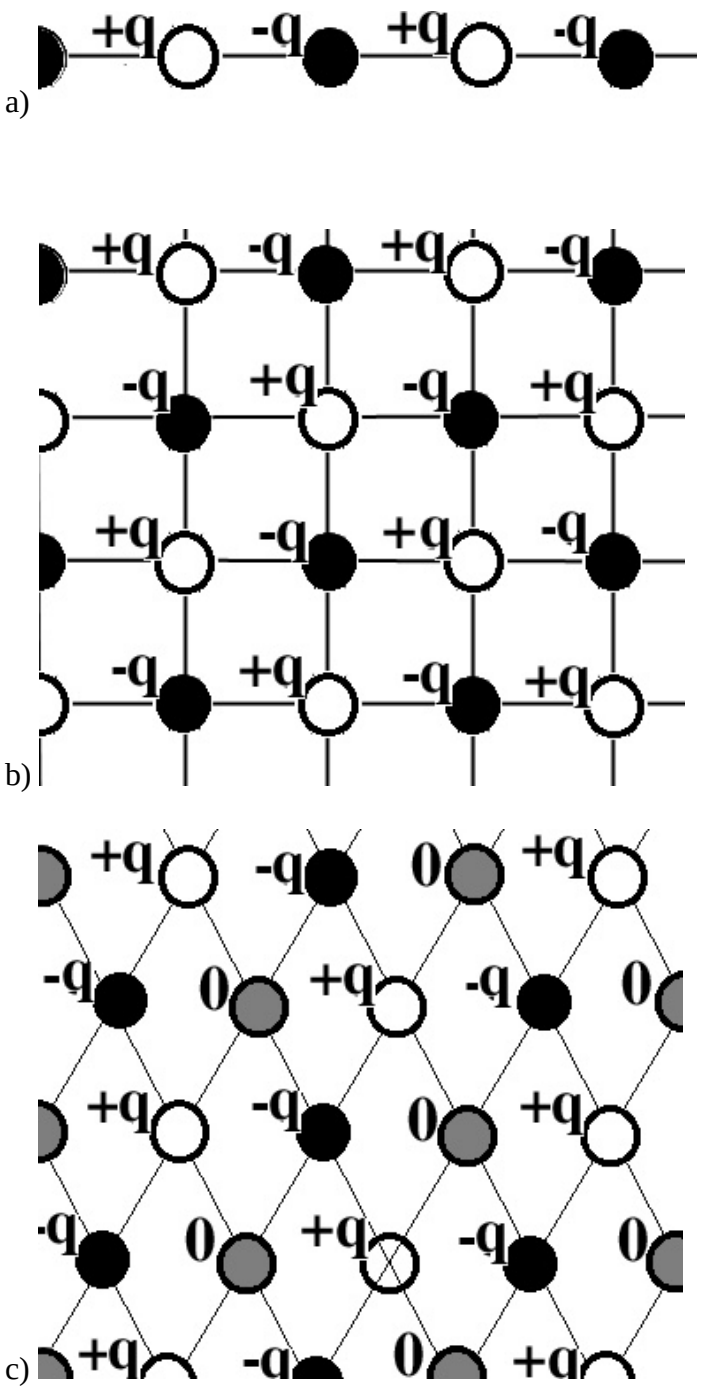

Figure 5.11 The lowest free energy solution for R>1/3 for infinite pure systems

a) linear chain
b) square lattice
c) triangular lattice

lattice sites ((3×3) periodicity in Sn/Ge(111)) with the charges of the atoms inside one (3×3) unit cell are q, 0, and –q, correspondingly with the value of q that can be obtained from substitution this form of solution into the equation (3.1). As a result we obtain:

$$F_{\min} = \sum^{All(3x3)} (2q^2 - 6Rq^2 + 2a_4 q^4)$$

$$= 2 \sum^{All(3x3)} ((1-3R)q^2 + a_4 q^4) \qquad (5.2.9)$$

This way we reduced N-dimensional order parameter $\{q_i\}$ to the one dimensional order parameter q. This can be done only for pure infinite system. For a system with defects only numerical solution can be found. The results of the numerical calculation for general case will be presented later.

We make the usual Landau theory assumption that the parameters in front of the powers of the order parameter are smooth functions of temperature and can be expanded in powers of $(T-T_0)$ near the onset temperature. Since the factor in front of q^2 must change sign near T_0, we assume that

$$a_2 = (1-3R) = a'(T - T_0) \qquad (5.2.10)$$

Here a' is some constant. The expression (5.2.8) does not contain a cubic term. This means that Eq. 5.2.8 describes a second order phase transition. Differentiation of free energy per one (3×3) unit cell gives an equation

$$\frac{\partial F_{3\times3}}{\partial q} = 4a_2 q + 8a_4 q^3 = 0 \qquad (5.2.11)$$

that has two solutions of this minimization problem. Assuming that a_4 is small and positive, they are

$$\begin{cases} q = 0 & \text{for } a_2 > 0 \\ q^2 = -\dfrac{a_2}{2a_4} = -\dfrac{(1-3R)}{2a_4} & \text{for } a_2 < 0. \end{cases} \qquad (5.2.12)$$

For R<1/3 there is the minimum of free energy is achieved if q=0 solution since q^2 has to be positive for q to be real in the second solution. But for R>1/3 we have a solution with nonzero q. The transition between these two solutions and corresponding phases happens when R crosses 1/3.

It is noteworthy that the solution for the low temperature has (3x3) symmetry with all three atoms different. Different theoretical groups suggested such a solution. (Santoro 1999) In the structure determination though it was always assumed that two atoms out of three are equivalent. This is not exactly what is observed by STM. The calculations with defect included show that the solution resembling one up two down structure can be obtained when defects have a certain configuration, to be exact when they are distributed uniformly on two out of three sublattices. The Figure 5.12 illustrates this point. The filled state STM image (Fig. 5.12a) was acquired at 55 K. (It displays an area in the vicinity of the line defect. Due to the charge transfer the last row of Sn atoms appear dark and the next neighbors row has a higher brightness. This feature will not be discussed here.) The issue considered above is demonstrated by a line scan (Fig. 5.12c) indicated by a white line in the Fig. 5.12a. It is clear that all three atoms in the (3x3) unit cell are different.

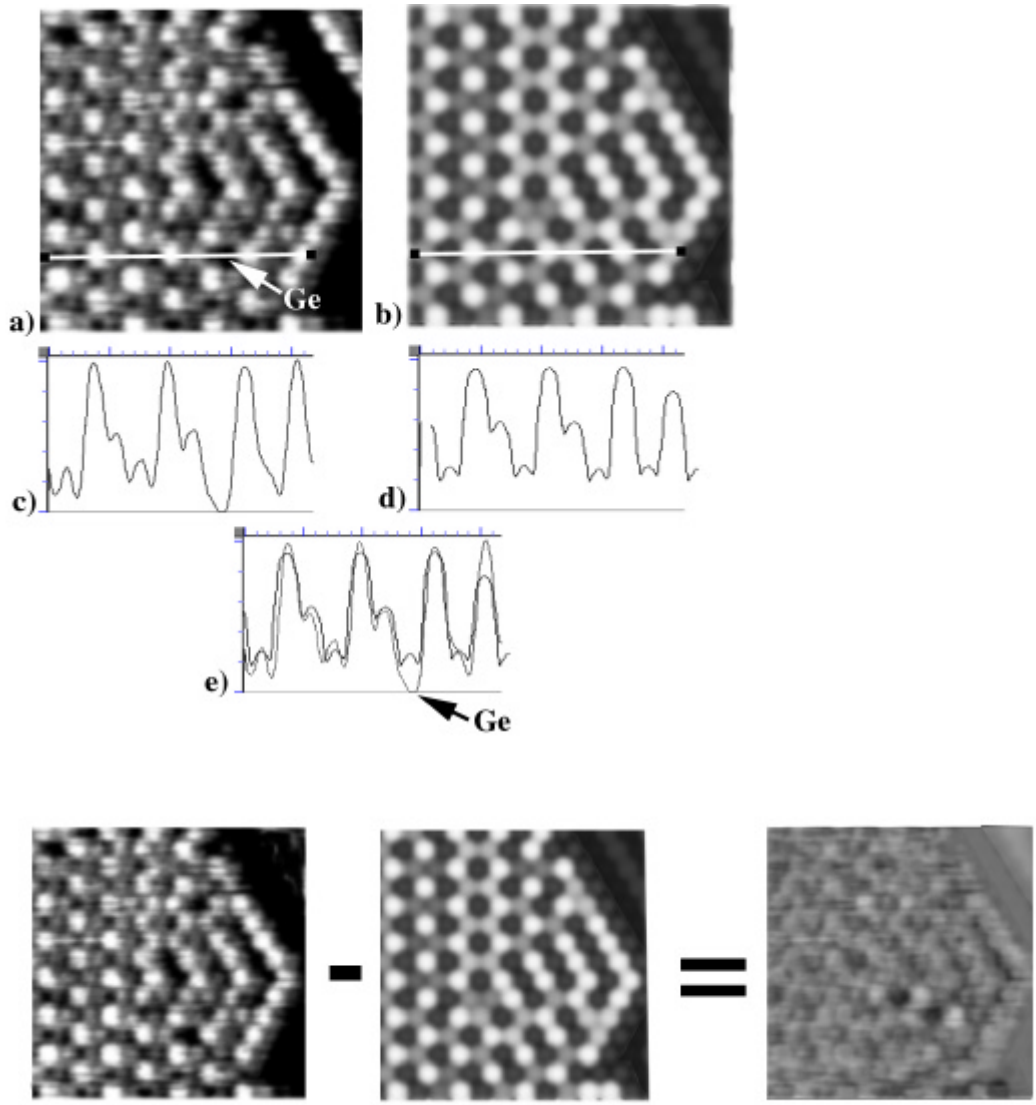

Figure 5.12 Comparison of the experimental STM image and calculated one using CCM

a) a filled state STM image at 55 K of the area containing a line defect ($(\sqrt{3}\times\sqrt{3})R30°$ domains boundary)
b) an image calculated using CCM. The value of charge on the Sn atoms right at the boundary was taken the same as Ge defect (-1).
c) a line profile along in the direction indicated in a)
d) a line profile from b). The rounded shape is artificial. STM image is simulated by spheres positioned at the height proportional to calculated charge.
e) comparison of the line profiles. The fit is almost perfect!
f) comparison by subtracting the experimental image from the calculated one.

The same structure is obtained by calculation using CCM (Fig. 5.12b) and the line scan shows that all three atoms are different (Fig. 5.12d). Finally in Fig 5.12e the experimental STM image was subtracted from the calculated one. The resultant image has only small features, hence the deviation of the theoretical image from the experimental is very small.

Second order phase transition

Since we have free energy it is easy to show when R is crossing R_c=1/3 the system undergoes a second order phase transition. The order parameter is a continuous function of temperature. For R<0 the minimum of free energy is at q=0 (Fig. 5.13, red curve). When R=1/3 the F(q) flattens (Fig. 5.13, blue curve), and when R cross 1/3 the q_{min} becomes small nonzero value (Fig. 5.13, green curve) and grows with R like root square according to Equation 5.2.10.

What is the role of defects in this phase transition? The curves of free energy F(R) and order parameter squared q^2(R) for system with 3% of defects (as in experiment for Sn/Ge(111) are shown in the Figure 5.14 a and b respectively. First of all q is not zero even for R< 1/3. The red line shows that the phase transition happens at R smaller than 1/3 (R=0.326). It means that the system with defects undergoes a CDW phase transition at higher temperature than a pure system. This is a very important result. It explains why the phase transition temperature determined by LEED (210 K) is much higher than the temperature at which the decay length diverges and where we would expect the CDW transition in the absence of defects. One of the most interesting conclusions of this work is that the phase transition temperature is at least 100 degrees lower than it was originally reported (Carpinelli 1997). This very important fact was left unnoticed for a long time. Tc=210K is cited in almost all papers up to date. What actually happens can be

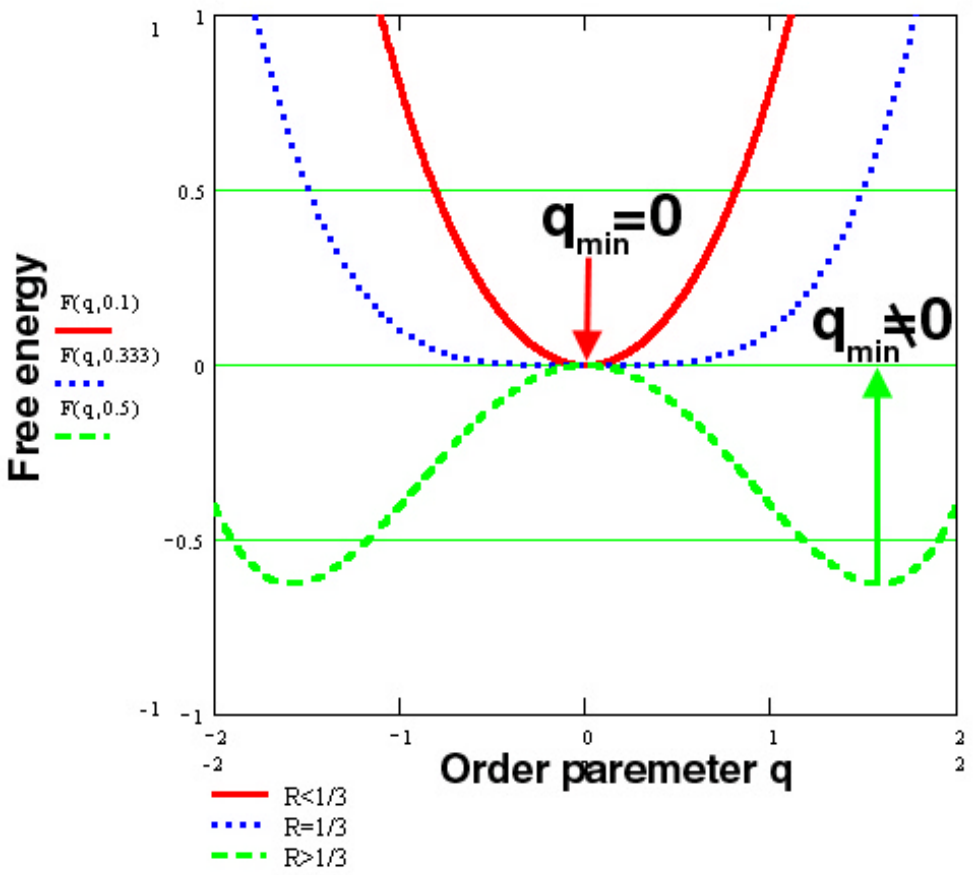

Figure 5.13 Free energy versus order parameter for different R
For R<1/3 the free energy curve has one minimum at q=0.
For R=1/3 the bottom of the curve is flat
For R>1/3 There are two minima at q not equal to 0. The absolute value of q grows with R.
This is a typical "textbook" behavior of a system undergoing a second-order phase transtion.

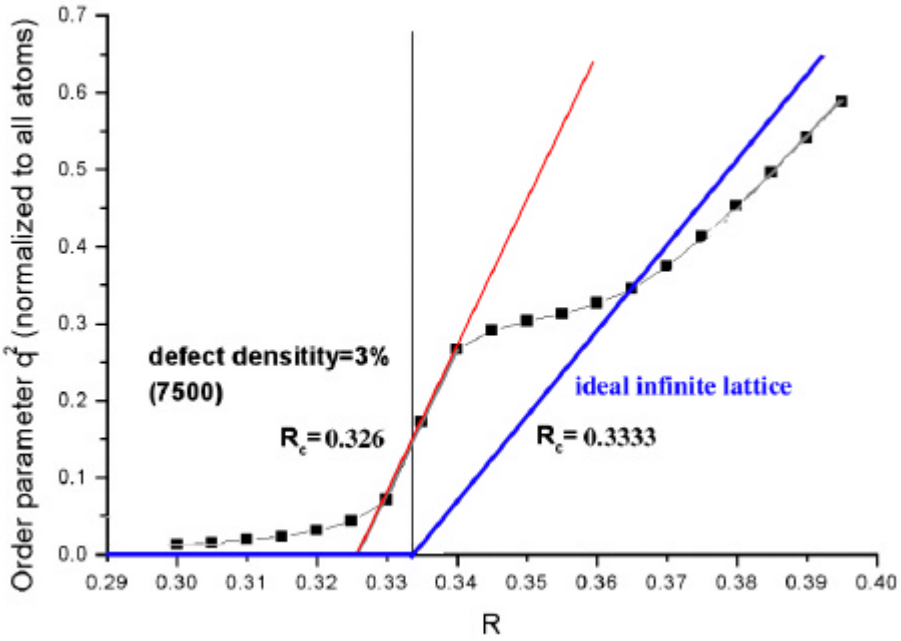

a)

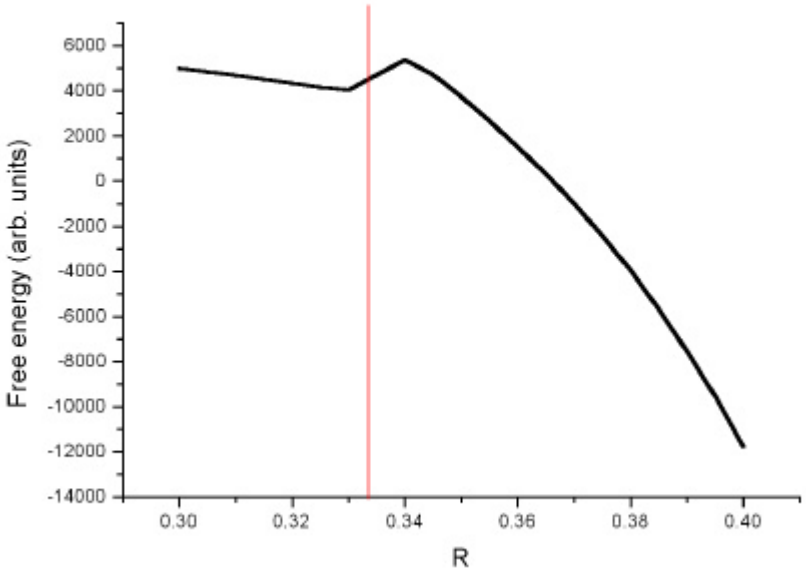

b)

Figure 5.14 Dependence of order parameter and free energy of system with 3% defect density.

a) Order parameter q^2 vs R for a system with 3% defect density. The blue lines are the solutions for an infinite pure system. The red line interpolated to intersect the q=0 line indicate the shift in R_c.

Free energy dependence of R for a system with 3% defect density.

demonstrated using Fourier transformation of STM images. Originally T_c was determined by appearance of (3x3) spots in LEED pattern when the temperature is lowered. Essentially LEED gives us Fourier transformation of the surface structure. We can use this fact and to compare Fourier transformation of the real space images obtained using CCM with diffraction experiments. Real space images and their Fourier transformations are shown in the Figure 5.15. The real space image calculated for R<Rc shows that (3x3) CDW is induced in the vicinity of the defects. These local CDWs give rise to fuzzy (3x3) spots in the Fourier transformation (Fig. 5.15c). When R is increased the size of the (3x3) perturbation around defects grows so the (3x3) in FT becomes more narrow and bright. When R becomes bigger than Rc the whole image appear as (3x3) structure but it is broken into many domains due to defects pinning (Fig.5.15 b). Thus the width of (3x3) spots stays finite (Fig. 5.15d). We can quantify the peak width by taking intensity profiles (Fig. 5.16a) across the (3x3) peaks as indicated by a the black line in Fig. 5.13a. The fitting was done using multi-peak function assuming Lorentzian shape (Fig. 5.14b):

$$I = I_0 + \frac{2A}{p}\frac{w}{4(k-k_i)^2 + w^2} \qquad (5.2.13)$$

Where I is intensity. The amplitude, A; the position of the peak, k_i; and the width of the peak, w are the fitting parameters. The result of these calculations is shown in the Figure 5.17. The Fig.5.17a displays the width of (3x3) peaks versus R. It is clearly dropping when R approaches Rc from below and then it stays constant for R>Rc. If we assume that R(T) has form (5.2.6) then we can plot the width versus temperature (Inset of Fig. 5.17a). The integrated intensity doesn't show any feature indicating critical behavior (Fig. 5.17b). This is totally due to influence of defects. The temperature dependence of the

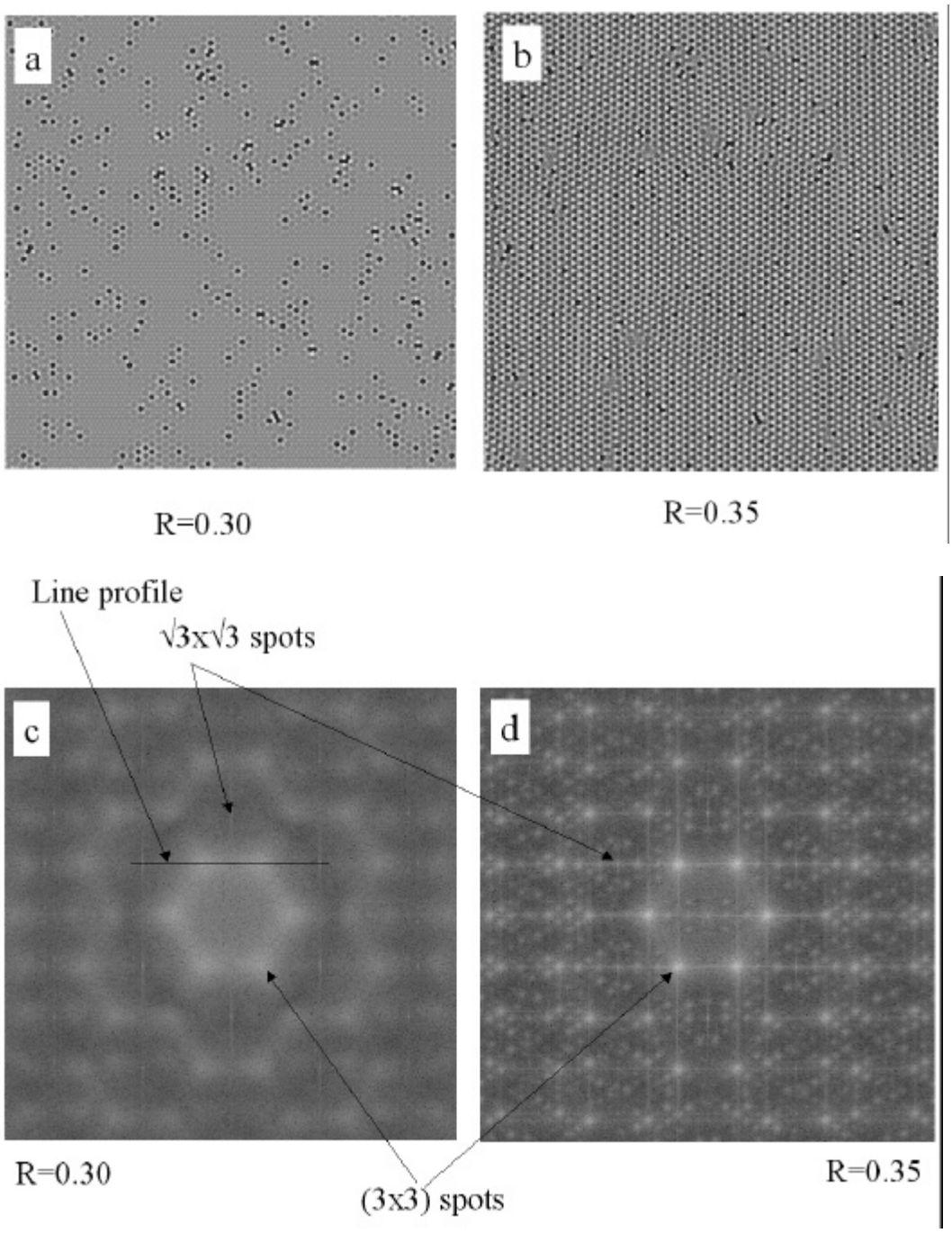

Figure 5.15 Calculated STM images and their Fourier transforms

a) An image calculated using CCM for 3% defect density, R=0.3 (corresponds to RT)
b) The same with R=0.35 (corresponds to LT)
c) FTT of a)
d) FFT of b)

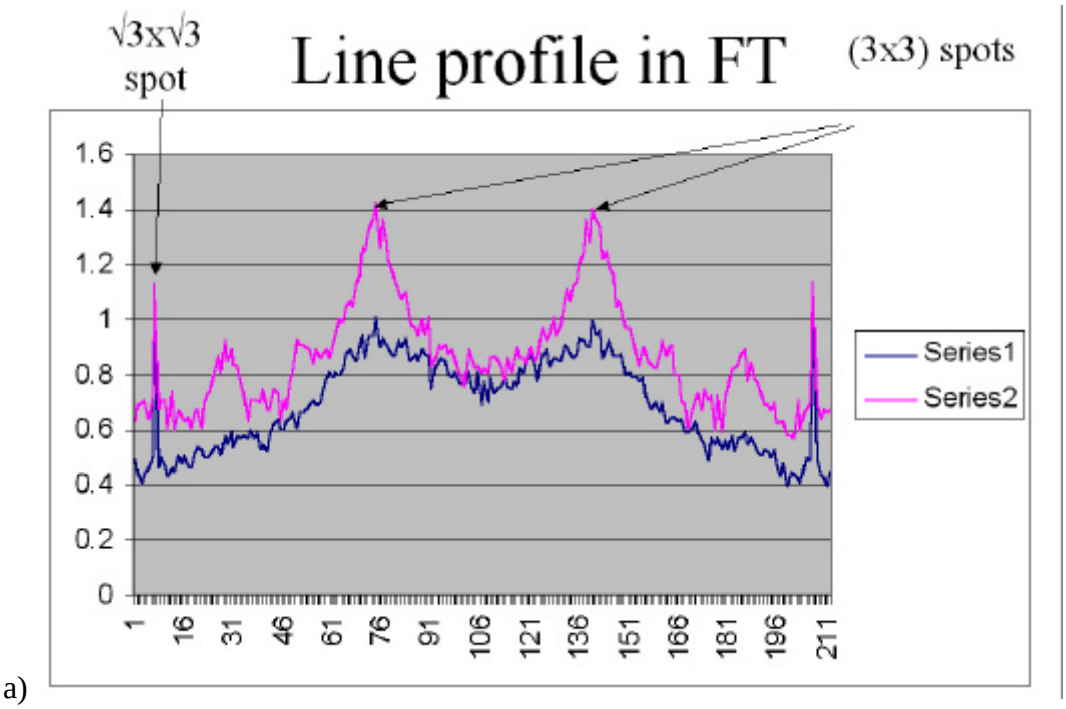

a)

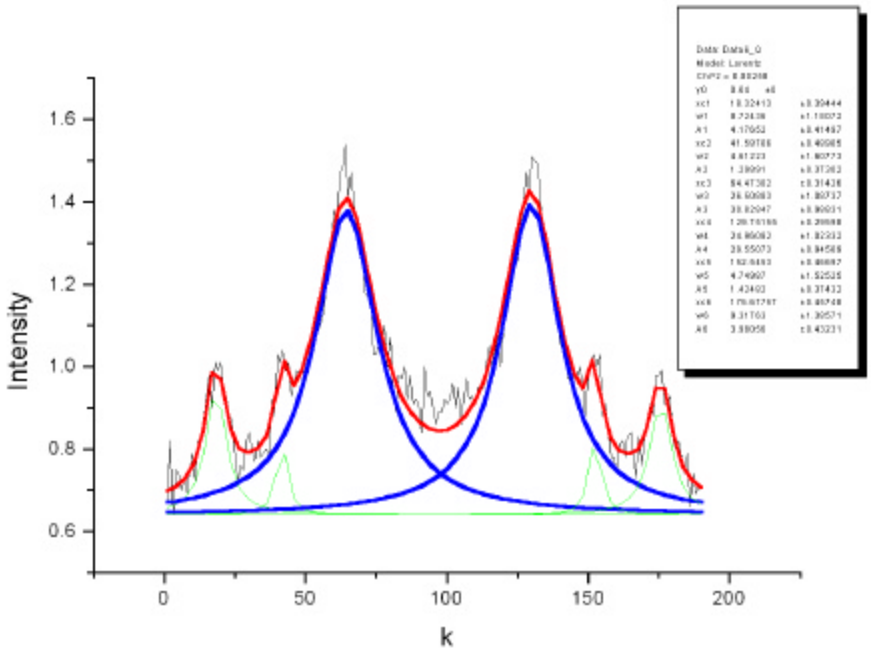

b)

Figure 5.16 Line profile from FT images and multi-peak fit

a) Line profiles of the FT images along the lines indicated in Fig. 5.15 c and d.
b) Fitting of line profiles like a) with multiple Loretzian peaks

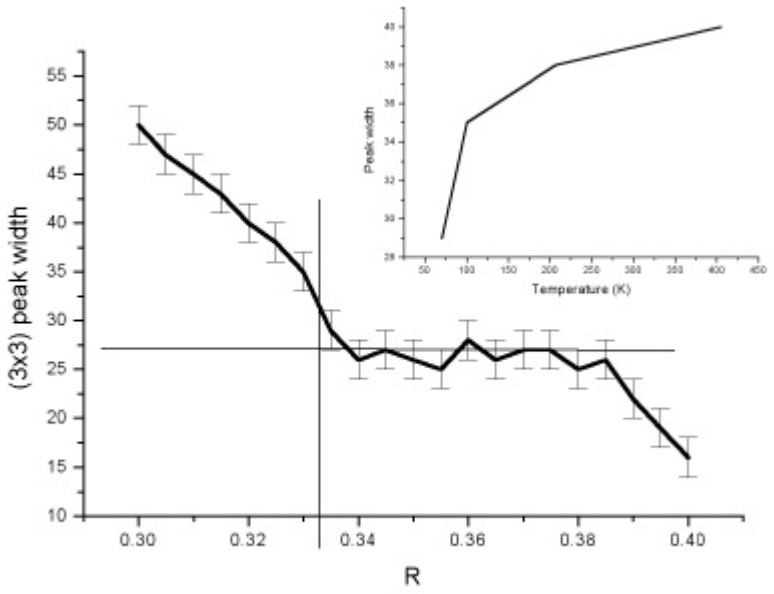

a)

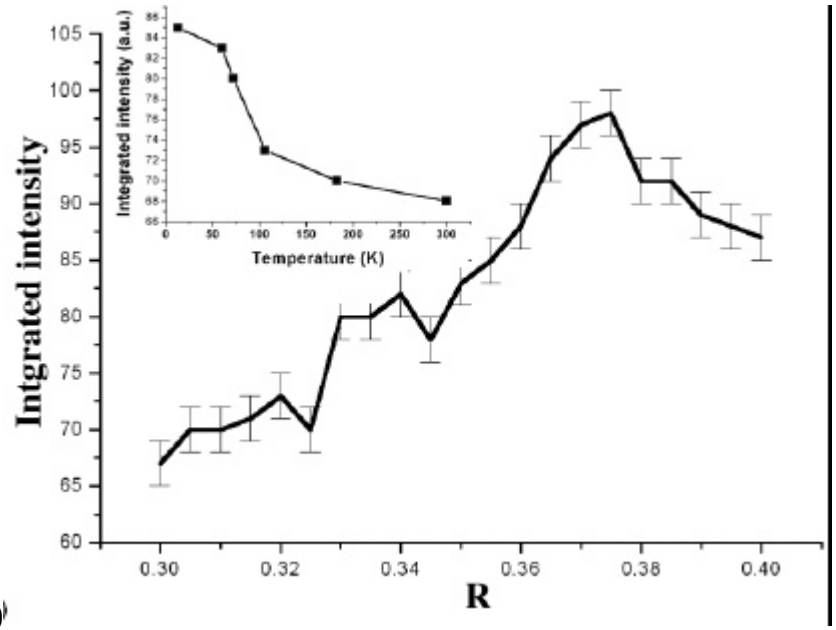

b)

Figure 5.17 Peak width and integrated intensity versus R for FT simulated images.

a) Peak width of the (3×3) spots in the FT images of the calculated STM images for 3% defect density. An inset show the temperature dependence of the peak width if the relation between R and temperature (5.2.6) is assumed.

b) Integrated intensity of the (3×3) peaks versus R for the same system. Inset shows the temperature dependence of integrated intensity.

integrated intensity calculated similar way as the width is plotted in the inset of the Fig. 5.17b.

5.3. Conclusions and summary

The symmetry lowering transition observed in α-phase of Sn/Ge(111) is actually a complex phenomenon that consists of two interconnected phase transitions. One is the CDW transition. This transition can be described by a Charge Compensation Model introduced here. The electronic response of the model system is such that charges on the nearest neighbors of a charged lattice node try to 'compensate' or screen it. This screening is temperature dependent and at certain temperature "overscreening" (Ashcroft 1976) leads to the formation of a Charge Density Wave state. This model can nicely reproduce STM images of Sn/Ge(111) at all temperatures. The great success of it is the ability to predict the shape and position of the domain walls at low temperature for a given distribution of defects. Even though phenomenological in character, it very well reproduces experimental data.

The same calculations are done for a model system whose free energy is written as certain function of order parameter, where the role of the order parameter is played by a charge on an atomic site. This dependence of free energy on the order parameters describes a classical second-order phase transitions in Landau theory.

These two observations bring us to conclusion that CDW transition in Sn/Ge(111) is a CDW transition and it is of the second order. This is the first time the order of this phase transition was determined.

The second phase transition that accompanies the CDW transition is of the first order order-disorder phase transition in the defect distribution. Defects create local CDW

and they interact with each other via these local CDW. The range of the defect-induced CDWs grows when the temperature approaches CDW transition temperature. When it reaches a certain value the interaction between defects acquires a collective character and they order.

In conclusion, defects create pretransitional effects, they interact and order, and they are responsible for pinning the domains and the shape of domain walls.

References for Part 5

Ashcroft, N. W. and Mermin N. D. (1976). Solid State Physics. New York, Holt, Reinhart and Winston.

Carpinelli, J. M., Weitering H. H., Barkowiak M., Stumpf R. and Plummer E. W. (1997). "Surface charge ordering transition: alpha phase of Sn/Ge(111)." Physical Review Letters **79**(15): 2859-2862.

McMillan, W. L. (1975). "Landau theory of charge-density waves in transition-metal dichalcogenides." Physical Review **B12**(4): 1187-1196.

Santoro, G., Scandolo S. and Tosatti E. (1999). "Charge-density waves and surface Mott insulators for adlayer structures on semiconductors: Extended Hubbard modeling." Physical Review B-Condensed Matter **59**(3): 1891-1901.

Weitering, H. H., Carpinelli J. M., Melechko A. P., Zhang J. D., Bartkowiak M. and Plummer E. W. (1999). "Defect-mediated condensation of a charge density wave." Science **285**(5436): 2107-2110.

Part 6

Electronic Instabilities and

Defect Density Waves

“Other Systems”

6.1 Introduction to Sn/Si(111).

In section 1.5.2 I discussed the surface bonding of isoelectronic atoms Sn and Pb on the (111) surfaces of Si and Ge. This portion of the periodic chart showing the IV column of elements with an electronic configuration of ns^2np^2, with n=3 for Si, 4 for Ge, 5 for Sn and 6 for Pb. The valence of each atom is 4 and the only thing that changes is the size and the ionization potential. After all of the work on the Sn and Pb on Ge(111) systems it is reasonable to expect the same behavior for the Sn/Si(111) system. There is very little change in the bond lengths or angles. But as this Part of the thesis will show we were really surprised when we looked at this system. This work was done with a visitor Luca L. Ottaviano from the Università dell'Aquila in Italy.

There have been several previous studies of the α-phase of Sn on Si(111). At RT this system exhibits the same structure as the Sn/Ge system (Conway 1989; Nogami 1989) with metallic character (Kinoshita 1986; Profeta 2000). In contrast to the Sn/Ge(111) system, no (3x3) CDW has been reported as the temperature is lowered (~70K) (Ottaviano 2000a; Uhrberg 2000b). The LEED pattern of this surface obtained at 70 K by Uhrberg at al. There are only $(\sqrt{3}\times\sqrt{3})R30°$ spots present (compare it with Fig. 2.1a for Pb/Ge(111)). There are no sharp (3×3) spots as in LEED images of Sn/Ge(111) or Pb/Ge(111) at such temperature (Fig. 2.1b). Very slight features indicated by arrows in Fig. 6.1a in the areas of where the (3×3) spots would be can be seen after substantial contrast enhancement. They do not depend on temperature and can be observed even at RT. Their origin can be understood if we apply a Fourier transformation (Fig. 6.1c) to the STM image shown in the Fig. 6.1b. The RT STM image has no (3×3). The only deviation

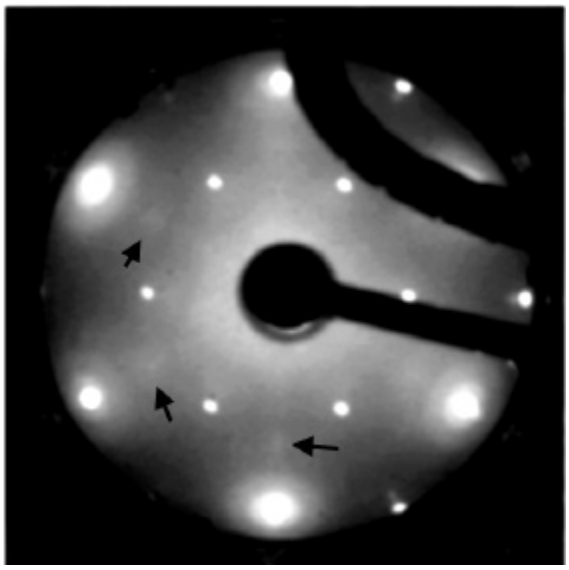

a)

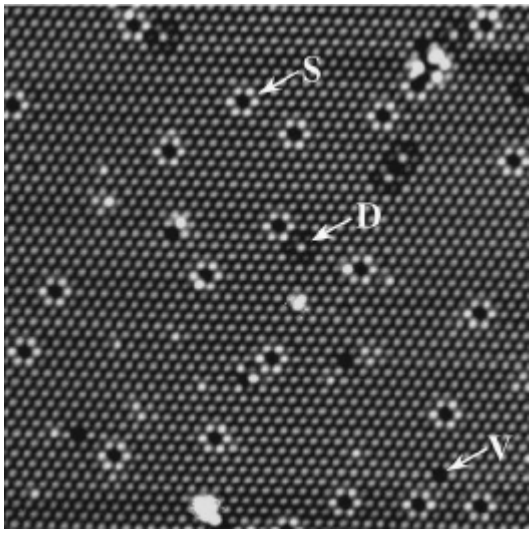

b)

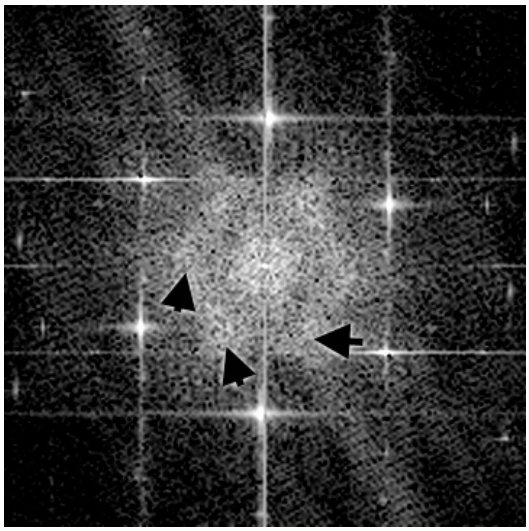

c)

Fig. 6.1 LEED and STM of Sn/Si(111)

(a) LEED image of (√3×√3)*R*30° Sn/Si(111) obtained at 70K (~37 eV).
(b) Filled state STM image (282Å×294Å) of the (√3×√3)R30° Sn/Si(111) surface obtained at RT (-1 V, 300 pA)
(c) FT of the STM image (b)

from the (√3×√3)R30° is caused by defects. Thus the features indicated by arrow in Fig. 6.1c originated from the defect induced perturbations. These features are not centered at the positions of the (3×3) spots but actually shifted to the low spatial frequency side (closer to (0, 0) spot).

Our STM measurements reveal a new periodicity at low temperature not seen in electron diffraction, i.e. an electronic transition. In this low temperature phase of the Sn/Si(111) system, the defects, primarily Si substitutional atoms, are aligned commensurate with the one-dimensional electronic wave (defect density wave), which appears to be incommensurate with the substrate. The α-phase of Sn/Si(111) is fundamentally different than the iso-electronic Sn/Ge(111) system!

In Part 1, I discussed the general properties on 2-D phase transitions and the role of defects. Here it is worth stressing what has been speculated about the role of defects in CDW phase transitions. It is generally recognized that the defects can play a critical role in phase transitions, especially in reduced dimensionality (Halperin 1976). Mobile defects and the onset of their spatial long range ordering are often invoked as the microscopic explanation of some experimental observations in low temperature phase transitions, such as the occurrence of thermal hysteresis effects (Baldea 1993). For example, it has been hypothesized that a modulation of the occupation probability of defects along the one-dimensional lattice occurs in potassium cyano-platinide (Baldea 1985; Baldea 1993). Even though the alignment of defects has not been directly demonstrated experimentally the concept has proven to be a useful microscopic description for a variety of experimental data (Baldea 1993).

6.2 Experimental results

The experiments were performed using only the UHV Omicron Variable Temperature STMs (30-300 K), equipped with standard surface preparation facilities and a LEED camera. The Si(111)-(7x7) reconstructed substrates were prepared by direct resistive heating at 1250°C for 1 min after out-gassing for 12 hours at dark glowing temperature (550°C). The α phase of Sn/Si(111) ($\sqrt{3}$x$\sqrt{3}$) was obtained by depositing 1/3 of a mono-layer of Sn at RT and then annealing it up to 500°C in front of LEED until the $\sqrt{3}$x$\sqrt{3}$ pattern was observed (Tornevik 1994; Ottaviano 2000b; Uhrberg 2000b). Our RT STM images were identical to those previously published and shown in Fig. 6.1 (b) (Tornevik 1994; Ottaviano 2000b; Uhrberg 2000b).

Fig. 6.2 is a four panel figure that summarizes our observations of the low temperature STM images at 60 $\pm$ 10 K. Fig. 6.2 (a) shows an empty state image and Fig. 6.2 (c) a filled state image for a film with an average defect density of 4%. On the right are the Fourier transforms (FT) of the respective STM images. Never have we observed a (3x3) CDW phase with the STM! LEED observations are consistent with this statement (Uhrberg 2000b). A casual inspection of the empty state image in Fig. 6.2(a) reveals what looks like a new structure with the symmetry ($2\sqrt{3}$x$\sqrt{3}$)R30^{o}. The primitive lattice vectors for the $\sqrt{3}$x$\sqrt{3}$ ($2\sqrt{3}$x$\sqrt{3}$) structure is shown in the top-left (top-right) insert of Fig. 6.2.(a). Defining the x axis as horizontal and y vertical in Fig. 6.2, the primitive lattice vectors of the $\sqrt{3}$x$\sqrt{3}$ can be defined as $\mathbf{a_1} = a\mathbf{i}$ and $\mathbf{a_2} = a/2(-\mathbf{i} + \sqrt{3}\mathbf{j})$ with reciprocal lattice vectors given by $\mathbf{b_1} = (2\pi/a)(\mathbf{i} + \mathbf{j}/\sqrt{3})$ and $\mathbf{b_2} = (2\pi/a)(2/\sqrt{3})\mathbf{j}$. a = 6.65 Å is the Sn-Sn nearest neighbor spacing. When the apparent $2\sqrt{3}$x$\sqrt{3}$ structure forms the new

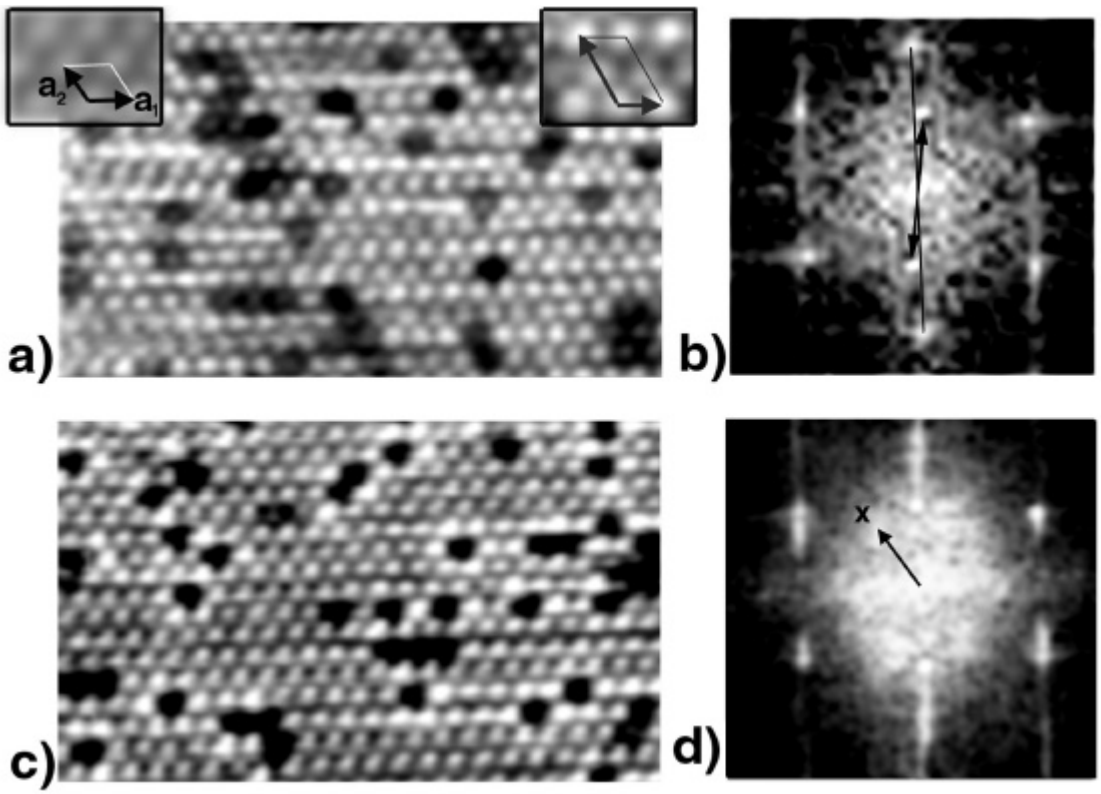

Figure 6.2. STM images of the α–phase of Sn/Si(111) at ~60 K

a) Empty state (+1.5V) STM image of an 153x98 $Å^2$ area showing 2√3-like structure. The √3x√3 and 2√3x√3 unit cells are shown in the insets.
b) Fourier transform (FFT) of an empty state image of 300Åx300Å containing the area imaged in (a). The √3x√3 reciprocal lattice vectors are indicated (thin line) as well as (thick arrows) the spots corresponding to the 1-D canted ***K*** wave-vector (see text)
c) Filled state (-1.5V) STM image at ~60 K ;
d) Fourier transform of the image of an area of 300x300$Å^2$, containing the area shown in (c). An arrow indicates a vector to the center of the diffused spot. An x shows the position of the (3x3) k-vector.

primitive lattice vectors are $\mathbf{a_1}$ and $\mathbf{2a_2}$, with reciprocal lattice vectors given by $\mathbf{b_1}$ and $\mathbf{b_2}/2$**.** The FTs of the empty and filled state images (Fig. 6.2 (b) and 6.2 (d)) clearly show the reciprocal lattice points indicative of the $(\sqrt{3}x\sqrt{3})R30^{o}$ phase, and new reciprocal lattice points created by the new $2\sqrt{3}$-like periodicity seen in STM images. Again, there is no sign in the FTs of the (3x3) CDW phase.

The main conclusion based on the low temperature STM observations are:

1) There is no evidence for the (3x3) CDW phase seen for Sn and Pb on Ge(111). We observed an increased background in LEED intensity in the area of (3x3) spots similar to what was reported by Uhrberg et al. (Uhrberg 2000b). (A higher intensity background in the vicinity of (3×3) spots in the LEED pattern can be observed at high defect density.) The real space image in Fig. 6.2 (c), and the RT image in Fig. 6.1b show the origin of this periodicity. Around every defect is a bright nearest neighbor ring of Sn atoms, reminiscent of a RT image of Sn on Ge(111). This is the damped CDW induced by each defect. The difference between Sn on Ge and Sn on Si is that for Si the extent of the waves does not dramatically increase as the temperature is lowered (Ottaviano 2000a). The broad diffuse background in the region of the (3x3) of the FT of the filled state STM image (Fig. 6.2 (d)) is due to the Sn nearest neighbor response to the Si defect. But the k-vectors to the centers of these spots are ~15% shorter than expected for (3x3). Fig. 6.3 (a) shows a line scan across the FT Fig. 6.2 (d) with the vertical lines indicating where the 3x3 spots should appear. The wave induced by defects in Sn/Si(111) has a longer period than the waves in Sn/Ge(111). For comparison, similar diffused spots in FT of RT STM images of Sn/Ge(111) are located exactly at the (3x3) positions, as seen in Fig. 6.3b

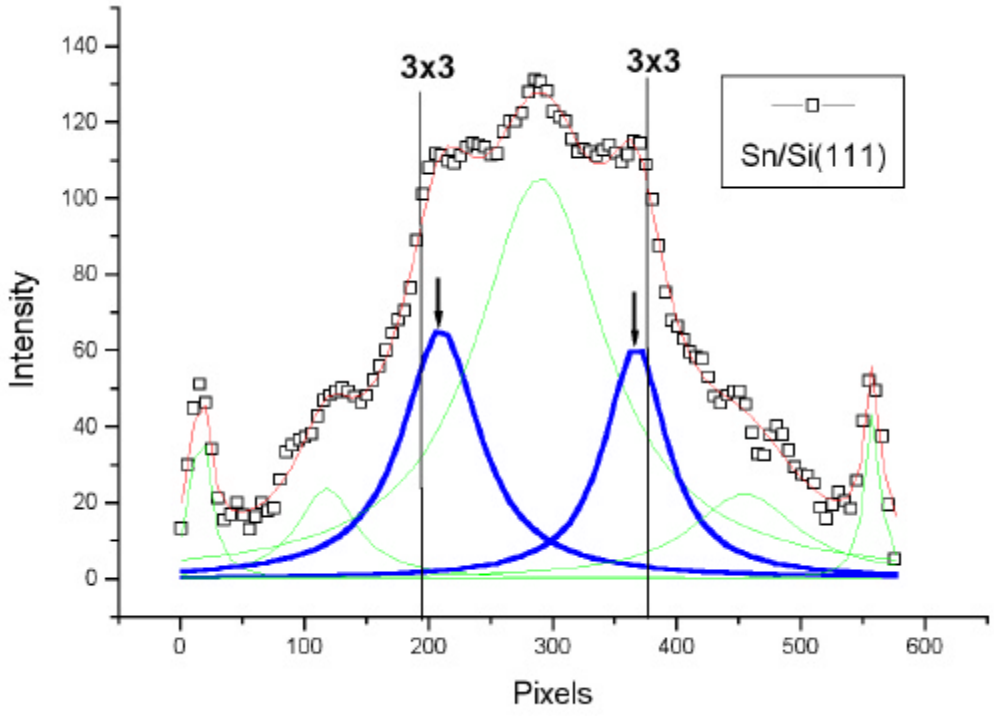

a)

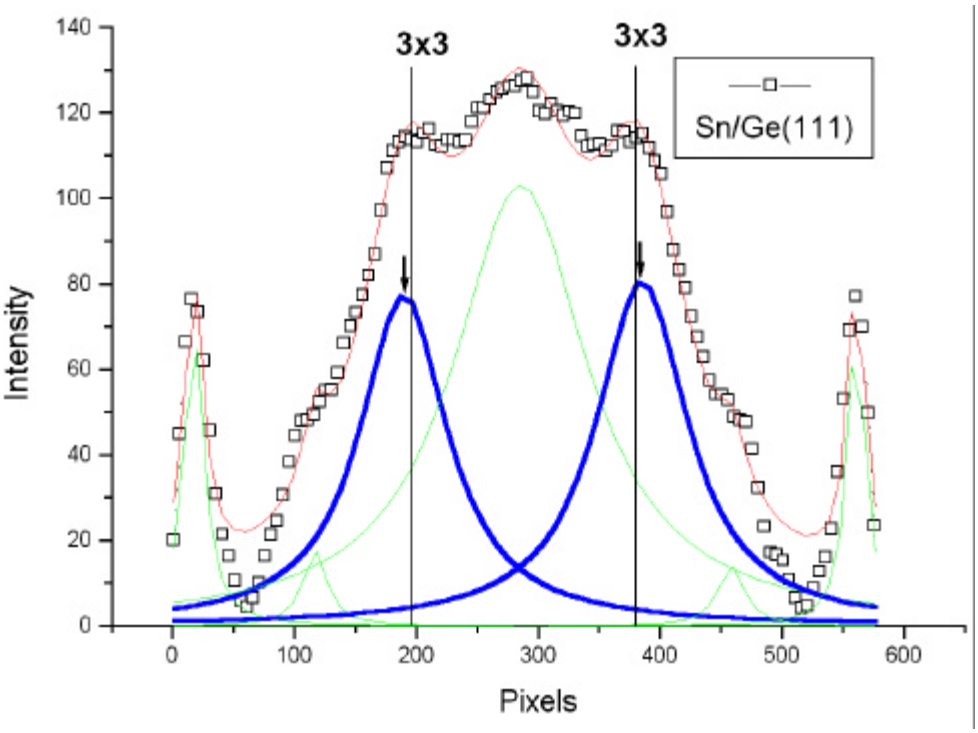

b)

Figure 6.3 Line scans across FTs.

(a) line scan from fig. 6.2 (d) across the q=0 to q = (3x3) diffraction spot.

(b) Line scan in the same q region as in (a) but for the room temperature STM image for the Sn/Ge(111) system

(Melechko 2000). (Very slight shit to the high spatial frequency side is due to exponential decay.) The obvious conclusion of this observation is that the CDW (3x3) configuration is not the ground state of a defect free or low defect α–phase of Sn on Si(111) (Flores).

2) The one-dimensional structure is incommensurate and dependent upon the bias voltage. The bright spot in the FT of the filled state image (Fig. 6.2 (d)) associated with the 2√3 reconstruction is exactly where the new reciprocal lattice vector should be. This is also shown in the line profile taken across the (√3×√3)R30° spots (indicated by vertical lines) and the position of a 2√3 spot (vertical line in the middle) in Fig. 6.4a. In stark contrast, this spot in the empty state FT is not in the same position (see arrow and vertical line in Fig. 1b). The spot is rotated slightly (7^o-8^o) from the perpendicular <112> direction. Fig. 6.4b shows this shift in a line scan across the FT in Fig. 6.2 (d). This new vector can be described by the vector $\boldsymbol{K} = (2\pi/\sqrt{3}a)((0.132\pm0.009)\mathbf{i} + \mathbf{j})$. There is no reason to believe that this is a commensurate vector, but a new periodicity along the horizontal rows of 7 or 8 would fall in the experimental uncertainty. Once this new periodicity has been identified in the FT it is easy to see it in the real space image (Fig. 6.2 (a)). Start with a bright atom and move along the horizontal rows, the bright rows seem to distort and become dim and then bright again. The ‘atoms” along a horizontal row in the empty state image are visibly laterally shifted from ideal T_4 position, i.e. the rows aren’t straight. There is an electronic superstructure in the empty state image, which is 1-D in character. It is clearly one-dimensional because there are no additional diffraction spots that would be associated with a periodicity in the horizontal direction. For example, if this were a commensurate reconstruction of the form 2√3x7√3 there

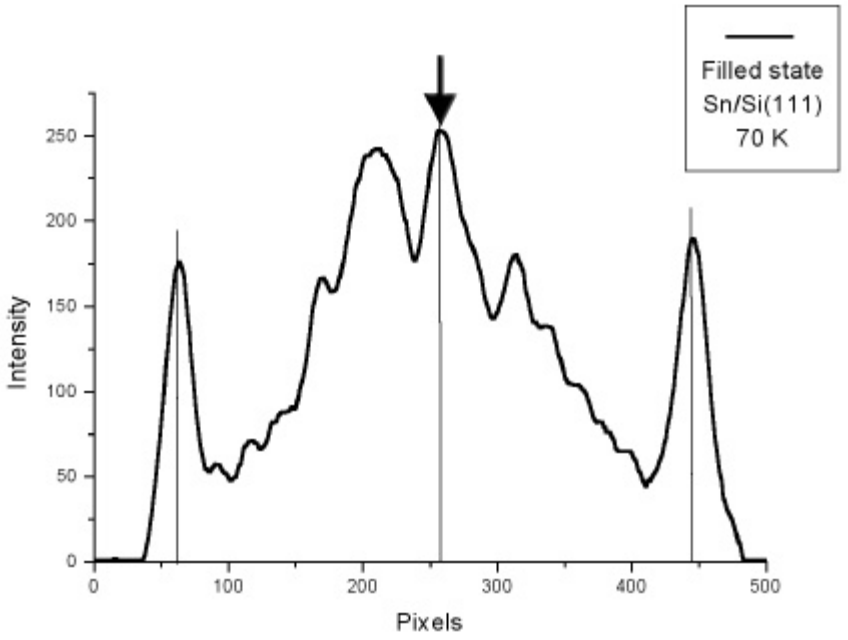

a)

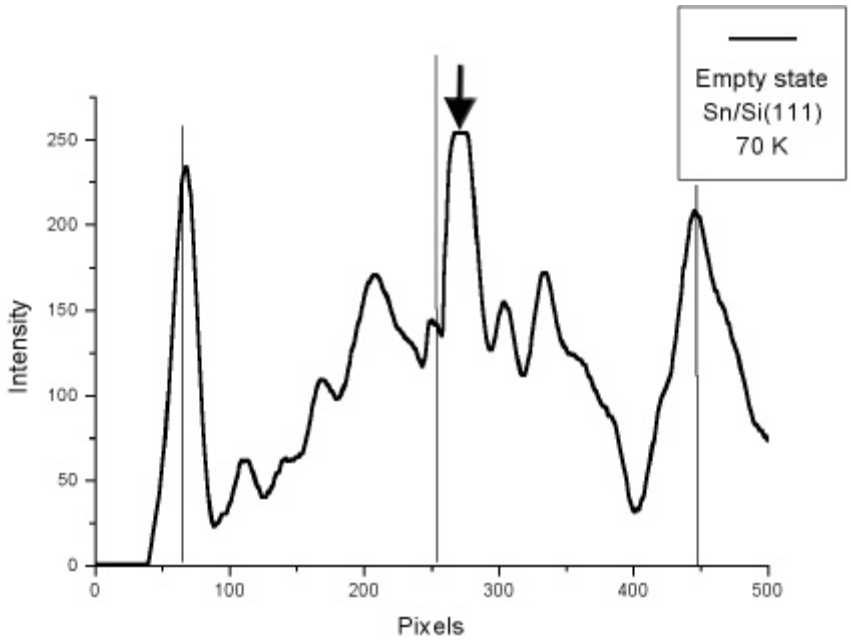

b)

Figure 6.4 Line scans across FT of LT STM images of Sn/Si(111)

a) The scan across FT of a filled state STM image. The position of the $2\sqrt{3}$ spot is indicated by arrow.
b) The scan across FT of an empty state STM image. The $2\sqrt{3}$ spot (indicated by arrow) is shifted with respect to the ideal position (vertical line)

would be many 7th order spots in the FT. It is electronic because it depends upon the bias voltage used to accumulate the STM image, and is not seen in the diffraction pattern.

It should be pointed out that in practice there are six different one-dimensional waves possible, two associated with each of the three √3 directions. Fig. 6.5 shows an STM image of a different area than displayed in Fig. 6.2 (a). In many images like that one waves in multiple directions are observed. The bright rows of atoms are indicated by the white arrows. Occasionally, STM images contain a superposition of 1D waves in two directions leading to 2√3x2√3 superstructure. For example, such superposition can be identified in the lower left quadrant of the Fig. 6.5.

If a real space image is constructed to isolate the electronic distortion using only the "diffraction spots" in the FT the defects will disappear unless they are ordered with this periodicity. This real space image has been fabricated in Fig. 6.6 (a) by creating an image composed of the √3x√3 spots and the canted spot (***K***) seen in the empty state image of Fig. 6.2 (b). In this artificial image there are no imperfections and the electronic distortion of the horizontal rows of Sn is quite evident. Fig. 6.6 is such a constructed real space image, where the √3x√3 spots have been filtered out of the FT shown in Fig. 6.2 (b) and then transformed back. This image reveals everything, if you look closely. There are bright and dark rows with the periodicity of the ***K*** vector shown by the arrow in Fig. 6.2 (b).

3) *In the low temperature phase the defects have aligned into rows forming defect density waves.* Most surprising is the fact that the defects seem to be aligned within the dark rows. To illustrate this alignment of defects or this Defect Density Wave a

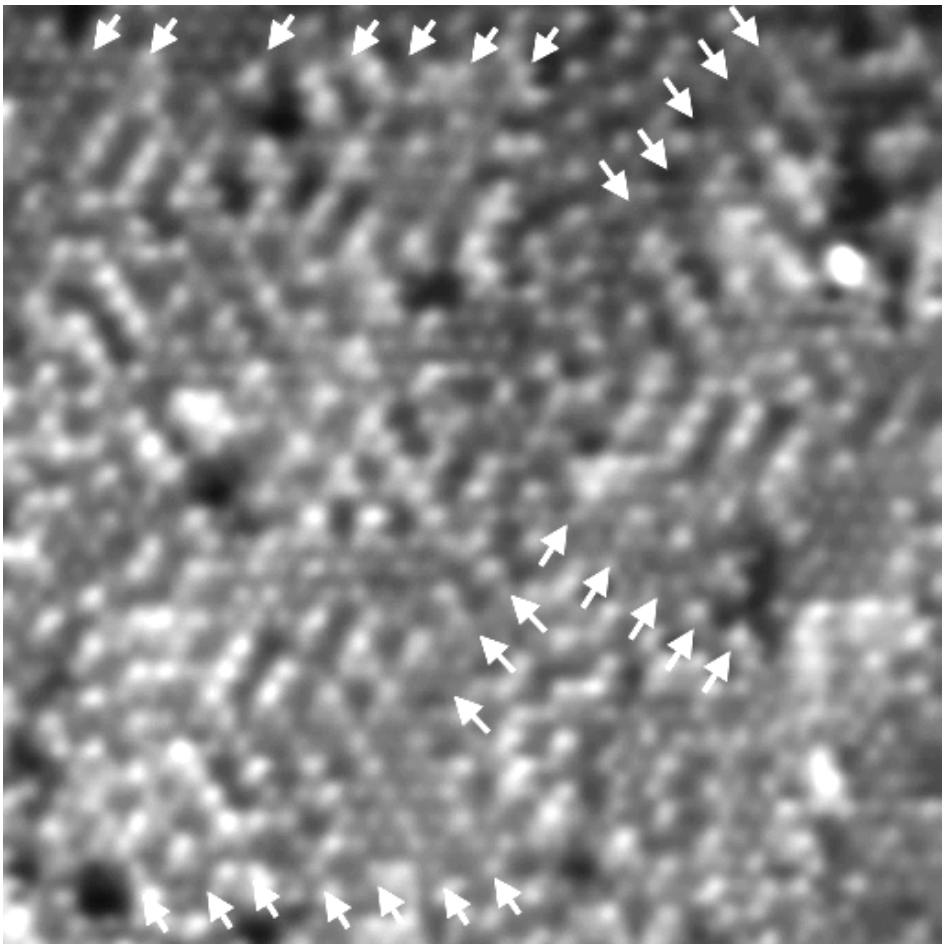

Figure 6.5 Large scale filled state STM image of Sn/Si(111) surface at 120 K showing several 1D waves in different directions.

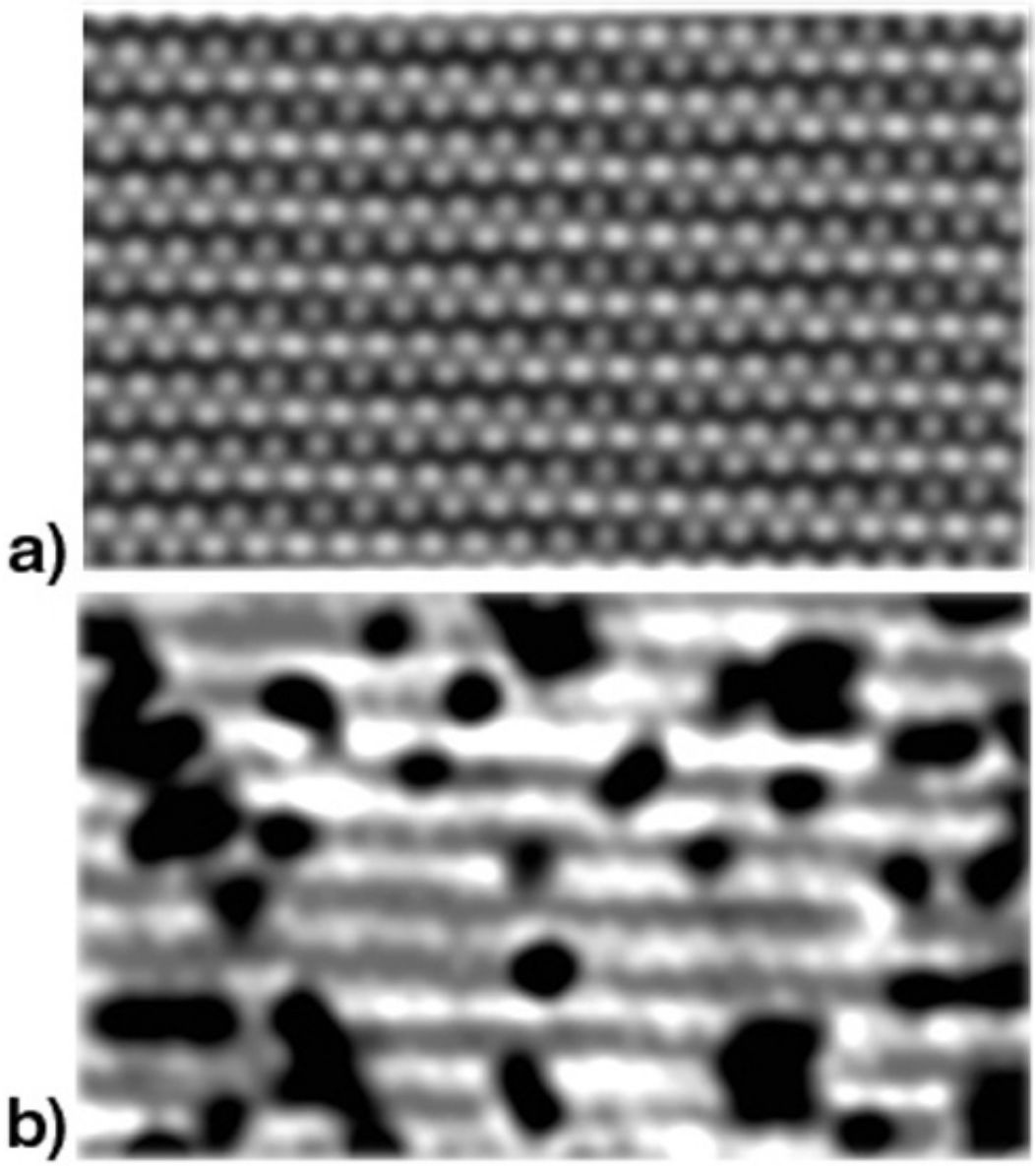

Figure 6.6. Simulated and filtered STM images showing 1D waves

a) Real space empty state STM image simulated from the main spots of the FT of Fig. 6.2 (b).
b) Back Fourier transform of Fig.1a after filtering out the $\sqrt{3}x\sqrt{3}$ spots of Fig.1b.

one-dimensional mask with a wavelength of $\lambda = 2\pi/\boldsymbol{K}$ has been placed on Fig. 6.2(a) and shown in Fig. 6.7. Here one half of a wavelength is transparent and the other half opaque. With the alignment of the phase of the mask according to Fig. 6.6 (b), the opaque sections cover the vast majority 75% of the Si substitutional defects. If the same procedure is used with the direction and wavelength of the mask given by the reciprocal lattice vector associated with the $2\sqrt{3}x\sqrt{3}$ structure $\boldsymbol{K} = \mathbf{b}_2/2$ ~50% of the defects are exposed. Thus we show that there is clearly periodic modulation of the defect density along the canted (***K***) direction. This is the first direct experimental evidence of a one dimensional defect density wave (DDW). Measurements of the defects in a $\sqrt{3}x\sqrt{3}$ phase at RT (never been cooled) show a random distribution. Defect alignment must be intimately associated with the formation of the new structure seen at low temperature with the STM.

4) The one-dimensional electron density wave and the aligned defect density wave do not create a measurable periodic lattice distortion. The apparent displacement of the atoms from the T_4 in the empty state image (Fig. 1a) is ~0.5Å along the inplane $2\sqrt{3}$ direction, and ~0.15 Å vertically. We have estimated the possible lattice distortion from the back ground intensity in LEED (Uhrberg 2000a) compared to the LEED intensities observed for the Sn/Ge system. This leads to an estimate of a vertical distortion less than 0.02 Å and a horizontal distortion slightly larger. Therefore it is clear that the STM images are caused solely by a one-dimensional electronic wave.

In a detailed LEED-photoelectron spectroscopy study of this system as a function of Sn coverage and temperature Uhrberg et al. reported that LEED shows no structural

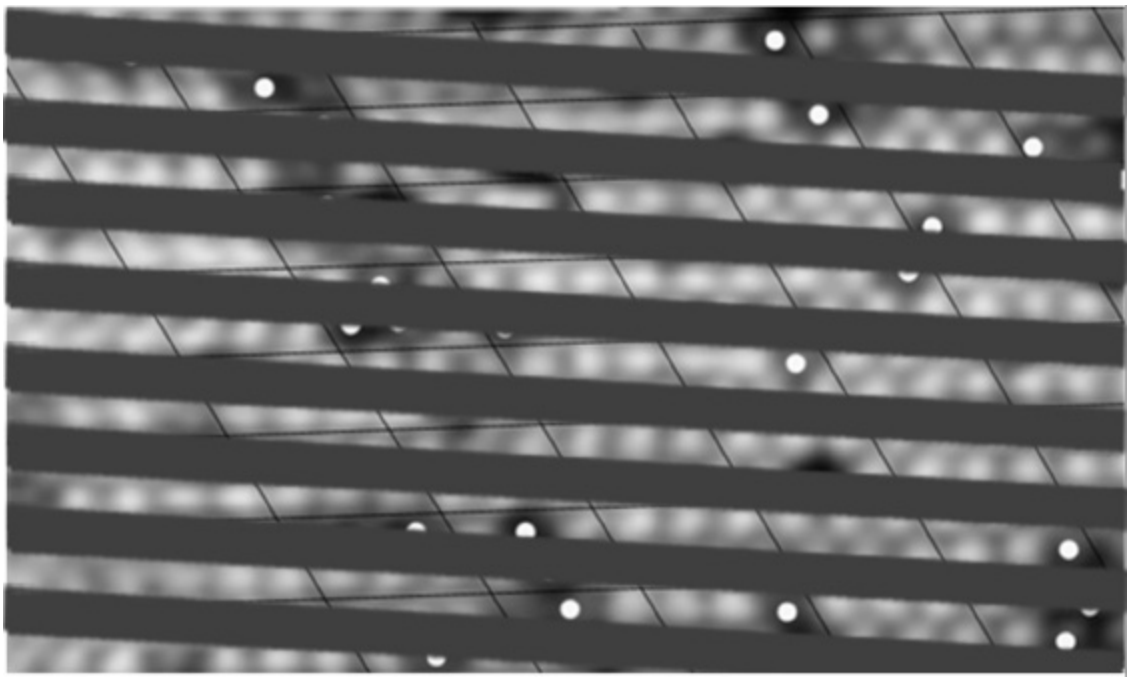

Figure 6.7 Defect Density Wave
Empty state STM image of Fig. 6.2 (a) with a half transparent mask with a wavelength $\lambda = 2\pi/\boldsymbol{K}$. The dark segments of the mask cover 3/4 of all of the Si substitutional defects.

transition down to 70K, but that there are dramatic changes in the electronic structure (Uhrberg 2000b). Combining the observations reported in this paper with what is reported by Uhrberg et al. leads to the conclusion that there is an electronic transition without an accompanying lattice distortion. The 1-D electronic transition is accompanied by the 1-D DDW.

Why is the behavior of the Sn/Si(111) system so different than the isoelectronic system Sn/Ge(111)? One possible explanation could be that the structure is different, but x-ray diffraction studies of these two systems (Conway 1989; Bunk 1999) indicate almost no difference except for the inherent difference in the Si-Si and Ge-Ge bond length. The only obvious difference between these two systems is the band gap of the substrate. There are, in our opinion, two key experimental differences in these systems. First, it has been reported (Ottaviano 2000b; Ottaviano 2000c) and confirmed by this study that most of the Si atoms in substitutional sites in the Sn film are not in the T_4 sites as they are for the Sn/Ge system. Instead, they are displaced towards the H_3 sites, breaking the point group symmetry at the defect site. The local reduction in symmetry around a Si defect at RT (Ottaviano 2000b) and the symmetry lowering long range ordering should be correlated. Second, the response of the two systems to the presence of defects is fundamentally different. For Sn on Ge there are temperature dependent damped CDW emanating from the defect indicating an instability in the system. In contrast, no such extended waves exist for the Sn/Si system (Ottaviano 2000a). It is interesting to note that the calculation of the Fermi surface and the response function performed for Sn/Ge(111) (Fig. 6.8) showed that Fermi surface nesting could occur near the vector associated with the formation of a $2\sqrt{3}$ CDW but not the observed (3×3) CDW. The red straight lines in

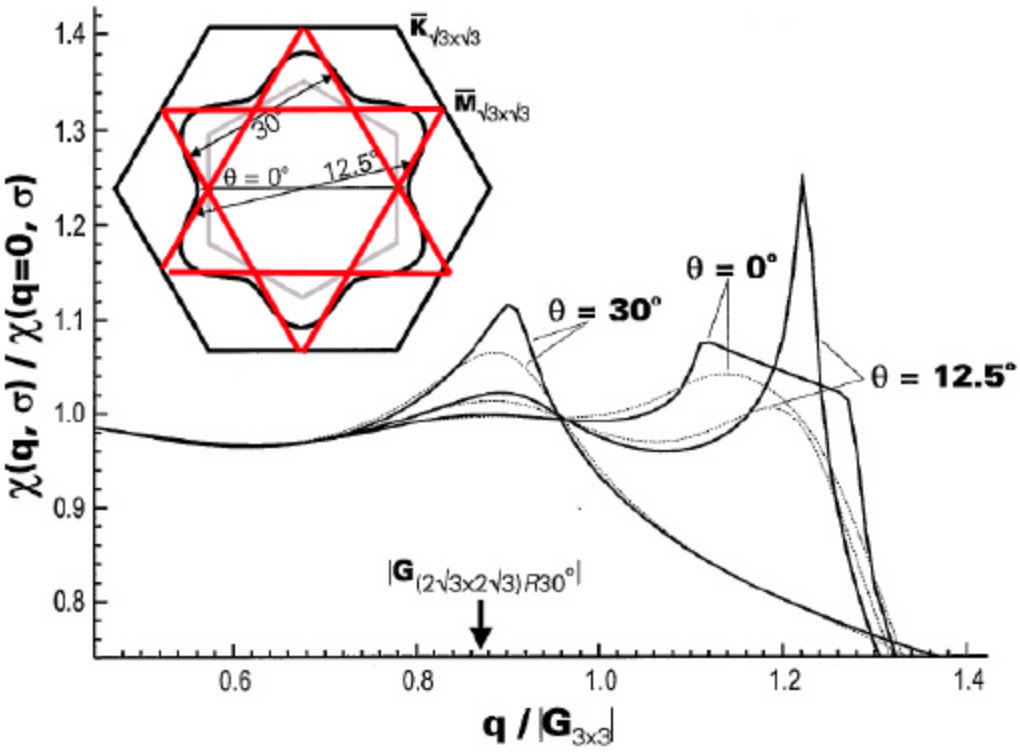

Figure 6.8. Hidden Fermi surface nesting and response function in the direction of the 2√3 waves
(from (Carpinelli 1997))

the Fig. 6.8 are adjacent to a large portion of the calculated Fermi surface. This situation could be similar to the behavior of some qusi-2D conductors, such as the purple molybdenum bronzes (Kmo_6O_{17}), and $Na_{0.9}Mo_6O_{17}$ and others, where the Fermi surfaces in these materials can be viewed as a combination of quasi-1D structures, with distinct 1D nesting vectors. This idea, hidden Fermi surface nesting was introduced by Whangbo et al. (Whangbo 1991) and was observed by Breuer et al (Breuer 1996). There was not measurement of the properties of the Fermi surface of α-phase of Sn/Si(111) but our observation of the 1D waves might indicate such behavior. The result presented in this Part could imply that Sn/Si(111) displays expected behavior, and that the Sn/Ge(111) system is abnormal.

6.3 Summary

In summary, it has been shown with STM the occurrence of a one-dimensional Defect Density Wave concurrent with a 1-D electronic wave, which is apparently incommensurate with the underlying lattice. Together, the Sn/Ge and Sn/Si thin film systems present a magnificent arena for the study of the dynamics of defects in a two dimensional phase transition. Undoubtedly, this is just the beginning since there are far more questions than answers.

References for Part 6

Baldea, I. and Apostol M. (1985). "Modulated-Impurity Mechanism of Pinning in Kcp." Journal of Physics C-Solid State Physics **18**(33): 6135-6147.

Baldea, I. and Badescu M. (1993). "Quasi-Regular Impurity Distribution Driven by a Charge-Density- Wave." Physical Review B-Condensed Matter **48**(12): 8619-8628.

Breuer, K., Stagerescu C., Smith K. E., Greenblatt M. and Ramanujachary K. (1996). "Observation of hidden Fermi surface nesting in a two dimensional conductor." Physical Review Letters **76**(17): 3172-3175.

Bunk, O., Zeysing J. H., Falkenberg G., Johnson R. L., Nielsen M., Nielsen M. M. and Feidenhans R. (1999). "Phase transitions in two dimensions: The case of Sn adsorbed on Ge(111) surfaces." Physical Review Letters **83**(11): 2226-2229.

Carpinelli, J. M., Weitering H. H., Barkowiak M., Stumpf R. and Plummer E. W. (1997). "Surface charge ordering transition: alpha phase of Sn/Ge(111)." Physical Review Letters **79**(15): 2859-2862.

Conway, K. M., Macdonald J. E., Norris C., Vlieg E. and Vanderveen J. F. (1989). "The Structure of the Si(111)(Square-Root3xsquare-Root3)R30- Degrees-Sn Surface Determined Using X-Ray-Diffraction." Surface Science **215**(3): 555-565.

Flores, F., Ortega J., Perez R., Charrier A., Thibaudau F., Debever J. M. and Themlin J. M. to be published in Prog. in Surf. Science.

Halperin, B. I. and Varma C. M. (1976). “Defects and Central Peak near Structural Phase-Transitions.” Physical Review B-Condensed Matter **14**(9): 4030-4044.

Kinoshita, T., Kono S. and Sagawa T. (1986). “Angle-resolved photelectron-spectroscopy study of the Si(111) root3xroot3-Sn surface: comparison with Si(111) root3xroot3-Al, -Ga, and -In surfaces.” Phys. Rev. **B34**(4): 3011.

Melechko, A. V., Braun J., Weitering H. H. and Plummer E. W. (2000). “Role of defects in two-dimensional phase transitions: An STM study of the Sn/Ge(111) system.” Physical Review B **61**(3): 2235-2245.

Nogami, J., Park S. I. and Quate C. F. (1989). “Structure of Submonolayers of Tin on Si(111) Studied by Scanning Tunneling Microscopy.” Journal of Vacuum Science & Technology a-Vacuum Surfaces and Films **7**(3): 1919-1921.

Ottaviano, L., Crivellari M., Lozzi L. and Santucci S. (2000a). “STM investigation of the alpha-Sn/Si(111) phase at 120 K.” Surface Science **445**(1): L41-L46.

Ottaviano, L., Crivellari M., Profeta G., Continenza A., Lozzi L. and Santucci S. (2000b). “Origin, symmetry, and temperature dependence of the perturbation induced by Si extrinsic defects on the Sn/Si(111) alpha surface: A scanning tunneling microscopy study.” Journal of Vacuum Science & Technology a-Vacuum Surfaces and Films **18**(4): 1946-1949.

Ottaviano, L., Profeta G., Continenza A., Santucci S., Freeman A. J. and Modesti S. (2000c). “Defect-induced perturbation on the 1/3 ML Sn-Si(111) surface: a

voltage-dependent scanning tunneling microscopy study." Surface Science **464**(2-3): 57-67.

Profeta, G., Continenza A., Ottaviano L., Mannstadt W. and Freeman A. J. (2000). "Structural and electronic properties of the Sn/Si(111)root 3x root 3R30 degrees surface." Physical Review B **62**(3): 1556-1559.

Tornevik, C., Gothelid M., Hammar M., Karlsson U. O., Nilsson N. G., Flodstrom S. A., Wigren C. and Ostling M. (1994). "Adsorption of Sn on Si(111)7x7 - Reconstructions in the Monolayer Regime." Surface Science **314**(2): 179-187.

Uhrberg, R. I. G. (2000a). Personal Communication.

Uhrberg, R. I. G., Zhang H. M., Balasubramanian T., Jemander S. T., Lin N. and Hansson G. V. (2000b). "Electronic structure of Sn/Si(111) root 3X root 3: Indications of a low-temperature phase." Physical Review B **62**(12): 8082-8086.

Whangbo, M. H., Canadell E., Foury P. and Pouget J. P. (1991). "Hidden Fermi-Surface Nesting and Charge-Density Wave Instability in Low-Dimensional Metals." Science **252**(5002): 96-98.

Appendixes

```
c234567
      program main
      implicit none

c     This is a program to simulate charge rearrangement around defects and vacancies

      integer ii,id,ndim1,ndim2
      parameter(ii=96,id=97,ndim1=3000,ndim2=100)
      integer i,i1,i2,j1,j2,np,ndef,nvac
      integer idf(ndim2,2), ivc(ndim2,2)
      real r3,a,amr3,amhc,dam,rx,ry,rdx,rdy,z,xymax,dxy
      real a1(2),a2(2),sz(ndim1,ndim1)
      real hcomb,rthree
c
      open(ii,file="sim.inp",form="formatted",status="old")
      open(id,file="sim.dat",form="formatted",status="unknown")
      read(ii,*) a
      r3=sqrt(3.)
      a1(1)=.5*r3*a
      a1(2)=.5*a
      a2(1)=-.5*r3*a
      a2(2)=.5*a
c
      read(ii,*) np,xymax
      i=np-1
      dxy=xymax/(1.*i)
      read(ii,*) amr3,amhc
      read(ii,*) ndef,dam
      do 10000 i=1,ndef
        read(ii,*) idf(i,1),idf(i,2)
10000 continue
      write(*,*) '10000 passed'
      read(ii,*) nvac
      do 10010 i=1,nvac
        read(ii,*) ivc(i,1),ivc(i,2)
10010 continue
c
c==== create the root 3 pattern
c
c     initialize array
      do 20010 i1=1,np
        do 20020 i2=1,np
          sz(i1,i2)=0.
```

```
20020   continue
20010 continue
c
c     calculate root 3 for each point of the surface (sz)
      write(*,*) 'create root 3 pattern'
      do 30010 i1=1,np
        j1=i1-1
        do 30020 i2=1,np
          j2=i2-1
          rx=j1*dxy
          ry=j2*dxy
          sz(i1,i2)=rthree(rx,ry,a,amr3)
30020   continue
30010 continue
c
c     add honey comb pattern around defects
      do 40000 i=1,ndef
        rdx=idf(i,1)*a1(1)+idf(i,2)*a2(1)
        rdy=idf(i,1)*a1(2)+idf(i,2)*a2(2)
        do 40010 i1=1,np
          j1=i1-1
          do 40020 i2=1,np
            j2=i2-1
            rx=j1*dxy-rdx
            ry=j2*dxy-rdy
            sz(i1,i2)=sz(i1,i2)+hcomb(rx,ry,a,dam,amhc)
40020     continue
40010   continue
40000 continue

c     add hexagonal pattern around vacancies
      do 40001 i=1,nvac
        rdx=ivc(i,1)*a1(1)+ivc(i,2)*a2(1)
        rdy=ivc(i,1)*a1(2)+ivc(i,2)*a2(2)
        do 40011 i1=1,np
          j1=i1-1
          do 40021 i2=1,np
            j2=i2-1
            rx=j1*dxy-rdx
            ry=j2*dxy-rdy
            sz(i1,i2)=sz(i1,i2)-hcomb(rx,ry,a,dam,amhc)
40021     continue
40011   continue
40001 continue
c
```

```
c==== write data file
      do 50010 i1=1,np
        do 50020 i2=1,np
          write(id,'(e12.4)') sz(i2,i1)
50020   continue
50010 continue
      close(id)
      end
c
cf====
      real function rthree(x,y,a,ampl)
      real pi,r3, kx1, kx2, kx3, ky1, ky2, ky3, kkx1, kkx2, kkx3
      parameter(pi=3.141592654,r3=1.732050808)
      real x,y,a,k0,f,ampl
c

      k0=pi/a
      kx1=4*k0/r3
      ky1=0
      kx2=2*k0/r3
      ky2=2*k0
      kx3=-kx2
      ky3=ky2
      f=cos(kx1*x+ky1*y)+cos(kx2*x+ky2*y)+cos(kx3*x+ky3*y)

      rthree=f*ampl
      return
      end
c
cf====
      real function hcomb(x,y,a,dam,ampl)
      real pi,r3, kx1, kx2, kx3, ky1, ky2, ky3, kkx1, kkx2, kkx3
      real kky1, kky2, kky3
      parameter(pi=3.141592654,r3=1.732050808)
      real x,y,a,dam,k0,f,ampl
c

      k0=pi/a
      kx1=4*k0/r3
      ky1=0
      kx2=2*k0/r3
      ky2=2*k0
      kx3=-kx2
      ky3=ky2
      kkx1=2*k0/r3
```

```
      kky1=2*k0/3.
      kkx2=0.
      kky2=4*k0/3
      kkx3=-kkx1
      kky3=kky1
      f=exp(-dam*sqrt(x**2+y**2))*ampl*
     #(cos(kkx1*x+kky1*y)+cos(kkx2*x+kky2*y)+cos(kkx3*x+kky3*y))

      hcomb=f
      return
      end
```

Sample input file:

```
0.7
601     45.
1.      -1.
75      0.5
30      0
32      1
33      1
33      9
34      14
36      15
36      17
38      13

… etc'

60      16
60      17
60      27
61      11
62      21
62      11
63      34
63      28
63      17
63      14
64      31
64      30
2
44      29
54      16
```

Appendix B: Statistical Analysis of defect distributions

Computer code (Fortran) for statistical analysis

```
C     Program to analyse defect distributions in STM-images
C     of alpha-Sn/Ge(111)
C
C     Input file: stsmall1.inp
C     Structure:
C     nsa   nsht   mindf
C     ndf
C     filename_1
C     filename_2
C          :
C     filename_ndf
C
C     nsa .... length of an edge of the sampling area in 3x3
C              lattice spacings (typical values: 3-5, most
C              frequently used: 4)
C     nsht ... number of sampling areas randomly selected from
C              one image (typical values: 10-50 (depends on the
C              size of the image), most frequently used: 25)
C     mindf .. minimum number of defect in the sampling area
C              (typical value and most frequently used: 3 (smaller
C              number doesn't make sense))
C     ndf .... number of data files
C
C     Data file:
C     Structure:
C     header line
C     header line
C     header line
C     1    defect_1_x   defect_1_y   1
C     2    defect_2_x   defect_2_y   1
C     :       :          :         :
C
C     defect_*_x, defect_*_y are the coordinates of defect_*
C
C     Jens Braun, 01/15/99

      program main
      implicit none
c
      integer in,id,il,if,maxfn,maxr,maxdf,maxcnt
```

```
      parameter(in=96,id=97,il=98,if=99,maxfn=300,maxr=300,maxdf=300,
     #          maxcnt=6)
      integer i,i1,i2,ix,j,k,l
      integer nsa,nsht,mindf,ndf
      integer c1(2),c2(2)
      integer ia,ib,ic,ra(2),rb(2),rc(2)
      integer nsa3,nsa3m,nsa3l
      integer asit(maxr,2),bsit(maxr,2),csit(maxr,2)
      integer nd,dmin1,dmin2,dmax1,dmax2,rdmax1,rdmax2
      integer dfct(maxdf,2)
      integer npa,npb,npc,r0(2),rp(2)
      integer nps,npgrp,npmin,ntot
      integer ncount(maxcnt),ncntf(maxcnt)
      real wrng,dcount,x1,x2,x,ev
      character*30 fname(maxfn)
      character*75 hline
      logical sigcnt
c
c
      write(6,'(/a/)') ' Sn/Ge small area statistics v.1'
c
c----- open input file for file names and parameters, dat file
      open(in, file="stsmall1.inp", form="formatted", status="old")
      open(id, file="stsmall1.dat", form="formatted", status="unknown")
      open(il, file="stsmall1.log", form="formatted", status="unknown")
c
c----- read parameters and file names
      read(in,*) nsa, nsht, mindf
      read(in,*) ndf
      do 10000 i=1,ndf
        read(in,*) fname(i)
10000  continue
      close(in)
      dcount=1./(3.*maxcnt)
      do 10005 i=1,maxcnt
        ncount(i)=0
10005  continue
c
c----- create 3 arrays with indices for A, B, C sites
c      vectors 3x3 cell
      c1(1)=2
      c1(2)=1
      c2(1)=1
      c2(2)=2
      nsa3=3*nsa
```

```
      nsa3m=nsa3-1
      nsa3l=5*nsa3
c----- write indices for A,B,C sites
      ia=0
      ib=0
      ic=0
      do 20010 i1=-nsa3l,nsa3l
        do 20020 i2=-nsa3l,nsa3l
          ra(1)=i1*c1(1)+i2*c2(1)
          ra(2)=i1*c1(2)+i2*c2(2)
          rb(1)=i1*c1(1)+i2*c2(1)+1
          rb(2)=i1*c1(2)+i2*c2(2)+1
          rc(1)=i1*c1(1)+i2*c2(1)+2
          rc(2)=i1*c1(2)+i2*c2(2)+2
          if ((ra(1).ge.0).and.(ra(1).le.nsa3m).and.(ra(2).ge.0)
     #     .and.(ra(2).le.nsa3m)) then
            ia=ia+1
            asit(ia,1)=ra(1)
            asit(ia,2)=ra(2)
          end if
          if ((rb(1).ge.0).and.(rb(1).le.nsa3m).and.(rb(2).ge.0)
     #     .and.(rb(2).le.nsa3m)) then
            ib=ib+1
            bsit(ib,1)=rb(1)
            bsit(ib,2)=rb(2)
          end if
          if ((rc(1).ge.0).and.(rc(1).le.nsa3m).and.(rc(2).ge.0)
     #     .and.(rc(2).le.nsa3m)) then
            ic=ic+1
            csit(ic,1)=rc(1)
            csit(ic,2)=rc(2)
          end if
20020     continue
20010   continue
c
c----- loop over all images
       do 30000 i=1,ndf
         do 30001 j=1,maxcnt
           ncntf(j)=0
30001     continue
         open(if,file=fname(i),form="formatted",status="old")
         read(if,'(a)') hline
         read(if,'(a)') hline
         read(if,'(a)') hline
         nd=1
```

```
        dmin1=100
        dmin2=100
        dmax1=-100
        dmax2=-100
30010    continue
         read(if,*,end=30020) ix,dfct(nd,1),dfct(nd,2),ix
         if (dfct(nd,1).lt.dmin1) dmin1=dfct(nd,1)
         if (dfct(nd,1).gt.dmax1) dmax1=dfct(nd,1)
         if (dfct(nd,2).lt.dmin2) dmin2=dfct(nd,2)
         if (dfct(nd,2).gt.dmax2) dmax2=dfct(nd,2)
         nd=nd+1
        goto 30010
30020    continue
        nd=nd-1
        close(if)
c------- write log file
        write(il,'(a,a)') '---------------------------- ',fname(i)
        write(il,'(a,i5)') '--- Defects:',nd
        write(6,'(a,a)') '--- ',fname(i)
        write(6,'(a,i5)') '    Defects:',nd
        write(il,'(a)')
   #  '   #    o1   o2    #Def.    A    B    C    w     G'
c------- set origin to (0,0)
        dmax1=dmax1-dmin1
        dmax2=dmax2-dmin2
        rdmax1=dmax1-nsa3
        rdmax2=dmax2-nsa3
        do 30100 j=1,nd
         dfct(j,1)=dfct(j,1)-dmin1
         dfct(j,2)=dfct(j,2)-dmin2
30100    continue
c
c------- random loop
c        initalization
        call srand(nd)
        j=0
30200    continue
         r0(1)=int(rand()*(rdmax1+1))
         r0(2)=int(rand()*(rdmax2+1))
         npa=0
         npb=0
         npc=0
         do 30210 k=1,nd
          rp(1)=dfct(k,1)-r0(1)
          rp(2)=dfct(k,2)-r0(2)
```

```
          if ((rp(1).ge.0).and.(rp(1).lt.nsa3).and.(rp(2).ge.0)
     #       .and.(rp(2).lt.nsa3)) then
c             defect inside patch
              sigcnt=.true.
c             check if site A
              do 30220 l=1,ia
                if ((rp(1).eq.asit(l,1)).and.(rp(2).eq.asit(l,2))) then
                  npa=npa+1
                  sigcnt=.false.
                end if
30220           continue
              if (sigcnt) then
                do 30230 l=1,ib
                  if ((rp(1).eq.bsit(l,1)).and.(rp(2).eq.bsit(l,2)))
     #             then
                    npb=npb+1
                    sigcnt=.false.
                  end if
30230             continue
              end if
              if (sigcnt) then
                npc=npc+1
              end if
            end if
30210       continue
c           analysis of the results
            nps=npa+npb+npc
            if (nps.ge.mindf) then
              j=j+1
              if (npa.lt.npb) then
                if (npa.lt.npc) then
                  npmin=npa
                else
                  npmin=npc
                end if
              else
                if (npc.lt.npb) then
                  npmin=npc
                else
                  npmin=npb
                end if
              end if
              wrng=1.*npmin/(1.*(npa+npb+npc))
              do 30400 k=1,maxcnt
                x1=(k-1)*dcount
```

```
            x2=k*dcount
            if ((wrng.ge.x1).and.(wrng.lt.x2)) npgrp=k
30400         continue
           ncount(npgrp)=ncount(npgrp)+1
           ncntf(npgrp)=ncntf(npgrp)+1
           write(il,'(i5,i6,i5,i9,i5,i5,i5,f6.2,i5)')
     #      j,r0(1)+dmin1,r0(2)+dmin2,nps,npa,npb,npc,wrng,npgrp
         end if
       if (j.lt.nsht) goto 30200
30300    continue
       write(il,'(a)') '--- Statistics:'
       write(il,'(a)') '    Group   Cnts'
       do 30301 j=1,maxcnt
         write(il,'(i9,i7)') j,ncntf(j)
30301    continue
       write(il,'(a,a/)') '--- End of ',fname(i)
30000  continue
c
c----- normalize and write data file
      do 40001 i=1,maxcnt
       ntot=ntot+ncount(i)
40001  continue
      ev=0.
      write(il,'(a)') '****************** Final Results'
      write(il,'(/a)') ' Group    Probab.'
      do 40002 i=1,maxcnt
       x=1.*ncount(i)/(1.*ntot)
       ev=ev+x*i
       write(id,'(i6,f10.3)') i,x
       write(il,'(i6,f10.3)') i,x
40002  continue
      write(il,'(a,f10.3)') ' Expectation Value: ', ev
      write(il,'(/a)') '****************** End'
      write(6,*)
      close(il)
      close(id)
      end
```

Appendix C: Charge Compensation Model

```
// This is an implementation of Charge Compensation Model
// It takes three input files: parameters.txt, coordefects.txt, and initial.txt
//  1.     density of defects
//  1a.  defect coordinates
//  2.     R
//  3.     number of iterations
//         4.         g4 for saturation
//  5.     area size  (for image output)
//  6.   origin positions (for image output)
//
//  version 6. Adding more terms beside cubic to saturation function
// slite change to the way I calculate q(atomZ)
// version 8. Separated calcAmpl into several function for better
// readability
//*************************************************************

#include <fstream.h>
#include <stdlib.h>
#include <stdio.h>
#include <math.h>
#include <string.h>
#include <iostream.h>

const unsigned short int NUM_PIX = 512; // Number of pixels in x and y directions
const unsigned short int NUM_ROW = 1000; // Number of atoms in a row
const unsigned short int NUM_COL = 1000; // Number of atoms in a colomn
const double AREA_SIZE=100.0;
const double PI=3.1419526654;


double **dmatrix(long nrow, long ncol);
int calcAmpl(double **atomZ, int numIter, int numDef,
                                    int *defCol, int *defRow, double amplDef,
                                    double Rcurrent, double g4_2,
                                    double g6_3, double g8_4, double convergeSteps,double
pres);
void readDefects(char *filename, int *numDef, int *defCol, int *defRow);
void readParameters(char *filename,
                                     double *amplDef, double *g4, double *g6, double *g8,
                                    int *originCol, int *originRow, int *numIter,
                                    double *Rini, double *Rfin, int *Rsteps, double
*convergeSteps,
                                    double *pres);
```

```
int calcPixZ(double **pixZ, double pixd,
                        int originCol, int originRow, double **atomZ);
void writeFilePixZ(char *filename, double **pixZ);
double saturate(double x, double g4, double g6, double g8,double pres);
double disPixAtom(double pixX, double pixY, int icol, int jrow);
void readInit(char *fileinit,int *numInit,
                        int *iInit,int *jInit,double *aInit);
double calcEnergy(double **atomZ,double Rcurrent,double g4, double g6, double g8);
double fun(double x,double g4_2,double g6_3,double g8_4,double Rsum);
double derfun(double x,double g4_2,double g6_3,double g8_4);
int calcCharge(int icol, int jrow,double **atomZ, int numDef,
                                int *defCol, int *defRow, double amplDef,
                                double Rcurrent, double g4_2,
                                double g6_3, double g8_4, double convergeSteps,
                                double pres, double **oldAtomZ);
int neutrality(int *defCol,int *defRow,int numDef,int icol,int jrow,
                        double deltaCharge,double **atomZ,double **oldAtomZ,
                        double convergeSteps);


//*************************************************************
//              MAIN
FILE   *writeFP;

int main()
{
        double Rcurrent; //sum of cosinus (3x3) waves times exponential
                                                // decay
        char    filenamePar[50]="parameters.txt";
        char    filenameCor[50]="coordefects.txt";
        char    fileblame[50];
        char    fileinit[50]="initial.txt";
        double  pixd;           // distance between pixels
        double **pixZ;
        double **pixDef;
        double **atomZ;
        double  Rini,Rfin;
        int             ki,kj;
        char    fileEnergy[50]="energy.dat";
        double stp;

        //*****    will come from input file   ******
        double amplDef;
        int             originCol;
```

```
int             originRow;
int             numDef;
int             numInit;
int             numIter;
int             *defCol,
                *defRow;
double g4,g4_2;
double g6,g6_3;
double g8,g8_4;
int             Rsteps;
double totCharge1;
double convergeSteps;

int             *iInit;
int             *jInit;
double *aInit;

double  pres;

//*****************

double energy;



//******    input from screen   **************

//      printf("Enter defect coords file name: ");
        //scanf("%s", filenameCor);
        //printf("Enter parameters file name: ");
        //scanf("%s", filenamePar);
        printf("Enter number of defects: ");
        scanf("%d", &numDef);
        //printf("Enter inital conditions file name: ");
        //scanf("%s", fileinit);
        printf("Enter number of atoms for initial condictions: ");
        scanf("%d", &numInit);

        //*******************************************



        pixd=AREA_SIZE/NUM_PIX;

        pixZ   = dmatrix(NUM_PIX, NUM_PIX);
```

```
        pixDef = dmatrix(NUM_PIX, NUM_PIX);
        atomZ  = dmatrix(NUM_COL, NUM_ROW);

defCol = (int *) malloc(sizeof(int)*numDef);
        defRow = (int *) malloc(sizeof(int)*numDef);

        iInit = (int *) malloc(sizeof(int)*numInit);
jInit = (int *) malloc(sizeof(int)*numInit);
        aInit = (double *) malloc(sizeof(double)*numInit);

        readDefects(filenameCor,&numDef, defCol,defRow);
        readParameters(filenamePar, &amplDef,&g4,&g6,&g8,

        &originCol,&originRow,&numIter,&Rini,&Rfin,&Rsteps,
                                        &convergeSteps,&pres);

        for (int k=0;k<numInit;k++)
        {
                iInit[k]=0;
                jInit[k]=0;
        }


        readInit(fileinit,&numInit,iInit,jInit,aInit);



        FILE *fp;


        fp=fopen(fileEnergy, "w");
        if (fp==NULL)
        {
                perror("charge1");
                exit(1);
        }

        stp=(Rfin-Rini)/Rsteps;

        //*************** initialization ********************
                for (int i=0; i<NUM_COL; i++)
                {
                        for (int j=0; j<NUM_ROW; j++)
                        {
                                atomZ[i][j]=0;
```

```
//                      oldAtomZ[i][j]=0;
                        }// end rows
                }// end colomns

                for (k=0;k<numInit;k++)
                {
                        ki=iInit[k];
                        kj=jInit[k];

                        atomZ[ki][kj]=aInit[k];
                        //printf("atomZ %d, %d = %lf\n",ki,kj,aInit[k]);
                }
                //*************** end initialization ***********88

        for(int countRstep=0;countRstep<Rsteps; countRstep=countRstep++)
        {

                //*************** initialization ********************
                for (int i=0; i<NUM_COL; i++)
                {
                        for (int j=0; j<NUM_ROW; j++)
                        {
                                atomZ[i][j]=0;
//                      oldAtomZ[i][j]=0;
                        }// end rows
                }// end colomns

                for (k=0;k<numInit;k++)
                {
                        ki=iInit[k];
                        kj=jInit[k];

                        atomZ[ki][kj]=aInit[k];
                //      printf("atomZ %d, %d = %lf\n",ki,kj,aInit[k]);
                }
                //*************** end initialization ***********88

                g4_2=g4*2;
                g6_3=g6*3;
                g8_4=g8*4;

                calcPixZ(pixZ,pixd,
                         originCol,originRow,atomZ);

                sprintf(fileblame,"imageInitial.dat");
```

```
                writeFilePixZ(fileblame, pixZ);


                Rcurrent=Rini+stp*countRstep;



        calcAmpl(atomZ,numIter,numDef,defCol,defRow,amplDef,Rcurrent,g4_2,g6_3,
g8_4,convergeSteps,pres);
                calcPi xZ(pixZ,pixd,
                        originCol,originRow,atomZ);


                sprintf(fileblame,"image%d.dat",countRstep);
                writeFilePixZ(fileblame, pixZ);
                //************* total charge calculation ************
                //************* total energy calculation ************
                energy=calcEnergy(atomZ,Rcurrent,g4,g6,g8);
                totCharge1=0;

//              for (int icol=0; icol<NUM_COL;icol++)// colomns
//              {
//                      for(int jrow=0;jrow<NUM_ROW;jrow++)//rows
//                      {
//                              totCharge1=totCharge1+atomZ[icol][jrow];
//                      }
//              }
//              fprintf(fp,"%8.3lf\n",totCharge1);
                fprintf(fp,"Rcurrent= %8.3lf, Energy= %8.3lf\n",Rcurrent,energy);
                //************ totoal charge ***************************


        } // end-for(countRstep)


        return 0;
}
//              End of MAIN
//************************************************************

double calcEnergy(double **atomZ,double Rcurrent,double g4,double g6,double g8)
{
        double energy;
        double x,x2,x4;
        double sumNN;
```

```
int nncol;
int nnrow;
int a[6];
int b[6];

        a[0]=1;
        b[0]=0;
        a[1]=0;
        b[1]=-1;
        a[2]=-1;
        b[2]=-1;
        a[3]=-1;
        b[3]=0;
        a[4]=0;
        b[4]=1;
        a[5]=1;
        b[5]=1;

energy=0;
for (int icol=0; icol<NUM_COL;icol++)// colomns
        {
                for(int jrow=0;jrow<NUM_ROW;jrow++)//rows
                {
                        x=atomZ[icol][jrow];
                        sumNN=0;
                        // **** sum over first nearest neighbors ****
                        for (int nn=0; nn<6; nn++)
                        {
                                nncol=icol+a[nn];
                                nnrow=jrow+b[nn];
                                //check if it is in the boundaries
                                if
((nncol<NUM_COL)&&(nncol>=0)&&(nnrow<NUM_ROW)&&(nnrow>=0))
                                {
                                        sumNN=sumNN+atomZ[nncol][nnrow];
                                }
                        }// end-for(nn) nearest neighbors
                        x2=x*x;
                        x4=x2*x2;

energy=energy+x*x+2*Rcurrent*x*sumNN+x4*(g4+g6*x2+g8*x4);

                }
        }
return energy;
```

```
}

void readInit(char *fileinit, int *numInit,
                        int *iInit,int *jInit,double *aInit)
{
        FILE *fp;
        char name[30];
        int  index;
        int  i;

        fp=fopen(fileinit, "r");
        if (fp==NULL)
        {
                perror("readInit");
                exit(1);
        }


        fscanf(fp, "%s %d",name, numInit);

        for (i=0; i<4; i++) fscanf(fp, "%s",name);

        for(i=0; i<*numInit; i++)
        {
                fscanf(fp, "%d\t%d\t%d\t%lf", &index, &iInit[i], &jInit[i],&aInit[i]);
                printf("reading initial %d\n",i);
        }
}

//*****************************************************************/
void writeFilePixZ(char *filename, double **pixZ)
{
        FILE *fp;

        fp=fopen(filename, "w");
        if (fp==NULL)
        {
                perror("writeFilePixZ");
                exit(1);
        }

        for (int j=0; j<NUM_PIX; j++)
        {
                for(int i=0; i<NUM_PIX; i++)
                {
```

```
                        fprintf(fp,"%8.3lf\t", pixZ[i][j]);
                }
                fprintf(fp,"\n");

        }

}

//*************************************************************
int calcPixZ(double **pixZ, double pixd,
                         int originCol, int originRow, double **atomZ)
{
        double mindis,dis;
        double originX,originY;
        int beginRow,beginCol;
        int currentAtomCol,currentAtomRow;
        int imin, jmin;
        int atomCol,atomRow;
                //---------------------------------
        // initialize pixZ
        double pixX, pixY;
        double const rad=0.7;  //radius of the ball
        double A1[2],A2[2];
        int a[7],b[7];

        for (int iPix=0; iPix<NUM_PIX; iPix++)
        {
                for (int jPix=0; jPix<NUM_PIX; jPix++)
                {
                        pixZ[iPix][jPix]=0;

                }// end rows
        }// end colomns
        //---------------------------------


                A1[0] = 1;              A1[1] = 0;
                A2[0] = -0.5;   A2[1] = sqrt(3)/2;


                a[0]=1;
                b[0]=0;
                a[1]=0;
                b[1]=-1;
                a[2]=-1;
```

```
		b[2]=-1;
		a[3]=-1;
		b[3]=0;
		a[4]=0;
		b[4]=1;
		a[5]=1;
		b[5]=1;
		a[6]=0;
		b[6]=0;

	originX=A1[0] * originCol + A2[0] * originRow;
	originY=A1[1] * originCol + A2[1] * originRow;

	beginRow=originRow;
	beginCol=originCol;
//printf("beginRow %d\n",beginRow);


	for (iPix=0; iPix<NUM_PIX; iPix++)
	{
		pixX=iPix*pixd+originX;
		pixY=originY;
	//	printf("doing colomn %d\n",iPix);

		//1. find in proximity of what atom (out of 6 nn ) it is located.
			mindis=1000;
			for (int inn=0; inn<7; inn++)
			{
				atomCol=beginCol+a[inn];
				atomRow=beginRow+b[inn];
			//	printf("atomRow %d\n",atomRow);
				dis=disPixAtom(pixX,pixY,atomCol,atomRow);
				if (dis<mindis)
					{
						imin=atomCol;
						jmin=atomRow;
						mindis=dis;

					}
			}

			beginCol=imin;
			beginRow=jmin;

//printf("\n\n\nBEGIN COL %d\n\n\n",beginCol);
```

```
		currentAtomCol=beginCol;
		currentAtomRow=beginRow;
	//	printf("\n\n\ncurrentAtomRow 1111 %d\n\n\n",currentAtomRow);
				//printf("currentAtomCol %d\n",currentAtomCol);


	for (int jPix=0; jPix<NUM_PIX; jPix++)
	{

		pixY=jPix*pixd+originY;

		//1. find in proximity of what atom (out of 6 nn ) it is located.
		mindis=1000;
		for (int inn=0; inn<7; inn++)
		{
			atomCol=currentAtomCol+a[inn];
			atomRow=currentAtomRow+b[inn];
			dis=disPixAtom(pixX,pixY,atomCol,atomRow);
			if (dis<mindis)
				{
					currentAtomCol=atomCol;
					currentAtomRow=atomRow;
					//	printf("currentAtomCol
%d\n",currentAtomCol);

					mindis=dis;
				}
		}

		for (inn=0; inn<7; inn++)
		{
			atomCol=currentAtomCol+a[inn];
			atomRow=currentAtomRow+b[inn];
			dis=disPixAtom(pixX,pixY,atomCol,atomRow);
			if (dis<mindis)
				{
					currentAtomCol=atomCol;
					currentAtomRow=atomRow;
					//	printf("currentAtomCol
%d\n",currentAtomCol);

					mindis=dis;
				}
		}
```

```
                        //printf("before pixZ currentAtomCol %d\n",currentAtomCol);
                //      printf("before pixZ currentAtomCol %d\n",currentAtomCol);
                //if(mindis>rad)
                //{printf("mindis is too big %lf\n", mindis);}

                        pixZ[iPix][jPix]=atomZ[currentAtomCol][currentAtomRow]+
                                1.5*sqrt(fabs(rad*rad-mindis*mindis));
                }// end rows
        }// end colomns
        return 0;
}

//*************************************************************************
*
double disPixAtom(double pixX, double pixY, int icol, int jrow)
{
        double dis;
        double A1[2],A2[2];
        double atomX,atomY;
        double disX, disY;


                A1[0] = 1;              A1[1] = 0;
                A2[0] = -0.5;   A2[1] = sqrt(3)/2;

      atomX = A1[0] * icol + A2[0] * jrow;
           atomY = A1[1] * icol + A2[1] * jrow;

                disX = pixX - atomX;
                disY = pixY - atomY;
                dis = sqrt(disX*disX + disY*disY);

        return dis;
}


//*****************************************************************
void readDefects(char *filenameCor, int *numDef, int *defCol, int *defRow)
{
        FILE *fp;
        char name[30];
        int  index;
        int  i;

        fp=fopen(filenameCor, "r");
```

```
	if (fp==NULL)
	{
		perror("readDefects");
		exit(1);
	}

	fscanf(fp, "%s %d",name, numDef);

	for (i=0; i<3; i++) fscanf(fp, "%s",name);

	for(i=0; i<*numDef; i++)
	{
		fscanf(fp, "%d %d %d", &index, &defCol[i], &defRow[i]);
	}
}

//*****************************************************************

void readParameters(char *filenamePar,
				double *amplDef, double *g4, double *g6, double *g8,
				int *originCol, int *originRow, int *numIter,
				double *Rini, double *Rfin, int *Rsteps, double
*convergeSteps,double *pres)
{
	FILE *fp;
	char name[30];


	fp=fopen(filenamePar, "r");
	if (fp==NULL)
	{
		perror("readDefects");
		exit(1);
	}


	fscanf(fp, "%s %lf",name, amplDef);
	fscanf(fp, "%s %lf",name, g4);
	fscanf(fp, "%s %lf",name, g6);
	fscanf(fp, "%s %lf",name, g8);
	fscanf(fp, "%s %d",name, originCol);
	fscanf(fp, "%s %d",name, originRow);
	fscanf(fp, "%s %d",name, numIter);
	fscanf(fp, "%s %lf",name, Rini);
	fscanf(fp, "%s %lf",name, Rfin);
```

```
	fscanf(fp, "%s %d",name, Rsteps);
	fscanf(fp, "%s %lf",name, convergeSteps);
	fscanf(fp, "%s %lf",name, pres);
}
//*****************************************************************
int calcAmpl(double **atomZ, int numIter, int numDef,
			int *defCol, int *defRow, double amplDef,
			double Rcurrent, double g4_2, double g6_3, double g8_4,
			double convergeSteps,double pres)
{
	double **oldAtomZ;
	char	filecharge[50]="charge.dat";
	int a[6],b[6];

	oldAtomZ = dmatrix(NUM_COL,NUM_ROW);

	a[0]=1;  b[0]=0;
	a[1]=0;  b[1]=-1;
	a[2]=-1; b[2]=-1;
	a[3]=-1; b[3]=0;
	a[4]=0;  b[4]=1;
	a[5]=1;  b[5]=1;

	for (int iter=0; iter<numIter; iter++)
	{

		printf("Doing iteration %d\n",iter);
		for (int i=0; i<NUM_COL; i++)
		{
			for (int j=0; j<NUM_ROW; j++)
			{
				oldAtomZ[i][j]=atomZ[i][j];
			}// end rows
		}// end colomns

		for (int icol=0; icol<NUM_COL;icol++)// froward colomns run
		{
			for(int jrow=0;jrow<NUM_ROW;jrow++)//forward rows run
			{
				calcCharge(icol,jrow,atomZ,numDef,
					defCol,defRow,amplDef,Rcurrent,g4_2,
					g6_3,g8_4,convergeSteps,pres,
oldAtomZ);
			}// end rows
```

```
                        for(int jrow1=0;jrow1<NUM_ROW;jrow1++)//backward rows run
                        {
                                jrow=NUM_ROW-jrow1-1;
                                calcCharge(icol,jrow,atomZ,numDef,
                                                defCol,defRow,amplDef,Rcurrent,g4_2,
                                                g6_3,g8_4,convergeSteps,pres,
oldAtomZ);
                        }// end rows
                }// end colomns

                for (int icol1=0; icol1<NUM_COL;icol1++)// backward colomns run
                {
                        icol=NUM_COL-icol1-1;

                        for(int jrow=0;jrow<NUM_ROW;jrow++)//forward rows run
                        {
                                calcCharge(icol,jrow,atomZ,numDef,
                                                defCol,defRow,amplDef,Rcurrent,g4_2,
                                                g6_3,g8_4,convergeSteps,pres,
oldAtomZ);
                        }// end rows

                        for(int jrow1=0;jrow1<NUM_ROW;jrow1++)//backward rows run
                        {
                                jrow=NUM_ROW-jrow1-1;
                                calcCharge(icol,jrow,atomZ,numDef,
                                                defCol,defRow,amplDef,Rcurrent,g4_2,
                                                g6_3,g8_4,convergeSteps,pres,
oldAtomZ);
                        }// end rows
                }// end colomns
        }// end iteractions
        return 0;
}
/*************************************************************/

double **dmatrix(long nrh, long nch)

/* allocate a double matrix to array of pointers to rows */
/* from Numerical Recipes in C */
{
  long nrl=0, ncl=0;
  long i, nrow=nrh-nrl+1,ncol=nch-ncl+1;
  double **m;
```

```
 /* allocate pointers to rows */
 m=(double **) malloc((size_t) ((nrow+1)*sizeof(double*)));
 if(!m) printf("allocation failure 1 in matrix()");
 m += 1;
 m -= nrl;

 /* allocate rows and set pointers to them */
 m[nrl]=(double *) malloc((size_t) ((nrow*ncol+1)*sizeof(double)));
 if(!m[nrl]) printf("allocation failure 2 in matrix()");
 m[nrl] += 1;
 m[nrl] -= ncl;

 for(i=nrl+1;i<=nrh;i++) m[i]=m[i-1]+ncol;
 /* return pointer to array of pointers to rows */
 return m;
}
//*****************************************************************


//*****************************************************************
double saturate(double x, double g4_2, double g6_3, double g8_4, double pres)
{
//      printf("I am saturating\n");
        double res,y;
        double Rsum;
        double der;

        Rsum=-x;

        y=fun(x,g4_2,g6_3,g8_4,Rsum);

        while (fabs(y)>pres)
        {
                y=fun(x,g4_2,g6_3,g8_4,Rsum);
                der=derfun(x,g4_2,g6_3,g8_4);
                x=x-y/der;
        }
        res=x;//sig*x;
        return res;
}
//*****************************************************************
double fun(double x,double g4_2,double g6_3,double g8_4,double Rsum)
{
        //printf("I am in fun\n");
        double res;
```

```
	double x2,x3;
	x2=x*x;
	x3=x2*x;

	res=x+Rsum+x3*(g4_2+g6_3*x2+g8_4*x*x3);

	return res;
}

//*********************************************************************
double derfun(double x,double g4_2,double g6_3,double g8_4)
{
	double res;
	double x2,x3;
	x2=x*x;
	x3=x2*x;
	res=1+3*g4_2*x2+5*g6_3*x2*x2+7*g8_4*x3*x3;

	return res;
}

//*********************************************************************
int neutrality(int *defCol,int *defRow,int numDef,int icol,int jrow,
			double diff,double **atomZ,double **oldAtomZ,
			double convergeSteps)
{
	int numNeighbors,nncol,nnrow,a[6],b[6],flag;
	double deltaCharge;
	numNeighbors=0;
	a[0]=1;  b[0]=0;
	a[1]=0;  b[1]=-1;
	a[2]=-1; b[2]=-1;
	a[3]=-1; b[3]=0;
	a[4]=0;  b[4]=1;
	a[5]=1;  b[5]=1;
	for (int nn=0; nn<6; nn++)
	{
		nncol=icol+a[nn];
		nnrow=jrow+b[nn];
		//check if it is in the boundaries
		if
((nncol<NUM_COL)&&(nncol>=0)&&(nnrow<NUM_ROW)&&(nnrow>=0))
		{
			flag = 0;
			//check if it is defect
```

```
                        for (int indDef=0; indDef<numDef; indDef++)
                        {
                                if
((nncol==defCol[indDef])&&(nnrow==defRow[indDef]))
                                {
                                        flag = 1;
                                        break;
                                }
                        } // end-for(indDef)
                        if (flag == 0)
                        {
                                numNeighbors++;
                        }
                }
        }// end-for(nn) nearest neighbors
        //*************** end of calculation of number of nearest neighbors
        if (numNeighbors > 0)
        {
           deltaCharge=-diff/(convergeSteps*numNeighbors);
        } else {
                deltaCharge = 0;
        }

        // update nearest neighbors
        for (nn=0; nn<6; nn++)
        {
                nncol=icol+a[nn];
                nnrow=jrow+b[nn];
                //check if it is in the boundaries
                if
((nncol<NUM_COL)&&(nncol>=0)&&(nnrow<NUM_ROW)&&(nnrow>=0))
                {
                        flag = 0;
                        //check if it is defect
                        for (int indDef=0; indDef<numDef; indDef++)
                        {
                                if
((nncol==defCol[indDef])&&(nnrow==defRow[indDef]))
                                {
                                        flag = 1;
                                        break;
                                }
                        } // end-for(indDef)
                        if (flag == 0)
                        {
```

```
        atomZ[nncol][nnrow]=oldAtomZ[nncol][nnrow]+deltaCharge;
                                oldAtomZ[nncol][nnrow]=atomZ[nncol][nnrow];
                        }
                }
        }// end-for(nn) nearest neighbors
        return 0;
}
//*************************************************************************
*****
int calcCharge(int icol, int jrow,double **atomZ, int numDef,
                                int *defCol, int *defRow, double amplDef,
                                double Rcurrent, double g4_2,
                                double g6_3, double g8_4, double convergeSteps,
                                double pres, double **oldAtomZ)
{
        double x,sumNeighbors,diff;
        char    filecharge[50]="charge.dat";
        int a[6],b[6],nncol,nnrow,flag;

        a[0]=1;  b[0]=0;
        a[1]=0;  b[1]=-1;
        a[2]=-1; b[2]=-1;
        a[3]=-1; b[3]=0;
        a[4]=0;  b[4]=1;
        a[5]=1;  b[5]=1;
        flag = 0;
        //check if it is defect and give it amplDef
        //printf("I am in calcCharg\n");
        for (int indDef=0; indDef<numDef; indDef++)
        {
                if ((icol==defCol[indDef])&&(jrow==defRow[indDef]))
                {
                        flag = 1;
                        break;
                }
        } // end-for(indDef)

        if (flag == 1)
        {
        //      printf("calcCharge, it is a defect\n");
                atomZ[icol][jrow]=amplDef;
                diff=atomZ[icol][jrow]-oldAtomZ[icol][jrow];
                atomZ[icol][jrow]=atomZ[icol][jrow];
```

```
                if(fabs(diff)>0.001)
                {

        neutrality(defCol,defRow,numDef,icol,jrow,diff,atomZ,oldAtomZ,convergeSteps
);
                }
        }
        else
        {
        //      printf("I am in calcCharg\n It is not a defect\n");
                sumNeighbors=0;
                // **** first nearest neighbors ****
                for (int nn=0; nn<6; nn++)
                {
                        nncol=icol+a[nn];
                        nnrow=jrow+b[nn];
                        //check if it is in the boundaries
                        if
((nncol<NUM_COL)&&(nncol>=0)&&(nnrow<NUM_ROW)&&(nnrow>=0))
                        {
                                sumNeighbors=sumNeighbors+oldAtomZ[nncol][nnrow];
                        //      printf("sumNeighbors= %lf\n",sumNeighbors);
                        }
                }// end-for(nn) nearest neighbors


                x=-sumNeighbors*Rcurrent;
                //printf("x= %lf\n",x);
                //printf("Rcurrent= %lf\n",Rcurrent);
                atomZ[icol][jrow]=saturate(x,g4_2,g6_3,g8_4,pres);

                //-----------------update the atom
                diff=atomZ[icol][jrow]-oldAtomZ[icol][jrow];
                atomZ[icol][jrow]=oldAtomZ[icol][jrow]+diff/convergeSteps;
                oldAtomZ[icol][jrow]=atomZ[icol][jrow];


        neutrality(defCol,defRow,numDef,icol,jrow,diff,atomZ,oldAtomZ,convergeSteps
);

        }//end else

        return 0;
}
```

Appendix D: Simulation of defect ordering phase transition

```
// Simulation of defects ordering phase transition
// Generates random numbers for defects distribution

//                                   INPUT PARAMETERS
//
//          thresh                   - threshold of the difference of z on
//          defect and the neighbor above which defect is moved.
//          DensDef                  - density of defects
//          NumDef=DensityDefects - number of defects
//          If NROWS and NCOLS is 100 then 600 correspond to 6%.
//          DecLen                   - the decay length
//          NROWS=24                 -j is always for rows
//          NCOLS=21                 -i is always for columns
//          on a triangular lattice
//          kB                       -is not really a Boltzman constant, it
//includes
//          another factor that controls mobility

//                    1.    GENERATE RANDOM DISTRIBUTION

#include <fstream.h>
#include <iostream.h>
#include <stdlib.h>
#include <stdio.h>
#include <time.h>
#include <math.h>
#include <string.h>

#define NROWS          100
#define NCOLS          100
#define NUM_BINS   6
const double PI=3.1415926654;
//#define kB           10              // ???? Boltzman's constant

void throwDefects(int *defCol, int *defRow, int numDef, int seed);
void measureOrder(int *defCol, int *defRow, int numDef, double *binSize, int numSA,
int seed);
void init_binSize(double *binSize);
void generateGrid(int shift, int sizeSA, int *colArray, int *rowArray, int *numSites);
void samlping(int sizeSA, int *defCol, int *defRow, int numDef,
                    int *siteACol, int *siteARow, int numASites,
                    int *siteBCol, int *siteBRow, int numBSites,
                    int *siteCCol, int *siteCRow, int numCSites,
```

```
                                double *binSize, int numSA, int seed);
double get_Zcoord(double ampl, double decLen, int atomCol, int atomRow,
                                        int *defCol, int *defRow, int numDef, double stepSat,
                                        double slopeSat);
void updateDefects(int numRepeat, double decLen, double thresh, double ampl,
                        double T, int *defCol, int *defRow, int numDef, double kB, int seed,
                        double stepSat, double slopeSat);
int is_movable(double atomZCoord, double defZCoord, double thresh, double T, double
kB, int seed);
int get_Zmin(double *atomZCoord, int *atomCol, int *atomRow, int numAtoms,
                                int *defCol, int *defRow, int numDef);
void initInputParams(char *file, double *T0, double *T1, double *dT, double *slope,
double *addParam,
                                                double *amplitude, double *threshold, int
*densDef, int *numRepeat,
                                                int *numSA, double *kB, double *stepSat, double
*slopeSat);
void dumpDefCoords2File(FILE *cfp, double T, double decLen,
                                                        int *defCol, int *defRow, int numDef,
double ampl,
                                                        double stepSat, double slopeSat);
void dumpBinSize2File(FILE *bfp, double T, double decLen, double *binSize);
double saturate(double x, double stepSat, double slopeSat);

ofstream writeTest("test.txt");

int k;


int main(int argc, char **argv)
{

  int           numDef;
  int           *defCol = NULL,
                        *defRow = NULL;
  int           numSteps;
  double        *binSize = NULL;
  double        decLen;
  double        T;
  char    coordFile[30];
  char    binFile[30] = "order.txt";
  char          inputFile[50];
  FILE          *cfp, *bfp;
  const int     BIG=123456;
  int           seed;
```

```
k=0;


  /* Input parameters */
  double        T0, T1, dT;
  double        slope, addParam;
  double        amplitude;
  double        threshold;
  int           densDef;
  int           numRepeat;
  int           numSA;
  double   kB;
  double        stepSat;
  double        slopeSat;
//  double       origin;

  //if (argc != 2)
  //{
        //  printf("Usage: sim.exe inputFile\n");
         // exit(1);
  //}

  //strcpy(inputFile, argv[1]);

  strcpy(inputFile, "inputFile.txt");

  //cout<<"Please input the density of defects (int: 1-100)  ";
  //cin>>densDef;


  bfp = fopen(binFile, "w");

  if (bfp==NULL)
  {
          perror("Error opening out files\n");
          exit(1);
  }

        srand( (unsigned)time( NULL ) );
        seed=rand()%BIG;

  initInputParams(inputFile, &T0, &T1, &dT, &slope, &addParam,
                                        &amplitude, &threshold, &densDef, &numRepeat,
                                        &numSA, &kB, &stepSat, &slopeSat);
```

```
writeTest<<"kB in main   "<<kB<<"\n";
numDef=densDef;
binSize = (double *) malloc(sizeof(double) * NUM_BINS);
defCol = (int *) malloc(sizeof(int) * numDef);
defRow = (int *) malloc(sizeof(int) * numDef);

        ofstream writePc("Pc.txt");


        T = T0;
        init_binSize(binSize);
        throwDefects(defCol, defRow, numDef, seed);
        decLen = 1./(addParam + slope * T);

        measureOrder(defCol, defRow, numDef, binSize, numSA, seed);

        sprintf(coordFile,"coordinates.%d.txt",0);
        cfp = fopen(coordFile, "w");
          if (cfp==NULL)
          {
            perror("Error opening out files\n");
            exit(1);
          }
        dumpDefCoords2File(cfp, T, decLen, defCol, defRow, numDef, amplitude,
                stepSat, slopeSat);
        fclose(cfp);

        dumpBinSize2File(bfp, T, decLen, binSize);
        writePc<<T<<"\t"<<binSize[0]<<"\n";


numSteps = (int)(fabs(T1-T0) / fabs(dT));

for (int i=1; i<numSteps; i++)
{
          sprintf(coordFile,"coordinates.%d.txt",i);
          cfp = fopen(coordFile, "w");
          if (cfp==NULL)
          {
            perror("Error opening out files\n");
            exit(1);
          }
          init_binSize(binSize);
          T = T + dT;
          decLen = 1./(addParam + slope * T);
```

```
            updateDefects(numRepeat, decLen, threshold, amplitude,
                                        T, defCol, defRow, numDef, kB, seed, stepSat,
slopeSat);

            measureOrder(defCol, defRow, numDef, binSize, numSA, seed);
            dumpDefCoords2File(cfp, T, decLen, defCol, defRow, numDef, amplitude,
                    stepSat, slopeSat);
            dumpBinSize2File(bfp, T, decLen, binSize);
            writePc<<T<<"\t"<<binSize[0]<<"\n";


            fclose(cfp);
   }


writeTest.close();
writePc.close();
   fclose(bfp);
   return 0;

} // end-main()

/*--------------------------------------------------------------------*/
void dumpDefCoords2File(FILE *cfp, double T, double decLen,
                                                int *defCol, int *defRow, int numDef,
double ampl,
                                                double stepSat, double slopeSat)
{

          fprintf(cfp,"T= %8.3lf    decLen= %8.3lf   numDef= %d ampl= %8.3lf stepSat=
%8.3lf slopeSat= %8.3lf\n",
                                    T, decLen, numDef, ampl, stepSat, slopeSat);
          fprintf(cfp,"indDef                defCol            defRow\n");
          for (int i=0; i<numDef; i++)
          {
                    fprintf(cfp, "%d\t%d\t%d\n",i, defCol[i], defRow[i]);
          }

          fprintf(cfp,"----------------------------------------\n");
} // end-dumpDefCoords2File()

/*--------------------------------------------------------------------*/
void dumpBinSize2File(FILE *bfp, double T, double decLen, double *binSize)
```

```
{
        fprintf(bfp,"T = %8.3lf    decLen=%8.3lf\n", T, decLen);
        fprintf(bfp,"indBin                binSize\n");
        for (int i=0; i<NUM_BINS; i++)
        {
                fprintf(bfp, "%d\t%8.3lf\n",i, binSize[i]);
        }
   fprintf(bfp,"----------------------------------------\n");
} // end-dumpBinSize2File()

/*--------------------------------------------------------------------------*/
void initInputParams(char *file, double *T0, double *T1, double *dT, double *slope,
double *addParam,
                                        double *amplitude, double *threshold, int
*densDef, int *numRepeat,
                                        int *numSA, double *kB, double *stepSat, double
*slopeSat)
{
        FILE *fp;
        char varName[30];

        if ((fp = fopen(file, "r")) == NULL)
        {
          printf("%s: No such file\n", file);
          exit(1);
        }

//      T0              value
//      T1              value
//      dT              value
//      slope   value
//      addParam value
//      amplitude value
//      threshold value
//      densDef value
//      numRepeat value

        fscanf(fp,"%s %lf",varName, T0);
        fscanf(fp,"%s %lf",varName, T1);
        fscanf(fp,"%s %lf",varName, dT);
        fscanf(fp,"%s %lf",varName, slope);
        fscanf(fp,"%s %lf",varName, addParam);
        fscanf(fp,"%s %lf",varName, amplitude);
        fscanf(fp,"%s %lf",varName, threshold);
```

```
        fscanf(fp,"%s %d",varName, densDef);
        fscanf(fp,"%s %d",varName, numRepeat);
        fscanf(fp,"%s %d",varName, numSA);
        fscanf(fp,"%s %lf",varName, kB);
        fscanf(fp,"%s %lf",varName, stepSat);
        fscanf(fp,"%s %lf",varName, slopeSat);
        //writeTest<<"kB   "<<kB<<"   in initInputParams\n";

        fclose(fp);

} // end-initInputParams()

/*---------------------------------------------------------------------------*/
void updateDefects(int numRepeat, double decLen, double thresh, double ampl,
                                        double T, int *defCol, int *defRow, int numDef,
double kB,
                                        int seed, double stepSat, double slopeSat)
{
        double atomZCoord[6],
                        defZCoord;
        int             indAtom;
        int             is;

        int             atomCol[6],
                        atomRow[6];

        for(int i=0; i<numRepeat; i++)
        {
                for(int j=0; j<numDef; j++) {
        defZCoord = get_Zcoord(ampl, decLen, defCol[j], defRow[j],
                                                                        defCol, defRow,
numDef, stepSat,
                                                                        slopeSat);
                        atomCol[0] = defCol[j] + 1;
                        atomRow[0] = defRow[j];
                        atomCol[1] = defCol[j];
                        atomRow[1] = defRow[j] - 1;
                        atomCol[2] = defCol[j] - 1;
                        atomRow[2] = defRow[j] - 1;
                        atomCol[3] = defCol[j] - 1;
                        atomRow[3] = defRow[j];
                        atomCol[4] = defCol[j];
                        atomRow[4] = defRow[j] + 1;
                        atomCol[5] = defCol[j] + 1;
                        atomRow[5] = defRow[j] + 1;
```

```
                for(int k=0; k<6; k++)
                {
                        atomZCoord[k] = get_Zcoord(ampl, decLen, atomCol[k],
atomRow[k],
                                                                defCol, defRow,
numDef, stepSat, slopeSat);
                } // end-for(k)

                indAtom = get_Zmin(atomZCoord, atomCol, atomRow, 6, defCol,
defRow, numDef);
                if (indAtom == -1)
                {
                        // printf("Do not update defect %d\n", j);
                } else
                {                       // update defect...
                        is=is_movable(atomZCoord[indAtom], defZCoord, thresh,
T, kB, seed);
                        //writeTest<<"is\t"<<is<<"\n";
                        if ( is )
                        {
                                //writeTest<<"is\t"<<is<<"\n";
                          defCol[j] = atomCol[indAtom];
                          defRow[j] = atomRow[indAtom];
                        }
                }

              } // end-for(j)

        } // end-for(i)

} // end-updateDefects()

/*---------------------------------------------------------------------------*/
int is_movable(double atomZCoord, double defZCoord, double thresh, double T, double
kB, int seed)
{
        double monte;
        double boltzman;
        double kT;
        double energy;

        //int rancycle;

        //srand( (unsigned)time( NULL ) );
```

```
        //rancycle=rand()%100;
        //for(int r=0; r<rancycle; r++)
        //seed=rand()+seed;
        //srand(seed);

    if ((defZCoord - atomZCoord) > thresh) return(1);

    //srand( (unsigned)time( NULL ) );

        // get random number between 0 and 1
    monte = ((double)(rand()%NCOLS)) / ((double)NCOLS);
        energy = (thresh - (defZCoord - atomZCoord));
        //writeTest<<"energy  "<<energy<<"\n";
        kT = kB * T;
        //writeTest<<"kT "<<kT<<"\n";
        //writeTest<<"kB "<<kB<<"\n";
        //writeTest<<"T "<<T<<"\n";
        boltzman = exp(-(energy / kT));
        //writeTest<<"monte "<<monte;
        //writeTest<<"boltzman  " <<boltzman<<"\n";

        if (monte < boltzman) return (1);

        return (0);

}

/*---------------------------------------------------------------------------*/
int get_Zmin(double *atomZCoord, int *atomCol, int *atomRow, int numAtoms,
                        int *defCol, int *defRow, int numDef)
{
  int           indAtom=-1;
  double        min;
  int           sameFlag,
                        firstTime;

  firstTime = 1;
  for (int i =0; i<numAtoms; i++) {
          sameFlag = 0;
          for (int j=0; j<numDef; j++) {
                  if ((atomCol[i] == defCol[j]) && (atomRow[i] == defRow[j]))
                  {
                          sameFlag = 1;
                          break;
                  }
```

```
            } // end-for(j)

            if (sameFlag == 0) // it is not a defect
            {
                    if (firstTime) // initialize min and indAtom
                    {
                            min = atomZCoord[i];
                            indAtom = i;
                            firstTime = 0;
                    } else
                    {
                                    if (atomZCoord[i] < min) // update min and indAtom
                                    {
                                            min = atomZCoord[i];
                                            indAtom = i;
                                    }
                    } // end-else

            } // if(sameFlag)

    } // end-for(i)

    return indAtom;

} // end-getZmin()

/*-------------------------------------------------------------*/
double get_Zcoord(double ampl, double decLen, int atomCol, int atomRow,
                                    int *defCol, int *defRow, int numDef, double stepSat,
                                    double slopeSat)
{
        double K1[2],
                    K2[2],
                    K3[2];
        double A1[2],
                    A2[2];
        double atomX,
                    atomY;
        double *defX,
                    *defY;
        double disX, disY, distance, sum,
                    scalar_1, scalar_2, scalar_3;

        double x, sig;
        double zCoord;
```

```
K1[0] = 4.* PI/3.;                  K1[1] = 0;
      K2[0] = -(2.* PI)/3.;         K2[1] = (2.* PI) / sqrt(3.);
      K3[0] = -(2.* PI)/3.;         K3[1] = -(2.* PI ) / sqrt(3.);

      A1[0] = 1;              A1[1] = 0;
      A2[0] = -0.5;   A2[1] = sqrt(3)/2;

defX = (double *) malloc(sizeof(double) * numDef);
      defY = (double *) malloc(sizeof(double) * numDef);

      for (int i=0; i<numDef; i++)
      {
  defX[i] = A1[0] * defCol[i] + A2[0] * defRow[i];
        defY[i] = A1[1] * defCol[i] + A2[1] * defRow[i];
      } // end-for(i)

      atomX = A1[0] * atomCol + A2[0] * atomRow;
      atomY = A1[1] * atomCol + A2[1] * atomRow;

      zCoord = 0.0;

      for (i=0; i<numDef; i++) {

            disX = atomX - defX[i];
            disY = atomY - defY[i];
            distance = sqrt(disX*disX + disY*disY);

            scalar_1 = K1[0] * disX + K1[1] * disY;
            scalar_2 = K2[0] * disX + K2[1] * disY;
            scalar_3 = K3[0] * disX + K3[1] * disY;

            sum = cos(scalar_1) + cos(scalar_2) + cos(scalar_3);
            zCoord = zCoord + (-1)*exp(-distance / decLen) * sum;

      } // end-for(i)

      zCoord = zCoord * ampl;
      if (zCoord <0)
      {
            sig= -1.;
      }
      else
            sig =+1.;
```

```
	if (k<200)
	{
		writeTest<<"bofore "<<zCoord<<"\t";
	}

	x= fabs (zCoord);

	zCoord = sig*saturate(x, stepSat, slopeSat);

	if (k<200)
	{
	   writeTest<<"zCoord  after  "<<zCoord<<"\n";
		k++;
	}

	free(defX);
	free(defY);

	return zCoord;

} // end-get_Zcoord()


//*****************************************************************
double saturate(double x, double stepSat, double slopeSat)
{

	int ratio,n;
	double res, resn, zn;


	ratio=static_cast<int>(x/stepSat);
	n=ratio+1;
	//writeTest<<"\n"<<"n=  "<<n<<"\n";

	zn=(n-1)*stepSat;
	resn=stepSat*(1-pow(slopeSat,(n-1)))/(1-slopeSat);

	res=resn+(pow(slopeSat,(n-1)))*(x-zn);

	return res;
}
```

```
/*-------------------------------------------------------------*/
void throwDefects(int *defCol, int *defRow, int numDef, int seed)
{

 int stopFlag,
          sameFlag,
          indDef;

 int rancycle;



  /* Seed the random-number generator with current time so that
   * the numbers will be different every time we run.
   */
        srand(seed);
        rancycle=rand()%100;
        for(int r=0; r<rancycle; r++)
                seed=rand()%10;


        indDef=0;  //     indDef is index of the defect
        defCol[indDef]=rand()%NCOLS;
        defRow[indDef]=rand()%NROWS;

        stopFlag = 1;
        indDef++;
        while (stopFlag)
        {
          defCol[indDef]=rand()%NCOLS;
          defRow[indDef]=rand()%NROWS;
          sameFlag = 0;
          for (int m=0; m<indDef;m++)
          {
                  if ((defCol[m]==defCol[indDef]) && (defRow[m]==defRow[indDef]))
                  {
                          sameFlag = 1;
                          break;
                  }
          } // end-for(m)

          if (sameFlag == 0)
          {
                  indDef++;
```

```
                if (indDef == numDef)
                {
                        stopFlag = 0;
                }
          }
        } // end-while(stopFlag)

} // end-throwDefects()

/*-----------------------------------------------------------------*/
void measureOrder(int *defCol, int *defRow, int numDef, double *binSize, int numSA,
int seed)
{


        int siteACol[50],
                siteARow[50],
                numASites,
                siteBCol[50],
                siteBRow[50],
                numBSites,
                siteCCol[50],
                siteCRow[50],
                numCSites;
        int sizeSA;                     //atoms along the side of the sampling area (SA)

        sizeSA = 12;

    generateGrid(0, sizeSA, siteACol, siteARow, &numASites);
        generateGrid(1, sizeSA, siteBCol, siteBRow, &numBSites);
        generateGrid(2, sizeSA, siteCCol, siteCRow, &numCSites);

        samlping(sizeSA, defCol, defRow, numDef,
                        siteACol, siteARow, numASites,
                        siteBCol, siteBRow, numBSites,
                        siteCCol, siteCRow, numCSites,
                        binSize, numSA, seed);

} // end-measureOrder()

/*-----------------------------------------------------------------*/
void samlping(int sizeSA, int *defCol, int *defRow, int numDef,
                         int *siteACol, int *siteARow, int numASites,
                         int *siteBCol, int *siteBRow, int numBSites,
                         int *siteCCol, int *siteCRow, int numCSites,
```

```
                        double *binSize, int numSA, int seed)
{
//cout<<"numASites\t"<<numASites<<"\n";
//cout<<"numBSites\t"<<numBSites<<"\n";
//cout<<"numCSites\t"<<numCSites<<"\n";

        //int numSA;
        int originSACol,
                originSARow;
        int numA,
                numB,
                numC,
                min,
                defTotal;
        int *defSACol,
                *defSARow;
        double fraction,
                        lowerBorder,
                        upperBorder;
        double testSum;

        //numSA = 1000;

        defSACol = (int *) malloc(sizeof(int) * numDef);
        defSARow = (int *) malloc(sizeof(int) * numDef);

        //int rancycle;

        srand( (unsigned)time( NULL ) );
        //srand(seed);
        //rancycle=rand()%100;
        //for(int r=0; r<rancycle; r++)
        //seed=rand();
        srand (seed+rand());

                                        // get the random number for SA origin
                        //srand( (unsigned)time( NULL ) );
                        int i=0;
                        for (; i<numSA;)
                        {

                                //writeTest<<"sampling\t"<<i<<"\n";
                                        /* Seed the random-number generator with current
time so that
                                         * the numbers will be different every time we run.
```

```
                                        */
                                                //srand( (unsigned)time( NULL ) );
                                                //srand(2099999);
                                                originSACol=rand()%NCOLS;
                                                originSARow=rand()%NROWS;


        //writeTest<<"origingSACol\t"<<originSACol<<"\n";

                                                // Check how many of defects
                                                // 0. recenter defects
                                                // 1. inside the SA
                                                // 2. on site A, B or C
                                                // 3. get the minimum of A, B and C


                                                // 0. recenter
                                                for (int indDef=0; indDef<numDef;
indDef++)
                                                {
                                                        defSACol[indDef] = defCol[indDef]
- originSACol;
                                                        defSARow[indDef] =
defRow[indDef] - originSARow;

        //writeTest<<"sampling\tdefSACol\t"<<defSACol[indDef]<<"\n";

        //writeTest<<"sampling\tdefSARow\t"<<defSARow[indDef]<<"\n";

                                                }

                                                numA=0;// number of defects on A sites
inside SA
                                                numB=0;//
B
                                                numC=0;//
C
                                                for (indDef=0; indDef<numDef; indDef++)
                                                {
                                                        if ((defSACol[indDef] >= 0) &&
                                                                (defSACol[indDef] <
sizeSA) &&
                                                                (defSARow[indDef] >= 0)
&&
```

```
                                                    (defSARow[indDef] <
sizeSA) )
                                                {
                                                    //defect is inside SA
                                                    //cout<<"\n\n\n Inside SA";

                                                    for (int indA=0;
indA<numASites; indA++)
                                                    {
                                                        if ((defSACol[indDef]
== siteACol[indA]) &&
        (defSARow[indDef] == siteARow[indA]))
                                                        {
                                                            numA++;
        //writeTest<<"numA\t"<<numA<<"\n";
                                                        }
                                                    }
                                                    // I could put more checkings
and branchings but who cares
                                                    for (int indB=0;
indB<numBSites; indB++)
                                                    {
                                                        if ((defSACol[indDef]
== siteBCol[indB]) &&
        (defSARow[indDef] == siteBRow[indB]) )
                                                        {
                                                            numB++;
        //writeTest<<"numB\t"<<numB<<"\n";
                                                        }
                                                    }

                                                    for (int indC=0;
indC<numCSites; indC++)
                                                    {
                                                        if ((defSACol[indDef]
== siteCCol[indC]) &&
```

```
        (defSARow[indDef] == siteCRow[indC]) )
                                                                {
                                                                        numC++;

        //writeTest<<"numC\t"<<numC<<"\n";
                                                                }

                                                        //      cout<<"In
sampling\n";
                                                        //
        cout<<"numA\tnumB\tnumC\n";
                                                        //
        cout<<numA<<"\t"<<numB<<"\t"<<numC<<"\t";
                                                        }
                                                }
                                        }

                                        // Analyze this!

                                        defTotal=numA+numB+numC;
                                        //cout<<"\ndefTotal   "<<defTotal<<"\n";

                                        if ((numA <= numB) && (numA <=
numC))
                                        {
                                                min=numA;
                                        } else if ((numB <= numA) && (numB <=
numC))
                                        {
                                                min=numB;
                                        } else
                                        {
                                                min=numC;
                                        }
                                        if (defTotal>3)
                                        {
                                                i++;
                                                //cout << "Is it ever nonzero";
                                                //writeTest<<"min\t"<<min<<"\n";

        //writeTest<<"defTotal\t"<<defTotal<<"\n";
                                                fraction = ((double) min) / ((double)
defTotal);
```

```
        //writeTest<<"fraction\t"<<fraction<<"\n";
                                                        // Put it in the bin
                                                        lowerBorder=0;
                                                        upperBorder=1./18.;
                                                        for (int indBin=0;
indBin<NUM_BINS; indBin++)
                                                        {

                                                        //
        writeTest<<"lowerBorder\t"<<lowerBorder<<"\n";
                                                        //
        writeTest<<"upperBorder\t"<<upperBorder<<"\n";

                                                                if ((fraction >= lowerBorder)
&& (fraction < upperBorder))
                                                                {
                                                                        binSize[indBin]++;

                                                                }
                                                                lowerBorder=upperBorder;

        upperBorder=lowerBorder+(1./18.);

                                                                } // end-for(indBin)
                                                        }//end-defTotal if

                                                //Continue with another SA
                        } // end-for(i)

                        // Normalization

                        for (int indBin=0; indBin<NUM_BINS; indBin++)
                        {
                                //writeTest<<"binSize\t"<<binSize[indBin]<<"\n";
                                binSize[indBin] = binSize[indBin] / numSA;

                        }
                        //writeTest<<"numSA\t"<<numSA<<"\n";
                        testSum=0;
                        for ( indBin=0; indBin<NUM_BINS; indBin++)
                        {

                                testSum=testSum+binSize[indBin];
```

```
                        }
                        //writeTest<<"testSum\t"<<testSum<<"\n";



        free(defSACol);
        free(defSARow);

} // end-sampling()

/*---------------------------------------------------------------------------*/

void generateGrid(int shift, int sizeSA, int *colArray, int *rowArray, int *numSites)
{
        int g1Column,
                g1Row,
                g2Column,
                g2Row;

        int devMax, ind;

        int intermCol,
                intermRow;

                        g1Column=2;   //3x3 vectors in root3 units
                        g1Row=1;

                        g2Column=1;
                        g2Row=2;

                        devMax=10;   // +/- 10 3x3 units each way
                        ind = 0;
                        *numSites = 0;

                        for (int m=-devMax; m<devMax; m++)
                        {
                                for (int n=-devMax; n<devMax; n++)
                                {
                                        //AAAAAAAAAAAAAAAAAAAAAAAAAAA
                                        intermCol = g1Column*m + g2Column*n + shift;
                                        intermRow = g1Row*m + g2Row*n;

                                        // check if it is inside the area

                                        if ((intermCol >= 0) &&
```

```
                                        (intermCol < sizeSA) &&
                                        (intermRow >= 0) &&
                                        (intermRow < sizeSA) )

                                {

                                        colArray[ind] = intermCol;
                                        rowArray[ind] = intermRow;
                                        ind++;
                                        *numSites = ind;
                                }

                                } // end-for(n)
                        } // end-for(m)
} // end-generateGrid()

/*-------------------------------------------------------------*/
void init_binSize(double *binSize) {

   for (int i=0; i<NUM_BINS; i++)
   {
           binSize[i] = 0;
   }
}
```

Appendix E: Simulation of STM images from defect distribution

```
//This code is to calculate pixels of an image for a given defect distribution
// read coordinates
// calculate the image
// write it into file



#include <fstream.h>
#include <iostream.h>
#include <stdlib.h>
#include <stdio.h>
#include <time.h>
#include <math.h>
#include <string.h>

#define NUM_RC       200  // Number of rows or columns
const double AREA_SIZE=40;
const double PI=3.1419526654;

double **dmatrix(long nrow, long ncol);


void readInput(double *mark_ptr, double *origin);
void readDefects(char *filename, double *T, double *decLen, int *numDef, double
*ampl,
                                    int *defCol, int *defRow, double *stepSat, double
*slopeSat);
double root3(double pixX, double pixY, double ampl);
double waves( int *DefCol, int *DefRow, double pixX, double pixY,
                          double decLen, double ampl, int numDef, double stepSat, double
slopeSat);
double defectSites(double zCoord, int *defCol, int *defRow, double pixX,
                                     double pixY, double mark, int numDef);
int calculatePixZ(double **pixZ, double d, int *defCol, int *DefRow,
                                    double decLen, double ampl, int numDef, double mark,
                                    double stepSat, double slopeSat, double origin);
void writeFilePixZ(char *filename, double **pixZ);
double saturate(double x, double stepSat, double slopeSat);

ofstream writeTest("test.txt");
//int k;
//*************************************************************
int main()
```

```
{
//      k=0;
        double d;                               //distance between pixels
        double T,
                        decLen,
                        ampl;
        double **pixZ;
        double  mark;
        double origin;

        int             numDef;
        int             *defCol,
                        *defRow;
        double stepSat;
        double slopeSat;

        char    filename[50];

   printf("Enter defect coords file name: ");
        scanf("%s", filename);

        printf("Enter number of defects: ");
        scanf("%d", &numDef);

        d=AREA_SIZE/NUM_RC;
        pixZ = dmatrix(NUM_RC, NUM_RC);
   defCol = (int *) malloc(sizeof(int)*numDef);
        defRow = (int *) malloc(sizeof(int)*numDef);

        readInput(&mark, &origin);
        readDefects(filename, &T, &decLen, &numDef, &ampl, defCol, defRow,
&stepSat, &slopeSat);
        mark=-ampl*3;
        calculatePixZ(pixZ,d,defCol,defRow,decLen,ampl,numDef,mark,stepSat,slopeSat
,origin);
        //for (int p=0; p<numDef;p++){
        //writeTest<<"defRow in main\t"<<defRow[p]<<"\n";
        //writeTest<<"defCol in main\t"<<defCol[p]<<"\n";
        //}


        printf("Enter pixZ filename: ");
        scanf("%s", filename);
        writeFilePixZ(filename, pixZ);
```

```
	ofstream writeTest("test.txt");

return 0;
}// end of main

//*****************************************************************/
void writeFilePixZ(char *filename, double **pixZ)
{
	FILE *fp;

	fp=fopen(filename, "w");
	if (fp==NULL)
	{
		perror("writeFilePixZ");
		exit(1);
	}

	for (int j=0; j<NUM_RC; j++)
	{
		for(int i=0; i<NUM_RC; i++)
		{
			fprintf(fp,"%8.3lf\n", pixZ[i][j]);
		}
	}

}
//*****************************************************************/
void readInput(double *mark_ptr, double *origin)
{
	FILE *fp;

	fp=fopen("input.txt", "r");
	if (fp==NULL)
	{
		perror("readInput");
		exit(1);
	}

	fscanf(fp,"%lf", mark_ptr);
	fscanf(fp,"%lf", origin);
}

//*****************************************************************/
void readDefects(char *filename, double *T, double *decLen, int *numDef, double
*ampl,
```

```
                                int *defCol, int *defRow, double *stepSat, double
*slopeSat)
{
        FILE *fp;
        char name[30];
        int  index;
        int  i;

        fp=fopen(filename, "r");
        if (fp==NULL)
        {
                perror("readDefects");
                exit(1);
        }

        fscanf(fp, "%s %lf",name, T);
        fscanf(fp, "%s %lf",name, decLen);
        fscanf(fp, "%s %d",name, numDef);
        fscanf(fp, "%s %lf",name, ampl);
        fscanf(fp, "%s %lf",name, stepSat);
        fscanf(fp, "%s %lf",name, slopeSat);


        for (i=0; i<3; i++) fscanf(fp, "%s",name);



        for(i=0; i<*numDef; i++)
        {
                fscanf(fp, "%d %d %d", &index, &defCol[i], &defRow[i]);
        }

}
//*****************************************************************
int calculatePixZ(double **pixZ, double d, int *defCol, int *defRow, double decLen,
                                double ampl, int numDef, double mark, double stepSat,
double slopeSat,
                                double origin)
{

        //--------------------------------
        // initialize pixZ
        double pixX, pixY;

        for (int iPix=0; iPix<NUM_RC; iPix++)
```

```
	{
		for (int jPix=0; jPix<NUM_RC; jPix++)
		{
			pixZ[iPix][jPix]=0;

		}// end columns
	}// end rows
	//---------------------------------

	//---------------------------------
	// calculate pixelZ

	for (iPix=0; iPix<NUM_RC; iPix++)
	{
		for (int jPix=0; jPix<NUM_RC; jPix++)
		{
			pixX=iPix*d+origin;
			pixY=jPix*d+origin;
			//cout<<"pixX\t"<<pixX<<"\t in the calculatePixZ\n";
			//cout<<"pixY\t"<<pixY<<"\t in the calculatePixZ\n";

			pixZ[iPix][jPix]=pixZ[iPix][jPix]
				+root3(pixX, pixY,ampl)
				+waves(defCol, defRow, pixX, pixY, decLen, ampl,
numDef, stepSat, slopeSat);


	pixZ[iPix][jPix]=defectSites(pixZ[iPix][jPix],defCol,defRow,pixX,pixY,mark,nu
mDef);

		}// end columns
	}// end rows
	//---------------------------------

	return 0;

}
//*****************************************************************
double root3(double pixX, double pixY, double ampl)
{
	double K1[2],
		K2[2],
		K3[2];
```

```
        double  scalar_1, scalar_2, scalar_3;

        double zCoord;

   K1[0] = 2.* PI;                  K1[1] = 2.*PI/sqrt(3);
        K2[0] = 0;                          K2[1] = (4.* PI) / sqrt(3.);
        K3[0] = -(2.* PI);          K3[1] = (2.* PI ) / sqrt(3.);

                scalar_1 = K1[0] * pixX + K1[1] * pixY;
                scalar_2 = K2[0] * pixX + K2[1] * pixY;
                scalar_3 = K3[0] * pixX + K3[1] * pixY;

                zCoord =0.1*ampl*( cos(scalar_1) + cos(scalar_2) + cos(scalar_3) );
                //cout<<"zCoord\t"<<zCoord<<"\t in the root3\n";
        return zCoord;
}

//*************************************************************
double waves( int *defCol, int *defRow, double pixX, double pixY, double decLen,
                        double ampl, int numDef, double stepSat, double slopeSat)
{
        double K1[2],
                   K2[2],
                   K3[2];
        double A1[2],
                   A2[2];

        double *defX,
                   *defY;
        double disX, disY, distance, sum,
                   scalar_1, scalar_2, scalar_3;

        double zCoord;
        double x, sig;

   K1[0] = 4.* PI/3.;               K1[1] = 0;
        K2[0] = -(2.* PI)/3.;       K2[1] = (2.* PI) / sqrt(3.);
        K3[0] = -(2.* PI)/3.;       K3[1] = -(2.* PI ) / sqrt(3.);

        A1[0] = 1;              A1[1] = 0;
        A2[0] = -0.5;   A2[1] = sqrt(3)/2;

   defX = (double *) malloc(sizeof(double) * numDef);
        defY = (double *) malloc(sizeof(double) * numDef);
```

```
        for (int i=0; i<numDef; i++)
        {
    defX[i] = A1[0] * defCol[i] + A2[0] * defRow[i];
      defY[i] = A1[1] * defCol[i] + A2[1] * defRow[i];
        } // end-for(i)



        zCoord = 0.0;

        for (i=0; i<numDef; i++) {

                disX = pixX - defX[i];
                disY = pixY - defY[i];
                distance = sqrt(disX*disX + disY*disY);

                scalar_1 = K1[0] * disX + K1[1] * disY;
                scalar_2 = K2[0] * disX + K2[1] * disY;
                scalar_3 = K3[0] * disX + K3[1] * disY;

                sum = cos(scalar_1) + cos(scalar_2) + cos(scalar_3);
                zCoord = zCoord + (-1)*exp(-distance / decLen) * sum;

        } // end-for(i)

        zCoord = zCoord * ampl;

                zCoord = zCoord * ampl;
        if (zCoord <0)
        {
                sig= -1.;
        }
        else
                sig =+1.;

        x= fabs (zCoord);

        zCoord = sig*saturate(x, stepSat, slopeSat);

        free(defX);
        free(defY);

        return zCoord;

}
```

```
//*****************************************************************
double saturate(double x, double stepSat, double slopeSat)
{

        int ratio,n;
        double res, resn, zn;


        ratio=static_cast<int>(x/stepSat);
        n=ratio+1;
        //writeTest<<"\n"<<"n=  "<<n<<"\n";

        zn=(n-1)*stepSat;
        resn=stepSat*(1-pow(slopeSat,(n-1)))/(1-slopeSat);

        res=resn+(pow(slopeSat,(n-1)))*(x-zn);

        return res;
}

//*****************************************************************
double defectSites(double zCoord, int *defCol, int *defRow, double pixX,
                                        double pixY, double mark, int numDef)
{

        double A1[2],
                A2[2];

        double *defX,
                *defY;
        double upperBorderX,
                lowerBorderX,
                upperBorderY,
                lowerBorderY,
                squareSize;



        squareSize = 1.;

        A1[0] = 1;              A1[1] = 0;
        A2[0] = -0.5;   A2[1] = sqrt(3)/2;

   defX = (double *) malloc(sizeof(double) * numDef);
```

```
    defY = (double *) malloc(sizeof(double) * numDef);

    for (int i=0; i<numDef; i++)
    {

            //if (k<200){
            //writeTest<<"defRow = " <<defRow[i]<<"\n";
            //writeTest<<"defCol = " <<defCol[i]<<"\n";
    //      k++;}
defX[i] = A1[0] * defCol[i] + A2[0] * defRow[i];
      defY[i] = A1[1] * defCol[i] + A2[1] * defRow[i];
    } // end-for(i)


    //draws a square around a defect
    for (i=0; i<numDef; i++)
    {

            upperBorderX=defX[i]+squareSize/2.;
            lowerBorderX=defX[i]-squareSize/2.;
            upperBorderY=defY[i]+squareSize/2.;
            lowerBorderY=defY[i]-squareSize/2.;

            //if (k<200)
            //{
            //      writeTest<<"ubx                 pixX    lbx\n";
            //
    writeTest<<upperBorderX<<"\t"<<pixX<<"\t"<<lowerBorderX<<"\n";
            //      writeTest<<"uby                 pixY    lby\n";
            //
    writeTest<<upperBorderY<<"\t"<<pixY<<"\t"<<lowerBorderY<<"\n";
            //      k++;
            //}

            if ( pixX<upperBorderX &&
                     pixX>lowerBorderX &&
                     pixY<upperBorderY &&
                     pixY>lowerBorderY )
            {
                     zCoord=mark;
                    // printf("zCoord in defectSites =  %lf\n",zCoord);
            }
    }

    free(defX);
```

```
        free(defY);
        return zCoord;
}

/*************************************************************/

double **dmatrix(long nrh, long nch)

/* allocate a double matrix to array of pointers to rows */
/* from Numerical Recipes in C */
{
  long nrl=0, ncl=0;
  long i, nrow=nrh-nrl+1,ncol=nch-ncl+1;
  double **m;

  /* allocate pointers to rows */
  m=(double **) malloc((size_t) ((nrow+1)*sizeof(double*)));
  if(!m) printf("allocation failure 1 in matrix()");
  m += 1;
  m -= nrl;

 /* allocate rows and set pointers to them */
 m[nrl]=(double *) malloc((size_t) ((nrow*ncol+1)*sizeof(double)));
 if(!m[nrl]) printf("allocation failure 2 in matrix()");
 m[nrl] += 1;
 m[nrl] -= ncl;

 for(i=nrl+1;i<=nrh;i++) m[i]=m[i-1]+ncol;
 /* return pointer to array of pointers to rows */
 return m;
}
```

VITA

Anatoli Vasilievich Melechko was born in Omsk, USSR on July 22, 1969. He graduated from the Division of Quantum Optics, Department of Physics, Novosibirsk State University, Novosibirsk, Russia in 1992 with a Master of Science degree in Physics. In 1989 he joined the laboratory of nonlinear optics headed by Prof. D.V. Petrov in the Institute of Semiconductor Physics (ISP), Siberian Division of Russian Academy of Science, Novosibirsk, Russia. He continued his work in ISP as a junior research scientist after receiving a MS degree until 1996. He began his studies as a Ph. D. student under the supervision of Prof. E. Ward Plummer at the Department of Physics and Astronomy, University of Tennessee, Knoxville in 1996 and received a degree of a Doctor of Philosophy in 2001. During the period from 1996 to 2001 he was a Graduate Research Assistant.

His research interests lie in the area of nanoscale science. He has a significant experience with Scanning Tunneling Microscopy and other surface characterization techniques such as Low Energy Electron Diffraction, Electron Energy Loss Spectroscopy, Auger Electron Spectroscopy, and Mass Spectrometry, as well as surface preparation techniques, thin film growth methods, and Ultra High Vacuum and cryogenic equipment. While performing scientific modeling and simulations of physical processes, he has gained an extensive computer programming experience in C and FORTRAN languages. He also has advance skills in using various image processing applications for experimental data analysis.